On Turbulent Coherent Structures in Transient Processes of Aerophones - Principles of Sound Generation

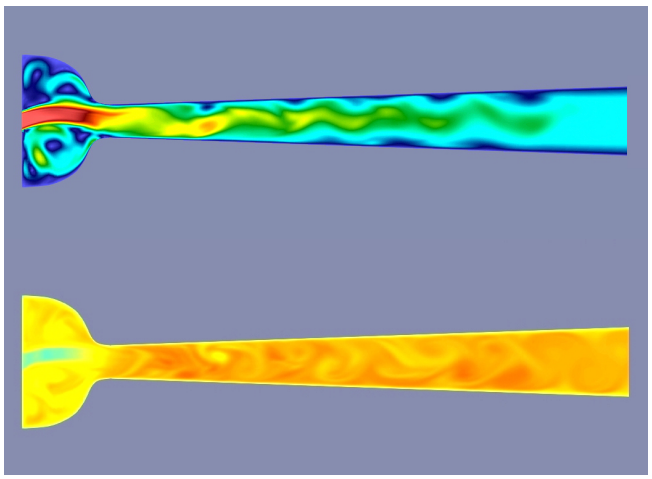

Habilitation thesis

submitted at the
Faculty of Humanities
of the University Hamburg

by

Dr. rer. nat. Jost Leonhardt Fischer

dedicated to my father

Dr. rer. nat. Jost Leonhardt Fischer

Bogenstraße 1
20144 Hamburg
Germany

jost.leonhardt.fischer@gmail.com

I hereby confirm that this thesis and the work presented in it is entirely my own. Where I have consulted the work of others this is always clearly stated. All statements taken literally from other writings or referred to by analogy are marked and the source is always given. This paper has not yet been submitted to another examination office, either in the same or similar form.

I agree that the present work may be verified with an anti-plagiarism software.

Hamburg, 26.06.2022

Jost Leonhardt Fischer

Contents

List of Figures

List of Tables

Preface

The present work has its investigative focus on transient processes of aerophones and the question how sound is created in this class of musical instruments. In order to do justice to the complexity of the research question, the author has carefully structured his approach. The work is divided into three parts. Part one starts with a short introduction into the topic in chapter 1, followed by an overview of historical milestones and the current state of the art of research on sound generation in aerophones in chapter 2. The second part provides the necessary mathematical, physical and numerical tools that are used in this work. This is particularly addressed to students of musicology. The preliminary remarks of chapter 3 should make it easier to get started with the complex topic of sound generation in aerophones and at the same time provide some basic concepts of mathematics, fluid mechanics and aeroacoustics. The interested reader with appropriate mathematical and physical knowledge can skip this part. It's in the nature of the research subject that for certain passages of the work, extended physical knowledge in fluid mechanics and in nonlinear dynamics is required. This will be carefully motivated and executed as far as the scope of the work allows. In cases where this framework is no longer sufficient, reference is made to the relevant literature. In order to understand the considerations in which numerical simulations are used, it is necessary to convey the basics and the methodical procedure for numerical calculations. This will be explained in the chapter 4. In the third part a broad range of aspects of sound generation will be discussed by acoustic measurements and by utilizing numerical simulations in chapter 5. We start with the class of brass instruments, and in particular discuss trans-sonic phenomena in the initial transient of the piccolo trumpet using acoustic measurements on the propagation speed of pressure waves in the initial transient in section 5.1. The results are discussed in detail. Subsequently, analogue acoustic measurements are carried out on other brass instruments such as on the trumpet, the trombone, the French horn, and on the tuba. Then we return to our role model, the piccolo trumpet. With the help of numerical simulations we look at the blowing process inside the instrument. In section 5.2 we also focus on velocity measurements and trans-sonic phenomena in the initial transient, but change the instrument class by examining the recorder and recorder-like instruments. After this we change the focus on optimization of sound generation. By looking at the reconstruction of a bone flute we introduce an interdisciplinary project where we show how different scientific and technical disciplines work together to make the fragment of a bone flute playable again. The next instrument we look at is the organ pipe in section 5.3. We focus on turbulent, coherent structures and on the role of shock waves in the genesis of the sound field inside the instrument. For this we use the methods of numerical simulation, advanced visualization techniques as well as the method of coarse-graining. In particular we discuss the jet of the organ pipe, its fluid mechanical properties and its stability properties. Subsequently the mutual interplay of the jet and the sound field in the resonator are discussed. In section 5.4 the focus switches to the overblowing, another important transient process related with aerophones, particularly the Turkish ney. With the presented work, the author would like to take the reader into the exciting world of aerophones and to a fundamental understanding of sound production in perhaps the most inspiring musical instruments we have - the aerophones.

Part I

Chapter 1

Introduction

Multi pertransibunt et augebitur scientia

Francis Bacon, Novum organum scientiarum, 1620

Humans have been making flute-like instrumemts since the beginning of their cultural development. The oldest testimony to date, the Divje Babe flute, was recovered during systematic archaeological excavations in 1995 in a cave close to the Idrijca River near Cerkno in Slovenia [Montagu (2017)]. The instrument, which is dated to 50,000-60,000 years according to recent ^{14}C, AMS, U/Th and ESR analysis[1], was made from a femur bone of a cave bear and shows clear traces of processing on the finger holes. The Fragment represents an important evidence that casts a light on the spiritual life of Neanderthals, their handcraft skills as well as their abilities as artists [Truk, Otte (2020)]. Other excavations, e.g. the bone flute fragments from caves in Geißenklösterle and Hoher Fels in the Swabian Jura in Germany, which are dated to about 42,000 years and 35,000 years, and which are made from bearded vulture bones and mammoth ivory, confirm a widespread culture of instrument making in the Paleolithic on the European continent.

The archaeological discoveries show that intuitive knowledge about the construction and the functionality of aerophones[2] was developed and passed on very early on in human cultural history. Despite this long tradition of instrument making, the principles of natural law of sound generation in aerophones are still largely misunderstood until today. On the one hand, this is due to the fact that the scientific understanding of the processes in nature was only placed on a solid mathematical basis by Newton by publishing the Philosophiae Naturalis Principia Mathematica in 1687 [Newton (1687)]. Another important aspect is that the sound production in aerophones is not just a purely linear acoustic process, but seems to be a complex nonlinear interplay of fluid-mechanical and aeroacoustic dynamic processes. Although nonlinear processes were already described phenomenologically by Huygens around 1640, the mathematical tools for the description were only developed almost 400 years later by Poincaré and Mandelstam [Poincaré (1892-1899)], Birkhoff [Birkhoff (1912)], van der Pol [van der Pol (1926).], Andronov [Andronov, Chaikin (1949)] and other. In addition, turbulent flow processes which apparently play an important role in sound generation of aerophones, couldn't have been flanked by a

[1] The ^{14}C method is also referred to as carbon-14 dating method or radiocarbon dating method, AMS method means accelerator mass spectrometry, U/Th method is a dating method using uranium and thorium, also referred to as thorium-230 dating. The ESR method means electron spin resonance dating method.

[2] Aerophones are, roughly speaking, musical instruments that produce sound mainly by setting a body of air in vibrations utilizing an air stream.

complete physical theory until today. The present work aims to approach these topics.

Aerophones have been classified by Hornborstel-Sachs as one of the four main classes of instruments[3]: idiophones, membranophones, chordophones and aerophones [Hornborstel, Sachs (1914)]. The aerophones split into the sub-classes of the free aerophones and the non-free aerophones. Denoted as free aerophones are instruments where the vibrating air volume is not within the instrument, for example the bullroarer. Non-free aerophones are so called because the vibrating volume of air is inside the instrument – and therefore not free. The latter class is divided into the edge-blown aerophones or flutes, trumpets and the reed instruments. The presented word will spare out reed and double reed instruments. The reason for this lies less in the fact that these instruments have already been sufficiently researched or are even less interesting, on the contrary. Rather, the author's decision is based on the fact that these instruments have an additional dynamic element, the reed, and thus the complexity of the sound generation is once again significantly increased, which would simply go beyond the scope of this study.

Complexity is the keyword that will guide us in this work. We will be confronted with complexity when we get an overview of the various fluid mechanical and aeroacoustic phenomena within the sound generation. We will deal with complexity when we discuss the interactions of turbulent coherent structures with geometrical constraints in different musical instruments. We will rediscover complexity in the mutual interactions of fluid mechanical structures and aeroacoustic objects. And last but not least, we will encounter complexity when we trace nonlinearities and delve into the dynamics of transient processes. But in the same breath, it's not so easy to define what complexity actually means in general. We will see that the blowing process in aerophones creates its own inherent dynamics involving a large number of elements that influence each other either directly or indirectly. This creates structures with their own properties, for instance coherency, that have a significant influence on the sound generation process. We will see how these structures and objects act simultaneously or with time delay on different spatial and temporal scales. We will find out how these structures and objects create both irreversible and reversible dependencies. All of these aspects lead to a variety of movements and characteristics, starting with relatively simple linear propagation, rotation, shearing and compression, through nonlinear damping and nolinear excitation to chaotic behavior like mixing and turbulence. All of this is an expression of complexity, and in the best case, it ends in a very beautiful goal - the generation of periodic vibrations, which we perceive as sound and which touches us deeply at one time after another.

As scientists, we try to unravel some of the details of this great mystery – as Darwin once wrote about music in his notes – by exploring the underlying laws of nature [Darwin (1858/1859)]. The maxim when reading this study should therefore always be: Stay humble and curious as you venture into the unknown every day, yet fearless and unreserved in mind. With this motto, I hope the reader enjoy studying this habilitation thesis.

[3]Later on the electrophones have been added to this systematic classification.

Chapter 2

Milestones and the Current State of the Art

> Everything great comes about because some do more than they have to.
>
> Hermann Gmeiner, social pedagogue, founder of SOS Children's Villages

The research of sound generation, sound formation and articulation in aerophones has a long-standing tradition of more that 100 years. In 1894 Sir William Strutt, better known as Lord Rayleigh, describes self-sustaining vibrations in acoustical systems in his famous book 'The Theory of Sound', Vol. I, §68a [Rayleigh (1896)]. Cremer and Ising follow these considerations to examine the self-excited oscillations of organ pipes experimentally and modelling the jet [Cremer, Ising (1967)].

Turbulence as a source of sound is primarily studied by Lighthill and Powell in the 1950s and 1960s. [Lighthill (1952)],[Powell (1964)]. Important contributions to this topic are also given by Ffowcs-Williams, Hawkings and Howe [Ffowcs-Williams, Hawkings], [Howe, M. (2002)]. The formation of sound in aerophones is intensively researched in the 1970s. Benade [Benade (1968)], Elder [Elder (1992)] and Coltman [Coltman (1976)] investigate the mechanisms that drive the jet in organ pipes experimentally, inter alia through detailed impedance measurements of sound generation as a function of jet speed. In 1974 Fletcher discusses the jet of organ pipes as part of a nonlinear excitation mechanism that leads to the creation of sound. The acoustic impedance of the jet is examined as a function of the frequency with the help of a lumped model [Fletcher (1974)], [Fletcher (1976)]. The main difficulties are to understand the role of turbulence in these formation processes.

In 1996 Fabre, Hirschberg and Wijnands research on the vortex shedding in the working mode of an organ pipe [Fabre et al.(1996)]. With their investigations of a physical model for organ pipes in 2000, Fabre and Hirschberg reasonably point out how uncertain the knowledge about the actual occurrence of sound formation in wind instruments is [Fabre, Hirschberg 2000]. They classify the problem into the investigation of edges and tips (labia), the exploration of boundary and shear layers, and the dynamics of temporal and spatial reinforcement mechanisms that influence the stability of the jet. The nonlinear dynamics of musical reed and brass wind instruments were investigated by Cambell. He works out the importance of the player's lip on sound generation of brass instruments, particularly the coupling between lips and aircolumn [Campbell (1999)].

In 2006 Abel, Bergweiler and Gerhardt-Multhaupt carry out experimental investigations of synchronization of organ pipes. The focus is on the effect of external acoustic drivers. First important insights into the structure of the complex interaction can be gained [Abel et al.(2009)]. In 2006 Paál, Angster, Garen and Miklós visualize the blowing process and the working process of closed and open organ pipes using the 'Schlieren' method [Paál, Angster, Garen, Miklós (2006)]. In the region of the organ pipe's mouth, speed measurements of the air flow in two directions are carried out using LASER-Doppler Anemometry (LDA) with the result that the unstable wave of the jet behaves differently, depending on whether the jet is moving in or out. Abel, Ahnert and Bergweiler can show that the phenomenon of the mutual sound canceling of two organ pipes can be explained by the dynamics of self-organizing oscillator system [Abel et al.(2009)]. For this purpose, the sound data are reduced to a nonlinear oscillator system using a phase space reconstruction method. In 2008 Bader investigate individual reed characteristics due to changed damping using coupled flow-structure and time-dependent geometry [Bader (2008)].

Miyamoto, Takahashi, Kobayashi investigate in 2010 the sound generation in a wind instrument with the help of numerical simulations [Miyamoto et al. (2010)]. In particular, the complex dynamics of the jet in the generator region can be simulated. In 2012 Fischer researches the synchronization phenomena of nonlinear oscillators using the example of organ pipes [Fischer (2012)]. For the first time, it is possible to map the mechanisms of sound generation in the organ pipe to a nonlinear oscillator model (van der Pol system) utilizing coarse-graining methods. In addition, the coupling elements and the coupling functions within the instrument can be separated. Particularly it succeeds to show how the instabilities in the shear layers of the jet flow influence the dynamics of the jet. In 2013 Bader gives a comprehensive overview of nonlinearities and synchronization in musical acoustics and music psychology [Bader (2013)]. This also a new approach on the inherent interplay between parts of musical instruments, the impulse pattern formulation. The basic basic assumption here is that the interactions between instrument parts are impulse-like.

Fischer investigate the nonlinear coupling mechanisms of two organ pipes experimentally and numerically in 2014 [Fischer (2014)]. The coupling strength that - under certain circumstances - leads to synchronization of the instruments are modeled as a bidirectionally nonlinear coupling function in a nonlinear oscillator system. In 2017 Fischer could show numerically how different room geometries influence the sound production and sound radiation of organ pipes [Fischer (2017)]. Fischer and Bader carry out numerical simulations of the rim-blown Turkish ney for the first time and examine the interaction between the turbulent flow field and the acoustic field [Fischer, Bader (2017)]. In 2019, Fischer, Bader and Abel examine the dynamics of the flow field and the acoustic field in the generator region of an organ pipe using numerical simulations. The turbulent flow field of the jet can be separated from the acoustic field in the instrument [Fischer, Bader, Abel (2019)]. Fischer also investigates the shock wave characteristics in the initial transient of an organ pipe [Fischer (2019)] and in recorder-like instruments. A completely new effect in terms of initial sound generation. In 2020, Fischer, Plath and Kirsch succeed with the reconstruction of the mouthpiece of a fragmentarily preserved bone flute from the 16th century [Plath, Fischer, Kirsch (2020)]. The fragment of the flute is digitized using X-ray and 3D image processing. The optimal response of the instrument is determined by using numerical simulations, modeling, and varying structurally relevant parameters of the geometry of the missing block of the flute. The best model, regarding the most effective sound generation, is 3D-printed. Thus, a playable copy of the original instrument is available now.

In 2022 Campbell, Gilbert and Myers publish a very comprehensive and equally readable compendium on the subject of brass instruments [Campbell, Gilbert, Myers (2021)]. In addition

to many exciting acoustic experiments, the lip dynamics when blowing and overblowing are discussed here, as well as shock waves and other nonlinearities and stability properties of this class of instruments.

Part II

Chapter 3

Preliminary Remarks

One and one gives three.

Gordon Matthew Thomas Sumner CBE,
known as Sting, English musician,
singer, songwriter, and actor

In this section the reader will be introduced to some mathematical and physical concepts that are constantly used in one form or another in musicology and in this study. Musicology has been studied since the first systematic studies by Ancient Greek philosophers such as Pythagoras, Archytas of Tarentum, Euclid and Aristotle understood as an interdisciplinary science that has a strong connection to mathematics. That alone justifies that we make a few comments on this at this point. The following explanations can make it easier for musicology students to get started with the subject. We will utilize tools from algebra, classical analysis, vector analysis and statistics as well as advanced techniques from nonlinear dynamics and stability theory. Also methods of coarse-grained modeling are utilized. The numerical aspects needed to perform the numerical simulations presented in the study will be discussed separately in chapter chapter 4. The physical concepts used in this study include notes on classical mechanics, fluid mechanics, thermodynamics and acoustics as well as of the theory of oscillations. As parentheses around the knowledge base we shall introduce some important applications in musicology in between.

3.1 Basic Mathematical Concepts

It's not our intention to recapitulate the whole foundation of mathematics here, but just to get assure of a few important concepts from algebra and analysis. In the study presented here we will deal with terms like set, sequence and series, limit, continuity, function, differentiation, differential equation, integration, linearization as well as differential operators, scalars, vectors, matrices and tensors. Let us remind you of these terms again shortly.

3.1.1 Some Notes on Algebra and Analysis

3.1.1.1 Sets

The definition of a set is quite young, compared to the history of mathematics which is more than 3,000 years old. It was not until 1896 that the mathematician Georg Cantor (⋆1873) proposed a useful definition of the term set:

> We understand a set M to mean any combination of certain, well-distinguishable objects x of our intuition or our thinking (which are called the elements of M) into

a whole.

Sets are well-determined and well-differentiated collections that are completely characterized by their elements. We write $x \in M$ to indicate that the object x is element of the set M. If not, we write $x \notin M$. Two sets are equal if and only if they have exactly the same elements. The Cantorian definition of a set can be seen as the starting point of modern understanding of what infinity is mathematically. Examples of sets in the sense of Cantor are:

$$L = \{1, 3, q, \frac{1}{17}, \odot, -1\}, \quad M = \{Alice, Bob\}, \quad N = \{x \in \mathbb{R} | x < 10\}, \quad A = \{\,\} = \emptyset \tag{3.1}$$

The latter example is called the empty set. There is only one empty set. The logical definition of the empty set goes back to the German mathematician Ernst Zermelo (1871-1853)

$$\exists M : \forall X : \neg(X \in M) \tag{3.2}$$

using the logical quantifiers $\exists$ 'there exists' and $\forall$ 'for all' and the logical 'non' operator $\neg$. Counterexamples for sets in the sense of Cantor are:

$$B = \{1, -2, 1, 100\}, \quad C = \{0.5, \frac{2}{4}\} \tag{3.3}$$

The first expression contains two indistinguishable numbers. The latter expression is unclear with respect to the fraction term. Reading the fraction as a symbol this expression is a set in the sense of Cantor, reading the fraction read as a number it is not.

Sets meet the De Morgan's laws, cf. Eq. (3.4) and all rules of propositional logic as can be gleaned in relevant mathematical textbooks, e.g. in[Heuser, H. (1994)].

$$\overline{\bigcap_{i \in I} M_i} = \bigcup_{i \in I} \overline{M_i} \quad \text{and} \quad \overline{\bigcup_{i \in I} M_i} = \bigcap_{i \in I} \overline{M_i} \tag{3.4}$$

Note that Cantor's definition of a set and the Cantor set are completely different terms with different mathematical meaning.

A further important concept is the so called ordered pair. Let M, N sets. For $x \in M, y \in N$ one can define the ordered pair:

$$(x, y) = \Big\{\{x\}, \{x, y\}\Big\} \tag{3.5}$$

An ordered pair (x, y) is a pair of objects in which the order the objects appear in the pair is significant. That means that $(x, y) \neq (y, x)$. This is because the elements are of different sets, namely $x \in M$ and $y \in N$ and $M \cap N = \emptyset$.

With the ordered pair one can define the Cartesian product as:

$$M \times N = \Big\{(x, y) : x \in M, y \in N\Big\} \tag{3.6}$$

The Cartesian product is a very powerful concept to define further, more complex mathematical structures.

3.1.1.2 Numbers and Number ranges

Numbers are essential tools of counting. The idea of counting is very old and wide spread in human societies as well as in animal kingdom. It is essential for understanding and doing

music as well as natural and other sciences. Depending on what is to be counted, one introduces different sets of numbers. Let's start with the most simple kind of counting, the counting with - so called - natural numbers. Counting with natural numbers requires two things: the definition of a set to label the things that has to be counted and the definition of the rules of counting which structures the set. The definition of the set must satisfy the following things:

- The definition of one element n which is part of the set. This is called the existence of n.
- The definition what the follower n' of the element n is.

This is essential part of the five Peano axioms[1] which characterize the natural numbers.
The Hungarian-American mathematician, physicist and computer scientist John von Neumann gave a very intuitive model to define the set of natural numbers generically just using the empty set $\emptyset$ and the axiom s of Peano as mentioned:

$$\begin{aligned} 0 &:= \quad \{\ \} = \emptyset \\ 1 &:= 0' = \{0\} = \{\emptyset\} \\ 2 &:= 1' = \{0,1\} = \{\emptyset, \{\emptyset\}\} \\ 3 &:= 2' = \{0,1,2\} = \{\emptyset, \{\emptyset, \{\emptyset\}\}\} \\ &\vdots \quad \vdots \quad \vdots \qquad \vdots \\ (n+1) &:= n' = \{0,1,...,n\} = n \cup \{n\} \end{aligned} \tag{3.7}$$

The set of natural numbers is labeled with the symbol $\mathbb{N}$. On $\mathbb{N}$ one can define an order:

$$0 < 1 < 2 < 3 < ... < n < n+1 < ... \tag{3.8}$$

as well as operations like addition and multiplication:

$$\begin{aligned} \text{Addition}: \quad & \mathbb{N} \times \mathbb{N} \to \mathbb{N} \\ & (x,y) \mapsto x + y \end{aligned} \tag{3.9}$$

$$\begin{aligned} \text{Multiplication}: \quad & \mathbb{N} \times \mathbb{N} \to \mathbb{N} \\ & (x,y) \mapsto x \cdot y \end{aligned}$$

with the following axiomatic properties:

[1] Giuseppe Peano (1858-1932) was an Italian mathematician who was a founder of set theory and mathematical logic.The Peano axioms are:

- $0 \in \mathbb{N}$
- $\forall n(n \in \mathbb{N} \Rightarrow n' \in \mathbb{N})$
- $\forall n(n \in \mathbb{N} \Rightarrow n' \neq 0)$
- $\forall n, m(m, n \in \mathbb{N} \Rightarrow (m' = n' \Rightarrow m = n))$
- $\forall X(0 \in X \wedge \forall n(n \in \mathbb{N} \Rightarrow (n \in X \Rightarrow n' \in X)) \Rightarrow \mathbb{N} \subseteq X)$

$$(A1)\quad (x+y)+z = x+(y+z) \quad \forall x,y,z \in \mathbb{N} \qquad \text{associativity of addition} \qquad (3.10)$$
$$(A2)\quad x+0 = x \quad \forall x,y \in \mathbb{N} \qquad \text{neutral element of addition} \qquad (3.11)$$
$$(A3)\quad \exists x : x+(-x) = 0 \quad \forall x \in \mathbb{N} \qquad \text{inverse element of addition} \qquad (3.12)$$
$$(A4)\quad x+y = y+x \quad \forall x,y \in \mathbb{N} \qquad \text{commutativity of addition} \qquad (3.13)$$

$$(M1)\quad (x \cdot y) \cdot z = x \cdot (y \cdot z) \quad \forall x,y,z \in \mathbb{N} \qquad \text{associativity of multiplication} \qquad (3.14)$$
$$(M2)\quad x \cdot 1 = x \quad \forall x,y \in \mathbb{N} \qquad \text{neutral element of multiplication} \qquad (3.15)$$
$$(M3)\quad \exists x : x \cdot (x^{-1}) = 1 \quad \forall x \in \mathbb{N} \qquad \text{inverse element of multiplication} \qquad (3.16)$$
$$(M4)\quad x \cdot y = y \cdot x \quad \forall x,y \in \mathbb{N} \qquad \text{commutativity of multiplication} \qquad (3.17)$$

$$(D)\quad (x+y) \cdot z = x \cdot z + y \cdot z \quad \forall x,y,z \in \mathbb{N} \qquad \text{distributivity} \qquad (3.18)$$

Note that sometimes one writes $\mathbb{N}_0$ to sign explicitly that the 0 is part of the set.

With the natural numbers and the concept of the ordered pair one can define the following relation. At the set $M = \mathbb{N} \times \mathbb{N}$ one defines an equivalence relation of ordered pairs of all natural numbers:

$$R = \Big\{ \big((a,b),(c,d)\big) : a+c = b+d \Big\} \tag{3.19}$$

The elements of the different set $M \setminus R$ are the elements:

$$\cdots, E[1,3], E[1,2], E[1,1], E[2,1], E[3,1], \cdots \tag{3.20}$$

One can now define the operation addition at the set $M \setminus R$ as:

$$E[a,b] \oplus E[c,d] = E[a+c, b+d] \tag{3.21}$$

and the operation multiplication as:

$$E[a,b] \otimes E[c,d] = E[ac+bd, ad+bc] \tag{3.22}$$

One can show that these are well-defined definitions. One identifies $E[1,1] = 0$, $E[1,2] = -1$, $E[1,3] = -2$ and $E[2,1] = 1$, $E[3,1] = 2$, etc. and writes $\mathbb{Z} := M \setminus R$ as well as $a+b$ in place off $a \oplus b$ and $a \cdot b$ in place off $a \times b$. The set $\mathbb{Z}$ is called the set of all integers.

The set of rational numbers $\mathbb{Z} \times \big(\mathbb{Z} \setminus \{0\}\big)$ can be defined as equivalence classes of pairs of integers (p,q) with $q \neq 0$, using an equivalence relation defined as:

$$(p_1,q_1) \sim (p_2,q_2) \iff p_1 q_2 = p_2 q_1 \tag{3.23}$$

Addition and multiplication can be defined as:

$$(p_1,q_1) + (p_2,n_2) = (p_1 n_2 + q_1 p_2, q_1 q_2)$$
$$(p_1,q_1) \times (p_2,n_2) = (p_1 p_2, q_1 q_2)$$

One writes:

$$\mathbb{Q} := \left\{ \frac{p}{q} : p \in \mathbb{Z}, q \in \mathbb{Z} \setminus \{0\} \right\}$$

Note, the rational numbers are countable. That means there is an one-to-one correspondence to the natural numbers. Both sets have the same cardinal number.
Many of the problems the ancient Greek dealt with when thinking about musicology and mathematics were closely related to ratios and rational numbers. In doing so, they encountered the problem of incommensurability

3.1.1.3 Complex Numbers

Starting with the idea writing the real equation $x^2 + 1 = 0$ and trying to solve it, leads to the task to solve a square root of a negative number $x_{1,2} = \pm\sqrt{-1}$. This problem cannot be solved in the range of real numbers$\mathbb{R}$, because of the role that the product of any real number with itself is always positive. An elegant way out of the dilemma is to assume the existence of a number which solves this problem. This number is called the imaginary number and it is defined by:

$$i := \sqrt{-1} \tag{3.24}$$

Extending the range of real numbers $\mathbb{R}$ by the imaginary number i and checking the associative, the commutative and the distributive properties for the operations addition and multiplication gives no violation of the rules of calculation. Therefore one can extent the range of real numbers by one more number, the imaginary number i. In this way one gets a new range of numbers, the range of complex numbers $\mathbb{C}$. A number $z \in \mathbb{C}$ consists of a real part and an imaginary part.
One writes $z = a + ib$ with

$$a = \Re(z) \in \mathbb{R} \qquad \text{the real part of z} \tag{3.25}$$
$$b = \Im(z) \in \mathbb{R} \qquad \text{the imarinary part of z} \tag{3.26}$$

The absolute value of a complex number is given by:

$$r = |z| = \sqrt{a^2 + b^2} \tag{3.27}$$

The argument or the phase φ of a complex number z is given by

$$\varphi = arg(z) = \left\{ \begin{array}{rl} \arccos\left(\frac{a}{r}\right), & b \geq 0 \\ -\arccos\left(\frac{a}{r}\right), & b < 0 \end{array} \right) \tag{3.28}$$

A complex number can be written with polar coordinates:

$$a = r \cdot cos(\varphi) \tag{3.29}$$
$$b = r \cdot sin(\varphi) \tag{3.30}$$

This leads to the Euler's formula:

$$\mathrm{e}^{\pm i\varphi} = \cos(\varphi) \pm i \sin(\varphi) \tag{3.31}$$

One often visualizes $\mathbb{C}$ with the complex plane as shown in Fig. 3.1.

3.1.1.4 Maps and Functions

Maps and functions are one of the most important concepts in mathematics and and indispensable part of all sciences.

A subset $F \subset M \times N$ is called a map from M in N if:

$$\Big((x, y) \in F \wedge (x, z) \in F\Big) \Rightarrow y = z \tag{3.32}$$

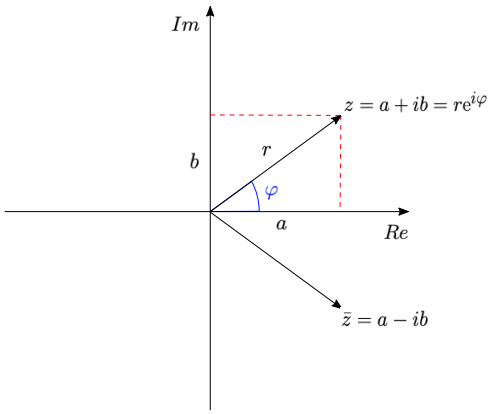

Figure 3.1: The complex plane. Shown are the complex number z its real part a, its imaginary part b , its absolute value r, the argument φ and the complex conjugate complex $\bar{z}$.

Let $F \subset M \times N$ be a map. The set:

$$D(F) := \{x | x \in M, \exists y \in N : (x, y) \in F\} \tag{3.33}$$

is called domain, the set

$$W(F) := \{y | y \in N, \exists x \in M : (x, y) \in F\} \tag{3.34}$$

is called range.

Let $F \subset M \times N$ a map:

F is a map from M into $N :\Leftrightarrow D(F) = M$.

F is called a surjective map $:\Leftrightarrow W(F) = N$.

F is called an injective map $:\Leftrightarrow \Big((x_1, y) \in F \wedge (x_2, y) \in F\Big) \Rightarrow x_1 = x_2$.

F is called a bijective map if it is a surjective as well as an injective map. The bijective map is a one to one and onto map and therefore it can be inverted by its inverse map F^{-1}.

The well known operations addition and multiplication in $\mathbb{R}$ are maps:

$$\begin{aligned} \text{Addition}: \quad & M \times M \to M \\ & (x, y) \mapsto x + y \end{aligned} \tag{3.35}$$

$$\begin{aligned} \text{Multiplication}: \quad & M \times M \to M \\ & (x, y) \mapsto x \cdot y \end{aligned} \tag{3.36}$$

Functions are maps. For example, let $m, n \in \mathbb{R}$ be constants. Then the linear function is given by the map:

$$\begin{aligned} f: \quad & \mathbb{R} \times \mathbb{R} \to \mathbb{R} \\ & (x, y) \mapsto y = mx + n \end{aligned} \tag{3.37}$$

Again, note that in the first set of the Cartesian product only live the x elements! In the second set, which is an identical copy of $\mathbb{R}$, live the y elements! Both set are disjunctive.

The linear function f has the domain $D(f) = \mathbb{R}$ (the first set in the Cartesian product) and maps into $W(f) = \mathbb{R}$ (the second set of the Cartesian product), the whole real range. It is a bijective map. Therefore one can find an inverse map. The inverse map of the example is given by:

$$\begin{aligned} f^{-1}: \quad & \mathbb{R} \times \mathbb{R} \to \mathbb{R} \\ & (y, x) \mapsto x = \frac{1}{m} y - \frac{n}{m}, \quad \text{after renaming the sets} \quad x \rightleftharpoons y: \\ & (x, y) \mapsto y = \frac{1}{m} x - \frac{n}{m} \end{aligned} \tag{3.38}$$

Usually the sets (variables) are renamed in order to represent the function and the inverse function in the same coordinate system, cf. Fig. 3.2a.

In the same way one defines other functions that are used in this study.

$$\begin{aligned} g: \quad & \mathbb{R} \times \mathbb{R} \to \mathbb{R} \\ & (x, y) \mapsto y = x^2 \end{aligned} \tag{3.39}$$

The quadratic function $g(x)$ has the domain $D(g) = \mathbb{R}$ but maps only to non-negative values $W(g) = \{y | y \in \mathbb{R} \setminus \{y < 0\}\}$. This map is not surjective because the preimage of (-1) is the empty set $\varnothing$. If one restricts the map to $g : \mathbb{R} \times \mathbb{R}_0^+ \to \mathbb{R}_0^+$ the maps becomes surjective. A further restriction of the domain to non-negative values $D(g) = \{x | x \in \mathbb{R} \setminus \{x < 0\}\}$ opens the door to a properly defined inverse map:

$$\begin{aligned} g^{-1}: \quad & \mathbb{R}_0^+ \times \mathbb{R}_0^+ \to \mathbb{R}_0^+ \\ & (x, y) \mapsto y = +\sqrt{x} \end{aligned} \tag{3.40}$$

The exponential function and its inverse function, the natural logarithm is given by:

$$\begin{aligned} h: \quad & \mathbb{R} \times \mathbb{R}^+ \to \mathbb{R}^+ \\ & (x, y) \mapsto y = \mathrm{e}^x \end{aligned} \tag{3.41}$$

$$\begin{aligned} h^{-1}: \quad & \mathbb{R}^+ \times \mathbb{R} \to \mathbb{R} \\ & (x, y) \mapsto y = \ln(x) \end{aligned} \tag{3.42}$$

With the introduced techniques of restriction one defines the trigonometric functions and their inverse functions:

$$\begin{aligned} i: \quad & [-\frac{\pi}{2}, \frac{\pi}{2}] \to [-1, 1] \\ & (x, y) \mapsto y = sin(x) \end{aligned} \tag{3.43}$$

$$\begin{aligned} i^{-1}: \quad & [-1, 1] \to \left[-\frac{\pi}{2}, \frac{\pi}{2}\right] \\ & (x, y) \mapsto y = \arcsin(x) \end{aligned} \tag{3.44}$$

$$\begin{aligned} j: \quad & [0, \pi] \to [-1, 1] \\ & (x, y) \mapsto y = cos(x) \end{aligned} \tag{3.45}$$

$$j^{-1}: \quad [-1,1] \to [0,\pi] \\ (x,y) \mapsto y = \arccos(x) \tag{3.46}$$

$$k: \quad \left[-\frac{\pi}{2},\frac{\pi}{2}\right] \to \mathbb{R} \\ (x,y) \mapsto y = \tan(x) \tag{3.47}$$

$$k^{-1}: \quad \mathbb{R} \to \left[-\frac{\pi}{2},\frac{\pi}{2}\right] \\ (x,y) \mapsto y = \arctan(x) \tag{3.48}$$

The introduced elementary functions and inverse functions are depicted in Fig. 3.2a and Fig. 3.2b.

Last but not least complex functions can be defined in the same way:

$$p: \quad \mathbb{C} \times \mathbb{C} \to \mathbb{C} \\ (\varphi,y) \mapsto y = exp(i\varphi) \tag{3.49}$$

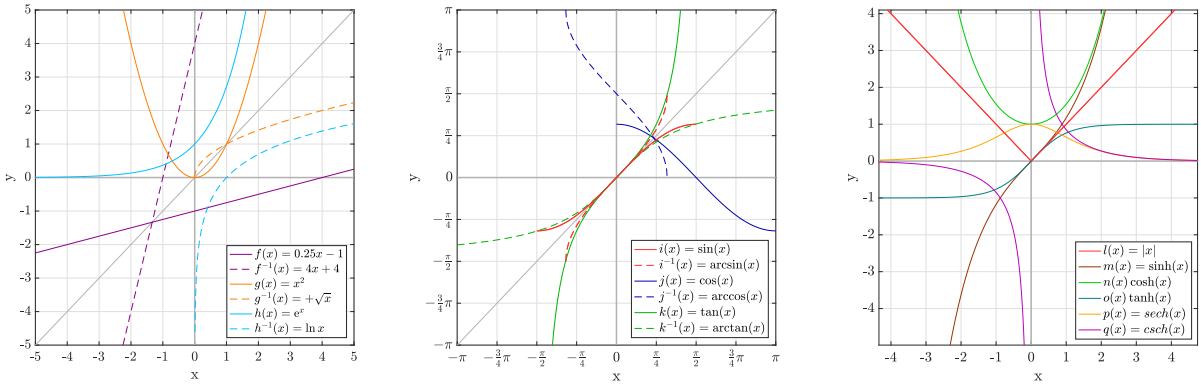

a) **b)** **c)**

Figure 3.2: Graphs of some elementary functions and their inverse functions. a) The linear function $f(x) = 0.25x-1$, its inverse function $f^{-1}(x) = 4x+4$, the quadratic function $g(x) = x^2$, the inverse function of the non-negative restriction of $g(x)$ $g^{-1}(x) = +\sqrt{x}$, the exponential function $h(x) = \mathrm{e}^x$ and its inverse $h^{-1}(x) = \ln(x)$. b) The trigonometric function $i(x) = \sin(x)$, its inverse function $i^{-1}(x) = \arcsin(x)$, $j(x) = \cos(x)$, its inverse function $j^{-1}(x) = \arccos(x)$, $k(x) = \tan(x)$ and its inverse function $k^{-1}(x) = \arctan(x)$, c) the absolute value function $l(x) = |x|$, the hyperbolic sine function $m(x) = \sinh(x)$, the hyperbolic cosine function $n(x) = \cosh(x)$, the hyperbolic tangent function $o(x) = \tanh(x)$, the hyperbolic secant $p(x) = \mathrm{sech}(x)$ and the hyperbolic cosecant function $q(x) = \mathrm{csch}(x)$.

3.1.1.5 Sequences

A sequence is defined as an enumerated collection of objects in which - in contrast to the definition of a set, repetitions are allowed and the order of the objects matters. Like a set, it contains members which are also called elements. The number of elements can be finite or possibly infinite and is called the length of the sequence. Unlike a set, same elements can appear multiple

times at different positions. Also unlike a set, the order does matter.

A first example of sequences is

$$\{a_n\}_{n=1}^{\infty} = 1, \frac{1}{2}, \frac{1}{3}, \frac{1}{4}, ..., \frac{1}{n} \tag{3.50}$$

The first example is called the harmonic sequence. The harmonic sequence is strongly related to music theory, particularly to the just intonation. The complementary ratios of the harmonic sequence are $1:1$, $1:2$, $2:3$, $3:4$ etc., cf. Fig. 3.3. Setting these ratios in vibrations on a string that is clamped on both sides one perceives sound at frequencies that are particularly pleasant to the human ear. This is called consonance or harmony. The corresponding frequencies are multiples of the fundamental frequency f_0 of the undivided string. The consonant intervals, also known as harmonic partials, are related to the following terms, ratios and frequencies: unison $(1:1)$, f_0, octave $(1:2)$, $f_1 = 2 \cdot f_0$, perfect fifths $(2:3)$, $f_2 = 3 \cdot f_0$ and perfect fourths $(3:4)$, $f_3 = 4 \cdot f_0$. Higher harmonic partials are major third $(4:5)$, minor third $(6:5)$, subminor third $(6:7)$, supermajor second $(7:8)$, greater tone $(8:9)$, lesser tone $(9:10)$ etc..

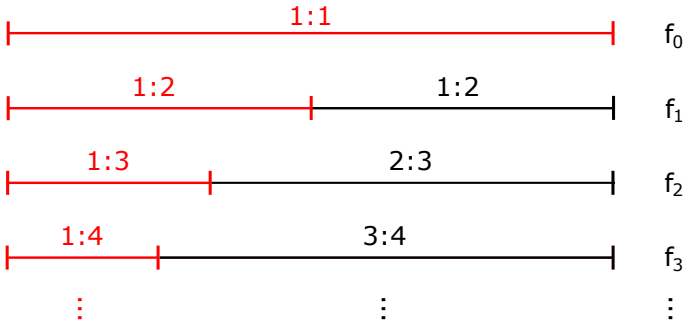

Figure 3.3: The Euclidean *Sectio Canonis* developed by the ancient Greeks and written by Euclid of Alexandria around 300 B.C. When a single string[2] with a defined length, clamped on both sides with tension is stimulated to vibration with the frequency f_0 then the sections of the string with integer ratios (black) sound harmonically in the sense of humans perception. The inherent mathematical sequence (red) is called the harmonic sequence, cf. Eq. (3.50). The complementary sequence is known as harmonic series - more more precisely it should be called the sequence of overtones.

The concept of consonances (ancient Greek: *σύμφωνος* =sýmphōnos sounding together) is very important in harmony theory. It was developed by the ancient Greece in particular by Pythagoras and the Pythagorean school in the 7^{th}-6^{th} B.C.. It was bequeathed as *Κατατομή κανόνος*, (Latin: *sectio canonis*), in the world famous book of mathematics 'The Elements' by Euclid, flourished in 300 B.C., the standard work for mathematics up to the 19th century in Anglo-American countries [Densmore (2007)] .

A second example of a sequence is the equal temperament in Eq. (3.51), a musical temperament, which divides the octave into 12 equal steps, called the semitones. The international code is 12-TET. In musicology one introduces a special logarithmic unit, the cent unit, to measure musical intervals. The 12-TET has 1200 cents, thus each semitone has 100 cents, (Latin: *cent*=hundred). Hence one cent is the part of $\sqrt[1200]{2}$ of an octave.

$$\{f_n\}_{n=0}^{12} = f_0 \left(\sqrt[12]{2^n} \right) \tag{3.51}$$

In general, if the frequencies f_i and f_j of two notes are known, the number of cents measuring the interval from f_i to f_j can be calculated by

$$n = 1200 \cdot \log_2 \left(\frac{f_i}{f_j} \right). \tag{3.52}$$

In Tab.: 3.1 the lengths of various just intervals are compared against their equal-tempered counterparts, which are given as ratios as well as in cents. The concept of equal tempered semitones made lead to build music instruments with one single keyboard like harpsichords, clavichords and pianos in contrast to pipe organs. A disadvantage of this concept is that the temperatures of the scales that caused by using the just intonation are getting lost. In the last column of Tab.: 3.1 the differences of the just intonation with respect to the 12-TET is listed for every single semitone.

3.1.1.6 Mathematical field, Convergence and Divergence

A field $\mathbb{K}$ in terms of mathematics is a set on which addition, subtraction, multiplication, and division are declared by axioms and which is partial ordered. A field is a fundamental algebraic structure which is widely used in many areas of mathematics. Here it is used to introduce the fundamental notion of convergence of a sequence is as follows:
Let $\mathbb{K}$ a mathematical field, say $\mathbb{R}$. A sequence $\{a_n\}$ is called convergent to the limit value $a \in \mathbb{R}$, if $\forall \varepsilon$, $\varepsilon > 0$ there exists an $N_\varepsilon \in \mathbb{N}$ such that $\forall n > N_\varepsilon$ applies to

$$|a_n - a| < \varepsilon \tag{3.53}$$

One writes:

$$\lim_{n \to \infty} a_n = a \tag{3.54}$$

A non-convergent sequence is called divergent. A sequence sequence has at most one limit value. There exist many criteria to proof the convergence property of sequences. At this point, again reference is made to a relevant mathematical textbook [Heuser, H. (1994)] the author can recommend.

3.1.1.7 Series

We now remind us the mathematical term of series. A series is defined as any finite or infinite sequence $(a_1, a_2, a_3, ...)$ of numbers or functions that can be added. The notations are

$$s_N = \sum_{n=1}^{N} a_n = a_1 + a_2 + a_3 + ...a_N \quad \text{and} \quad \sum_{n=1}^{\infty} a_n = a_1 + a_2 + a_3 + ... \tag{3.55}$$

The finite series is called partial sum. In other words, a series is a sequence whose enumerated objects are partial sums. The value of the series is defined by the limit N if it exists.
For infinite series the value is:

$$\sum_{n=1}^{\infty} a_n = \lim_{N \to \infty} \sum_{n=1}^{N} a_n. \tag{3.56}$$

When this limit exists, the series is called convergent, otherwise the series is called divergent. Some important examples of series in musicology context are the:

Name	Exact value in 12-TET	Decimal value in 12-TET	Cents	Just intonation interval	Cents in just intonation	Difference
Unison (C)	$\sqrt[12]{2^0}$	1	0	$1:1=1$	0	0
Minor second ($C\sharp/D\flat$)	$\sqrt[12]{2^1}$	1.059463	100	$16:15=$ 1.06666...	111.73	-11.73
Major second (D)	$\sqrt[12]{2^2}$	1.122462	200	$9:8=1.125$	203.91	-3.91
Minor third ($D\sharp/C\flat$)	$\sqrt[12]{2^3}$	1.189207	300	$6:5=1.2$	315.64	-15.64
Major third (E)	$\sqrt[12]{2^4}$	1.259921	400	$5:4=1.25$	386.31	$+13.69$
Perfect fourth (F)	$\sqrt[12]{2^5}$	1.334840	500	$4:3=$ 1.333...	498.04	$+1.96$
Tritone ($F\sharp/G\flat$)	$\sqrt[12]{2^6}$	1.414214	600	$7:5=1.4$ $10:7=$ 1.42857	582.51 617.49	$+17.49$ -17.49
Perfect fifth (G)	$\sqrt[12]{2^7}$	1.498307	700	$3:2=1.5$	701.96	-1.96
Minor sixth ($G\sharp/A\flat$)	$\sqrt[12]{2^8}$	1.587401	800	$8:5=1.6$	813.69	-13.69
Major sixth (A)	$\sqrt[12]{2^9}$	1.681793	900	$5:3=$ 1.6666...	884.36	$+15.64$
Minor seventh ($A\sharp/B\flat$)	$\sqrt[12]{2^{10}}$	1.781797	1000	$16:9=$ 1.7777...	996.09	$+3.91$
Major seventh (B)	$\sqrt[12]{2^{11}}$	1.887749	1100	$15:8=1.875$	1088.27	$+11.73$
Octave (C')	$\sqrt[12]{2^{12}}$	2	1200	$2:1=2$	1200	0

Table 3.1: The equal temperament 12-TET compared with the just intonation. Shown are the names, the exact values, the values in decimal values, the cents, the just intonation intervals in ratios, decimal value and cents and the difference in cents of the 12 semitones of the octave interval.

$$\sum_{n=1}^{N} a_N = \frac{N(N+1)}{2} \qquad \text{Arithmetic series (Gauss formula)} \qquad (3.57)$$

$$\sum_{n=1}^{\infty} \frac{1}{n} = 0 \qquad \text{Harmonic series} \qquad (3.58)$$

$$\sum_{k=1}^{\infty} a^k = \frac{1}{1-a} \qquad \text{Geometric series} \qquad (3.59)$$

$$f(x,a) = \sum_{n=0}^{\infty} \frac{f^n(a)}{n!}(x-a)^n \qquad \text{Taylor series} \qquad (3.60)$$

$$f(t) = \sum_{n=-\infty}^{\infty} c_n \cdot \exp\left(i \cdot \frac{2\pi}{T} \cdot n \cdot t\right) \qquad \text{Fourier series} \qquad (3.61)$$

3.1.2 Calculus

3.1.2.1 Differentiation

The calculus is the mathematical theory of continuous change. It has two parts, the differential calculus and the integral calculus. The first concerns with infinitesimal rates of change, slopes of function graphs, curvatures, skewnesses and so on. The second part, the integral calculus concerns accumulation of quantities. With this, roughly speaking, one calculates areas under or between function graphs. The two parts are connected to each other by the fundamental theorem of calculus [Heuser, H. (1994)]. The calculus is built up by using the fundamental mathematical ideas of infinite sequences and infinite series to a well-defined limit - a circumstance called convergence.

The concept of the derivative combines the knowledge of the slope of a linear function $f(x) = mx + n$ which is given by

$$m := \frac{\Delta y}{\Delta x} = \frac{f(x) - f(x_0)}{x - x_0} \qquad (3.62)$$

and the concept of convergence and a limit value. This leads to the definition of the first derivative of a function A function $f : D \subset \mathbb{R} \to \mathbb{R}$ which is defined at the open domain D is differentiable if the derivative

$$f'(x) := \frac{\mathrm{d}y}{\mathrm{d}x} = \lim_{\Delta x \to 0} \frac{f(x + \Delta x) - f(x)}{\Delta x} \qquad (3.63)$$

exists. This implies that the function f is a continuous function at the point x. Differentiable functions can be locally approximated by linear functions. The function f is differentiable on D if it is differentiable at every point of D. In this case, the derivative of f is thus a function from D into $\mathbb{R}$. The converse is not hold. There exist countinious functions that are not differentiable at every point, for instance the absolute value function:

$f(x)$	$f'(x)$	$f(x)$	$f'(x)$
c	0	$\sin(x)$	$\cos(x)$
$ax+b$	a	$\cos(x)$	$-\sin(x)$
ax^n	anx^{n-1}	$\tan(x)$	$\frac{1}{\cos^2(x)}$
e^{ax}	$a\mathrm{e}^{ax}$	$\cot(x)$	$-\frac{1}{\sin^2(x)}$
a^x	$a^x \cdot \ln(a)$	$\arcsin(x)$	$\frac{1}{\sqrt{1-x^2}}$
$\ln(x)$	$\frac{1}{x}$	$\arccos(x)$	$-\frac{1}{\sqrt{1-x^2}}$
$\log_a x$	$\frac{1}{\ln(a) \cdot x}$	$\arctan(x)$	$\frac{1}{1+x^2}$
$\sqrt{x}$	$-\frac{1}{x^2}$	$\operatorname{arccot}(x)$	$-\frac{1}{1+x^2}$

Table 3.2: Selected elementary functions and their first derivatives.

$$\begin{aligned} f: \quad & \mathbb{R} \times \mathbb{R}_0^+ \to \mathbb{R}_0^+ \\ & (x,y) \mapsto y = |x| = \begin{cases} -x, & x < 0 \\ x, & x \geq 0 \end{cases} \end{aligned} \tag{3.64}$$

This function is not differentiable at the point $x = 0$. At this point the function cannot be approximated by linear functions, because its sharp turn in slope crossing the y-axis. The derivative of a differentiable function $f(x)$ generates a new function $f'(x)$. The derivative gives the rate of change of the given function $f(x)$ at the point x. Geometrically the derivative is a measure for the local slope, namely the slope of the function at point x.

Of cause the new function f' can be differentiated again. This is called the second derivative $f''(x)$. Geometrically the second derivative is a measure for the curvature of the function at point x. The third derivative $f'''(x)$ is called the skewness of the function at the point x. Higher derivatives leave unnamed.

Chained functions and products of functions get differentiated using the chain rule:

$$[f(g(x)]' = \frac{\mathrm{d}f}{\mathrm{d}g}\frac{\mathrm{d}g}{\mathrm{d}x} = f' \cdot g' \tag{3.65}$$

and the product rule of differentiation:

$$\Big(f(x) \cdot g(x)\Big)' = f'(x) \cdot g(x) + f(x) \cdot g'(x) \tag{3.66}$$

For some elementary functions the ives are summarized in Tab. 3.2
Functions that depend on more than one variables, e.g. $f(x_1, x_2, ..., x_i, ..., x_N)$, $i \in \mathrm{N}$ also can be differentiated. The derivative is called partial derivative with respect to the variable one wants

to differentiate. The definition of the partial derivative is similar to this of the one-dimensional case:

$$\frac{\partial f}{\partial x_i}(x_1, x_2, ..., x_i, ..., x_N) = \lim_{\Delta x_i \to 0} \frac{f(x_1, x_2, ..., x_i + \Delta x_i, ..., x_N) - f(x_1, x_2, ..., x_i, ..., x_N)}{\Delta x_i} \quad (3.67)$$

The partial derivative with respect to x_i gives the rate of change of the function $f(x_1, x_2, ..., x_i, ..., x_N)$ in x_i-direction. Higher partial derivatives are defined in analogy to the one-dimensional case with the same meanings as already stated.

For a numerical treatment of problems containing derivatives it is necessary to discretize the derivative. This is done by approximation of the derivative using a properly small step h:

$$f'(x) \approx \frac{f(x+h) - f(x)}{h} \quad (3.68)$$

Methods of discretization will be discussed further below in sub-item 3.1.2.3.

3.1.2.2 Integration

Integration is the second part of the calculus. In some sense it is the inverse operation of the differentiation. The idea of the integration is to combine the concepts of summation of small rectangles and the concept of convergence and limit. This implies the calculation of areas under the graphs of functions. One distinguishes between definite integration and indefinite integration.

The integral $\int f(x)\,\mathrm{d}x$ is equal to the total change of a function that has at every point $x \in [a, b]$ the derivative $f(x)$. Let $F : [a, b] \to \mathbb{R}$ such a function. Because of the fact that the derivative describes the current rate of change it results that $F'(x) = f(x), \forall x \in [a, b]$. Such a function F is called indefinite integral of f.
The total change of F in the interval $[a, b]$ is equal to the difference $F(b) - F(a)$. One writes:

$$\int_a^b f(x)\,\mathrm{d}x = F(b) - F(a) \quad (3.69)$$

This statement is called the **fundamental theorem of calculus**. It is one of the most important theorems in analysis.

The definite integral calculates a signed area $A = \int_a^b f(x)\,\mathrm{d}x = F(b) - F(a)$ bounded by the graph of a given function $f(x)$ at interval $[a, b]$.
For some elementary functions $f(x)$ the indefinite integrals are summarized in Tab. 3.3
The concept of integration also works in higher dimensions $\mathbb{R}^n$.

$$\int \cdots \int_{\mathbf{D}} f(x_1, x_2, \ldots, x_n)\, dx_1 \cdots dx_n \quad (3.70)$$

3.1.2.3 Discretizations

For numerical applications of the calculus one has to discretize the differential and integral operators. There a several methods to do this. The most simple way is called the explicit Euler method also known as "forward in time" method. Consider a problem:

$$y'(t) = f(y(t), t) \qquad y_0(t) = y_0 \quad (3.71)$$

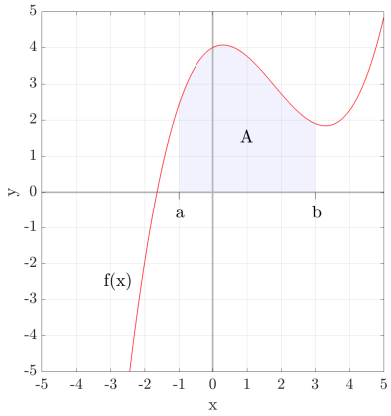

Figure 3.4: Example of a definite integral. Shown is the function $f(x) = \frac{1}{6}t^3 - \frac{9}{10}t^2 + \frac{1}{2}t + 4$ and the integrated area A in the interval $[-1, 3]$. The result of the integration is $12.9\bar{3}AE$ (area units).

$f(x)$	$F(x)$	$f(x)$	$F(x)$
0	$\int 0\,\mathrm{d}x = C$	$\sin(x)$	$\int sin(x)\,\mathrm{d}x = -\cos(x) + C$
a	$\int a\,\mathrm{d}x = ax + C$	$\cos(x)$	$\int cos(x)\,\mathrm{d}x = \sin(x) + C$
ax^n	$\int ax^n\,\mathrm{d}x = \frac{a\,x^{n+1}}{n+1} + C$	$\tan(x)$	$\int tan(x)\,\mathrm{d}x = \ln(\lvert sec(x)\rvert) + C$
e^{ax}	$\int \mathrm{e}^{ax}\,\mathrm{d}x = \frac{1}{a}\cdot \mathrm{e}^{ax} + C$	$\cot(x)$	$\int cot(x)\,\mathrm{d}x = \ln(\lvert sin(x)\rvert) + C$
a^x	$\int a^x\,\mathrm{d}x = \frac{a^x}{\ln(a)} + C$	$\frac{1}{\sqrt{1-x^2}}$	$\int \frac{1}{\sqrt{1-x^2}}\,\mathrm{d}x = \arcsin(x) + C$
$\ln(x)$	$\int \ln(x)\,\mathrm{d}x = x(\ln(x) - 1) + C$	$-\frac{1}{\sqrt{1-x^2}}$	$\int -\frac{1}{\sqrt{1-x^2}}\,\mathrm{d}x = \arccos(x) + C$
$\log_a x$	$\int \log_a x\,\mathrm{d}x = \frac{x(\ln(x)-1)}{\ln(x)} + C$	$\frac{1}{1+x^2}$	$\int \frac{1}{1+x^2}\,\mathrm{d}x = \arctan(x) + C$
$\sqrt{x}$	$\int \sqrt{x}\,\mathrm{d}x = \frac{2}{3}x^{\frac{3}{2}} + C$	$\frac{1}{\sqrt{1+x^2}}$	$\int \frac{1}{\sqrt{1+x^2}}\,\mathrm{d}x = \operatorname{arcsinh}(x) + C$

Table 3.3: Selected elementary functions and their integrals.

Choosing a value h for every time step and set $t_n = t_0 + nh, n = 0, 1, 2, \cdots$. One time step $t_{n+1} = t_n + h$ of the Euler method is than:

$$y_{n+1} = y_n + hf(t_n, y_n) \qquad n = 0, 1, 2, \cdots \tag{3.72}$$

The method rectifies the continuous solution into small pieces of linear approximations, called polygonal approximation. The smaller the time steps the better the approximation. In some cases this method do not lead to convergent solutions. In such cases one often uses another procedure:

$$y_{n+1} = y_n + hf(t_{n+1}, y_{n+1}) \qquad n = 0, 1, 2, \cdots \tag{3.73}$$

This is called the implicit Euler method, also known as Euler backward method. The criteria for convergence of the Euler methods are formulated using the Courant-Lewy-Friedrichs condition, which satisfies the stability of the solution. This is discussed in more detail in section 4.

3.1.2.4 Differential Equations

A differential equation is an equation that represents the relationship between a function and its derivatives. The derivatives represent the rates of change of the quantity which is concerned. There exist ordinary differential equations ODE's which depend on one single variable and its derivative as well as partial differential equations PDE's that include more than one variables and derivatives. They can be linear or nonlinear whether they contain nonlinear terms ($x^3, x\dot{x}, x^2\dot{x}, \sin(x)$, etc.) or not. They can be homogeneous or non-homogeneous whether they are driven by a function e.g. $f(x)$ or not. Generally one writes

$$y^{(n)}(x) + a_1 y^{(n-1)}(x) + \cdots + a_{n-1}y'(x) + a_n y(x) = 0 \quad \text{(homogeneous)} \tag{3.74}$$

$$y^{(n)}(x) + a_1 y^{(n-1)}(x) + \cdots + a_{n-1}y'(x) + a_n y(x) = f(x) \quad \text{(non-homogeneous)} \tag{3.75}$$

Some ODE's are mentioned as important examples regarding this work:

$$m \cdot \frac{d^2\vec{r}(t)}{dt^2} = \vec{F} = \vec{0} \quad \text{(equation of motion)} \tag{3.76}$$

$$\frac{dN}{dt} = -\lambda N \quad \text{(exponential decay)} \tag{3.77}$$

$$\ddot{x} + \omega^2 x = 0 \quad \text{(harmonic oscillator)} \tag{3.78}$$

$$\ddot{x} - \mu(1 - \beta x^2)\dot{x} + \omega^2 x = 0 \quad \text{(van der Pol oscillator)} \tag{3.79}$$

There exit also systems of differential equations:

$$(y_1, \ldots, y_{n-1}, y_n)' = (y_1, \ldots, y_n, f(x, y_1, \ldots, y_n)) \tag{3.80}$$

As an example the harmonic oscillator Eq. (3.78) is written as a (coupled) system of first order differential equations, utilizing the substitution, that the deflection's x rate of change in time $\frac{\mathrm{d}x}{\mathrm{d}t} = \dot{x}$ is the definition of the velocity v:

$$\begin{aligned} \dot{x} &= v \\ \dot{v} &= -\omega^2 x \end{aligned} \tag{3.81}$$

This can be written in matrix notation:

$$\begin{pmatrix} \dot{x} \\ \dot{v} \end{pmatrix} = \begin{pmatrix} 0 & 1 \\ -\omega^2 & 0 \end{pmatrix} \begin{pmatrix} x \\ v \end{pmatrix} \quad \text{or:}$$

$$\dot{\mathbf{y}} = \mathcal{L}\mathbf{y} \tag{3.82}$$

The matrix representation can be transferred into a so-called eigenvalue equation. This can be solved with methods of linear algebra using the ansatz:

$$\mathbf{y} = \vec{a}\, \mathrm{e}^{\lambda t} \qquad \text{with} \quad \vec{a} \in \mathbb{C} \quad \text{and} \tag{3.83}$$

$$\dot{\mathbf{y}} = \lambda \mathbf{y} \qquad \text{leads to:} \tag{3.84}$$

$$\mathcal{L}\mathbf{y} = \lambda \mathbf{y} \tag{3.85}$$

$$(\mathcal{L} - \lambda \mathbb{E})\mathbf{y} = 0 \qquad \text{with} \quad \mathbb{E} = \begin{pmatrix} 1 & 0 \\ 0 & 1 \end{pmatrix} \tag{3.86}$$

The latter equation defines the eigenvalues λ of the problem and is an homogeneous linear system of equations. This can be solved using the determinant. Provided $\boldsymbol{y} \neq 0$ it applies:

$$\det\left(\mathcal{L} - \lambda \mathbb{E}\right) = 0 \tag{3.87}$$

This leads to the characteristic polynomial:

$$\lambda^2 + \omega^2 = 0 \tag{3.88}$$

The solution is:

$$\lambda_{1,2} = \pm i\omega \tag{3.89}$$

Thus the general solution of the differential equation of the harmonic oscillator can be written as:

$$\boldsymbol{y} = \vec{a} \cdot \mathbf{e}^{\pm i\omega t} \quad \text{with:} \vec{a} = \begin{pmatrix} A \\ \pm i\omega A \end{pmatrix} \tag{3.90}$$

or:

$$x(t) = \quad A \cdot \mathbf{e}^{\pm i\omega t} \tag{3.91}$$

$$\dot{x}(t) = v(t) = \pm i\omega A \cdot \mathbf{e}^{\pm i\omega t} \tag{3.92}$$

Generally the set of eigenvalues is called the spectrum $\sigma\left(\mathcal{L}\right)$:

$$\sigma(\mathcal{L}) = \{\lambda_i \in \mathbb{C}, i \in \mathbb{N} \,|\, \exists \boldsymbol{y} \neq 0 \colon \mathcal{L}\boldsymbol{y} = \lambda \boldsymbol{y}\} \tag{3.93}$$

The spectral radius is the maximum absolute value of all eigenvalues $\rho(\mathcal{L}) := \max\limits_{1 \leq i \leq n} |\lambda_i(\mathcal{L})|$.

3.1.3 On Vector Differential Operators

In this study some basic elements of the vector differential calculus are used. The focus is on the so called differential operators. Such operators are widely used, particularly to formulate fluid mechanical and aeroacoustic problems, cf. chapter 4.

3.1.3.1 Time-derivative Operator

The time derivative operator is a differential operator that takes the time derivative of a scalar function $T(\vec{r},t)$ or of a vector function $\vec{v}(\vec{r},t)$. The time derivative operator is defined as

$$\frac{\mathrm{d}(\ \cdot\ )}{\mathrm{d}t} \quad \text{or} \quad \frac{\partial(\ \cdot\ )}{\partial t} \tag{3.94}$$

depending on whether the function depends on one or more variables. Higher time derivatives are noted as

$$\frac{\partial^2(\ \cdot\ )}{\partial t^2}, \frac{\partial^3(\ \cdot\ )}{\partial t^3}, \quad \text{etc.} \tag{3.95}$$

Time derivatives are often notated using dots or index notation, namely $\dot{x}, \ddot{\vec{r}}$, or v_t, u_{tt} and so forth.

3.1.3.2 Del-Operator (Nabla-Operator)

Another important differential operator is the del-operator, also known as nabla-operator. The del-operator is defined as:

$$\nabla := \begin{pmatrix} \frac{\partial}{\partial x} \\ \frac{\partial}{\partial y} \\ \frac{\partial}{\partial z} \end{pmatrix} \quad \text{or in short notation:} \quad \nabla := \begin{pmatrix} \partial_x \\ \partial_y \\ \partial_z \end{pmatrix} \tag{3.96}$$

The name "nabla" comes, by reason of the symbol's shape, from the Ancient Greek word: $\nu\acute{\alpha}\beta\lambda\alpha$ for a Phoenician harp. The del-operator calculates the local spatial rates of change of a quantity. It can be applied to a scalar function as well as to a vector function.
The del-operator applied to a scalar function is called the gradient. The gradient captures the total spatial rate of change of the scalar valued quantity. Let $T(x,y,z)$ be a scalar function, the temperature in a room, for instance. Then

$$\operatorname{grad} T = \nabla T(x,y,z) = \begin{pmatrix} \frac{\partial T}{\partial x} \\ \frac{\partial T}{\partial y} \\ \frac{\partial T}{\partial z} \end{pmatrix} = \frac{\partial T}{\partial x}\vec{e}_x + \frac{\partial T}{\partial y}\vec{e}_y + \frac{\partial T}{\partial z}\vec{e}_z \tag{3.97}$$

Applying the del- operator to a scalar function creates a vector, cf. Eq. (3.97).

The del-operator applied to a vector valued function can be realized in three different ways, depending on which product is used, the scalar product which leads to a scalar function, the vector product (known as cross product) which produced a vector or the dyadic product, which

leads to a tensor field. The first application mentioned is called the divergence of the vector field. Let $\vec{v}(x, y, z)$ be a vector field. Then the divergence is given by

$$\operatorname{div} \vec{v} = \frac{\partial v_x}{\partial x} + \frac{\partial v_y}{\partial y} + \frac{\partial v_z}{\partial z} = \nabla \cdot \vec{v} \tag{3.98}$$

The divergence of a vector field is a scalar which indicates whether the considered control volume contains a sink ($\operatorname{div} \vec{v} < 0$), a source ($\operatorname{div} \vec{v} > 0$) , or is source-free ($\operatorname{div} \vec{v} = 0$).

The second application mentioned is called the curl of the vector field. It is given by

$$\operatorname{curl} \vec{v} = \nabla \times \vec{v} = \begin{vmatrix} \vec{e}_x & \vec{e}_y & \vec{e}_z \\ \frac{\partial}{\partial x} & \frac{\partial}{\partial y} & \frac{\partial}{\partial z} \\ v_x & v_y & v_z \end{vmatrix} = \begin{pmatrix} \frac{\partial v_z}{\partial y} - \frac{\partial v_y}{\partial z} \\ \frac{\partial v_x}{\partial z} - \frac{\partial v_z}{\partial x} \\ \frac{\partial v_y}{\partial x} - \frac{\partial v_x}{\partial z} \end{pmatrix} \tag{3.99}$$

The curl of a vector field leads to a new vector, which is perpendicular to the vectors ∇ and $\vec{v}$ and thus normal to the plane containing them. Mathematically $\operatorname{curl} \vec{v}$ is a pseudo-vector. A pseudo-vector transforms like a vector under a proper rotation, but in three dimensions it gains an additional sign flip under an improper rotation such as a reflection. Geometrically, the direction of a reflected pseudo-vector is opposite to its mirror image, but with equal magnitude. In contrast, the reflection of a "true" vector is exactly the same as its mirror image, see also footnote [9] in chapter 5, subsection 5.3.2.2.

The third application of the del-operator is called the tensor derivative of a vector field $\vec{v}(\vec{r}, t)$. It is defined as:

$$\nabla \otimes \vec{v} = \begin{pmatrix} \frac{\partial v_x}{\partial x} & \frac{\partial v_y}{\partial x} & \frac{\partial v_z}{\partial x} \\ \frac{\partial v_x}{\partial y} & \frac{\partial v_x}{\partial y} & \frac{\partial v_x}{\partial y} \\ \frac{\partial v_x}{\partial z} & \frac{\partial v_x}{\partial z} & \frac{\partial v_x}{\partial z} \end{pmatrix} = D \tag{3.100}$$

This leads to a second-rank tensor, which has 9 terms. It is also known as 3×3 matrix. The transposition D^T of this quantity leads to the Jacobi-matrix:

$$D^T = J = \begin{pmatrix} \frac{\partial v_x}{\partial x} & \frac{\partial v_x}{\partial y} & \frac{\partial v_x}{\partial y} \\ \frac{\partial v_y}{\partial x} & \frac{\partial v_y}{\partial y} & \frac{\partial v_y}{\partial z} \\ \frac{\partial v_z}{\partial x} & \frac{\partial v_z}{\partial y} & \frac{\partial v_z}{\partial z} \end{pmatrix} \tag{3.101}$$

or in general:

$$= \left(\frac{\partial v_i}{\partial x_j} \right)_{(i=1,\cdots,m\,;\,j=1,\cdots,n)} \tag{3.102}$$

The terms of the Jacobi-matrix are the transposed gradients of the components of the vector field $\vec{v}(\vec{r}, t)$. Note, the matrix operation transposition mirrors the terms of the matrix with respect to the main diagonal. The transposition operation converses important parameters of the matrix, like the trace, the rank, the determinant and the eigenvalues. The Jacobi matrix, or more simply, the Jabobian gives us all the information about the field. In other words: the Jacobian determines the flux completely!

3.1.3.3 Laplace-Operator and D'Alembert-Operator

The double execution of the del-operator is called Laplace-Operator Δ or shorter, the Laplacian:

$$\Delta := \nabla\nabla u = \nabla^2 u = \frac{\partial^2 u}{\partial x^2} + \frac{\partial^2 u}{\partial y^2} + \frac{\partial^2 u}{\partial z^2} \tag{3.103}$$

This differential operator is part of many differential equations like the compressible Navier-Stokes equations which we discuss in section 4.1 and the wave equation. The wave equation is given by

$$\frac{\partial^2 u}{\partial t^2} = c^2 \left(\frac{\partial^2 u}{\partial x^2} + \frac{\partial^2 u}{\partial y^2} + \frac{\partial^2 u}{\partial z^2} \right) \tag{3.104}$$

The left hand side is the acceleration of the displacement u. The constant c at right hand side is the velocity of propagation in the medium and the rightmost term is the curvature. With the combination of the time derivative operator and the Laplacian one can define the D'Alembert operator or short the D'Alembertian, also known as the box operator

$$\Box := \frac{1}{c^2}\frac{\partial^2}{\partial t^2} - \sum_{i=1}^{3} \frac{\partial^2}{\partial {x_i}^2} \tag{3.105}$$

With this short notation the becomes

$$\Box u = 0 \tag{3.106}$$

This example offers the power and the efficiency of the notation with differential operators.

3.1.4 Integral Operators

Another class of mathematical operators used in this study are integral operators, also called integral transforms. An integral transform maps a function from its original function space into another function space via integration. This is done because properties of the original function can be accessed more easily than in the original function space. In general, the transformed function can be mapped back to the original function space using the inverse transform.

3.1.4.1 Convolution, Cross-correlation

The convolution is a mathematical operation on two functions h and g that produces a third function $(h * g)$ that expresses how the shape of one is modified by the other. The term convolution refers to both the result function and to the process of computing it. It is defined as

$$(h * g)(t) = \int_{-\infty}^{+\infty} h(t-\tau) \cdot g(\tau) \mathrm{d}\tau \tag{3.107}$$

the integral of the product of the two functions after one is reversed and shifted. And the integral is evaluated for all
values of shift, producing the convolution function. Some features of convolution are similar to cross-correlation: for real-valued functions, of a continuous or discrete variable, it differs from

cross-correlation $(x \star y)(\tau)$ only in that either $x(t)$ or $y(t)$ is reflected about the y-axis. Thus it's a cross-correlation of $x(t)$ and $y(-t)$, or $x(-t)$ and $y(t)$. For complex-valued functions, the cross-correlation operator is the adjoint of the convolution operator.

The cross-correlation is given by

$$R_{xy}(\tau) = (x \star y)(\tau) = (x^*(-t) * y(t))(\tau) = \int_{-\infty}^{\infty} \bar{x}(t)\, y(t+\tau)\, \mathrm{d}t \tag{3.108}$$

where $\bar{x}(t)$ is the conjugate complex function of $x(t)$. The discrete cross-correlation function is given by:

$$R_{xy}[\tau] = (x \star y)[\tau] = \sum_{t=-\infty}^{\infty} \bar{x}[t]\ y[t+\tau] \tag{3.109}$$

3.1.4.2 Fourier Transforms

Fourier transform are integral transforms that decompose functions depending on space or time into functions depending on spatial or temporal frequency and vice versa:

$$F(\omega) = \frac{1}{\sqrt{2\pi}} \int_{-\infty}^{\infty} f(t) \mathrm{e}^{-2\pi i \omega t}\, \mathrm{d}t \qquad \text{(analysis)} \tag{3.110}$$

$$f(t) = \frac{1}{\sqrt{2\pi}} \int_{-\infty}^{\infty} F(\omega) \mathrm{e}^{2\pi i \omega t}\, \mathrm{d}\omega \qquad \text{(synthesis)} \tag{3.111}$$

Eq. (3.110) is called Fourier-analysis, Eq. (3.111) is called Fourier-synthesis.

3.1.4.3 Hilbert Transform

Another integral operator and an application of convolution is the Hilbert transform. With the Hilbert transform one calculates an analytic signal from a real valued time series $x(t)$:

$$H(x)(t) = -\frac{1}{\pi} \lim_{\varepsilon \to 0} \int_{\varepsilon}^{+\infty} \frac{x(t+\tau) - x(t-\tau)}{\tau}\, \mathrm{d}\tau \tag{3.112}$$

In terms of signal processing[3] spoken an analytic signal means, that the function is complex-valued and consists only of non-negative frequencies $f_n \geq 0$. This can be used to find the phases of the real data signal.

[3] In mathematics an analytic function is a function that is locally given by a convergent power series:

$$f(x) = \sum_{n=0}^{\infty} a_n (x - x_0)^n = a_0 + a_1(x - x_0) + a_2(x - x_0)^2 + a_3(x - x_0)^3 + \ldots$$

with a_0, a_1 ... are real numbers and the series convergent to $f(x)$ for x in a neighborhood of x_0. A real analytic function is a function that is infinitely differentiable at any point x_0 and converges pointwise to $f(x)$ for x in the neighborhood of x_0. An example is the Taylor-series, cf. Eq. 3.60.

3.1.5 Notes on Linear and Nonlinear Dynamics

Linear systems are systems that follow the principle of superposition. Superposition means two things - additivity as well as homogeneity. Additivity means that all linear combinations of solutions are also solutions of the system: $f(x_1 + x_2) = f(x_1) + f(x_2)$. Homogeneity means $f(a\,x) = a\,f(x)$ where a is a scalar. If the check of homogeneity fails, the system is nonlinear. So, superposition is a sufficient and a necessary condition to proof the linearity of the system.

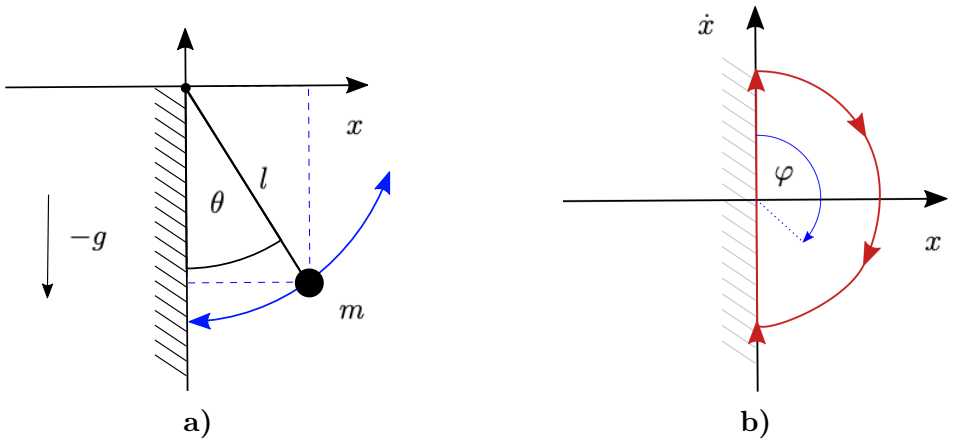

Figure 3.5: a) Shown is a pendulum of mass m and length l moving without friction in a gravitational field and reflecting perfectly on a hard wall (no elasticity, no deformation). The current position can be measured by the displacement $x = \sin(\theta)$. b) The phase space representation of the dynamical system depicted in a). The trajectory is labeled red. the product of $x \cdot \dot{x}$ is equal to the total energy of the system. The ratio $\frac{\dot{x}}{x}$ gives the phase angle φ. At the deflection point $x = 0$ the system changes its velocity direction. This causes the instantaneous phase shift in the phase portrait of $\varphi = 2\pi$.

Nonlinear systems and nonlinear dynamics are a part of mathematical physics that explores nonlinear functional dependencies in natural, social and mathematical contexts. Many linear physical laws and differential equations are approximations of nonlinear dynamical systems, for instance the wave equation Eq. (3.104) and the differential equation of the mathematical pendulum, which is nonlinear, because of the sinus term:

$$\ddot{\varphi} + \frac{g}{l}\sin(\varphi) = 0 \tag{3.113}$$

which is not solvable by means of elementary mathematics (one needs knowledge about elliptic integrals). For small displacements $|\varphi| \ll 1$ one can utilize the Taylor-expansion Eq. (3.60) to approximate the function $f(\varphi) = \sin(\varphi)$ at the point $a = 0$, which leads to:

$$\begin{aligned} f(\varphi; a)) &= \sum_{n=0}^{\infty} \frac{f^n(a)}{n!} \cdot (\varphi - a)^n \\ &= \frac{\sin(0)}{0!}(\varphi - 0)^0 + \frac{\cos(0)}{1!}(\varphi - 0)^1 - \frac{\sin(0)}{2!}(\varphi - 0)^2 - \frac{\sin(0)}{3!}(\varphi - 0)^3 + \cdots \\ &= \quad 0 \quad + \quad \varphi \quad - \quad 0 \cdot \varphi^2 \quad - \quad \frac{1}{6}\varphi^3 \quad + \quad \cdots \\ &\approx \quad \varphi \end{aligned} \tag{3.114}$$

The process of breaking off the Taylor-expansion after the linear term is called linearization. In the present example this leads to the well-known equation of the harmonic oscillator:

$$\ddot{\varphi} + \omega^2 \varphi = 0 \qquad \text{with:} \quad \omega := \sqrt{\frac{g}{l}} \tag{3.115}$$

Nonlinear dynamics deals with problems where linear approximations are no longer sufficient to understand the dynamics. Nonetheless techniques like Taylor-expansion, linearization and linear algebra are essential to explore nonlinear phenomena.

Another important concept to study nonlinear systems is the phase portrait. The phase portrait is a representation of the dynamical system in the phase space, also known as phase diagram or phase plot. For one-dimensional systems the phase space representation is $2D$, defined by the quantity of interest (x-axis) and its time derivative (y-axis). The dynamics of the system (the temporal evolution of the quantity) is represented by a path in the phase space which is called trajectory. Because of the principle of causality - the state of the quantity has always and exactly one cause - this means: a trajectory can never intersect. A movement $x(t)$ in one dimension (cf. Fig. 3.5a) can be visualized by a $2D$-phase space representation $(x, \dot{x})$, cf. Fig. 3.5b. In general a dynamical system of N degrees of freedom can be represented by a $2N$-dimensional phase space[4]. Nonlinear systems can show much more complex dynamics than linear systems.

Exemplifying this, let's consider the van der Pol oscillator:

$$\ddot{x} - \mu(1 - x^2)\dot{x} + \omega^2 x = 0 \tag{3.116}$$

which is characterized by the nonlinear damping term $-\mu(1 - x^2)\dot{x} = -\mu\dot{x} + \mu x^2\dot{x}$. The damping has two terms. For different control parameters μ the system shows different dynamics. In Figs. 3.6b - 3.6e the trajectories for two different initial conditions $(0; 1)$ (blue) and $(-1.8; 4)$ (green) are shown. For $\mu < 0$, and depending on the different initial conditions the system either spirals into the fix point $(0; 0)$ (blue) or get repelled (green). For $\mu = 0$ the system becomes the harmonic oscillator.

For $\mu > 0$ and for small displacements $|x| \ll 1$ the first term of the damping term, which represents now negative damping, dominates the dynamics of the system. The negative damping implies self-exciting oscillations as shown in Fig. 3.6d the blue trajectory. For displacements $|x| > 1$ the second term which denotes positive damping (or normal damping) dominates the dynamics of the system. Depending on the initial displacement at time $t = 0$ (initial condition: $x(0), \dot{x}(0)$) the system shows opposite dynamics. For parameters $0 < \mu < 2$ and after a transient the systems evolves to a so called limit cycle. The nonlinear damping term self-adjusts the oscillations regardless of the initial conditions.
For increasing $\mu > 0$, e.g. $\mu = 0.35$, $\mu = 3.0$ and $\mu = 10.0$ the system becomes more and more anharmonic associated with an increase of the oscillation period (cf. 3.7b, 3.7c). In comparison with the harmonic oscillator $\mu = 0$, where the phase is a linear increasing quantity, the phase dynamics of the nonlinear cases are more complex. This is shown in Figs. 3.8a- 3.8c. In next section we will classify the observations by investigating the stability properties of the fix point of the system.

[4]N-dimensional systems $\dot{x}_n = F_n(x_n,)$ are represented by the $2N$-phase space, two variables, x_i and $\dot{x}_i$, $(i = 1, \cdots, N)$ for each degree of freedom.

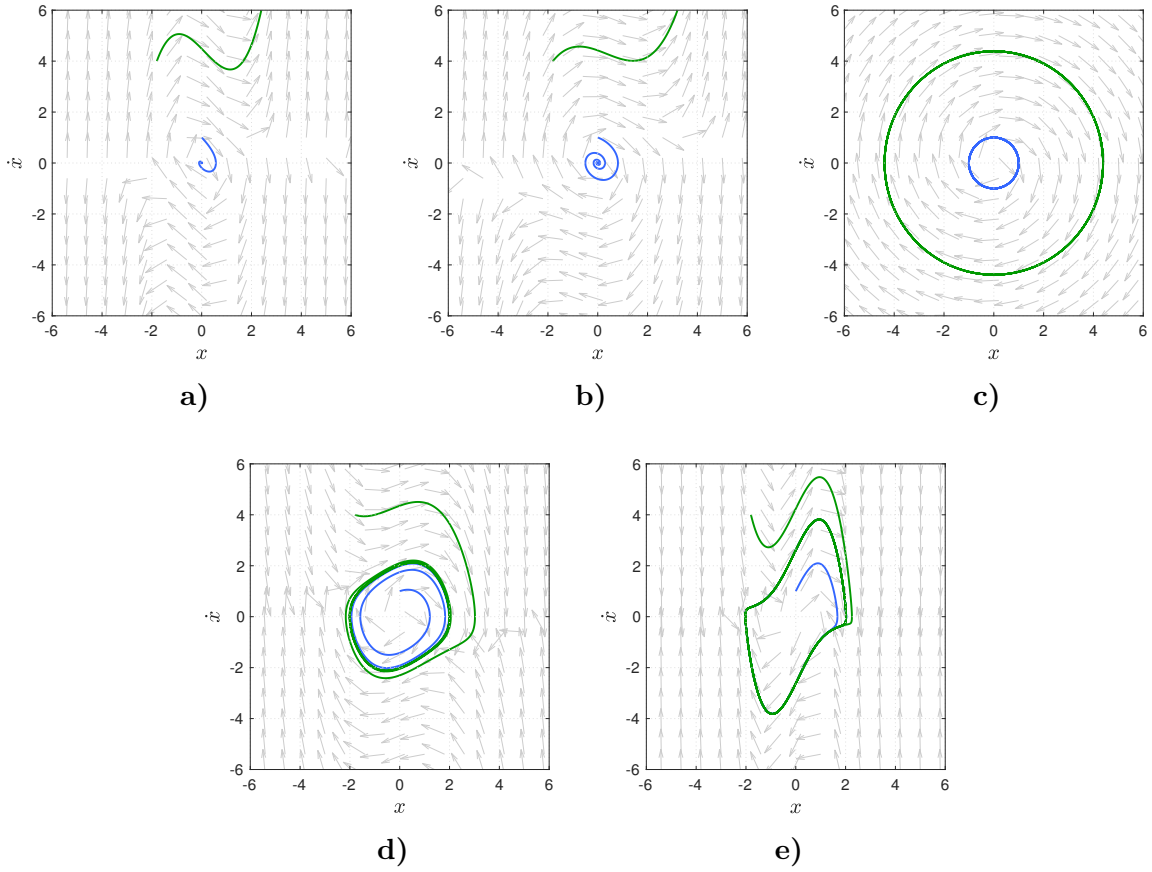

Figure 3.6: The van der Pol oscillator system $\ddot{x} - \mu(1 - x^2)\dot{x} + \omega_0^2 x = 0$ for different values of the control parameter μ and different initial conditions $x(0) = 0; \dot{x}(0) = 1$ (blue) and $x(0) = -1.8; \dot{x}(0) = 4$ (green). a) $\mu = -1$ and b) $\mu = -0.35$: in order to the initial conditions the system either spirals into the fix point $(0; 0)$ (blue) or get repelled and accelerates for $t \to \infty$, the displacement diverges, $x(t) \to \infty$ (green), c) $\mu = 0$ which means, the damping term vanishes and the system becomes the harmonic oscillator, d) $\mu = 0.35$ and e) $\mu = 2.0$. The dynamics of the systems shown in d) and e) lead to so called limit cycles.

3.1.6 Notes on Stability Theory

When a dynamical system X does not change in time ($\dot{X} = 0$), it is in an equilibrium state, also called fix point $(x^*; y^*)$. One can find and analyze such states with techniques of stability theory. We first consider linear systems before we come to the nonlinear systems.

3.1.6.1 One-dimensional Linear Systems

We start with some simple one-dimensional linear dynamical systems. One of the most simple linear dynamical systems is the differential equation

$$\dot{x} = f(x) \tag{3.117}$$

with a scalar function $f(x) = a$, $a \in \mathbb{R}$ on the right hand side[5]. One can solve this system

[5]Since Newton's famous *Philosophiæ Naturalis Principia Mathematica* first published in 1687 we've been writing dynamical systems as a clear assignment of cause and effect. We always write the terms representing the causes on the right side of the equation while we write the terms of the effect on the left side. Several causes can lead to one effect. Please do not confuse this with the statement further up in the text about the violation of causality if a trajectory in phase space would intersect!

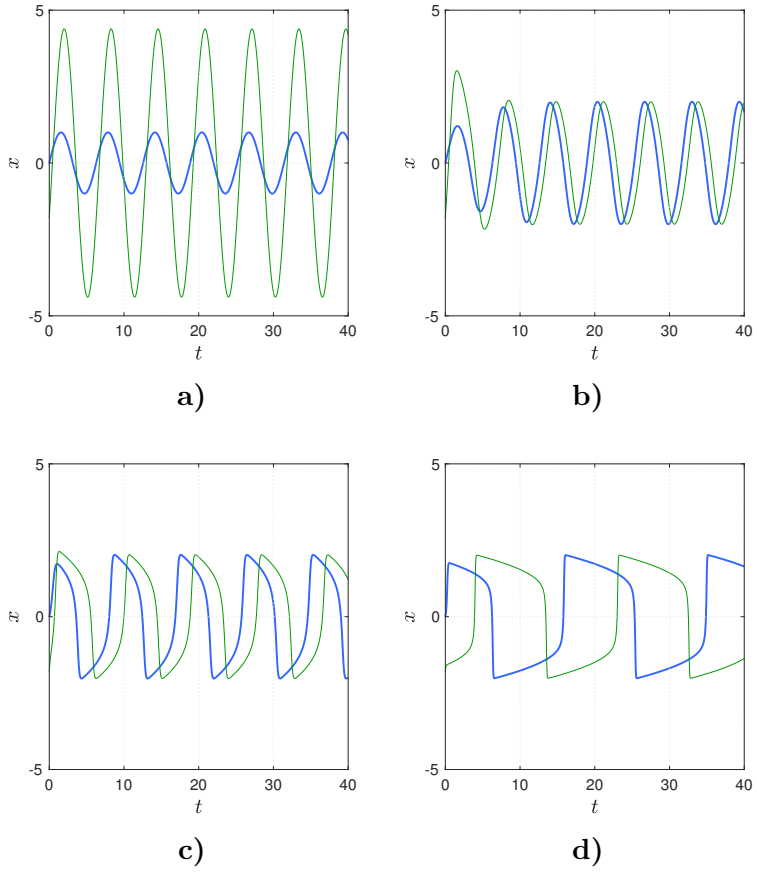

Figure 3.7: Signal $x(t)$ of the van der Pol system for various control parameter μ and the two different initial conditions $x(0) = 0; \dot{x}(0) = 1$ (blue) and $x(0) = -1.8; \dot{x}(0) = 4$ (green). a) $\mu = 0$, harmonic oscillations, no transient, b) $\mu = 0.35$, more anharmonic oscillations with a transient. The small parameter $\mu = 0.35$ generates weakly nonlinear oscillations. c) $\mu = 3$, oscillations with stronger anharmonicity compared with b), d) $\mu = 10$. With increasing control parameter $\mu > 0$ the period decrease and the oscillations get more and more anharmonic. The oscillations shown in b), c) and d) are known as relaxation oscillations.

directly by integration. The solution is:

$$\dot{x} = a \tag{3.118}$$

$$\mathrm{d}x = a\,\mathrm{d}t \quad \Rightarrow \quad \int_{x_0}^{x} \mathrm{d}\tilde{x} = \int_{t_0}^{t} a\,\mathrm{d}\tilde{t} \tag{3.119}$$

$$x(t) = a \cdot t + x_0 \tag{3.120}$$

The system has no critical points, the solutions are straight lines with slope a, cf. Fig. 3.9a. The next examples are the two linear dynamical systems:

$$\dot{x} = \pm x \tag{3.121}$$

These systems can also be solved easily by separating the variables and then integrating them. We show this for the system $\dot{x} = x$:

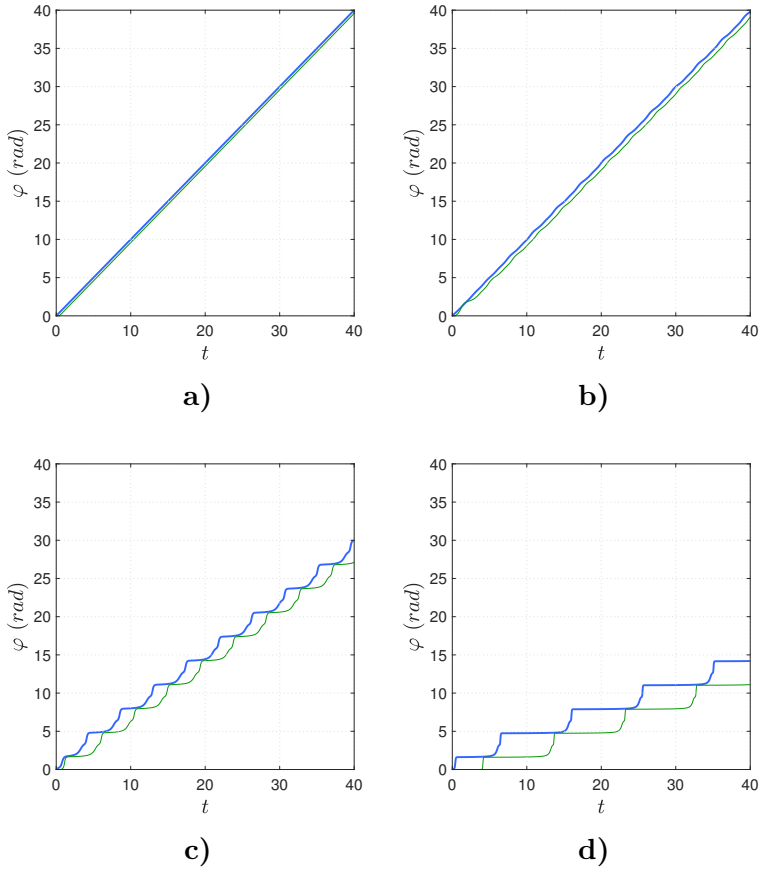

Figure 3.8: Phase $\varphi(t)$ of the van der Pol system for various control parameter μ and the two different initial conditions $x(0) = 0; \dot{x}(0) = 1$ (blue) and $x(0) = -1.8; \dot{x}(0) = 4$ (green). a) $\mu = 0$, b) $\mu = 0.35$, c) $\mu = 3$, d) $\mu = 10$. The development of the phase over time show that with increasing parameter $\mu > 0$ the phase dynamics changes from linear growth (harmonic oscillations, $\dot{\varphi} = const$) to a more complex dynamics represented by a periodically nonlinear growth, followed by a temporal resist of the phase.

$$\begin{aligned} \frac{\mathrm{d}x}{x} = \mathrm{d}t \quad \Rightarrow \quad \int_{x_0}^{x} \frac{1}{x}\,\mathrm{d}\tilde{x} &= \int_{t_0=0}^{t} \mathrm{d}t \\ \ln\left(\frac{x}{x_0}\right) &= (t - t_0) \\ \left(\frac{x}{x_0}\right) &= \exp(t - t_0) \\ x(t) &= x_0\,\mathrm{e}^{t} \end{aligned}$$

The calculation for the system $\dot{x} = -x$ is analogue, the solution is: $x(t) = x_0\,\mathrm{e}^{-t}$. In Figs. 3.9a - 3.9c the graphs of the solutions of the dynamical systems Eq. (3.118) and Eq. (3.121) are shown for some various initial conditions.

3.1.6.2 One-dimensional Nonlinear Systems

We know discuss one of the most simple nonlinear dynamical systems, a system with a quadratic dependency of the rate of change of the quantity:

$$\dot{x} = x^2 \tag{3.122}$$

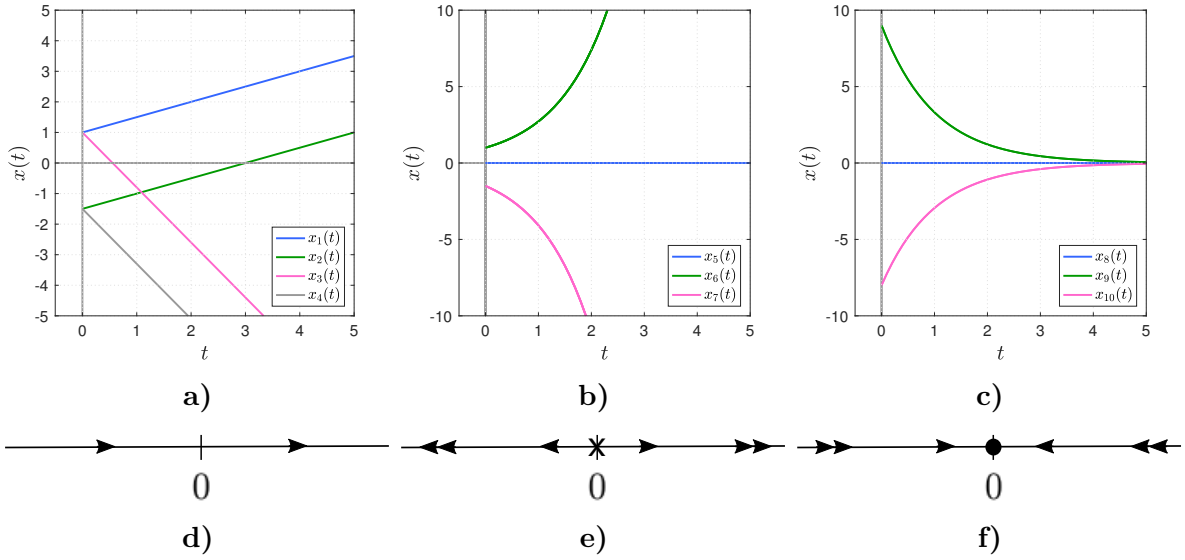

Figure 3.9: Some simple one-dimensional linear dynamical systems. a) Dynamical system: $\dot{x} = a$. Exemplary solutions: $x_1(t) = 0.5x+1, x_2(t) = -1.8x+1, x_3(t) = 0.5x-1.5, x_4(t) = -1.8x-1.5$. b) Dynamical system: $\dot{x} = x$. Exemplary solutions: $x_5(t) = 0\,\mathrm{e}^t, x_6(t) = 1\,\mathrm{e}^t, x_7(t) = -1\,\mathrm{e}^t$. c) Dynamical system: $\dot{x} = -x$. Exemplary solutions: $x_8(t) = 0\,\mathrm{e}^{-t}, x_9(t) = 9\,\mathrm{e}^{-t}, x_10(t) = -8\,\mathrm{e}^{-t}$. The corresponding pseudo-trajectories: d) no critical point, e) global repeller or global unstable fix point $x_c = 0$ (usually labeled by a black x), f) global attractor or globally stable fix point $x_c = 0$ (usually labeled by a black dot).

What kind of dynamics has the system? The critical point is again $x_c = 0$, but now it is a double root. If $x > 0$, the trajectory must move away from x_c. If $x < 0$, the square root is also positive and therefore x increases too. cf. Fig. 3.10.

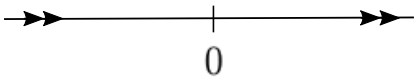

Figure 3.10: Pseudo-trajectory of the nonlinear dynamical system $\dot{x} = x^2$, ($\varepsilon = 0$)

Has $x_c = 0$ an attractive or a repelling characteristics? To analyze the stability of the critical point $x_c = 0$ we introduce a very small disturbance quantity $|\varepsilon| \ll 1$. We split our consideration of the roots into positive and negative values of ε. For $\varepsilon > 0$ let's have:

$$\dot{x} = x(x - \varepsilon) \tag{3.123}$$
$$= x^2 - \varepsilon x \tag{3.124}$$

What happens in the neighborhood of $x_c = 0$? For small values of $x \ll 1$ the term $-\varepsilon x$ dominates the dynamics and we can write:

$$\dot{x} \simeq -\varepsilon x \tag{3.125}$$
$$\tag{3.126}$$

In the neighborhood of point $x_c = 0$ the system locally behaves like an attractor (red dot) because of the negative sign of ε in the exponent of the solution of the differential equation,

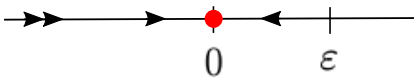

Figure 3.11: Pseudo-trajectory of the nonlinear dynamical system in the neighborhood of this fix point $x_c = 0$.

cf. Fig.: 3.121. Let's analyze now what happens in the neighborhood of the small disturbance $\varepsilon > 0$. To do this, we transform the coordinate to $u = x - \varepsilon$. This leads to:

$$\dot{u} = (u + \varepsilon)u \tag{3.127}$$
$$= u^2 + \varepsilon u \tag{3.128}$$

and

$$\dot{u} \simeq +\varepsilon u \quad \text{near u=0!} \tag{3.129}$$
$$\tag{3.130}$$

Back-transformation leads to the fact that in the neighborhood of ε the system behaved like a repeller, cf. Fig. 3.12.

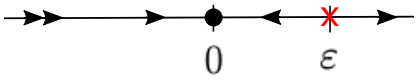

Figure 3.12: Pseudo-trajectory of the nonlinear dynamical system $\dot{x} = x^2$ in the neighborhood of the small disturbance $\varepsilon > 0$.

The picture changes dramatically when we assume the small disturbance as negative $\varepsilon < 0$. Now ε behaves like an attractor while the critical point $x_c = 0$ acts as a repeller!

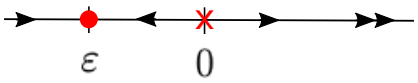

Figure 3.13: Pseudo-trajectory of the nonlinear dynamical system $\dot{x} = x^2$ in the neighborhood of the small disturbance $\varepsilon < 0$.

What happens when the variables x_c and $\pm\varepsilon$ come together? Then the variables interchange their stability properties! This behavior is called bifurcation, or more precisely in this case trans-critical bifurcation. Critical points that show such complex behavior are called critical points of higher order.

One can still solve problem of Eq. (3.122) explicitly by direct integration. The solution is:

$$x(t) = \frac{x(0)}{1 - x(0) \cdot t} \tag{3.131}$$

For $x(0) = 0$ the system remains at zero for ever, nothing happens. For $x(0) < 0$ the system converges to:

$$\lim_{t \to \infty} x(t) = 0 \tag{3.132}$$

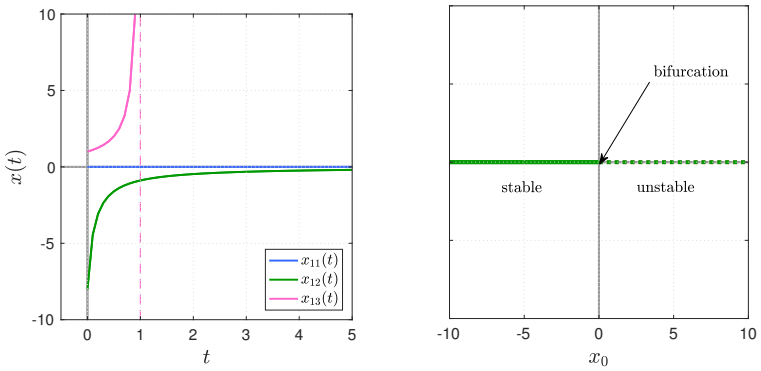

a) **b)**

Figure 3.14: a) Nonlinear dynamical system $\dot{x} = x^2$. Solutions for various initial conditions: $x_{11}(t), x(0) = 0$ (blue), $x_{12}(t), x(0) < 0$ (green) and $x_{13}(t), x(0) > 0$ (pink). b) Bifurcation diagram. When the initial condition passes zero the system switches from stable to unstable behavior.

For $x(0) > 0$ the system diverges in finite time:

$$\lim_{t \to t_f} x(t) = \frac{1}{x(0) \cdot t_f} \tag{3.133}$$

We can summarize that such complex behavior as shown here is characteristically for critical points of higher order.

3.1.6.3 Stability

In general it can be very challenging to find solutions for nonlinear systems. One often has to change the strategy and do qualitative considerations. Nevertheless, important statements about the dynamics of non-linear systems can also be found. Stability studies are an important tool in this regard. As we have already mentioned in the previous examples, critical points play a decisive role. Without wanting to anticipate, the idea of stability analysis should be briefly outlined here. One distinguishes local and global stability. With local stability one examines the dynamics close to critical points utilizing a reference trajectory $x_r(t)$ with an initial value $x_r(t_0)$ and a small disturbance $x(t_0)$. By intuition the trajectory through the initial point should be characterized as stable if all trajectories $x(t)$ remain close to the initial one, for all times later than t_0. Mathematically speaking this can be expressed by the so called Lyapunov stability: For an arbitrarily small disturbance, say $\varepsilon > 0$ exits a $\delta > 0$ ($\delta = \delta(\varepsilon)$ such that the solution $x(t)$ with the initial condition $|x(t_0) - x_r(t_0)| < \delta(\varepsilon)$ holds $|x(t) - x_r(t)| < \varepsilon$, for all $t > t_0$. If one cannot find such a δ-neighborhood for a given ε-neighborhood, then $x(t)$ is said to be unstable. This definition do not make any statement about the behavior for the long term dynamics of the system, in particular, not whether the trajectories come arbitrarily close to each other for $t \to \infty$. If that can be guaranteed, then (and only than) one speaks of asymptotic stability.

The Figures. 3.15a and 3.15b illustrate both statements. The limit cycle of the van der Pol oscillator in Fig. 3.6d is an example of a system that shows asymptotic stability. Another kind of stability is the neutral stability, where the solution neither growths nor decays, but remains in its initial amplitude. The phase of the undamped harmonic oscillator is an example

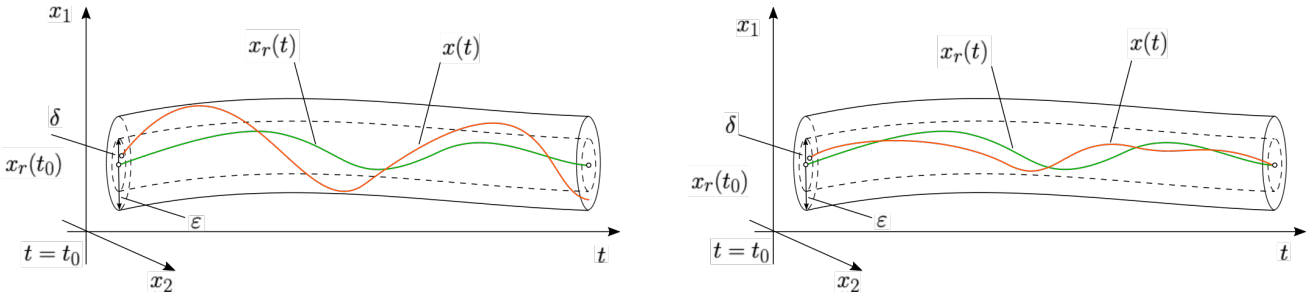

Figure 3.15: a) Lyapunov stability: Every solution $x(t)$ with the initial condition $|x(t_0) - x_r(t_0)| < \delta(\varepsilon)$ applies $|x(t) - x_r(t)| < \varepsilon$ for all $t > t_0$. b) Asymptotic stability: in addition to the Lyapunov stability criterion, every solution $x(t)$ applies $\lim_{t\to\infty} |x(t) - x_r(t)| = 0$.

of a system that shows neutral stability. Note, that the van der Pol system degenerates to the undamped harmonic oscillator for $\mu = 0$, cf Fig. 3.6c. In the following we will learn more about nonlinear systems, their dynamics and its classification using stability arguments.

3.1.6.4 Two-dimensional Linear Systems

We now discuss two-dimensional linear dynamical systems. Let's assume the general system:

$$\dot{x} = f(x, y) \tag{3.134}$$
$$\dot{y} = g(x, y) \tag{3.135}$$

The critical points are again the roots of $f(x, y) = 0$ and $g(x, y) = 0$. What set of solutions are possible? Firstly we assume the critical point (x^*, y^*). Taylor-expansion of the system gives:

$$\dot{x} \simeq (x - x^*) \cdot \left(\frac{\partial f}{\partial x}\right)\Big|_{(x^*;y^*)} + (y - y^*) \cdot \left(\frac{\partial f}{\partial y}\right)\Big|_{(x^*;y^*)} + h.o. \tag{3.136}$$
$$\dot{y} \simeq (y - y^*) \cdot \left(\frac{\partial g}{\partial y}\right)\Big|_{(x^*;y^*)} + (y - y^*) \cdot \left(\frac{\partial g}{\partial y}\right)\Big|_{(x^*;y^*)} + h.o. \tag{3.137}$$

$$\dot{x} \simeq ax + by + h.o. \tag{3.138}$$
$$\dot{y} \simeq cx + dy + h.o. \tag{3.139}$$

By applying the linearization terms of higher order (h.o) can be neglected. Coordinate transform (shift the origin and use the same symbols) leads to the coefficient matrix:

$$\mathcal{L} = \begin{pmatrix} a & b \\ c & d \end{pmatrix} = \begin{pmatrix} \frac{\partial f}{\partial x} & \frac{\partial f}{\partial y} \\ \frac{\partial g}{\partial x} & \frac{\partial g}{\partial y} \end{pmatrix} \tag{3.140}$$

which is the Jacobian, cf. Eq. (3.102). Remember, the Jacobian describes the flux of the field completely!
The resulting equation is the general two-dimensional equation:

$$\frac{\mathrm{d}}{\mathrm{d}t}\begin{pmatrix} x \\ y \end{pmatrix} = \begin{pmatrix} a & b \\ c & d \end{pmatrix}\begin{pmatrix} x \\ y \end{pmatrix} \quad \text{or:} \tag{3.141}$$

$$\dot{\boldsymbol{x}} = \mathcal{L}\boldsymbol{x} \tag{3.142}$$

which can be solves by utilizing the techniques of linear algebra, cf. Eqs: (3.82) - (3.87). The general solution is:

$$x(t) = c_{11}\mathrm{e}^{\lambda_1 t} + c_{12}\mathrm{e}^{\lambda_2 t} \tag{3.143}$$

$$y(t) = c_{21}\mathrm{e}^{\lambda_1 t} + c_{22}\mathrm{e}^{\lambda_2 t} \tag{3.144}$$

with $\lambda_i, i = 1, 2$ the eigenvalues. The constants c_{ij} are determined by the initial conditions of the problem:

$$\begin{aligned} x(0), &\quad y(0) \\ \dot{x}(0), &\quad \dot{y}(0) \end{aligned} \tag{3.145}$$

Note, the considerations are only valid, if the matrix $\mathcal{L}$ is not singular, which means the matrix has a unique solution, so if holds $\det \mathcal{L} \neq 0$ and $\lambda_1 \neq \lambda_2$.
If $\lambda_1 = \lambda_2$ we have $(\mathrm{e}^{\lambda t}; t\,\mathrm{e}^{\lambda t})$ and the solution is:

$$x(t) = \mathrm{e}^{\lambda t}(c_{11} + c_{12}\,t) \tag{3.146}$$

$$y(t) = \mathrm{e}^{\lambda t}(c_{21} + c_{22}\,t) \tag{3.147}$$

How do we get the differential equation from these considerations?
Applying the time derivative operator:

$$\begin{aligned} \dot{x} &= ax + by \quad \big| \ \partial_t \\ \dot{y} &= cx + dy \quad \big| \ \partial_t \end{aligned}$$

gives:

$$\begin{aligned} \ddot{x} &= a\dot{x} + b\dot{y} \\ \ddot{y} &= c\dot{x} + d\dot{y} \end{aligned} \tag{3.148}$$

Rearranging and replacing of the variable $\dot{y}$ leads to:

$$\ddot{x} - (a + b)\dot{x} + (ad - cb)x = 0$$

This is the general differential equation for linear two-dimensional dynamical systems without external driving forces. The equation is a homogeneous and second order linear differential equation. For $(a + b) > 0$ the system has positive damping, for $(a + b) < 0$ the damping is negative. For $(ad - cb) > 0$ the system generates oscillations. The mentioned pre-factors are the trace: $\mathrm{Tr}\,\mathcal{L} = (a + b)$ and the determinant $\det \mathcal{L} = (ad - cb)$ of the coefficient matrix $\mathcal{L}$.

The general solution is:

$$\lambda_{1,2} = \frac{(a+b)}{2} \pm \sqrt{\frac{(a+b)^2}{4} - (ad - cb)} \tag{3.149}$$

With the abbreviations T for trace and Δ for determinant one writes:

$$\lambda_{1,2} = \frac{T}{2} \pm \sqrt{\frac{T^2}{4} - \Delta} \tag{3.150}$$

The eigenvalues determine the possible dynamics of the system. Note the eigenvalues do not change under similarity transformations, e.g. linear coordinate transforms. Eigenvalues are determined by the trace and the determinant of the matrix.
We will now study the various possible cases.

3.1.6.5 Classification of Linear Two-dimensional Fluxes

To classify the two-dimensional fluxes we consider the characteristics of the eigenvalues of the dynamical system, their signs and if they are real, complex or purely imaginary numbers. We con distinguish the following cases:

1.) $\boxed{\lambda_1 > 0,\ \lambda_2 > 0}$

We start with a very simple dynamical system:

$$\dot{x} = x \tag{3.151}$$
$$\dot{y} = y \tag{3.152}$$

The system is uncoupled, which means the variables x and y do not depend on each other. The solutions are proportional to:

$$x(t) \sim \mathrm{e}^t \tag{3.153}$$
$$y(t) \sim \mathrm{e}^{2t} \tag{3.154}$$

The fix point of the system is $(0;0)$. The phase portrait is shown in Fig.: 3.16a. One can see some trajectories of different initial conditions, which repel exponentially from the fix point in a perfectly star-like manner. The trajectories of the very similar systems $\dot{x} = x, \dot{y} = 2y$ and $\dot{x} = 2x, \dot{y} = y$ are shown in Figs.: 3.16b and 3.16c. These trajectories repel from the fix point $(0;0)$ but in curved trajectories corresponding to the different eigenvalues in x- and y-direction. The repelling property of the fix point is called a globally unstable node.

2.) $\boxed{\lambda_1 < 0,\ \lambda_2 < 0}$

The next case are linear dynamical systems that have negative eigenvalues, for instance:

$$\dot{x} = -x \tag{3.155}$$
$$\dot{y} = -y \tag{3.156}$$

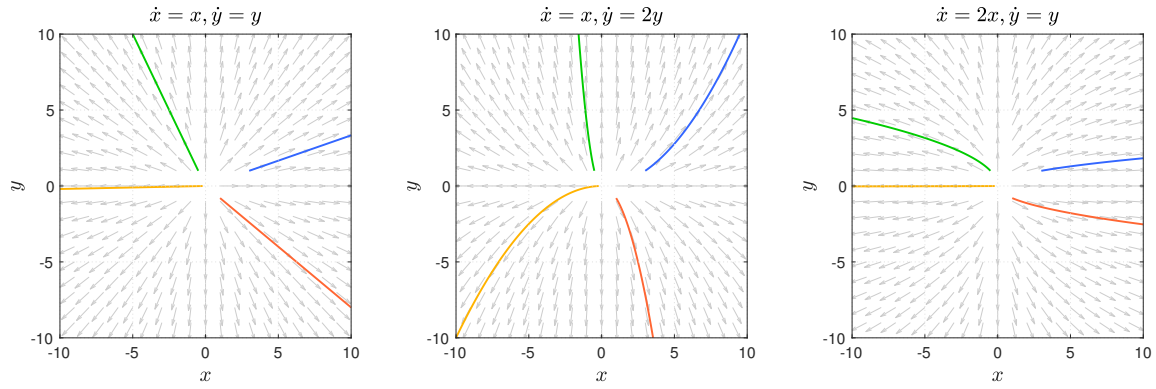

a) **b)** **c)**

Figure 3.16: Positive eigenvalues generate a globally unstable node. Shown are solutions of similar linear dynamical systems: a) the system: $\dot{x} = x, \dot{y} = y$, b) the system: $\dot{x} = x, \dot{y} = 2y$ and c) the system: $\dot{x} = 2x, \dot{y} = y$, for various initial conditions: $[3.0; 1.0]$ (blue), $[-0.5; 1.0]$ (green), $[1.0; -0.8]$ (red) and $[-0.2; -0.004]$ (yellow).

The system is uncoupled too, the solutions are proportional to:

$$x(t) \sim \mathrm{e}^{-t} \tag{3.157}$$
$$y(t) \sim \mathrm{e}^{-t} \tag{3.158}$$

The system has an asymptotically stable fix point at $(0; 0)$. All trajectories get attracted by the fix point, cf. Fig.: 3.17.

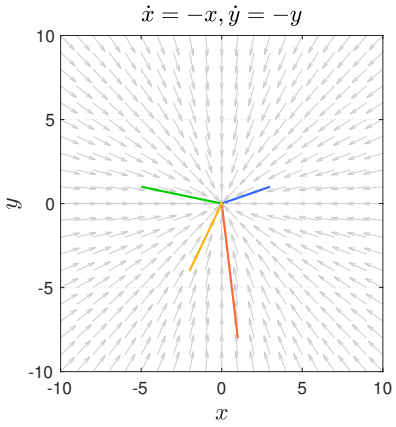

Figure 3.17: Phase portrait and eigenvalues of the system $\dot{x} = -x, \dot{y} = -y$ for various initial conditions: $[3.0; 1.0]$ (blue), $[-5.0; 1.0]$ (green), $[1.0; -8.0]$ (red) and $[-2.0; -4.0]$. The fix point at $(0; 0)$ is called stable node.

3.) $\boxed{\lambda_1 > 0,\ \lambda_2 > 0}$

The next system has a negative and a positive eigenvalue, for example:

$$\dot{x} = -x \tag{3.159}$$
$$\dot{y} = 2y \tag{3.160}$$

The system is uncoupled. The solutions are attractive in y-direction and repel in x-direction, cf. Fig.: 3.18. The fix point is stable in y-direction and unstable in x-direction. Such fix points are called saddle nodes, or saddle for short.

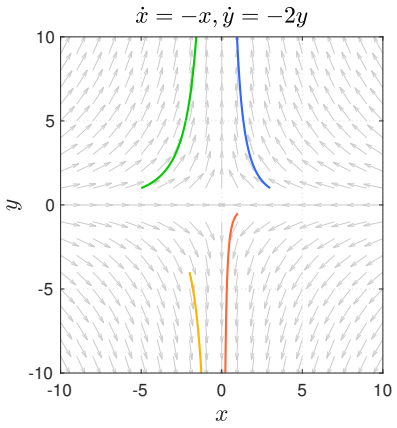

Figure 3.18: Phase portrait and eigenvalues of the system $\dot{x} = -x, \dot{y} = 2y$ for various initial conditions: $[3.0; 1.0]$ (blue), $[-5.0; 1.0]$ (green), $[1.0; -0.5]$ (red) and $[-2.0; -4.0]$. The fix point at $(0; 0)$ is called saddle node or saddle.

4.) $\boxed{\lambda_{1,2} = \gamma \pm i\omega, \gamma < 0}$

In the following case the eigenvalues are complex numbers with a negative real part $\gamma < 0$, for instance the system:

$$\dot{x} = -y \tag{3.161}$$
$$\dot{y} = -\omega x - \gamma y \tag{3.162}$$

The system is coupled, which means that the variables x and y depend on each other, or more precisely the $\dot{x}$ is a function of y and $\dot{y}$ is a function of x. One solution of the system is:

$$x(t) = \mathrm{e}^{\lambda_1 t} = \mathrm{e}^{-\gamma t} \cdot \mathrm{e}^{i\omega t} \tag{3.163}$$
$$= \mathrm{e}^{-\gamma t} \cdot \underbrace{\Big(\cos(\omega t) + i \sin(\omega t)\Big)}_{oscillations!} \tag{3.164}$$

One can see, the solution has two terms, one with exponential decay and one that represents oscillations. All together this leads to trajectories that attracts to the fix point at $(0; 0)$ in spirals. Such fix point is called stable focus or stable spiral point. One can re-write the system to:

$$\ddot{x} + \gamma\dot{x} + \omega^2 x = 0 \tag{3.165}$$

Now one can see better why this is called positive damping
The parameter $\gamma < 0$ is called damping.
The trajectories spiral into the fix point at $(0; 0)$, cf. Fig.: 3.19. Such kind of fix point is called an asymptotically stable focus.

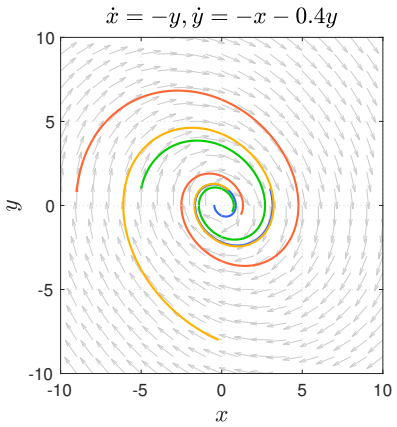

Figure 3.19: The phase portrait and the eigenvalues of the system $\dot{x} = y, \dot{y} = -x - \gamma y$, with the negative damping parameter $\gamma = -0.4$, for various initial conditions: $[3.0; 1.0]$ (blue), $[-5.0; 1.0]$ (green), $[-9.0; 0.8]$ (red) and $[-0.2; -8.0]$. The fix point at $(0; 0)$ is called asymptotically stable focus.

The parameter $\gamma < 0$ is called negative damping. Note that $\gamma < 0$ is connected to the temporal rate of change of $\dot{x}$ which can be interpreted as the velocity, in accordance to our experiences that damping is connected to the velocity of the dynamical system, for instance riding a bike where the damping by the frontal wind increase at higher velocities[6].

5.) $\boxed{\lambda_{1,2} = \gamma \pm i\mu, \gamma > 0}$

The next case we study is when the eigenvalues are complex numbers but with a positive real part $\gamma > 0$. An example is the system:

$$\dot{x} = -y \tag{3.166}$$
$$\dot{y} = -x + \gamma y, \quad \gamma \in \mathbb{R}^+ \tag{3.167}$$

The system is coupled. That means the variables x and y depend on each other, or more precisely the $\dot{x}$ is a function of y and $\dot{y}$ is a function of x. One solution of the system is:

$$x(t) = \mathrm{e}^{\lambda_1 t} = \mathrm{e}^{\gamma t} \cdot \mathrm{e}^{i\mu_1 t} \tag{3.168}$$
$$= \mathrm{e}^{\gamma t} \cdot \underbrace{\Big(\cos(\mu t) + i \sin(\mu t)\Big)}_{oscillations!} \tag{3.169}$$

[6]The aerodynamic damping is an effect that can be described by the back-pressure formula

$$F = \frac{p}{A} = \frac{1}{2}\rho C_W \overline{v}^2$$

The force F or the back-pressure p respectively is increasing quadratically with the velocity. The parameter C_W is characterizing the aerodynamical quality of the shape of the moving object.

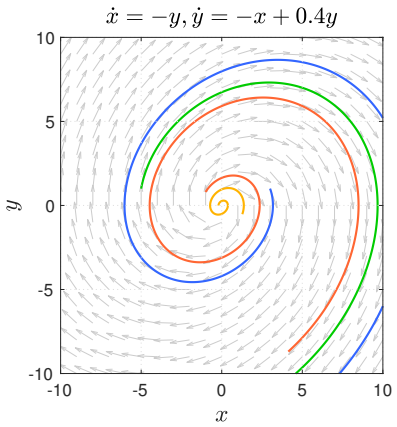

Figure 3.20: Phase portrait and eigenvalues of the system $\dot{x} = y, \dot{y} = -x + \gamma y$, with the positive damping parameter $\gamma = 0.4$, for various initial conditions: $[3.0; 1.0]$ (blue), $[-5.0; 1.0]$ (green), $[-1.0; 0.8]$ (red) and $[-0.2; -0.004]$. The fix point at $(0; 0)$ is called unstable focus.

One can see, the solution has two terms, one with exponential growth and one that represents oscillations. All together this leads to trajectories that repel from the fix point at $(0; 0)$ in spirals. Such fix point is called unstable focus or unstable spiral point. The parameter $\gamma > 0$ is called positive damping. The negative damping parameter $\gamma < 0$ is connected to the temporal rate of change of x which can be interpreted as the velocity $\dot{x} = y$. This can be interpreted as a kind of velocity-dependent excitement of the system.

6.) $\boxed{\lambda_{1,2} = \pm i\mu_{1,2},\ \mu \in \mathbb{R}}$

The last case is that both eigenvalues become purely imaginary. An example of such a the system is the famous harmonic oscillator:

$$\dot{x} = y \tag{3.170}$$
$$\dot{y} = -x \tag{3.171}$$

or in more physical notation $\ddot{x} + \frac{k}{m}x = 0$, and with the substitution (definition of the momentum) $p = m\dot{x}$

$$\dot{x} = \frac{p}{m} \tag{3.172}$$
$$\dot{p} = -m\,\omega^2\,x \tag{3.173}$$

where $\dot{p} = F$ is the force, m the mass and $\omega = \sqrt{\frac{k}{m}}$ the angular frequency with k the spring constant.

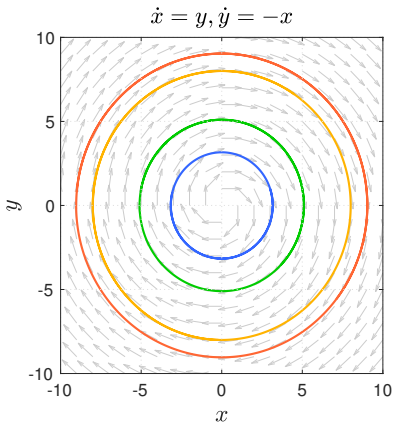

Figure 3.21: Phase portrait and eigenvalues of the system with no damping. This is identical the harmonic oscillator

In the phase space the system is represented by closed trajectories, each for exact one total amount of energy E_{tot}. Every trajectory turns around the center $(0, 0)$ describing a circle or an ellipse, depending on the scaling. The center is a stable critical point.

We now want to consider the van der Pol system again and calculate its eigenvalues explicitly. The van der Pol system can also be written as:

$$\begin{aligned} \dot{x} &= f(x, y) \qquad \text{with:} \quad f(x, y) = y \\ \dot{y} &= g(x, y) \qquad \text{with:} \quad g(x, y) = -\omega^2 x + \mu(1 - x^2)y \end{aligned}$$

We already have seen that the van der Pol system has one single fix point at $(0; 0)$, namely when the velocity $\dot{x} = y$ is equal to zero. If follows that also $\dot{y} = 0$:

$$(\dot{x}; \dot{y}) = (0; 0) \rightarrow (x^*, y^*) = (0; 0)$$

Assuming a fix point $(x^*; y^*)$ one can replace the variables by:

$$u = x - x^*, \; v = y - y^*$$

The Taylor-expansion of the transformed system is then:

$$\begin{aligned} \dot{u} &= u\frac{\partial f}{\partial x} + v\frac{\partial f}{\partial y} + \mathbf{O}(u^2, v^2, uv) \\ \dot{v} &= u\frac{\partial g}{\partial x} + v\frac{\partial g}{\partial y} + \mathbf{O}(u^2, v^2, uv) \end{aligned}$$

with $\mathbf{O}(u^2, v^2, uv)$ the terms of quadratic order. Linearization leads to the Jacobi-matrix:

$$\begin{pmatrix} \dot{u} \\ \dot{v} \end{pmatrix} = \begin{pmatrix} \frac{\partial f}{\partial x} & \frac{\partial f}{\partial y} \\ \frac{\partial g}{\partial x} & \frac{\partial g}{\partial y} \end{pmatrix}_{(x^*;y^*)} \begin{pmatrix} u \\ v \end{pmatrix} \tag{3.174}$$

$$\begin{pmatrix} \dot{u} \\ \dot{v} \end{pmatrix} = \begin{pmatrix} 0 & 1 \\ -2\mu xy - \omega^2 & \mu(1-x^2) \end{pmatrix}_{(0;0)} \begin{pmatrix} u \\ v \end{pmatrix} \tag{3.175}$$

$$\begin{pmatrix} \dot{u} \\ \dot{v} \end{pmatrix} = \begin{pmatrix} 0 & 1 \\ -\omega^2 & \mu \end{pmatrix}_{(0;0)} \begin{pmatrix} u \\ v \end{pmatrix} \tag{3.176}$$

One can see that the stability of the linearized van der Pol system (close to the fix point) depends on the control parameter μ. The characteristic polynomial is:

$$0 = \lambda^2 - \mu\lambda + \omega^2 \tag{3.177}$$

The eigenvalues are:

$$\lambda_{1,2} = \frac{\mu \pm \sqrt{\mu^2 - 4\omega^2}}{2} \tag{3.178}$$

The linear stability criteria of a dynamical system with a nonlinear functions $f(x, y)$ and $g(x, y)$ are:

$$f'(x^*) < 0 \quad stable \qquad g'(x^*) < 0 \quad stable \tag{3.179}$$

$$f'(x^*) > 0 \quad unstable \qquad g'(x^*) < 0 \quad unstable \tag{3.180}$$

and

$$f'(y^*) < 0 \quad stable \qquad g'(y^*) < 0 \quad stable \tag{3.181}$$

$$f'(y^*) > 0 \quad unstable \qquad g'(y^*) < 0 \quad unstable \tag{3.182}$$

Depending on the value of μ the van der Pol system has different behavior. For $\mu = 0$ the system is equal to the harmonic oscillator. There is only one single fix point, namely the trivial one, when the system starts at $(0; 0)$ and stays forever. For $|\mu| > 0$ the system enters a limit cycle after a transient. The limit cycle is an isolated periodic solution and it is represented by a closed trajectory where almost all other trajectories spirals in asymptotically (exclude the trivial one). The limit cycle of the van der Pol system is a stable one. Other nonlinear systems can evolve limit cycles that are unstable or semi-stable. Limit cycles are purely nonlinear phenomena!

The change of the characteristics of the behavior of the dynamical system is called bifurcation. This corresponds to a characteristic change of the eigenvalues of the system, namely their signs and/or their change into complex numbers. The bifurcation diagrams in Fig. 3.22a and 3.22b show the change of the eigenvalues λ of the linearized van der Pol system with respect to the parameter μ.

At the end of the section, we want to summarize the knowledge we have gained about dynamical systems. Figure 3.23 shows the relationships between stability properties, eigenvalues and the

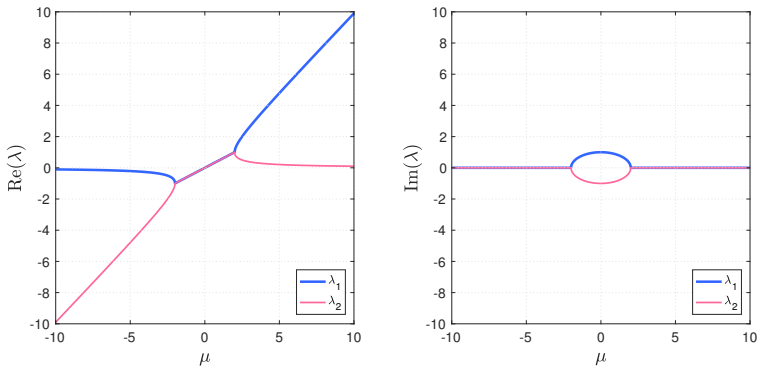

Figure 3.22: Bifurcation of the eigenvalues of the linearized van der Pol system depending on the parameter μ. a) the real part $\mathrm{Re}(\lambda_i)$ depending on parameter μ, b) the imaginary part $\mathrm{Im}(\lambda_i)$ depending on parameter μ .

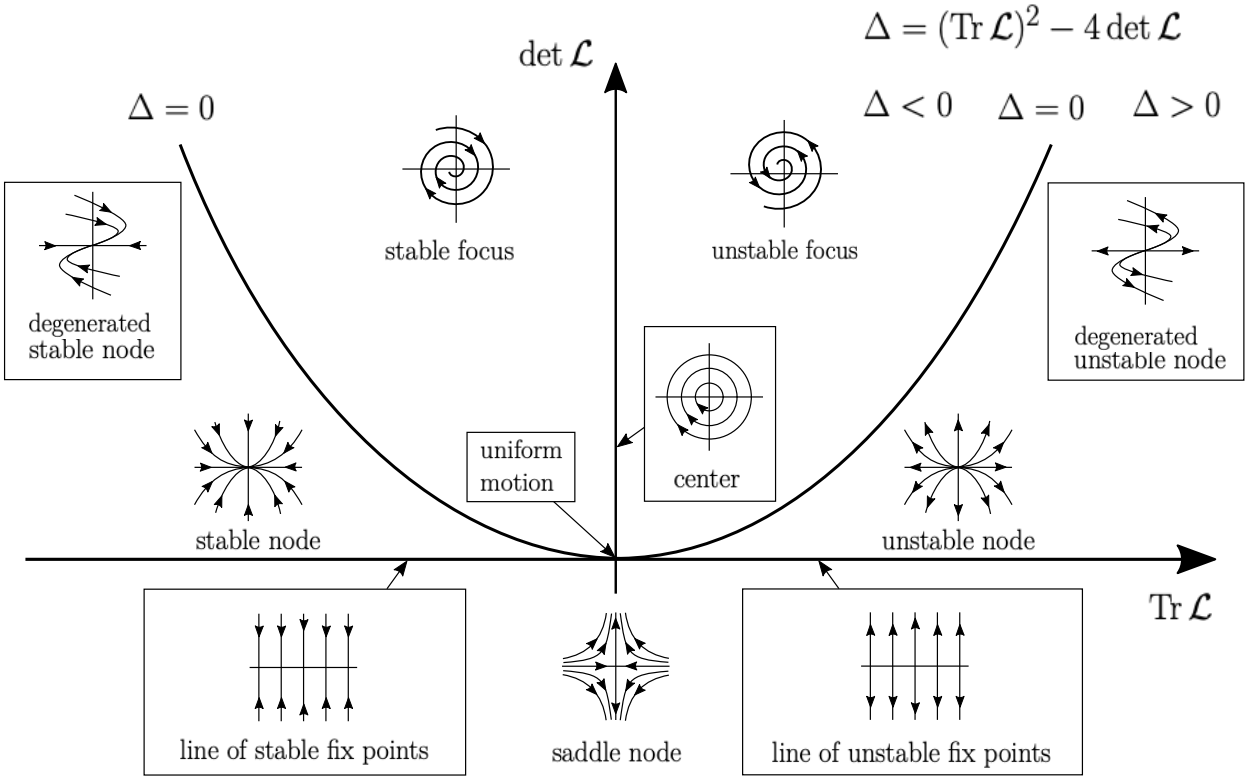

Figure 3.23: Poincaré diagram: Classification of phase portraits in the $(\det\mathcal{L}; \mathrm{Tr}\,\mathcal{L})$-plane.

qualitative dynamics of two-dimensional dynamic systems. Plotted is the determinant $det\mathcal{L}$ over the trace of the the Jacobi-matrix $Tr\mathcal{L}$.
It can be seen that any small perturbation in systems forming centers leads to the loss of the center property – and to qualitatively different dynamics! This is a remarkable point because it means that ideal harmonic oscillators are extremely rare and almost never occur in practice. Responsible for this are internal and external forces (e.g. friction), which lead to interesting as well as complicated dynamics, such as intermittency, chaos or synchronization.

3.2 Physical Quantities and Fields

3.2.1 Volumes in Fluid mechanics

In fluid mechanics one operates with different terms of volume. One distinguishes control volumes, finite volume elements and fluid elements or fluid parcels with respect to their descending size.

A control volume in a given physical set-up is the area of interest for the derivation of the conservation of mass, the conservation of momentum and the conservation of energy. It is usually defined along a stream-tube (cf. Fig. 3.24) and can be fixed or moving as well as rigid or deformable. Normally it is a macroscopic physical quantity.

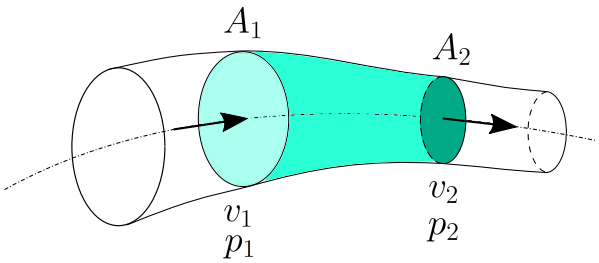

Figure 3.24: Control volume along a stream-tube.

$$\int_V = f(\vec{r})\mathrm{d}V \tag{3.183}$$

Finite volume elements are used in computational fluid mechanics and computational aeroacoustics (CFD/CAA) to model the computational space where the fluid mechanics act on. Finite volume elements in euclidean space are given by products of sufficient small differences $\Delta V = \Delta u_1 \Delta u_2 \Delta u_3$ depending on the spatial resolution of the area of interest. The u_i are the coordinates.
A fluid parcel is a very small amount of fluid, but big enough that atoms and molecules, the particles that constitute the volume element satisfy the Maxwell-Boltzmann. That means the thermodynamic quantities like temperature, internal energy, enthalpy or entropy are well defined [Callen (1985)]. The concept of the fluid parcel is that the average particle velocity and other properties of the fluid parcel are averaged over a length scale which is large compared to the mean free path length, but small compared to the characteristic length scale of the given fluid mechanical set-up. The fluid parcel can be distorted, can change its shape and its volume as well. The latter is constitutive for compressible flows which lead to acoustical effects like sound waves. If the fluid parcel conserves the volume the flow is called incompressible. These aspects are discussed now.

3.2.2 Fields

3.2.2.1 Scalar fields

In mathematics a scalar field is a function that associates a scalar value with every point in a (multidimensional) space. In physics this association is connected to the physical space. Scalar fields in the physical context are independent of the choice of a reference frame. In the 1-dimensional space the harmonic potential $V(x) = \frac{m}{2}\omega^2 x^2$ is scalar field as well as the gravitational field $\Phi(r) = -G\frac{M}{r}$ of the earth. Fig. 3.25a shows the temperature field $T(\vec{r}) = T(x, y, z)$ of a room which is also a scalar field.

3.2.2.2 Vector fields

A vector field assigns vectors with every point in a subset of space. Examples are the position vector field $\vec{r} = \sum_{i=1}^{3} x_i \cdot \hat{\mathbf{e}}_\mathbf{i}$, the time dependent velocity field in $\vec{v}(\vec{r}, t)$, the harmonic potential's negative gradient $\vec{F} = -\nabla V(x) = -\nabla\frac{m}{2}\omega^2 x^2 = -m\omega^2 x$, called force or the temperature gradient field $\nabla T(x, y, z)$, cf. Fig. 3.25b.

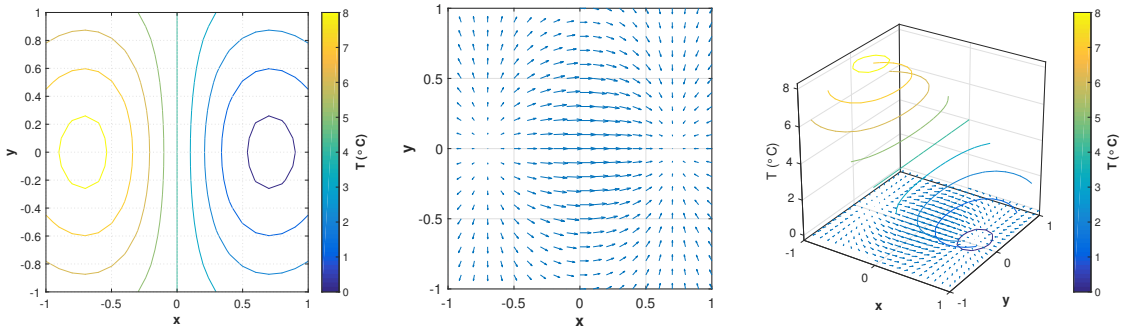

a) **b)** **c)**

Figure 3.25: Visualizations of physical fields. a) Contour plot of a scalar field. Shown is the temperature distribution $T(x, y, z)$. Color-coded are the isotherms ($T = const.$). b) A vector field that corresponds to the addressed scalar field in a) is the temperature gradient field $\nabla T(x, y, z)$. c) The scalar field and the vector field in a 3D-visualization.

3.2.2.3 Tensor fields

Tensors are algebraic objects that describe a multilinear relationship between sets of algebraic objects related to a vector space. Scalars are the simplest tensors, called zeroth order tensors. Vectors are first order tensors, matrices are second tensors and so on. An example for a second order tensor is the Cauchy stress tensor $\bar{\bar{\sigma}}$ which describes all possible transformations of a fluid parcel caused by the stress, cf. Eq. (3.184). The first index is assigned to the normal direction of the respective surface. The second index indicates the direction the stress is acting.

$$\bar{\bar{\sigma}} = \boldsymbol{\sigma} = \begin{bmatrix} \sigma_{11} & \sigma_{12} & \sigma_{13} \\ \sigma_{21} & \sigma_{22} & \sigma_{23} \\ \sigma_{31} & \sigma_{32} & \sigma_{33} \end{bmatrix} \equiv \begin{bmatrix} \sigma_x & \tau_{xy} & \tau_{xz} \\ \tau_{yx} & \sigma_y & \tau_{yz} \\ \tau_{zx} & \tau_{zy} & \sigma_z \end{bmatrix} \tag{3.184}$$

The nine components of the Cauchy stress tensor σ_{ij} on a fluid parcel are depicted in Fig. 3.26. The shear stress components ($i \neq j$) of the Cauchy stress tensor are also written as $\tau_{i,j}$.

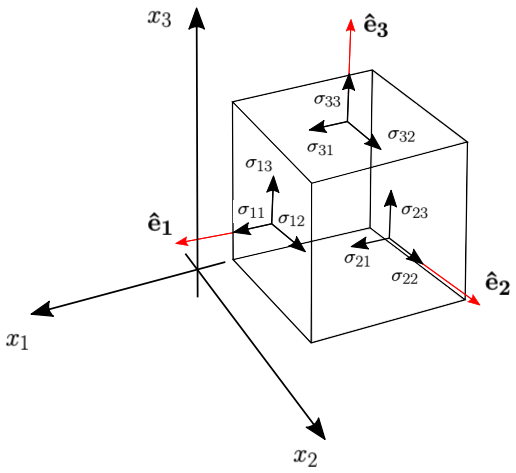

Figure 3.26: Illustration of the components of the Cauchy stress tensor. The first index is assigned to the normal direction $\hat{\mathbf{e}}_\mathbf{i}$ of the surface of the fluid parcel under consideration. The second index indicates the direction the stress is acting.

The stress tensor σ_{ij} can be expressed as the sum of two other stress tensors:

a) the mean hydrostatic stress tensor or volumetric stress tensor or mean normal stress tensor, $\pi\delta_{ij}$ which tends to change the volume of the stressed body.

b) The deviatoric component called the stress deviator tensor s_{ij}, which tends to distort it.

$$\sigma_{ij} = s_{ij} + \pi\delta_{ij} \tag{3.185}$$

where π is the mean stress given by

$$\pi = \frac{\sigma_{kk}}{3} = \frac{\sigma_{11} + \sigma_{22} + \sigma_{33}}{3} = \tfrac{1}{3} tr\left(\bar{\bar{\sigma}}\right) \tag{3.186}$$

The pressure p is generally defined as negative one-third the trace of the stress tensor minus any stress the divergence of the velocity contributes with, i.e.:

$$p = \lambda \nabla \cdot \vec{u} - \pi = \lambda \frac{\partial u_k}{\partial x_k} - \pi = \sum_k \lambda \frac{\partial u_k}{\partial x_k} - \pi \tag{3.187}$$

where λ is a proportionality constant, $\nabla \cdot \vec{u}$ is the divergence of $\vec{u}$, x_k is the k$^{\text{th}}$ Cartesian coordinate, $\vec{u}$ is the velocity and u_k is the k$^{\text{th}}$ Cartesian component of $\vec{u}$.
The deviatoric stress tensor can be obtained by subtracting the hydrostatic stress tensor from the Cauchy stress tensor:

$$s_{ij} = \sigma_{ij} - \frac{\sigma_{kk}}{3}\delta_{ij} \tag{3.188}$$

$$\begin{bmatrix} s_{11} & s_{12} & s_{13} \\ s_{21} & s_{22} & s_{23} \\ s_{31} & s_{32} & s_{33} \end{bmatrix} = \begin{bmatrix} \sigma_{11} & \sigma_{12} & \sigma_{13} \\ \sigma_{21} & \sigma_{22} & \sigma_{23} \\ \sigma_{31} & \sigma_{32} & \sigma_{33} \end{bmatrix} - \begin{bmatrix} \pi & 0 & 0 \\ 0 & \pi & 0 \\ 0 & 0 & \pi \end{bmatrix} \tag{3.189}$$

$$= \begin{bmatrix} \sigma_{11} - \pi & \sigma_{12} & \sigma_{13} \\ \sigma_{21} & \sigma_{22} - \pi & \sigma_{23} \\ \sigma_{31} & \sigma_{32} & \sigma_{33} - \pi \end{bmatrix} \tag{3.190}$$

3.2.3 The Bernoulli's Principle

The Bernoulli 's principle is based on the energy balance. If only the gravity is acting along the stationary streamline of an ideal, compressible fluid the relation between fluid velocity $\vec{v}$, pressure p and the height h the Bernoulli's principle is given by:

$$\frac{1}{2}(\vec{v}^2 - \vec{v}_0^2) + g(h - h_0) + \int_{p_0}^{p} \frac{\mathrm{p}}{\rho(p)} = 0 \tag{3.191}$$

For a constant density[7] Eq. (3.191) reduced to the incompressible formulation:

$$\frac{1}{2}\rho\vec{v}^2 + p + \rho g h = \frac{1}{2}\rho\vec{v}_0^2 + p_0 + \rho g h_0 \tag{3.192}$$

For laminar, incompressible, non-viscous flows in a tube with variable area cross-section A the following relations:

$$A\,v = A_m\,v_m \qquad \text{continuity equation} \tag{3.193}$$

$$\frac{1}{2}\rho v^2 + p = p_0 = \frac{1}{2}\rho v_m^2 \qquad \text{Bernoulli equation} \tag{3.194}$$

where v_m denotes the maximal velocity and A_m the minimal area. With these relations one calculates the area A and the pressure p as functions of the velocity as:

$$\frac{A_m}{A} = \frac{v}{v_m}\,, \qquad \frac{p}{p_0} = 1 - \left(\frac{v}{v_m}\right)^2 \tag{3.195}$$

For compressible fluid the relations differ significantly from the relations in Eqs: (3.195). In fast flows of ideal gases the change of state variables is adiabatic:

$$\frac{p}{p_0} = \left(\frac{\rho}{\rho_0}\right)^{\kappa} \qquad \text{with} \quad \kappa = \frac{C_p}{C_V} \approx 1.4 \tag{3.196}$$

Using the state equation for ideal gases:

$$p = \frac{\rho R T}{M} \tag{3.197}$$

and neglecting the gravitation leads to the Bernoulli's principle for compressible fluids:

$$\frac{\kappa}{\kappa - 1}\frac{p_0}{\rho_0} = \frac{1}{2}v_m^2 = \frac{C_P}{M}T_0 \tag{3.198}$$

In compressible media are characterized by a finite speed of sound c:

$$c = \sqrt{\kappa \cdot \frac{p}{\rho}} \tag{3.199}$$

The flow velocity v equal to c is called critical velocity v^*:

$$v^* = u^* = \sqrt{2}(\kappa + 1)^{-1/2}u_0 = \left(\frac{\kappa - 1}{\kappa + 1}\right)^{1/2} v_m \quad \text{with} \quad v_m = \left(\frac{2\kappa}{\kappa - 1}\frac{RT_0}{M^*}\right)^{1/2} \tag{3.200}$$

with the flow parameter of air:

[7] $\rho = const$ leads to $\int_{p_0}^{p} \frac{\mathrm{p}}{\rho(p)} = \frac{p - p_0}{\rho}$.

$u^* = 314\,\mathrm{m/s}$	$u_0 = 343\,\mathrm{m/s}$
$\kappa = 1.4$	$v_m = 770\,\mathrm{m/s}$
$\rho_0 = 1.205\,\mathrm{kg/m^3}$	$p_0 = 101325\,\mathrm{Pa}$
$M^* = 0.029\,\mathrm{kg/mol}$	$T_0 = 293.17\,\mathrm{K}$
$R = 8.3145\,\mathrm{J/K/mol}$	

The continuity equation for stationary laminar compressible flows is given by:

$$A\rho v = A^*\,\rho^*\,v^* = A^*\,\rho_0\,v_m\,2^{\left(+\frac{1}{\kappa-1}\right)}(\kappa-1)^{\frac{1}{2}}(\kappa+1)^{\left(-\frac{\kappa+1}{2(\kappa-1)}\right)} \tag{3.201}$$

with A the cross-section, and A^* the cross-section at the critical velocity. Assuming that the flow remains approximately laminar even for high velocities, one obtains from the Bernoulli equation, the continuity equation and the relation for adiabatic changes of state:

$$\frac{p}{p_0} = \left(\frac{\rho}{\rho_0}\right)^{\kappa} \tag{3.202}$$

the physical quantities M, p, ρ, T and A as functions of v:

$$M = \frac{v}{u} = 2^{\frac{1}{2}}\,(\kappa-1)^{-\frac{1}{2}}\left(\frac{v}{v_m}\right)\left[1-\left(\frac{v}{v_m}\right)^2\right]^{-\frac{1}{2}}$$

$$\frac{p}{p_0} = \left[1-\left(\frac{v}{v_m}\right)^2\right]^{\frac{\kappa}{\kappa+1}} \quad , \quad \frac{\rho}{\rho_0} = \left[1-\left(\frac{v}{v_m}\right)^2\right]^{\frac{1}{\kappa+1}}$$

$$\frac{T}{T_0} = 1-\left(\frac{v}{v_m}\right)^2$$

$$\frac{A^*}{A} = 2^{\left(-\frac{1}{\kappa-1}\right)}\,(\kappa-1)^{-\frac{1}{2}}\,(\kappa+1)^{\left(+\frac{\kappa+1}{2(\kappa-1)}\right)}\left(\frac{v}{v_m}\right)\left[1-\left(\frac{v}{v_m}\right)^2\right]^{\left(+\frac{1}{\kappa-1}\right)}$$

Chapter 4

Numerics

> The model separates the important from the unimportant
>
> own credo

The complex interplay between the flow field and the sound field, the interactions between coherent fluid mechanical structures, the sound generation and the sound propagation are in general described by the compressible Navier-Stokes equations [Schlichting (2003)], [Morse (1968)]. For a successful numerical implementation of a given set-up of interest, one has to apply the compressible Navier-Stokes equations with appropriate initial and boundary conditions. The set of equations have to be solved on an suitable computational grid, the numerical space which is called mesh. Some aspects of this chapter are exemplified by the set-up of the numerical simulations of the organ pipe in section 5.3.

The numerical treatment of compressible problems announced here is still an advanced task. The main difficulties arise from reproducing the interactions between the flow field and the sound field [Fabre et al.(1996)] because of the different scales the flow velocity and the particle velocity act on. Numerical simulations allow studying the dynamics of coherent fluid mechanical structures like jets, vortices as well as of acoustical phenomena like the generation of sound waves, their propagation in the resonator and their radiation into the free space simultaneously. Also trans-sonic phenomena are accessible. In principle, a successful numerical simulation can be divided into the following tasks:

- Physical previews
- Pre-processing
- Processing
- Post-Processing

The tasks include the following sub-tasks and relate to questions that need to be being answered appropriately:

Physical Previews:

- Which set of equations is constitutive for the given problem?
- Which are the characteristic fluid dynamical numbers to be taken into account?

- What are the scales of the problem?
- Software-decision.
- Hardware-decision.

Pre-Processing:

- How to write an appropriate mesh for the given case?
- Determine the relevant thermo-physical properties.
- Implement suitable initial and boundary conditions for each physical quantity to be calculated, e.g. pressure p, the velocity vector $\vec{U}$, temperature T, density ρ, turbulent kinetic Energy k, etc..
- Discretization schemes for the differential operators in the constitutive equations (del operator, Laplacian, time derivative, etc.) inclusive proper correctors.
- Select an appropriate turbulence model to model the energy transfer into and out of the sub-grid scales.
- Solver for the compressible fluid dynamical problem, determination of numerical schemes and their tolerances.
- Adequate matrix solvers.
- Configure relevant numerical parameters, e.g. numerical time step size, simulation time, write precision etc..
- Define suitable sample sets and probe points in the mesh for analysis.
- Parallelize the calculation.
- Take care of numerical stability parameters, e.g. Courant number.
- Control during simulation run time.
- Calculate additional physical quantities, e.g. vorticity, etc.

Post-Processing:

- Data handling
- Visualize the simulation.
- Analysis.

For more detailed information the reader is referred to the author's Ph.D. thesis [Fischer (2014)]. Some of the general issues which are of special importance are pointed out in the following sections.

4.1 Constitutive Equations

The set of constitutive equations to describe compressible fluid dynamical and aeroacoustic phenomena includes: the continuity equation, Eq. (4.1), the momentum balance equations (compressible Navier-Stokes equations), Eq. (4.2), the energy balance equations, Eq. (4.3) with Fourier's law, Eq. (4.4), the equation for the total energy (internal and kinetic energy), Eq. (4.5), the calorimetric state equation (enthalpy), Eq. (4.6), the equation to closure the problem, here the relation between pressure and internal energy, Eq. (4.7) with the isentropic coefficient, Eq. (4.8):

$$\frac{\partial \rho}{\partial t} + \nabla \cdot (\rho \boldsymbol{u}) = 0 \tag{4.1}$$

$$\rho \left(\frac{\partial \boldsymbol{u}}{\partial t} + (\boldsymbol{u} \cdot \nabla) \boldsymbol{u} \right) + \boldsymbol{u} \frac{\partial \rho}{\partial t} = -\nabla p + (\lambda + \eta) \nabla (\nabla \cdot \boldsymbol{u}) + \eta \Delta \boldsymbol{u} + \rho \cdot \boldsymbol{g} \tag{4.2}$$

$$\frac{\partial (\rho E)}{\partial t} + \nabla \cdot (\rho E \boldsymbol{u}) = -\nabla (p \boldsymbol{u}) + \nabla (\boldsymbol{\tau} \boldsymbol{u}) - \nabla \boldsymbol{q} \tag{4.3}$$

$$\text{with} \qquad \boldsymbol{q} = -\kappa \nabla T \tag{4.4}$$

$$E = e + \frac{1}{2} |\boldsymbol{u}|^2 \tag{4.5}$$

$$H = e + \frac{p}{\rho} = C_p T \tag{4.6}$$

$$p = (\gamma - 1) \rho e \tag{4.7}$$

$$\gamma = \frac{C_p}{C_V} \approx 1.4 \tag{4.8}$$

The given set of equations one has to discretize utilizing appropriate discretization schemes for each differential operator, e.g. backward for the time derivative operator or Gauss linear for the del operator, the divergence operator and the Laplacian, cf. [OpenFoam-3.0.0 U.G. (2016)].

4.2 Fluid Mechanical Characteristic Numbers

An important and necessary step is to estimate the relevant characteristic fluid mechanical numbers for the given set-up to fit the numerical implementation of the problem. The probably most important fluid mechanical characteristic number one has to estimate in order to solve the problem under review is the Reynolds number. The Reynolds number is the dimensionless ratio of inertial forces to viscous forces [Schlichting (2003)]. The forces are represented by the characteristic length L of the dynamic in the case and the absolute value of the characteristic velocity U of the flow field, on the one hand, and the kinematic viscosity on the other, cf. Eq. (5.4). The Reynolds number is used to valuate the transition of laminar to turbulent in a particular flow field, e.g. in a pipe flow with diameter d turbulent flow occurs if $Re_d > 4,000$ [Schlichting (2003)].

In case of the numerical setup of a stopped wooden organ pipe in section 5.3 the characteristic length is given by the length of the cut-up of the organ pipe, $L = 5.5 \cdot 10^{-3}\,\mathrm{m}$ which determines the jet flow area. The characteristic velocity is assumed as $U = |u_y| = 18\,\mathrm{m/s}$, the absolute value of the initial velocity profile of the jet at the windway. The kinematic viscosity $\nu = \mu/\rho$ of the medium air is about $\nu = 1.53 \cdot 10^{-5}\,\mathrm{m^2/s}$. With these values the Reynolds number can be estimated as follows

$$Re = \frac{L \cdot U}{\nu} \approx 6470 \tag{4.9}$$

The Reynolds number obtained for the adressed problem indicates that the flow field in the mouth region of the organ pipe is of weak turbulence [Schlichting (2003)]. Note, that the Reynolds number estimates the flow characteristics relative to the viscous characteristics of the medium and not the characteristics of the sound field, which acts on a much faster time scale. Therefore the flow velocity has to take into account and not the speed of sound.

As a further important characteristic number the Strouhal number is discussed. The Strouhal-number is the dimensionless ratio between an aeroacoustical quantity, the so-called vortex shedding frequency f, and the fluid mechanical quantities, the characteristic length L and the characteristic velocity U of the flow [Schlichting (2003)]. The vortex shedding frequency in the mouth region of the organ pipe in section 5.3 is caused by the oscillations of the jet of the working organ pipe. Here the hypothesis is that the vortex shedding frequency corresponds to the fundamental frequency of the real operating musical instrument. In the case of the organ pipe in section 5.3 the fundamental frequency is $f_0 \approx 750\,\mathrm{Hz}$, which is obtained by acoustic measurements. The Strouhal number is estimated by

$$St = \frac{L \cdot f}{U} \approx 0.23 \tag{4.10}$$

The estimated Strouhal number corresponds to values one would expect for the problem considered.

The Prandtl number is defined as the ratio of kinematic viscosity, also known as momentum diffusivity, to the thermal diffusivity, cf. Eq. (5.7). The thermal diffusivity of the medium air at normal conditions ($p = 1013.25\,\mathrm{hPa}$, $T = 293\,\mathrm{K}$) is given by $\alpha = \kappa/(\rho \cdot C_p)$. Hereby $\kappa = 0.0257\,\mathrm{W}/(m \cdot K)$ is the thermal conductivity, cf. Eq. (4.4) and C_p the specific heat capacity at constant pressure conditions, cf. Eq. (4.6) and Tab. 4.1. The thermal diffusivity is calculated as $\alpha = 1.9 \cdot 10^{-5}\,\mathrm{m^2/s}$. This leads to the estimation of the Prandtl number of

$$Pr = \frac{\nu}{\alpha} \approx 0.72 \tag{4.11}$$

Last but not least the Mach number is important to estimate. The Mach number is defined as the ratio of the characteristic velocity U to the speed of sound c_0. The Mach number in the case of the organ pipe being considered is estimated to

$$Ma = \frac{U}{c_0} \approx 0.052 \tag{4.12}$$

with $c_0 = 343\,\mathrm{m/s}$ the speed of sound at normal conditions. Note, that the occurrence of pressure waves that show shock wave characteristics in the initial transient is not yet expected taking this estimation.

4.3 Kologorov-scales, Grid Size

The second essential step is to estimate the Kolmogorov microscales [Kolmogorov (1941)] needed to evaluate the chosen computational grid sizes as well as the resolution of the numerical time step size. The Kolmogorov length scale η and time scale τ_η are the micro-scales where the viscosity dominates and the turbulent kinetic energy is dissipated into the heat bath. The estimation of the Kolmogorov micro-scales is as useful as necessary to find the optimal grid size and time scale to solve the problem numerically. The Kolmogorov micro-scales are defined as

$$\eta = \left(\frac{\nu^3}{\epsilon}\right)^{1/4}, \qquad \tau_\eta = \left(\frac{\nu}{\epsilon}\right)^{1/2} \tag{4.13}$$

where $\epsilon = U^3/L$ is the average rate of dissipation of turbulence kinetic energy k per unit mass. The Kolomogorov micro-scales in the case in section 5.3 are estimated at $\eta = 7.62 \cdot 10^{-6}\,\mathrm{m}$ and $\tau_\eta = 3.8 \cdot 10^{-6}\,\mathrm{s}$. The time increment of the numerical simulations is set to $\delta t = 10^{-8}\,\mathrm{s}$ to ensure numerical stability, and therefore smaller by the factor 380 than the Kolomogorov time scale requires. Note that numerical stability of explicit time integration schemes, which are, inter alia, utilized in the numerical simulations, is given by the Courant-Friedrichs-Lewi condition (CFL-condition)

$$\mathrm{CFL} = \frac{U \cdot \delta t}{\delta x} \leq C_{max} = 1 \tag{4.14}$$

The smallest grid sizes of the created mesh in section 5.3 are $\delta x = 1 \cdot 10^{-4}\,\mathrm{m}$ and $\delta y = 2 \cdot 10^{-4}\,\mathrm{m}$. Hence $\mathrm{CFL}_{\max} = 0.35 \leq 1$ and therefore Eq. (4.14) is satisfied by choosing δt as mentioned. Compared with the Kolmogorov length scale the smallest grid sizes are too large by the factor 14. That means, that turbulent structures smaller than the grid size cannot be resolved by the mesh. This fact makes a turbulence model necessary, which models the energy transfer into and out of the sub-grid scales. This is introduced shortly in section 4.8.

4.4 Software and Hardware

The numerical simulations for investigating the transient prosecces in aerophones were realized by using parts of the C++ toolbox OpenFoam-3.0.0 [OpenFoam-3.0.0 U.G. (2016)] and OpenFOAM-v7 [OpenFoam-v7 U.G. (2019)]. The libraries include customized numerical solvers as well as pre- and post-processing utilities for the solution of problems in continuum mechanics, including computational fluid dynamics (CFD) and computational aeroacoustics (CAA). The code is released as free and open source software under the GNU General Public License. General aspects about pre-processing, run and post-processing are documented in the OpenFOAM user guides as well as in the OpenFOAM programmer's guides [OpenFoam-3.0.0 P.G. (2016)], [OpenFoam-v7 P.G. (2019)].
The numerical simulations were calculated on the high-performance-cluster (HPC) at the University of Hamburg using up to 16 nodes with a total up to 256 CPU's in parallel. Because of the nature of the numerically treated problems, which are compressible and transient problems, the OpenFOAM solver `rhoPimpleFoam` was used. An amount of data of about 81 - 500 GB per simulation run was generated. The run time of the simulations varied between $5.5 - 48\,\mathrm{h}$. The simulation times varied from $10\,\mathrm{ms}$ up to $t_s = 100\,\mathrm{ms}$.

The visualizations of the numerical simulations were performed using the open source multiplatform data analysis and visualization application ParaView-5.6.0 - ParaView-5.10.1. The

data analysis and signal processing were programmed using MATLAB® , Python and C++.

4.5 Thermo-physical Properties

The thermo-physical properties one has to take care of are the molar mass of the medium which is the gas air, the specific heat capacity and the dynamic viscosity. An often used simplification is the assumption of air as a perfect, one-atomic gas. The values of the thermo-physical properties which are used in the numerical cases are summarized in Tab. 4.1:

Property	Value	Unit
Molecules	1	
Molar mass M	28.9	g/mol
Specific heat capacity (p=*const*) C_p	1007	J/(kg · K)
Dynamic viscosity μ	$1.8 \cdot 10^{-5}$	Pa · s

Table 4.1: Implemented thermo-physical properties.

4.6 Boundary and Initial Conditions

One has to define the boundary conditions at the peripheries of the mesh, e.g. the wall properties of the organ pipe and the inlet conditions at the organ pipes languid in section 5.3. The surfaces of the instrument are considered as acoustically inert (boundary condition: no slip). The peripheries of the meshes are configured as open. This means that the radiated sound as well as all other physical quantities can propagate through the boundaries without any restrictions.
In the case of the numerical simulation of the organ pipe for example the initial conditions ($t_0 = 0\,\mathrm{s}$) of the physical properties to be calculated are implemented in separated files in the root directory of the OpenFOAM case, e.g. the velocity profile of the flow field in the file `0/U`. Here all initial conditions for all patches (inlet, walls, outlet, etc.) are coded, for instance the windway of the organ pipe (inlet), which is assumed to be uniform (hat-profile): $\boldsymbol{u}(x, y, z, t_0) = 18\,\mathrm{m/s} \cdot \mathbf{e_y} = u_y$, the value of the initial pressure field $p(x, z, y, t_0) = 1013.25\,\mathrm{hPa}$, the value of the initial temperature field $T(x, y, z, t_0) = 293\,\mathrm{K}$. The boundary conditions at the instruments inner walls are modeled by appropriate wall functions to describe the transport processes of turbulent kinetic energy k and other physical quantities close to the walls. For the pressure at the walls the zero-gradient model, for the velocity the no-slip boundary condition is chosen.

4.7 Wall Functions

With wall functions one models the physics of wall boundary layers and the near wall conditions in numerical simulations without resolving the boundary layer by the calculation grid. The basic idea were first introduced by [Spalding (1961)]. Usually one introduces near wall quantities like the distance to the wall y^+ which is non-dimensional, the friction velocity u_τ and the non-dimensional wall velocity u^+:

$$u_\tau = \sqrt{\frac{\tau_\omega}{\rho}} \tag{4.15}$$

$$y^+ = \frac{y u_\tau}{\nu} \tag{4.16}$$

$$u^+ = \frac{u}{u_\tau} \tag{4.17}$$

with τ_ω the wall shear stress, y the distance to the wall, and ν the kinematic viscosity. The definition of y^+ is similar to the definition of the Reynolds number in Eq. 4.9, thus y^+ can be interpreted as the local Reynolds number close to the wall. In the near wall region one distinguishes three sub-layers, the viscous sub-layer, the buffer-sub-layer and the so called log-area. In the viscous sub-layer ($y^+ < 5$) the fluid is dominated by viscous forces which mean that the shear stress here is equal to the wall shear stress τ_ω, the specific rate of dissipation of the turbulence kinetic energy k into internal thermal energy, also referred to as the heat bath. Here $u^+ = y^+$. In the buffer-sub-layer ($5 < y^+ < 30$) one assumes that viscous and turbulent stress are of similar magnitude. In the log-area ($30 < y^+ < 200$) the turbulent stress get dominant which leads to a slow (logarithmic) variation of the flow and the velocity profile:

$$u^+ = \frac{1}{\kappa} \ln(E y^+) \tag{4.18}$$

with $\kappa \approx 0.41$ the Kármán constant and $E = 9.8$ for smooth walls. For more information the reader is recommended to study the specialist literature.

4.8 Turbulence Model

A spatial refinement of the mesh down to the Kolmogorov micro-scales would lead to an extensive increase of computing effort. To limit the costs and the effort a turbulence model is utilized. It models the transfer of turbulent kinetic energy k into and out of the sub-grid scales (SGS). The turbulent kinetic energy k can be split into a grid-scale term k_{GS} and a sub-grid scale term k_{SGS} as follows

$$k = \frac{1}{2}\overline{u_k u_k} = \underbrace{\frac{1}{2}\overline{u}_k \overline{u}_k}_{k_{GS}} + \underbrace{\frac{1}{2}(\overline{u_k u_k} - \overline{u}_k \overline{u}_k)}_{k_{SGS}} \tag{4.19}$$

using Einstein's summation convention for the spatial indices $k = 1, 2, 3$ of the velocity components u_k. As a suitable LES-Model for the SGS turbulent kinetic energy k_{SGS} (SGS-k model) a one-equation dynamic sub-grid scale model is selected [**?**]. The model equation for the transport of the turbulent kinetic energy k is given by Eq. (4.20). Further explanations of the mentioned terms are given by Eqs. (4.21)–(4.27). More detailed information about the turbulence model used can be found in the OpenFOAM user guide [OpenFoam-v7 U.G. (2019)] as well as in the OpenFOAM programmer's guide [OpenFoam-v7 P.G. (2019)].

$$\frac{\partial(\rho k_{SGS})}{\partial t} + \frac{\partial(\rho \overline{u}_j k_{SGS})}{\partial x_j} - \frac{\partial}{\partial x_j}\left[\rho(\nu + \nu_{SGS})\frac{\partial k_{SGS}}{\partial x_j}\right] = -\rho\tau_{ij} : \overline{D}_{ij} - C_\epsilon \frac{\rho k_{SGS}^{3/2}}{\Delta} \tag{4.20}$$

with

$$k_{SGS} = \frac{1}{2}\tau_{kk} = \frac{1}{2}\left(\overline{u_k u_k} - \overline{u}_k \overline{u}_k\right) \tag{4.21}$$

$$-\rho\tau_{ij} : \overline{D}_{ij} = -\frac{2}{3}\rho k_{SGS}\frac{\partial \overline{v}_k}{\partial x_k} + \rho\nu_{SGS}\frac{\partial \overline{u}_i}{\partial x_j}\left(2\overline{D}_{ij} - \frac{1}{3}tr\left(2\overline{D}\right)\,\delta_{ij}\right) \tag{4.22}$$

$$\overline{D}_{ij} = \frac{1}{2}\left(\frac{\partial \overline{u}_i}{\partial x_j} + \frac{\partial \overline{u}_j}{\partial x_i}\right) \tag{4.23}$$

$$C_\epsilon = 1.05 \tag{4.24}$$

$$\Delta \quad \text{(Sauter mean diameter of the grid cell)} \tag{4.25}$$

$$\nu_{SGS} = C_k k_{SGS}^{1/2}\Delta \tag{4.26}$$

$$C_k = 0.07 \tag{4.27}$$

4.9 The Mesh

The set of equations, the initial and boundary conditions, the thermo-physical and the turbulent properties of the problem of concern have to be solved on an suitable computational grid, the numerical space which is called the mesh. To simulate the sound generation and the sound radiation of a stopped wooden organ pipe produced and provided by the German organ builder Alexander Schuke Orgelbau GmbH [Schuke (2016)], depicted in Fig. 5.36a, the corresponding mesh is shown in Fig.5.36b. Exemplarly the geometry of the organ pipe and its surrounding area is transferred into a structured 2D computational grid shown in Fig. 5.36b. The mesh size (length $\times$ width $\times$ depth) is (260 mm $\times$ 180 mm $\times$ 1 mm) with 254, 342 mesh points, 505, 170 faces and 126, 000 hexahedra. The technique how to write an appropriate mesh file and how to generate a mesh can be found in the OpenFOAM user guide [OpenFoam-3.0.0 U.G. (2016)].

Part III

Chapter 5

Acoustic Measurements and Numerical Experiments

> Hindewhu announces return from hunting.
>
> Ba Benzélé Pygmy

In this chapter acoustic measurements in combination with numerical simulations are presented investigating important aspects of sound generation within selected aerophones. The investigations are focused on the initial transient process, the working mode[1] and overblowing processes. Furthermore the sound radiation and the mutual interplay via sound signals are take into account. Both methodologies acoustic measurements and numerical experiments have advantages and disadvantages we should be briefly discuss.

The spatial-temporal sound signal propagation, the sound radiation, and sound characteristics can be realized easily and very well by measurements with microphones and microphone arrays. Microphone arrays are groups of microphones with precisely defined positions and distances from the measurement object, which record the signals simultaneously. The different locations of the microphones can be used to get phase information, information about the evolution of the signal's amplitude and frequency as well as of its propagation speed. A two-dimensional microphone array also allows to get information about the spatial energy distribution of the radiated sound field which is why it is also referred to as an acoustic camera. Linear microphone arrays are often used to measure acoustic propagation processes. Using high-precision recording hardware in combination with linear microphone arrays allows to measure very fast phenomena within the transient processes. For our acoustic measurements we used a two-dimensional and a high-precision linear microphone array, cf. Fig. 5.29a and Fig. 5.3. More details are given in the descriptions of the respective measurements.

With the help of acoustic measurements first important indications for characterizing sound generation processes in aerophones can be found. In addition acoustic measurements help to identify nonlinear processes in the transient and nonlinear oscillations in the working mode of the musical instruments. However, a complete metrological recording of the processes of sound generation in aerophones with acoustic measuring methods quickly reaches its limits, since the investigation volumes are small compared to the size of the microphones. Another disadvantage is the limitation to the measurement of phenomena related with or inducing acoustics. Flows

[1] The working mode is often referred to as the operation mode. In this study, both terms are used interchangeably.

and other fluid mechanical aspects as well as coupling mechanisms of the flow field and the sound field can only be measured very rudimentary with acoustic measuring methods. Furthermore, inside complex fluid mechanical and aeroacoustic set-ups, microphones would significantly impede the processes of interest and thus the measurement results.

To avoid such undesired influences one utilize computational fluid dynamics (CFD) and computational aeroacoustics (CAA). The great advantage compared to acoustic measurements is that a huge number of measurement positions is accessible without disturbing the process by the measurement. In addition, all information on any desired measured variable is obtained simultaneously at high time resolution. This makes all physical details visible and accessible within the framework of the grid resolution of the numerical set-up. The disadvantages of the method of numerical simulation are the high computational effort, numerical artifacts and the short simulation times compared with acoustic measurements. The computational effort depends on the temporal resolution as well as of the kind of problem one deals with. For investigations of coupled fluid dynamical and aeroacoustic phenomena one has to solve the full compressible Navier-Stokes equations under suitable initial and boundary conditions. This makes the use of high-performance computer systems necessary. The basic procedure for successfully carrying out numerical simulations was discussed in chapter 4.

The alternating use of both methodologies depending on the object of investigation opens the door to understanding the basic principles of sound production in their entire phenomenological range.

5.1 Brass Instruments

Brass instruments are typically played by vibrating the lips while pressing onto the mouthpiece. Because of that such instruments are also called labrosons. The lip vibrations are realized by the musician by creating an air flow. The air flow can be modified and controlled by various techniques changing the oral cavity volume, the lip's pressure, their position, or by breathing techniques. All techniques of sound generation are summarized under the term articulation technique. Early brass-like instruments like the *chazozra*, the sheneb and the *lure* can be dated back to around 3,000 B.C. in Ancient Egypt, in Ancient Greece and in the Etruscan culture in 700 B.C. Archaeologists have been found strait instruments as well as coiled instruments made from brass, bronze or other metal alloys. Also instruments made of horn like the *shofar*, important in the Jewish religion, typically made from a ram's horn, are counted among the brass instruments because of the similarities in sound generation process [Campbell, Gilbert, Myers (2021)]. The alphorn, made by slow grown spruce as well as the Australian didgeridoo, which is made by a peace of Eucalyptus tree that have been hollowed by termites, are also counted as labrosones. Because of their loudness, brass instruments were repeatedly used as a weapon of war to psychologically weaken the opponent. Examples of this are the vertically played *carnyx* of the Celtic peoples, a long S-shaped bronze trumpet with a bell styled as a open-mouthed monster, and the Uzbek and Uighur *karnai*, a long straight trumpet made of copper or brass.

After [Hornborstel, Sachs (1914)] one distinguishes valveless brass instruments from valved brass instruments. Valveless brass instruments are also called natural trumpets (Hornborstel and Sachs: 423.1), because one only can play the notes of harmonic series. Such trumpets have a long tradition as hunting and military instruments for commands and signals, e.g. the

a) b) c)

d) e)

Figure 5.1: The selected brass instruments are: a) the piccolo trumpet, b) the trumpet, c) the trombone, d) the French horn B, e) the tuba.

bugle (*clairon*) or the *fanfare*, which is derived from the Arabic word *fanáre*: trumpet. With valved brass instruments (Hornborstel and Sachs: 423.23) the player can reach notes of various harmonic series by changing the length of the tube pressing valves. Examples are the piccolo trumpet (Fig: 5.1a), the trumpet (Fig: 5.1b), the French horn (Fig: 5.1d), and the tuba (Fig: 5.1e). Another way of changing the resonator's length is to slide the tube's length like the trombone (Fig: 5.1c). All brass instruments shown here have the mouthpiece in common. The mouthpiece is build as a semi-spherical cavity, called the cup, as a kind of pre-chamber that leads to a cylindrical or conical air channel which is called the backbone, cf. Fig: 5.2a, 5.2b.

The measurements on brass instruments were carried out in close cooperation with the traditional brass instrument manufacturer Vogt Instruments in Leipzig, Germany, who kindly provided us with the musical instruments. The high performance measurements of the blow on process were realized with a linear microphone array consisting of 4× iSEMcon EMX-7150 microphones which were mounted at a bar of aluminum at relative positions $y_{mic1} = 0.0\,\text{mm}$, $y_{mic2} = 243.0\,\text{mm}$, $y_{mic3} = 486.0\,\text{mm}$ and $y_{mic4} = 729.0\,\text{mm}$. The positions of the microphones were measured to within a half of a millimeter, the signals were recorded with a sampling rate of $f_s = 500\,\text{kHz}$. This allows sound speed measurements with a precision of $\pm 1.5\,\text{m/s}$. The measurement set-up is depicted in Fig. 5.3. The measurements have been executed at constant room conditions, humidity: 64.7 %, temperature: 19.2 °C, and air pressure: 1021.8 hPa. The resulting speed of sound were calculated after [Cramer (1993)] and [Davis (1992)] as $c_0 = 344.02\,\text{m/s}$.

5.1.1 Speed Measurements on the Piccolo Trumpet

The piccolo trumpet is the smallest instrument of the trumpet class. Its pitch is usually one octave higher than the normal trumpet B♭ corresponding to one half of the tube length. On the piccolo trumpet the propagation velocity of the maximums in the initial transient as well as the singals velocity in the working mode is measured. This is also known as the phase velocity of the peaks of the signal which is expected to be equal to the speed of sound. The instrument was expressed by a professional player with a mezzo-forte dynamics (moderately loud).

a) **b)**

Figure 5.2: The mouthpiece of a trumpet. a) Axial view of the mouthpiece with the cross-sectional view of the cup and the conical backbone as a dashed line. b) Top view of the mouthpiece with the cup.

Figure 5.3: High speed measurement set-up. To record the propagation speed of the initial pressure waves leaving the instrument a linear microphone array with four iSEMcon EMX-7150 microphones at relative positions $y_{mic1} = 0.0\,\text{mm}$, $y_{mic2} = 243.0\,\text{mm}$, $y_{mic3} = 486.0\,\text{mm}$ and $y_{mic4} = 729.0\,\text{mm}$ is used. The microphones are mounted at a bar of aluminum. The signals were recorded with a sampling rate of $f_s = 500\,\text{kHz}$.

5.1.1.1 Observations

Examples of the measurement results of the initial pressure waves of the blow on process are depicted in Figs. 5.4a and 5.4b The temporal evolution of the pressure signal during the blow on process is characterized by some kind of excitation mechanism that leads to the formation of a stable sound. The whole initial transient of the piccolo trumpet takes only about 10 ms. In the period of time of $0.34 - 0.39\,\text{s}$ the system starts to develop a stable set of frequencies, the fundamental frequency as well as higher harmonics. From $t = 0.39\,\text{ms}$ the oscillations get triggered such that the deflections rise up to a range of amplitudes of about $[-30\,\text{Pa} - 20\,\text{Pa}]$,

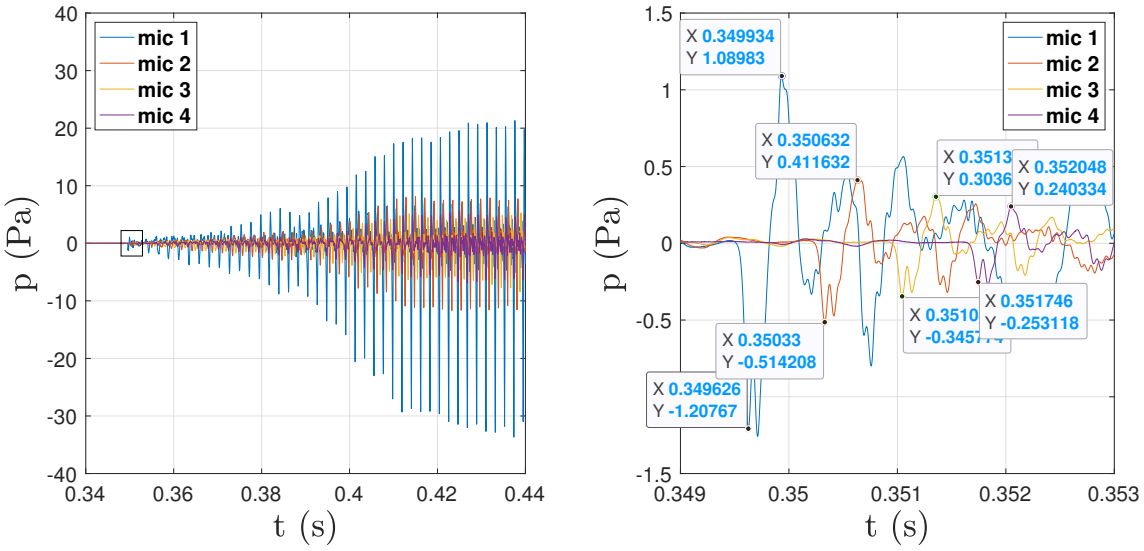

a) **b)**

Figure 5.4: Initial transient of the piccolo trumpet measured at the microphones $mic1 - mic4$ of the linear microphone array. a) The blow on process and the tone formation in time. The range of the initial pressure waves is marked by the frame. b) Propagation of the initial pressure waves in time. The peaks of the initial minimum and initial maximum used to evaluate the propagation speed are marked.

measured at microphone $mic\,1$. The blow on process ends in a stable sound production, the so-called working mode of the instrument. The initial wave front passing the positions of the microphones $mic\,1$ - $mic\,4$ is shown in Fig. 5.4b.

From the microphone positions and the transit time differences one calculates the propagation speed of the initial wave front passing die microphone array. The initial maximum $max\,1$ propagates with $c_{max\,1} = 345.9\,\mathrm{m/s}$, the initial minimum propagates with a speed of $344,3\,\mathrm{m/s}$. The values measured are slightly higher than the speed of sound of $c_0 = 344.02\,\mathrm{m/s}$. The deviations from the speed of sound are $\Delta c_{max,init} = 0.546\,\%$ and $\Delta c_{min,init} = 0.08\,\%$. As the signal passes the microphone array, its amplitudes gets attenuated. The attenuation of the initial wave fronts is nonlinear in time and space as illustrated in Figs: 5.5. To get an idea of the temporal and spatial decay rates one can use curve fitting. The data are best fitted by the exponential curve fitting functions $fit(t) = A \cdot \exp(B \cdot t)$ and $fit(x) = C \cdot \exp(D \cdot x)$ respective, where B and D are the temporal and spatial decay rates. The damping in time of the initial maximum can be fitted by

$$fit_{max\,1}(t) = 7.73 \cdot 10^{147} \exp(-973 \cdot t)$$

the damping in time of the initial minimum can be fitted by

$$fit_{min\,1}(t) = -5.32 \cdot 10^{139} \exp(-920 \cdot t)$$

The spatial damping of the initial maximum and the initial minimum is fitted by

$$fit_{max\,1}(x) = 1.053 \cdot \exp(-2.828 \cdot x)$$

and

$$fit_{min\,1}(x) = -1.176 \cdot \exp(-2.683 \cdot x)$$

where x denotes the direction determined by the positions of the microphones. The temporal and spatial damping of the amplitudes of the initial maximum and the initial minimum propagating along the microphone array is shown in Figs.5.5a and 5.5b. Note, the results represent the situation before the signal gets triggered to the working mode!

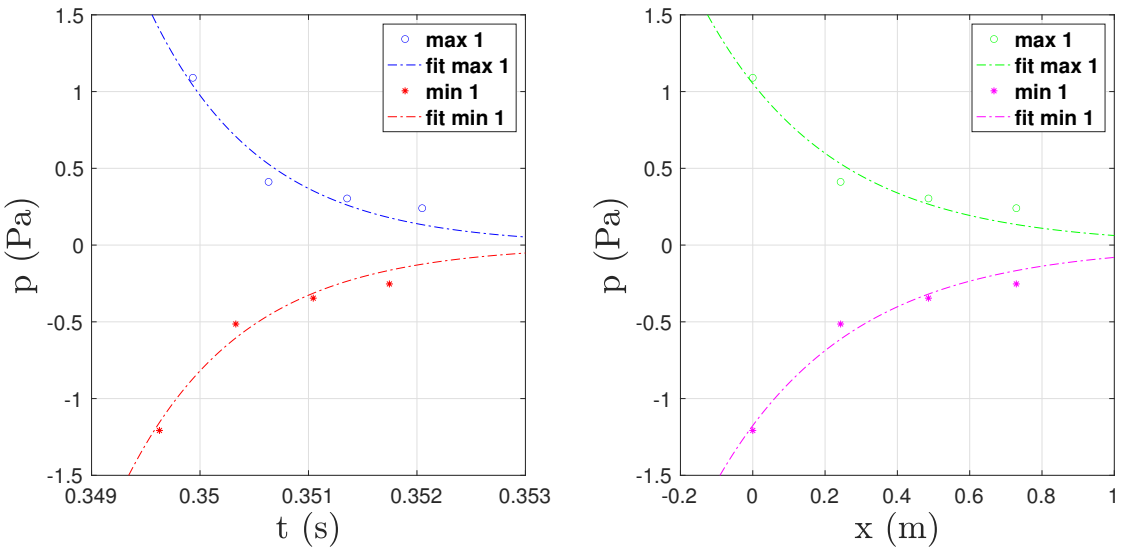

Figure 5.5: Attenuation of the amplitudes of the initial pressure wave fronts in the blow on process of the piccolo trumpet measured at the microphones $mic\,1$ - $mic\,4$: a) Damping of the initial wave maximum's amplitude in time. b) Damping of the initial wave minimum's amplitude in space.

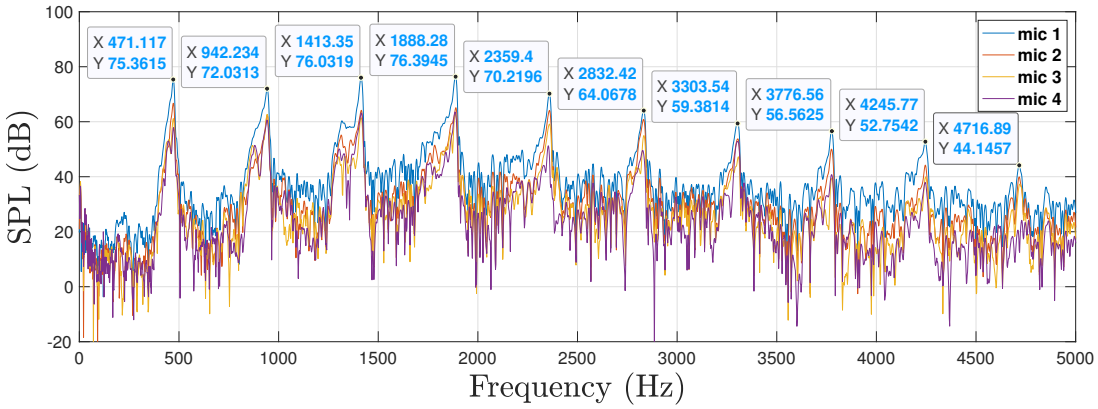

Figure 5.6: SPL-spectra of the signals of the blow on process recorded at the microphones $mic\,1$, $mic\,2$, $mic\,3$ and $mic\,4$. Labeled are the first 10 harmonics measured by microphone $mic\,1$.

Before analyzing the speed of propagation of the peaks of the fundamental frequency in the instrument's working mode, let's take a look at the SPL-spectra of the signals and the time dependent spectrum. Figure 5.6 shows the SPL-spectra calculated for the signals y_1 - y_4 recorded by

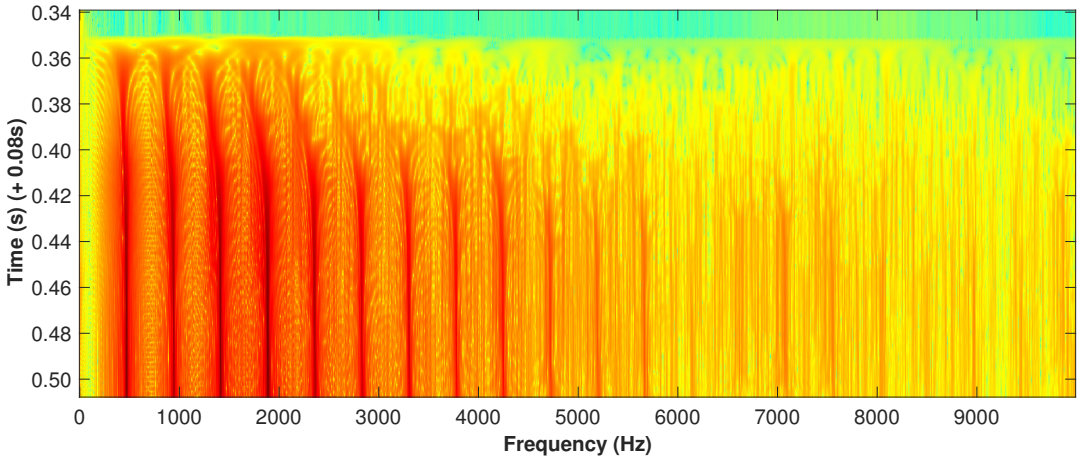

Figure 5.7: Time dependent SPL-spectrum of the signal of the blow on process recorded at microphone *mic* 1.

the microphones *mic* 1 - *mic* 4 mounted at the microphone array. One observes the fundamental frequency with a frequency of $f_0 = 471\,\text{Hz}$ and with a SPL of 75.35 dB. In fact the fundamental is not the only frequency with prominent SPL. The SPL's of the first, the second and the third overtone ($f_1 = 942.23\,\text{Hz}/72.03\,\text{dB}$, $f_2 = 1413.35\,\text{Hz}/76.03\,\text{dB}$, $f_3 = 1888\,\text{Hz}/76.39\,\text{dB}$) are just as strong as the SPL of the fundamental. This applies to all measurements at the four microphones of the microphone array.

The time dependent spectrum shown in Fig:5.7 reveals how the individual frequencies emerge. One can see that the set of harmonics (resonance frequencies) get generated step by step in time, starting with the fundamental frequency. The process is, in some sense, ordered in time. This phenomenon can also be argued from the energy point of view, since the formation of the fundamental oscillation and the higher harmonics is an expression of the occupation of the energy states of the system. In analogy to quantum mechanical systems, where the potential well leads to discrete energy levels and their occupation probabilities depending on the total energy of the system, the resonator of the acoustic system can be understood as a potential well of "well"-defined boundary conditions[2] that leads to certain discrete acoustic modes, the resonance frequencies[3], that, depending on the total energy of the system, get filled according to the potential step by step. Thereby higher acoustic modes correspond to higher energy states of the system which get filled when lower states are already occupied. This is true no matter

[2]In one dimension this is the resonator's length. In three dimensions the potential is defined by the resonator's length, width, and depth.

[3]In one dimension the acoustic modes are often simply referred to as resonator modes. In three dimensions the width and the depth of the resonator lead to so called transverse modes.

whether quantum mechanical or classical systems are considered[4]

We now turn our attention to the propagation speed of the peaks of the fundamental in the working mode. For this we analyze the time interval $t = 0.4 - 0.5\,\mathrm{s}$. Again, we look at the maximums and the minimums of the fundamental. Figure 5.8 shows the signal measured by the microphone array. The peaks for evaluation are marked with circles (max) and stars (min). The results of the analysis of the transit time differences of the maximums between the microphones are illustrated in Fig. 5.9.

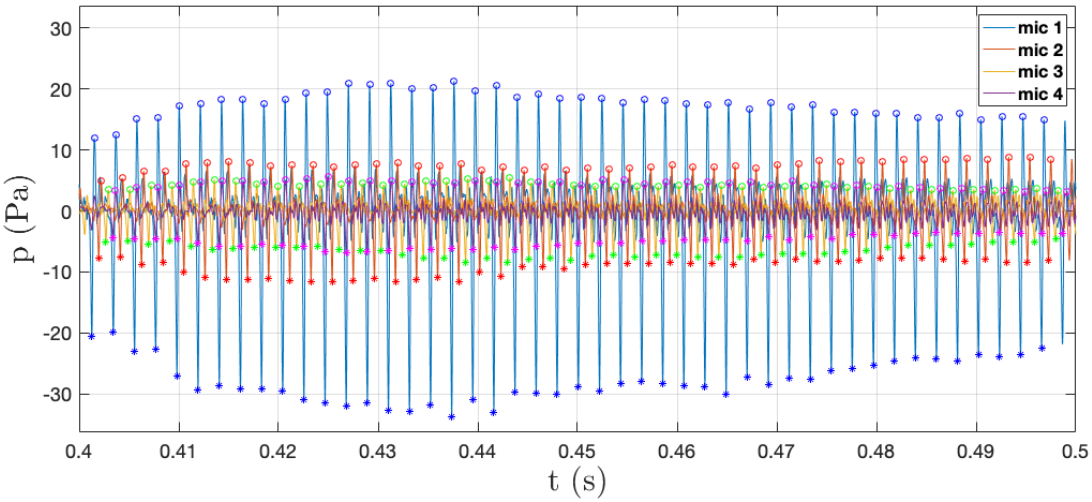

Figure 5.8: Working mode of the piccolo trumpet. Signals measured at the microphones *mic* 1, *mic* 2, *mic* 3 and *mic* 4 of the linear microphone array. The peaks used for analysis the propagation speed are marked by circles (max) and stars (min).

Between *mic* 1 and *mic* 2 one observes propagation speeds that are significantly higher than the speed of sound! The mean value is $\langle c_{max,2,1} \rangle = 358.66\,\mathrm{m/s}$, the highest propagation speed

[4]The analogy arises from the same mathematical structure of both concepts, the acoustic wave equation in classical mechanics and the Schrödinger equation in quantum mechanics:
The Helmholtz equation

$$\nabla^2 \xi + k^2 \xi = 0$$

leads for the potential well of length $L = 2a$ to the solutions $k_n = n\pi/L$ and the relation of the wave number k to the frequency gives the resonance frequencies :

$$f_n = \frac{n\omega}{2L} = \frac{n\omega}{4a} \qquad n = 1, 2, 3, ...$$

The substitution $k = \sqrt{2m(E-V)\hbar^2}$, with the energy E and the potential V leads to:

$$\nabla^2 \Psi + \frac{2m}{\hbar}(E - V)\Psi = 0$$

with Ψ the quantum mechanical wave function and the energy eigenvalues:

$$E_n = \frac{n^2\pi^2\hbar^2}{2mL} = \frac{n^2\pi^2\hbar^2}{8ma^2} \qquad n = 1, 2, 3, ...$$

is reached at $mic\,1$ at $t = 0.46\,\mathrm{s}$ with a maximum value of $max(c_{max,2,1,max}) = 371.56\,\mathrm{m/s}$. While the signal passes the distances between $mic\,2$ and $mic\,3$ the propagation speed decreases to the order of the speed of sound. The mean value is $\langle c_{max,3,2}\rangle = 338.66\,\mathrm{m/s}$, the maximal value is $max(c_{max,3,2,max}) = 357.35\,\mathrm{m/s}$. The prominence of this maximal value indicates an accumulation of the wave traveling from $mic2$ to $mic3$. After passing microphone $mic\,3$ the propagation speed holds on decreasing and gets damped down to values substantially lower than the speed of sound. This indicates that the wave front disperses.

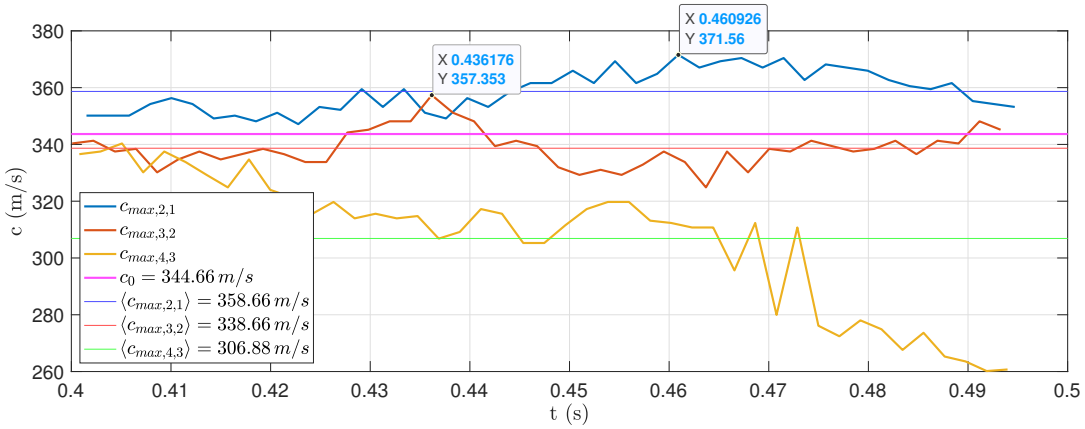

Figure 5.9: Speed of the pressure wave maximums of the fundamental in the working mode $0.4-0.5\,\mathrm{s}$. The measurements of the transit time difference of microphones $mic\,2$ to $mic\,1$ (blue) show speeds that are significantly higher than the speed of sound. The transit time differences between $mic\,2$ and $mic\,3$ (red) are decreased down to the order of the speed of sound but with passing a maximum of 357.35 m/s at 0.436 s. The propagation speed goes on decreasing passing the distance between $mic\,3$ and $mic\,4$ (yellow). The calculated speed of sound is marked by the pink line. The mean values of the mentioned propagation velocities are marked by the thin blue, red and green lines.

The results of the analysis of the transit time differences of the minimums of the signal differ from that of the maximums. While passing the distance between $mic\,1$ and $mic\,2$ the signal propagate with speeds of the order of the speed of sound even if it rises slightly. The mean value of $\langle c_{min,2,1}\rangle = 346.07$ is slightly higher than the sound speed. This is also true for passing the distance between $mic\,2$ and $mic\,3$. In contrast to the propagation speeds of the first distance one observes here an event where the speed shows a sharp increase up to 366 m/s at time 0.427 s followed by a period of decay. Again this event is an indication for wave front accumulation. The picture of the passage from $mic\,3$ to $mic\,4$ is in some sense mirrored to the one we just mentioned. One obverses a sharp decrease of the propagation speed at time 0.428 s from 338.44 m/s down to 321.43 m/s followed by an increase in the period of time from $0.46 - 0.495\,\mathrm{s}$. The decrease indicates a wave front dispersion.

5.1.1.2 Discussion

The speed measurements on the piccolo trumpet blown on with a mezzo-forte dynamics show that the immediately emitted sound signal ($mic\,1$ of the microphone array) exceeds the speed of sound slightly but significantly. This only can happen when the instrument generates shock waves, or at least pressure waves with a shock wave characteristic with respect to the values mea-

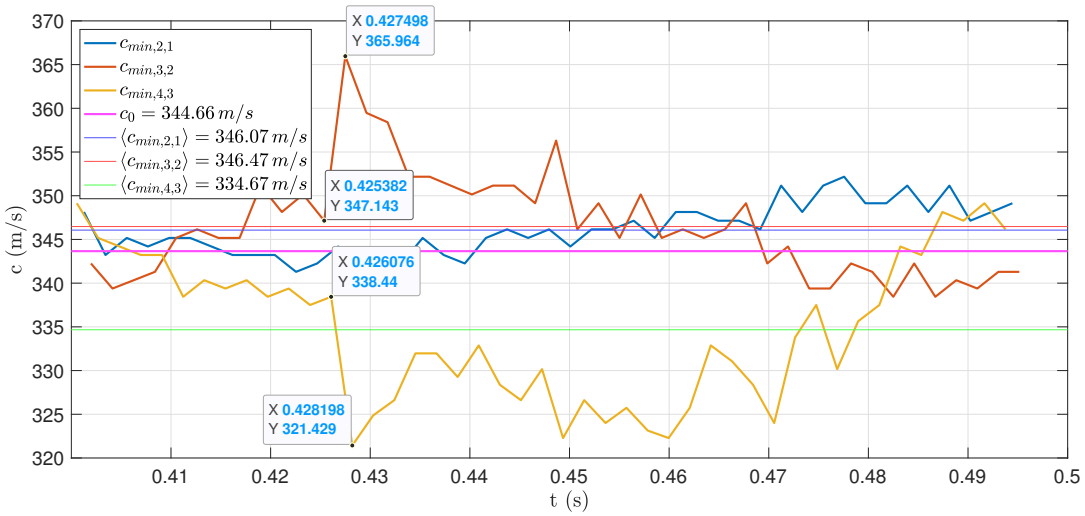

Figure 5.10: Speed of the pressure wave minimums in the working mode $0.4 - 0.5\,\mathrm{s}$. The measurements of the transit time difference of microphones *mic* 2 to *mic* 1 (blue) show that the mean speed $\langle c_{min,2,1}\rangle = 346.07\,\mathrm{m/s}$ is slightly higher compared with the speed of sound. The transit time differences from *mic* 2 to *mic* 3 (red) show a temporal sharp increase of the propagation speed at $t = 0.427\,\mathrm{s}$ followed by a decreasing. The mean value $\langle c_{min,3,2}\rangle = 346.47\,\mathrm{m/s}$ is also slightly higher than the speed of sound. The propagation speed between *mic* 3 and *mic* 4 is in some sense mirrored to the picture of the evolution between *mic* 2 and *mic* 3. The calculated speed of sound of $c_0 = 344.66\,\mathrm{m/s}$ is marked by the pink line. The mean values of the mentioned propagation speeds are marked by the thin blue, red and green lines.

sured. This raises the question of how these shocks arise in the instrument. The phenomenon has already been found in trombones, but blown on at fortissimo levels [Hirschberg et al. 1996]. The observations on the recorder discussed in subsection 5.2.1 as well as the numerical investigations on organ pipes in section 5.3 also indicate an occurence of such shocks, at least in the initial transient [Fischer (2019)]. In fact, shock waves seem to be relevant elements of sound generation in the aerophones mentioned so far. In order to get closer to the phenomenon of the blowing process in the piccolo trumpet, we look at the temporal development of the dynamics of the phase velocity and the representation in the phase space.

We are particularly interested in the short-term changes in the propagation velocities of the fundamental oscillation peaks measured as transit time differences between the microphones *mic* 3 and *mic* 4. For that we take the Hilbert transform (Eq:3.112) of the signal to get the phase information of the oscillations which is complex. Because we want to identify positive slopes in the signal (blue) with positive values of the phase velocity (red) we plot the negative imaginary part of the Hilbert transformed signal versus time. The dynamics at *mic* 3 at the period of time $t = 0.42 - 0.43\,\mathrm{s}$ is shown in Fig: 5.11. It can be seen that both physical quantities increase in the time interval under consideration, the amplitude of the signal and the phase velocity. In the phase space, this is shown by a repelling trajectory in time with respect to the origin of coordinates at $(0;0)$. If we assume a constant fundamental frequency, this can only mean that the flanks of the fundamental oscillations become steeper per period. This is a clear indication that a shock wave characteristic is evolving here. From the dynamical point of view changing the amplitude of an oscillator needs a strong driving force [Pikovsky et al.(2001)]. Weak forces only influence the phase. The force amplifying the oscillations amplitudes in the

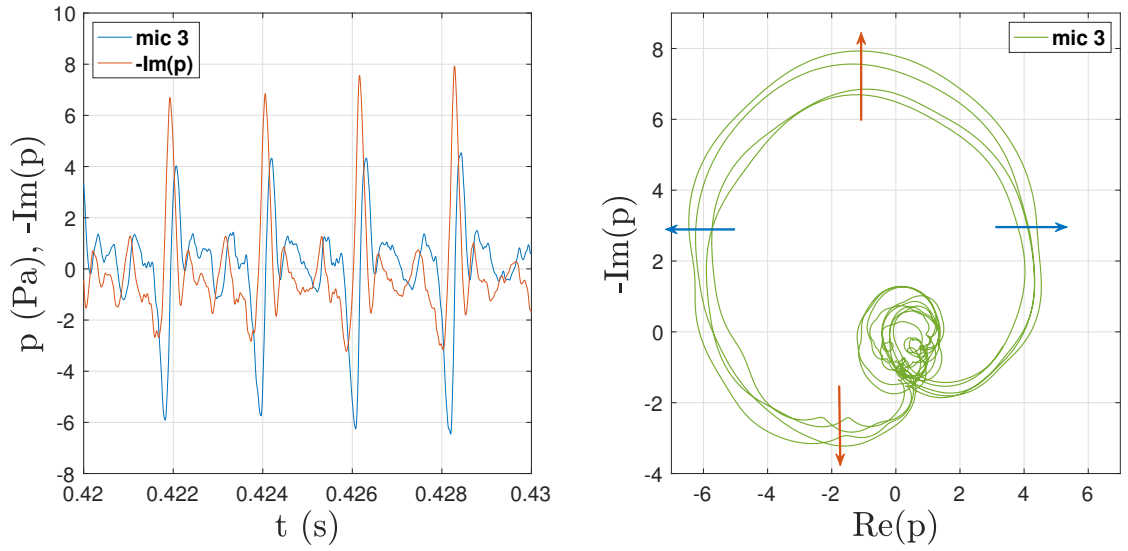

a) **b)**

Figure 5.11: Signal and Phase velocity of the fundamental (blue graph) in the working mode of the piccolo trumpet measured at *mic* 3 in the period of time of $0.42 - 0.43$ s. a) The signal's amplitudes and corresponding the phase velocities (red graph) increase in time. This implies that the signal's flanks become steeper. b) The corresponding phase diagram of the sequence shows that the trajectory generated by the deflection over the phase velocity repels in time.

working mode is delivered by the instrumentalist by blowing the instrument. In such sense the player is the external driver of the system.

The dynamics of *mic* 4 in the period under consideration differ from those of *mic* 3. In figure 5.12a one can see decreasing amplitudes of the signal and a decrease in the phase velocity over time. In the phase space representation in Fig: 5.12 this implies a shrinking trajectrory with respect to the period of the fundamental. At the same time the loops of the higher harmonics become much more prominent. This indicates that the sound formation is a process that does not end when the sound waves leave the instrument! Consequently one has to distinguish the sound generation process and the sound formation process.

As a last point, we want to consider the phase dynamics in the initial transient process and in the working mode of the instrument by analyzing the signals recorded at the microphones *mic* 1 - *mic* 4 of the microphone array. Before that, we want to briefly visualize what happens during the blowing process. In the initial transient, the player produces high air pressure with their lungs in their oral cavity. The pressure hits the lips, which are initially kept closed. If the pressure exceeds a critical value, the lips can no longer be kept closed and the air flow can escape. This reduces the pressure in the oral cavity and the lips close again. This process repeats itself if the lung pressure is adequately maintained. The lips then begin to open and close periodically. The instrumentalist can control this process precisely by carefully controlling the lip pressure, the position of the jaw and the volume of the oral cavity, cf. [Campbell, Gilbert, Myers (2021)].

This creates an impulsive flow of air that enters the stagnant air column inside the instrument. The air flow is further compressed in the mouthpiece, more precisely in the cup and in the waist of the backbone. At this point, at the latest, sound waves are generated by coupling of the flow

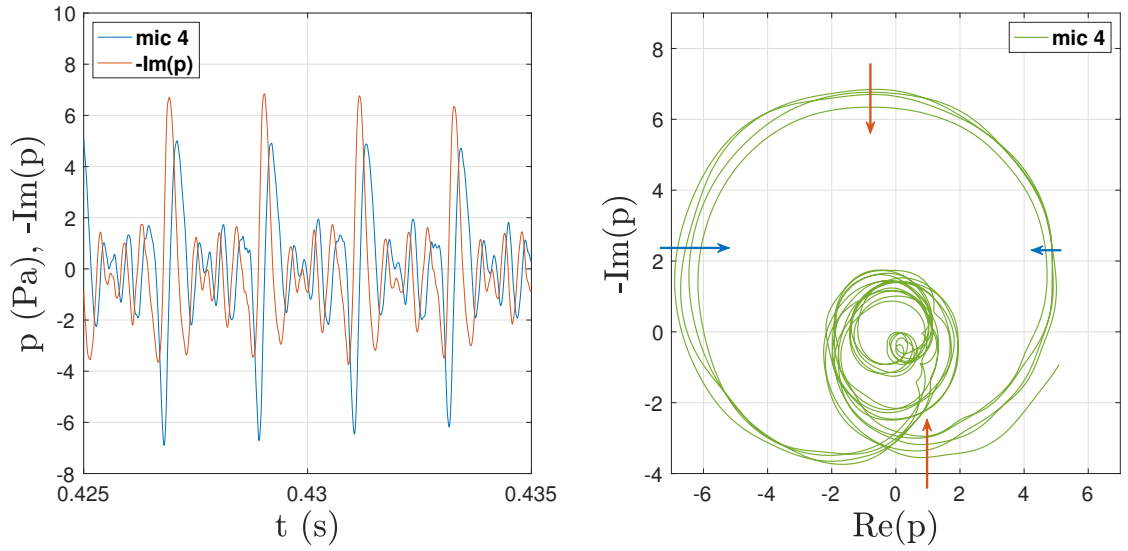

a) **b)**

Figure 5.12: Signal and Phase velocity of the fundamental in the working mode of the piccolo trumpet measured at *mic* 4 in the period of time of $0.425 - 0.435$ s. a) The signal's amplitudes (blue graph) decreases in the period of time $t = 0.424 - 0.43$ s. The phase velocity (red graph) also decreases in time. This implies that the fundamental's signal flanks become less steeper. b) The corresponding phase diagram of the sequence shows that the trajectory shrinks which implies an attraction of the fundamental oscillations. At the same time the loops of the higher harmonics increase which implies that the higher harmonics become more prominence.

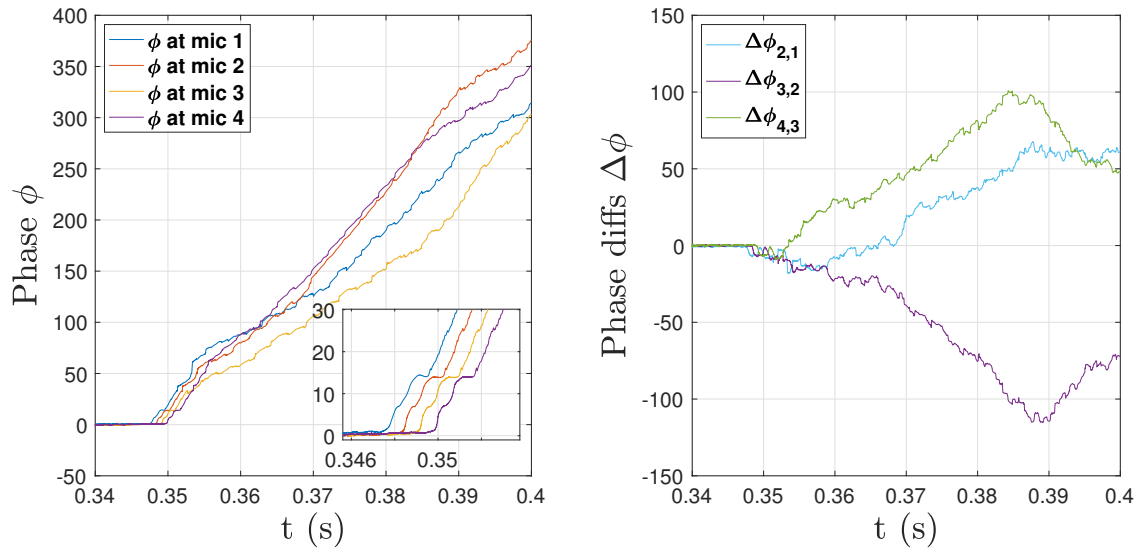

a) **b)**

Figure 5.13: Phase evolution in the initial transient process of the piccolo trumpet.

field onto the acoustic field in the resonator. The sound waves travel through the resonator to the bell and are emitted. A fraction of the sound waves get reflected at the instruments open end, the bell, travel back to the mouthpiece and influence the sound generation with a

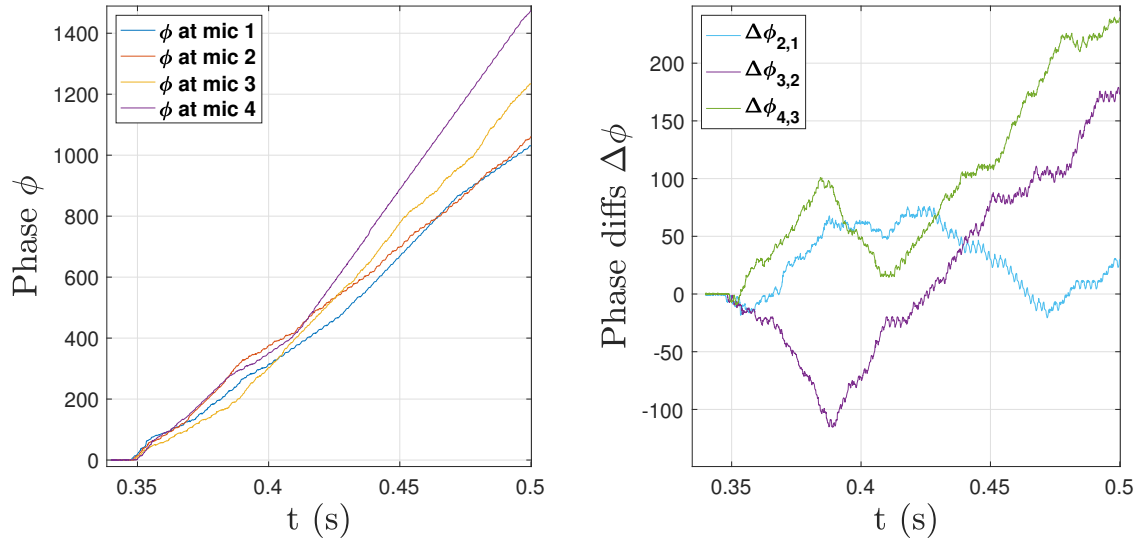

a) **b)**

Figure 5.14: Phase evolution of the whole blow on process of the piccolo trumpet.

time delay that is dependent on the resonator's length. Keeping this in mind we are now well prepared to read the phase information of the initial transient.

As mentioned at the beginning of this section the initial transient of the measurements presented starts at about $t = 0.34\,\mathrm{s}$ and lasts to $0.39\,\mathrm{s}$. Figure 5.13a shows the evolution of the phase of the signals which are recorded with the microphone array and evaluated using the Hilbert transform. As expected, the phases increase with time but not uniformly linear. One identifies different growth rates depending on time and depending on the microphone positions. A closer look at the very first part of development at $t = 0.347 - 0.355\,\mathrm{s}$ shows oscillations with a linear phase growing (despite of a tiny discontinuity) followed by forming a plateau and then continue to grow linearly. We already know from subsection 3.1.5 that such behavior, the forming of a plateau, characterizes a nonlinear oscillating system, cf. Figs: 3.9c. We associate this with the initial sound generating process. One obverses coherency between the signals measured at the different microphone positions. From about $t = 0.355\,\mathrm{s}$ the phases start to grow with different slopes regarding the microphone positions – with a very steep increase followed by a flat increase in phase, and in turn a period of moderate growing up to $t = 0.39\,\mathrm{s}$, measured at microphone $mic\,1$, a moderate growth at $mic\,2$ and $mic\,3$, and with a flat growth at $mic\,4$, that switches to a moderate growth from $t = 0.385\,\mathrm{s}$. The different grow rates of the phases in the initial transient indicate a complex re-arrangement of phases and therefore a creation of different phase velocities. In Figure 5.13b the phase differences of the signals at the microphone positions are plotted. Thereby $\Delta\phi_{2,1}$ means the phase differences of the signal at $mic\,2$ minus the signal at $mic\,1$ and so on. Also here, it becomes clear that we are looking at a differentiated picture when we look at the initial sound generation process of the piccolo trumpet. The evolution of the phase differences in the initial transient grow more or less linearly passing the distances between $mic\,1$ and $mic\,2$ and $mic\,3$ and $mic\,4$ as well. Passing the distance between $mic\,2$ and $mic\,3$ the phase differences growth also linearly in the same way but with a negative slope. At about $0.395\,\mathrm{s}$ a change in the behavior can be observed. Note, this is the time, where the signal gets triggered to large amplitudes, cf. Fig: 5.4a. The phase dynamics of the whole blow on process is shown in Figs: 5.14a and 5.14b. The process of

amplifying the deflections starting from $t = 0.4\,\mathrm{s}$ marks a change of phase growth that is more or less linearly but with different slopes depending on the microphone positions. Interesting is that the phases just grow consistently linear on the $mic\,4$. In other words, more or less harmonic oscillations of the system can only be observed from distances of more than 700 mm apart from the bell of the instrument. This is an indication that the sound formation process is completed and any nonlinear processes are dampened out. The initial transient is a complicated sound generation and sound forming process that takes place inside and outside the instrument.

We briefly summarize the results of the acoustic measurement on the piccolo trumpet using the linear microphone array:

- In the initial transient of the piccolo trumpet propagation velocities slightly higher than the speed of sound.
- The initial pressure waves that enter the trans-sonic regime show both accumulation and dispersion. They can be characterized as weak shocks
- The weak shocks get damped strongly nonlinear with time and with respect to their propagation length as well.
- The generation of harmonic frequencies takes place step by step in time, starting with the fundamental, in analogy to the occupancy of energy states in quantum mechanical oscillatory systems.
- In the initial transient the oscillations are nonlinear.
- One has to distinguish the sound generation process and the sound forming process which exceeds the dimensions of the instrument.
- Under normal blowing conditions (mezzo-forte) the nonlinearities of the sound generation damp out when the sound leaves the instrument such that the emitted sound can be characterized as harmonic sound.

5.1.2 Speed Measurements on the Trumpet, the Trombone, the French horn and the Tuba

The speed measurements done on the piccolo trumpet were also carried out on the trumpet, the trombone, the French horn, and on the tuba. We can summarize these investigations because they show quite similar results with respect to the propagation speed of pressure waves in the initial transient. For measurement we used again the high precision microphone array as described above. We found in all selected instruments propagation speeds of the initial pressure waves slightly higher than the speed of sound. For the trumpet we found the following propagation speeds: $c_{tru,max1} = 345\,\mathrm{m/s}$, $c_{tru,max2} = 371.8\,\mathrm{m/s}$, $c_{tru,max3} = 342.5\,\mathrm{m/s}$. The 8^{th} maximum speed was $c_{tru,max3} = 344.0\,\mathrm{m/s}$. The 4^{th} - 7^{th} maximums could not be tracked clearly, which is why they were useless for a serious analysis. The mean speed of the initial wave maximums is $\langle c_{tru,max} \rangle = 350.82\,\mathrm{m/s}$. The speed of sound determined by the room conditions where calculated as $c_0 = 344.02\,\mathrm{m/s}$. One recognizes that may not all initial waves enter the trans-sonic regime. One the other hand some waves seem to accrue such that it becomes difficult to identify and track them along the microphone array. We already have seen this variability (kind of complexity or may difficulty) in measurement the propagation speed of the initial pressure waves in the piccolo trumpet. This need further investigations. Fig: 5.15a exemplary shows the signal of the blow on process of the trumpet and the corresponding phase

portrait measured at $mic1$ of the microphone array. After the initial wave fronts have passed the microphone, from $t = 0.45\,\text{ms}$ the system is triggered, resulting in a increase in amplitudes. The increase in amplitudes tends to saturate, which can also be seen in the phase portrait, where the amplitudes, plotted on the x-axis ($Re(p)$), converge at each revolution. The system develops higher harmonics (small loops) and a fundamental which is harmonic, not anharmonic (nonlinear.)

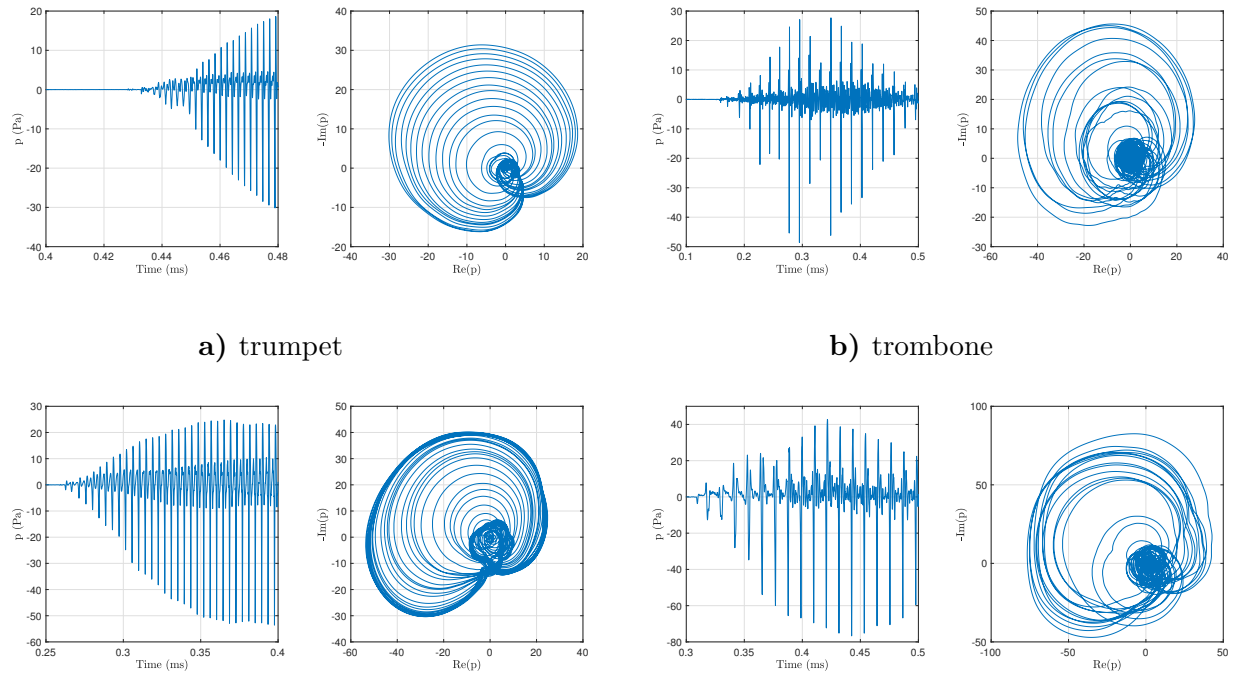

a) trumpet **b)** trombone

c) French horn **d)** tuba

Figure 5.15: Signal and Phase portrait of the trumpet, the trombone, the French horn and the tuba.

Although the measurement was only good enough the trombone show trans-sonic behavior with more significance compared with the trumpet, specifically $c_{tro,max1} = 358.2\,\text{m/s}$, $c_{tro,max2} = 359.4\,\text{m/s}$, $c_{tro,max3} = 350.1\,\text{m/s}$ and $c_{tro,max4} = 348.5\,\text{m/s}$. The mean speed of the initial wave maximums is $\langle c_{tro,max} \rangle = 354.05\,\text{m/s}$. The speed of sound determined by the room conditions where same as already mentioned $c_0 = 344.02\,\text{m/s}$. Fig. 5.15b shows the signal and the phase portrait of the measurement on the trombone. We deliberately show this sufficient measurement for several reasons. On the one hand, the focus of the investigations was primarily on the initial pressure waves and their speed measurement, not on the measurement of the entire transient process. On the other hand, the author did not discard the measurement for didactic reasons. When students study textbooks and relevant specialist literature, they are often presented with only the best results. This can feed the impression that as a scientist one only ever produce the best measurements and then only have to evaluate them. The author believes that sometimes showing students the difference between a good measurement and a mediocre measurement in order to learn from it is useful for gaining knowledge. This is to be shown with this measurement.

Fig: 5.15c shows the signal and the corresponding phase portrait of the measurement on the French horn. The initial pressure waves propagate trans-sonic, $c_{frh,max1} = 373.7\,\text{m/s}$, $c_{frh,max2} = 357.5\,\text{m/s}$, $c_{frh,max3} = 378.7\,\text{m/s}$ and $c_{frh,max4} = 354.7\,\text{m/s}$. The mean speed of

the initial wave maximums is $\langle c_{frh,max} \rangle = 366.15\,\mathrm{m/s}$. This value is substantially above the speed of sound of $c_0 = 344.02\,\mathrm{m/s}$. From the signal, but even more from the trajectory in the phase portrait, it can be seen that the system develops a state of constant amplitudes during the transient process, the so-called working mode. In the terms of nonlinear dynamics, this is appropriately called a limit cycle. From the signal, but even more from the trajectory in the phase portrait, it can be seen that the system develops into a state of constant amplitudes during the transient process, the so-called working mode. In the terms of nonlinear dynamics this is appropriately called a limit cycle. Also clearly recognizable, in comparison to the trumpet, is the deviation of the trajectory from the circular or elliptical shape. This is a clear indication that the system already generates non-linear oscillations in the fundamental mode.

Last but not least Fig: 5.15d shows the signal and the corresponding phase portrait of the measurements on the tuba, one of the biggest brass instruments. The analysis of the velocity measurements of the emitted initial pressure waves at the microphone $mic1$ result $c_{tub,max1} = 351.9\,\mathrm{m/s}$, $c_{tub,max2} = 354.8\,\mathrm{m/s}$, $c_{tub,max3} = 360.0\,\mathrm{m/s}$ and $c_{tub,max4} = 359.6\,\mathrm{m/s}$. The mean speed of the initial wave maximums is $\langle c_{tub,max} \rangle = 356.65\,\mathrm{m/s}$. This value is also substantially higher than the speed of sound of $c_0 = 344.02\,\mathrm{m/s}$. Compared with the trumpet the phase portrait of the transient process of the tuba shows a deformed trajectory compressed in both in the amplitude and in the velocity. Such oscillations are called relaxation oscillations.

We can summarize our experimental investigations on brass instruments with the following statements:

- In the initial transient of brass instruments piccolo trumpet, trumpet, trombone, French horn and tuba, pressure waves with slightly but significantly trans-sonic characteristics occur. Such waves are known as shock waves or shocks.
- The propagation velocities of the initial pressure waves are 0.7 % - 3.7 % higher that the speed of sound increasing with the size of the instrument.
- Also increasing with the size of the instrument is the anharmonic character of the oscillations the instrument generates.
- The nonlinear oscillations are accompanied by the formation of a limit cycle, the operating mode of the instrument.
- The larger the instrument, the stronger the relaxation oscillations.

Experimentally, many questions remain unanswered. For example: What happens inside the instrument in the initial transient process? Or, what happens if the instrument gets overblown? Do shocks also occur when the blowing process is piano or, as is often the case with jazz, noise is deliberately generated? The viewpoint of the considerations in this section was from outside the instrument. In the following section we will look at the sound generation process within the instrument. In the next section we will evaluate numerical simulations to investigate the blow on process of the piccolo trumpet.

5.1.3 Numerical Investigations on the Piccolo Trumpet

For the numerical experiment of blowing the piccolo trumpet, the instrument and the radiation region were transferred to a numerical computational grid. The instrument has a total length of 830 mm. The mouthpiece with a length of 80 mm has a cup and a conical cross-section that

widens uniformly from about 3 mm to 8 mm. The resonator tube is designed as a cylinder. At the end of the instrument is a bell with an opening cross section of 24 mm. The free space adjoining the bell is designed as a cuboid with three open ends (top, right, bottom).

The blowing process was modeled with the following initial conditions: the opening and closing of the lips was modeled by saw-tooth functions, in which the blowing speed increases linearly from $0 - 50\,\mathrm{m/s}$ within a period of $T = 1\,\mathrm{ms}$. The angle of the incoming airflow at the instrument's cup was varied between $0\,^\circ$ and $20\,^\circ$ in different simulation runs. The standard normal pressure of $p_0 = 1013.25\,\mathrm{hPa}$ and a room temperature of $T_0 = 20\,^\circ\mathrm{C}$ were specified for the room conditions.

The computational grid has 260,342 points with a total of 128,200 cells (hexahedra) and 514,770 faces. The simulations were calculated fully compressible. The open source C++ toolbox OpenFOAM with the solver `rhoPimpleFoam` was used for this. The simulations are large eddy simulations (LES) and use the turbulence model `kEqn`.

$$\frac{\mathrm{D}}{\mathrm{D}t}(\rho k) = (\rho \mathrm{D}_k \nabla k) + \rho G - \frac{2}{3}\rho k \nabla \mathbf{u} - \frac{C_e \rho k^{1.5}}{\Delta} + S_k \tag{5.1}$$

with the model coefficients $C_e = 1.048$ and $C_k = 0.094$. The temporal resolution of the simulations is $\delta t = 1 \cdot 10^{-6}\,\mathrm{s}$, with every 50th time step being saved. Figure 5.16 gives an impression of the set-up of the numerical simulation. First we want to look at the situation at the mouthpiece before we deal with the wave propagation in the resonator and with the sound radiation.

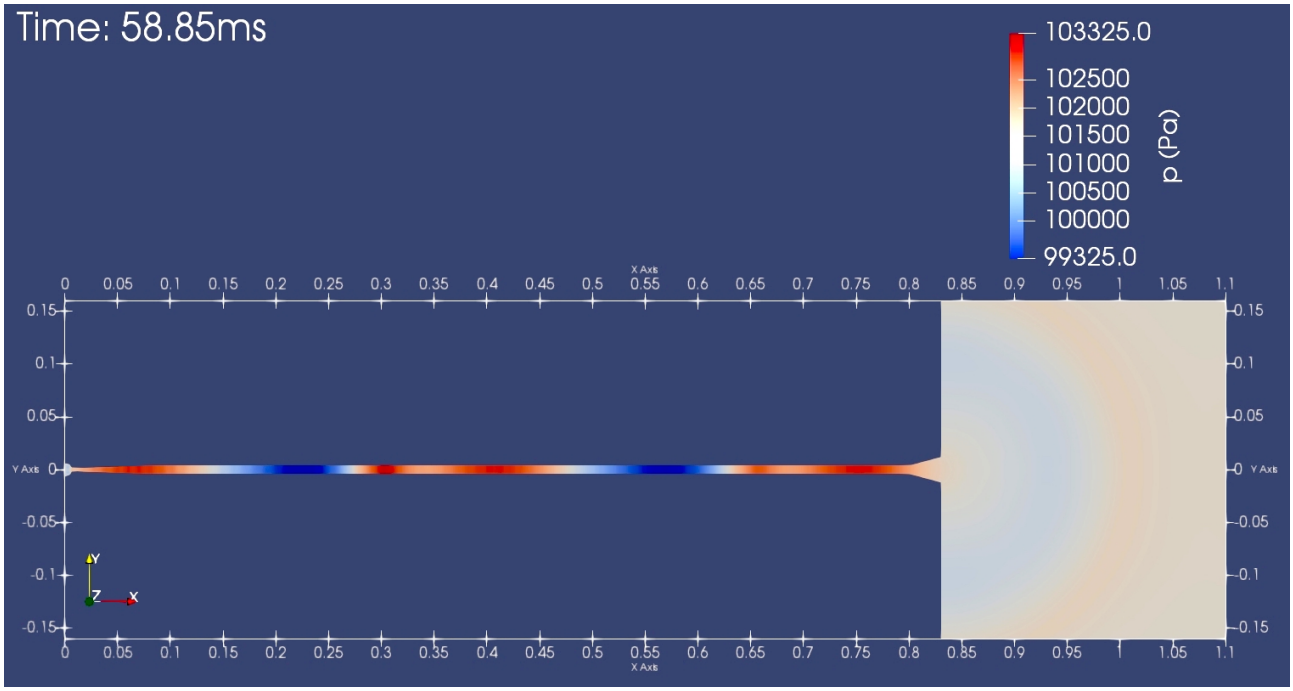

Figure 5.16: Visualization of the numerical simulation of the blow on process of the piccolo trumpet at time $t = 58.85\,\mathrm{ms}$. Color-coded is the spatio-temporal pressure distribution inside the instrument and the radiation of sound into the free space as well.

5.1.3.1 Observations

The initial transient of the piccolo trumpet at the mouthpiece is visualized in Figures 5.17a - 5.18h. Color-coded is the velocity magnitude in the period of time $t = 0 - 3$ ms. The sequences show the periodic airflow of $v = 50$ m/s entering the cup at an angle of 20 ° and generating a shock wave. The waist in the mouthpiece acts as a nozzle. The shock wave propagates through the mouthpiece into the resonator. In the cup, vortices form above and below the jet, which is enters the cup with an angle of 20 ° due to the asymmetry of the inlet condition. With each periodic entering of the airflow, a mass flow is created, which propagates into the mouthpiece and induces further turbulent coherent structures. The range of amplitudes of the velocity magnitudes are too large to resolve all the details of the flow field and acoustic field simultaneously. Therefore the same sequence is presented by color-coding the temperature field $T(x, y, z, t)$ which in compressible flows also becomes a variable (beside the density $\rho(t)$), cf. Figs: 5.19a - 5.20h.

One obverses fine structures of the turbulent air flow in the cup and in the conical backbone of the mouthpiece of the piccolo trumpet. The periodic interruption of the air flow produces a significant decrease in temperature - a consequence of the density fluctuation caused by the gas (air) that has just been accelerated in the direction of propagation. For even more details, the author recommends studying the animations in the supplement.

5.1.3.2 Discussion

The pressure signal of the case presented was sampled at three relevant points along the rotational axis of the instrument. The cross-section with the name Cs_0 has a total length of 1100 mm and passes through the mouthpiece, the resonator, the bell and the free space. 11,000 sample points were extracted for this length. Therefore the cross-section has a spatial resolution of 0.1 mm. Figure 5.21 shows the initial pressure waves passing the cup's waist at $Cs\_0(100) = 10$ mm, the bell $Cs\_0(8000) = 800$ mm and the free space at $Cs\_0(10500) = 1050$ mm.
Very steep pressure wave fronts of amplitudes of about 4 kPa are formed in the cup's waist. They back-propagate after reflection at the open end at about 5 ms. A fraction of a fifth of the amplitudes (5 kPa) passes the bell and get radiated. The fraction of about $200/usk/pascal$ reaches the point $Cs\_0(10500) = 1050$ mm outside the instrument. The reflected signal already has higher harmonics. Figure 5.22 shows the evolution of the signals over the period of time from $0 - 100$ ms. Of cause, the modulation of about 10ms correspond to the resonator length of the instrument. This becomes even clearer looking at the SPL-spectrum. Here we see the fundamental mode of the resonator of $f_1 = 97.7$ Hz as well as the odd higher harmonics of $f_3 = 312.66$ Hz, $f_5 = 517.84$ Hz, $f_7 = 742.56$ Hz and $f_9 = 996.56$ Hz. This is exactly what we expect for a half-open resonator of length 830 mm because of the relation of the eigenmodes:

$$f_n = (2n-1) \cdot f_1 = (2n-1) \cdot \frac{c_0}{4L} \qquad n = 1, 2, 3, 4 \tag{5.2}$$

with the speed of sound $c_0 = 344$ m/s. By inserting the resonator length $L = 830$ mm the results of the numerical simulation are obtained in very good accordance.

The dynamic of the lips can be also seen in the SPL-spectrum. Figure 5.24 shows the SPL-spectrum in a frequency range up to 10 kHz. The harmonics associated with lip dynamics are the fundamental F_0 of 996.57 Hz as well as the higher harmonics $F_1 = 2002.95$ Hz, $F_2 = 2999.55$ Hz, $F_3 = 4005.91$ Hz, $F_4 = 5002.5$ Hz, $F_5 = 5999.09$ Hz, $F_6 = 7005.45$ Hz, $F_7 = 8002.05$ Hz, $F_8 = 9008.41$ Hz and $F_9 = 10000$ Hz, which occur because of the superposition of the propagat-

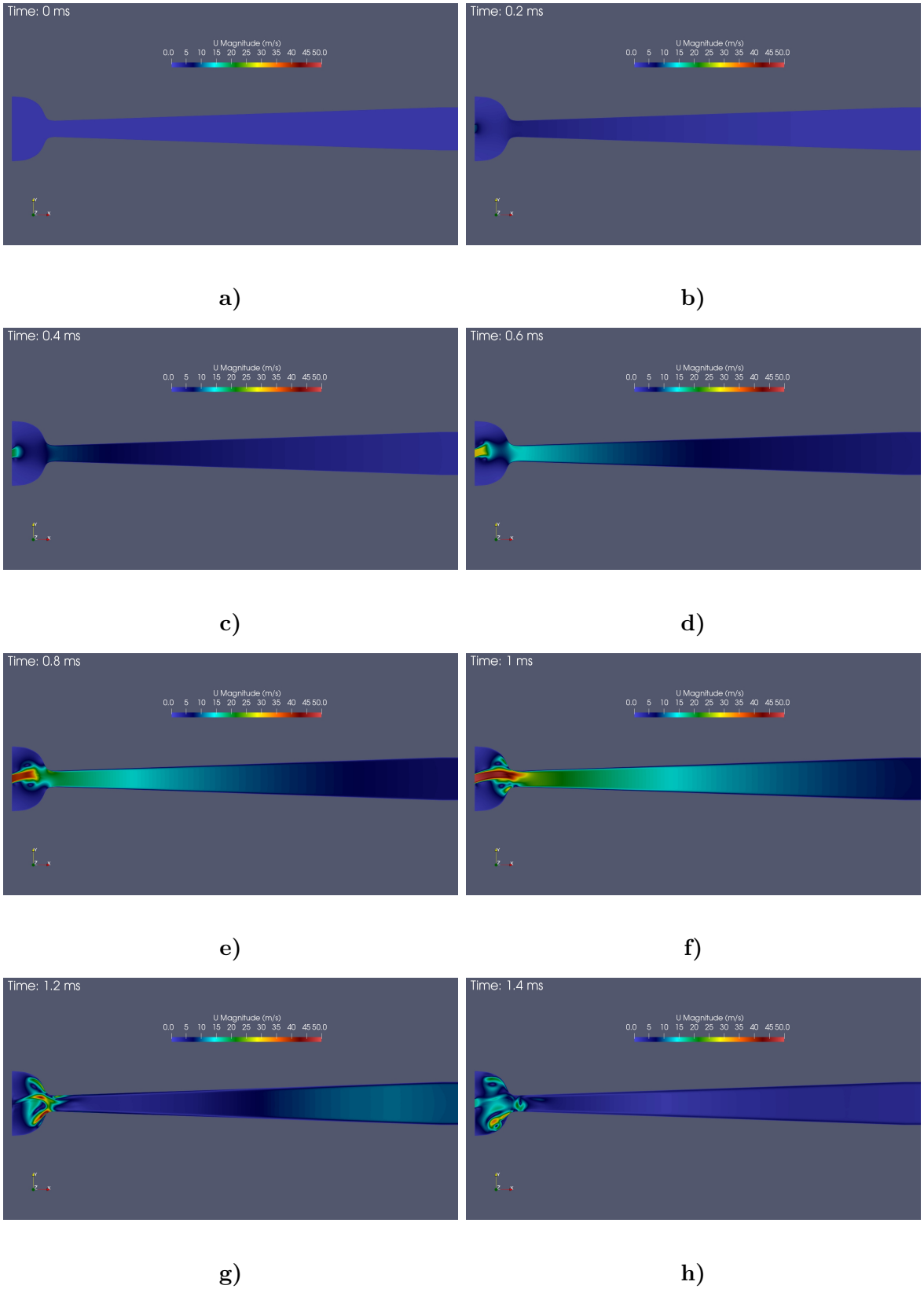

Figure 5.17: Visualization of the numerical simulation of the initial transient of the piccolo trumpet. Shown is the sequence in the period of time $t = 0 - 1.4\,\text{ms}$. Color-coded is the spatio-temporal distribution of the velocity magnitude in the mouthpiece.

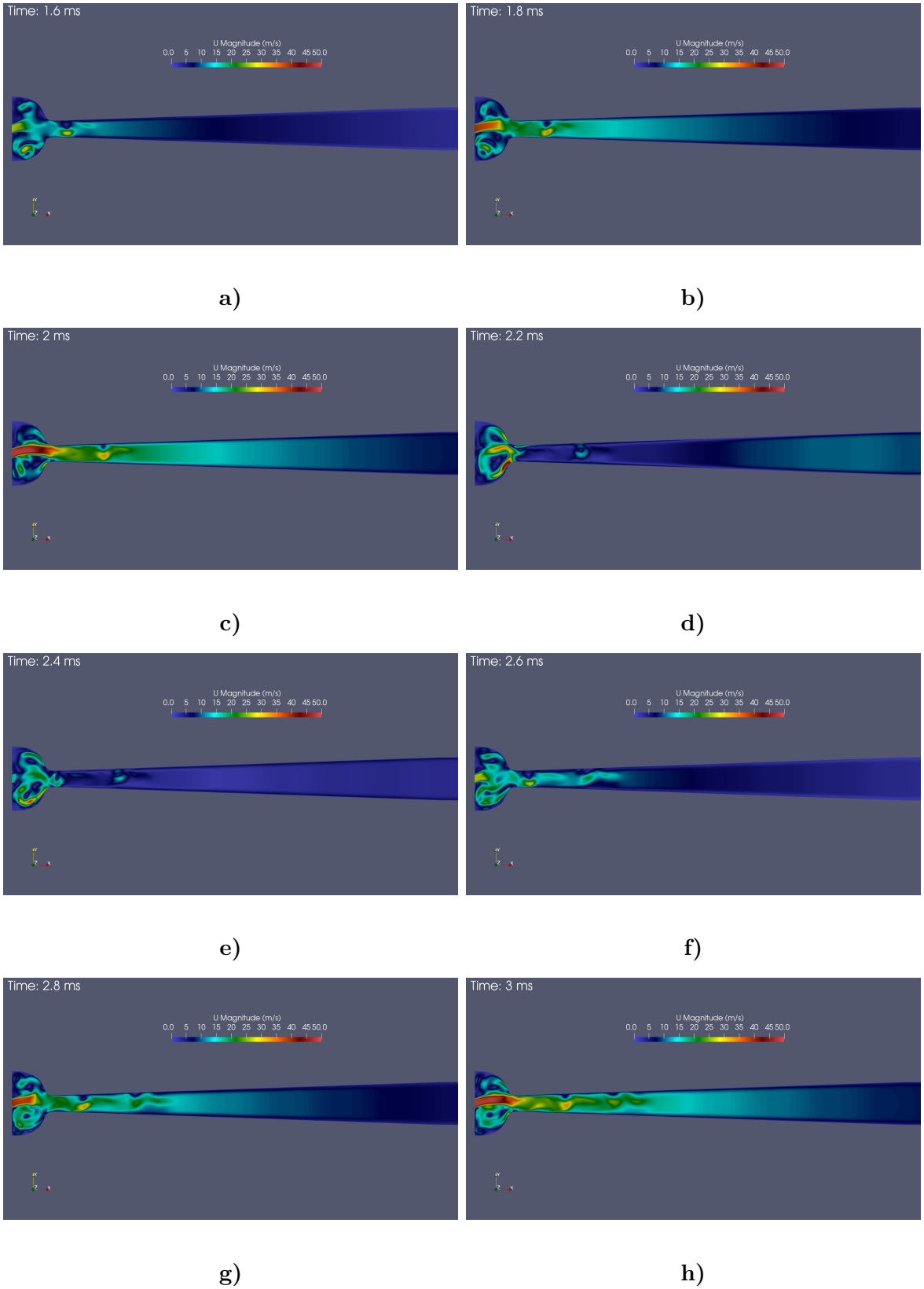

Figure 5.18: Visualization of the numerical simulation of the initial transient of the piccolo trumpet. Shown is the sequence in the period of time $t = 1.6 - 3.0\,\text{ms}$. Color-coded is the spatio-temporal distribution of the velocity magnitude in the mouthpiece.

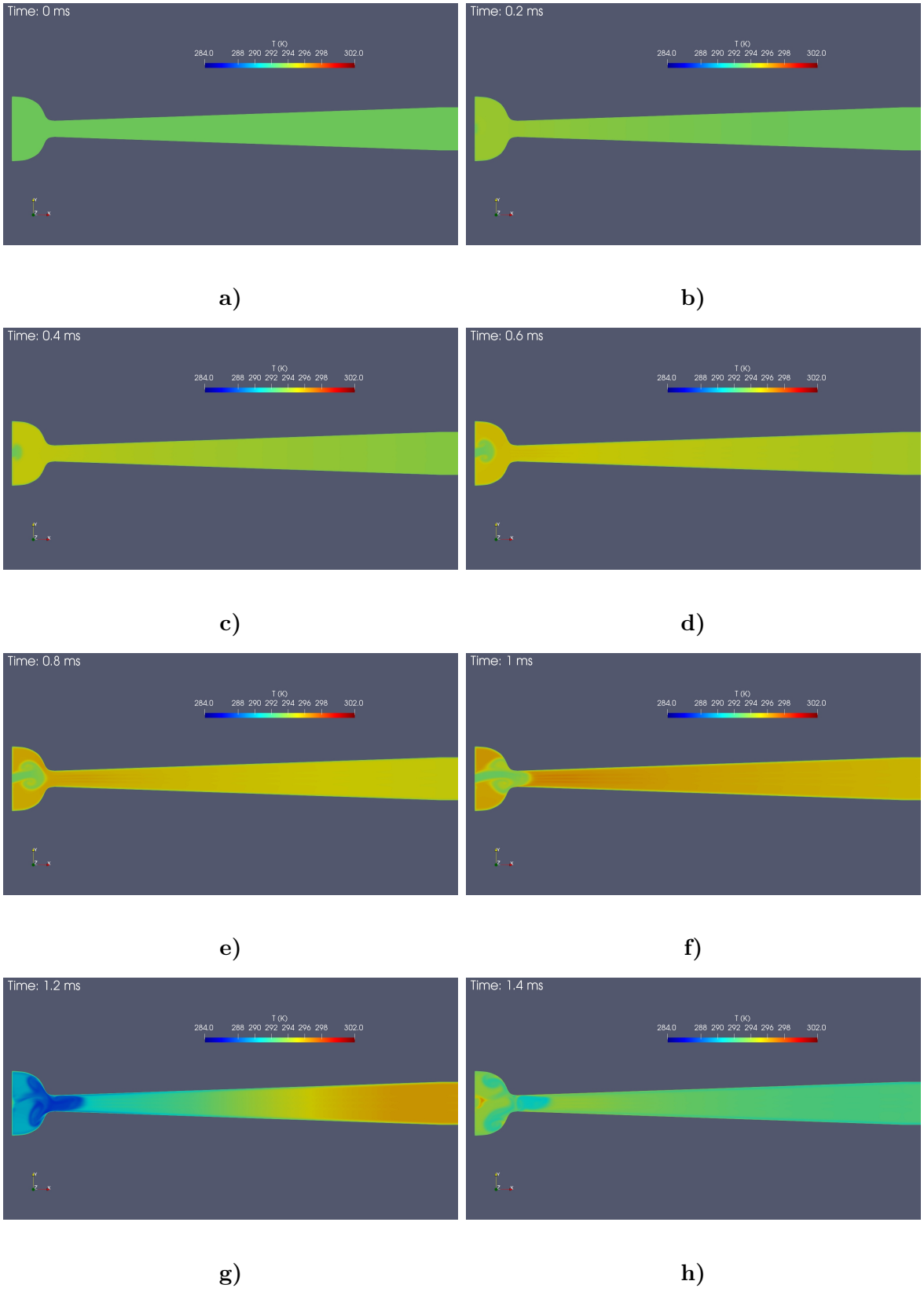

Figure 5.19: Visualization of the numerical simulation of the initial transient of the piccolo trumpet. Shown is the sequence in the period of time $t = 0 - 1.4\,\text{ms}$. Color-coded is the spatio-temporal distribution of the temperature in the mouthpiece.

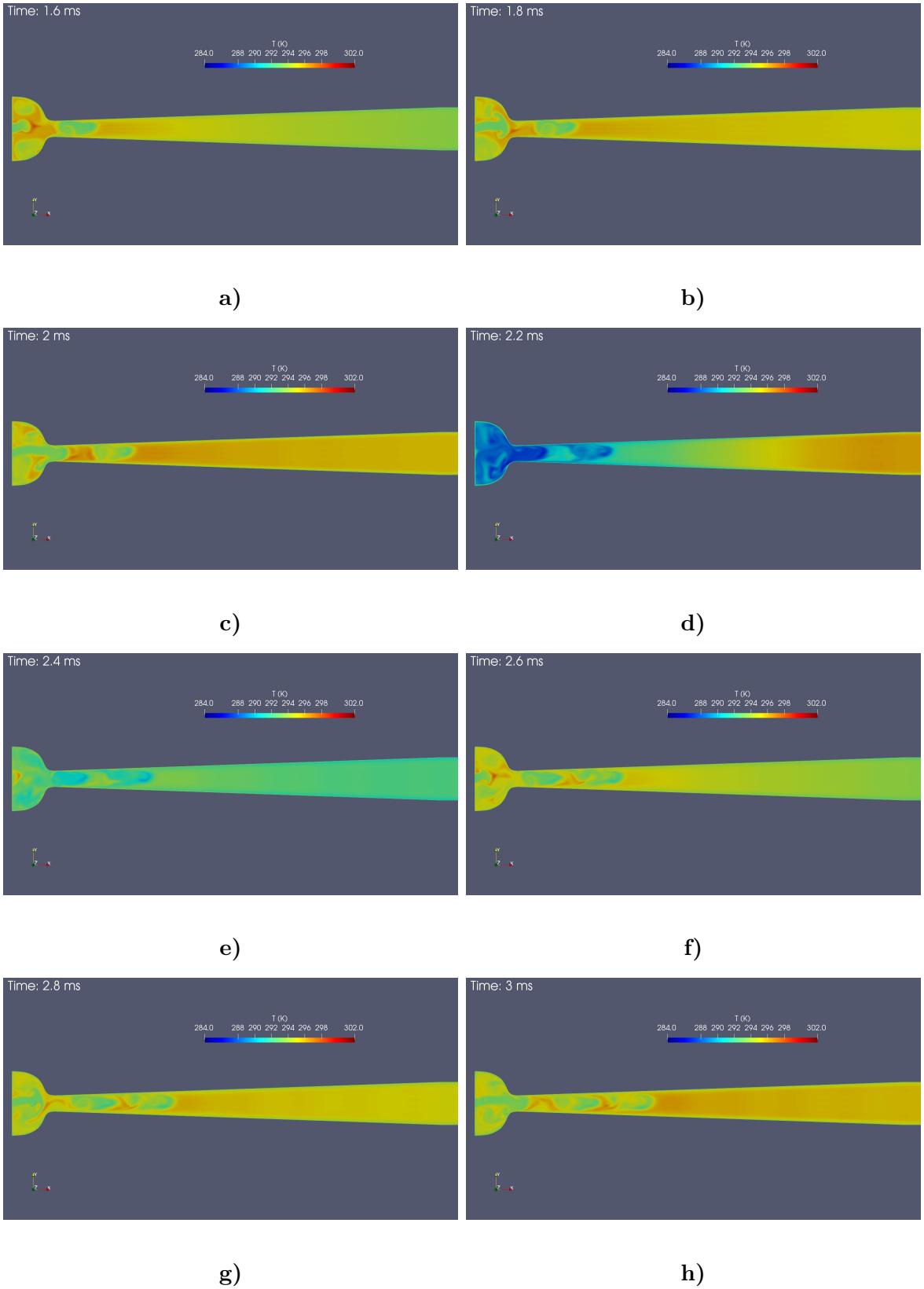

Figure 5.20: Visualization of the numerical simulation of the initial transient of the piccolo trumpet. Shown is the sequence in the period of time $t = 1.6 - 3.0\,\text{ms}$. Color-coded is the spatio-temporal distribution of the temperature in the mouthpiece.

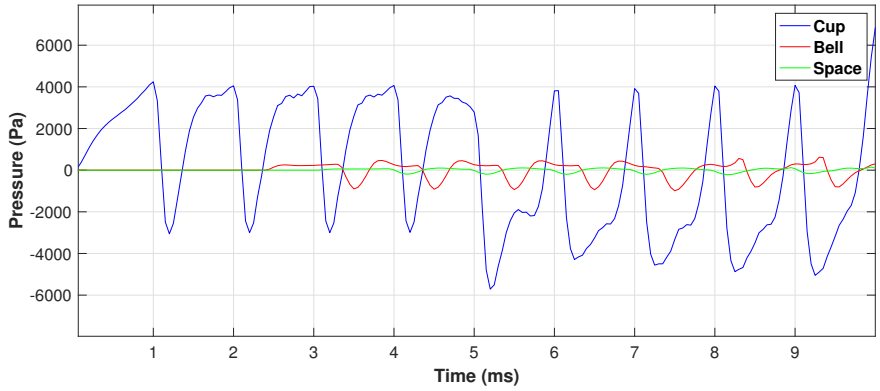

Figure 5.21: Initial pressure waves in the blow on process of the piccolo trumpet.

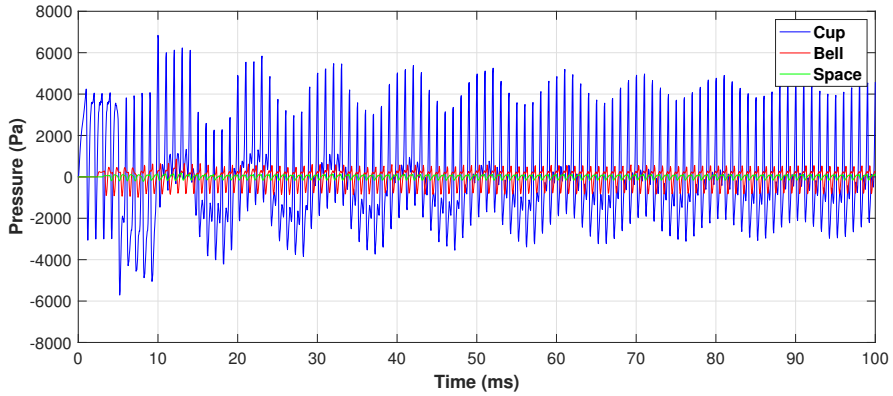

Figure 5.22: Numerical simulation of the blowing process in the piccolo trumpet. Propagation of the initial pressure waves in time $t = 0 - 100\,\text{ms}$. The signals are sampled along the rotational axis of the instrument, close to the cup's waist at $x = 1\,\text{mm}$, at the bell at $x = 800\,\text{mm}$ and in the free space at $x = 1050\,\text{mm}$.

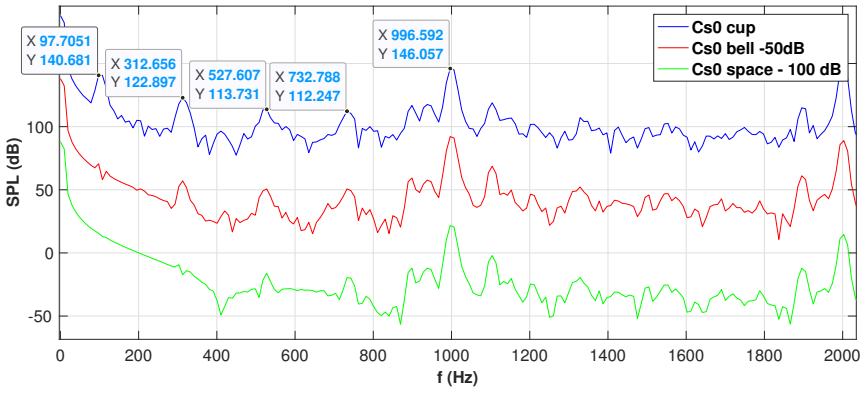

Figure 5.23: SPL-spectra of the signals sampled at the cup's waist, the bell and the free space in the range of $0 - 2\,\text{kHz}$. The SPL's are separated by offsets each of -50dB for reasons of clarity. Labeled are the odd modes of the resonator of the instrument, the fundamental mode $f_1 = 97.7\,\text{Hz}$ as well as the odd higher harmonics $f_3 = 312.66\,\text{Hz}$, $f_5 = 517.84\,\text{Hz}$, $f_7 = 742.56\,\text{Hz}$ and $f_9 = 996.56\,\text{Hz}$..

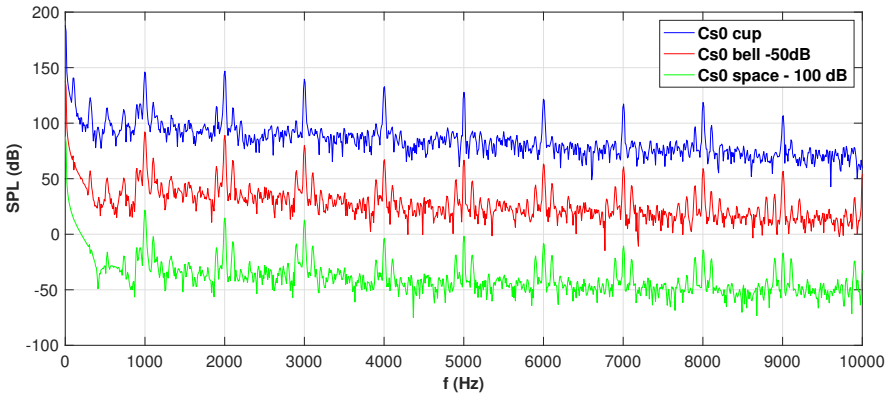

Figure 5.24: SPL-spectrum in a frequency range up to 10 kHz. The harmonics caused by the lip dynamics are the prominent amplitudes at multiples of about 1 kHz. The SPL's are separated by offsets each of −50dB for reasons of clarity.

ing and the back-propagating waves. This can be studied in detail by watching the animations of the case in the supplement, in particular the temporal evolution of the pressure wave along the cross-section Cs_0 .

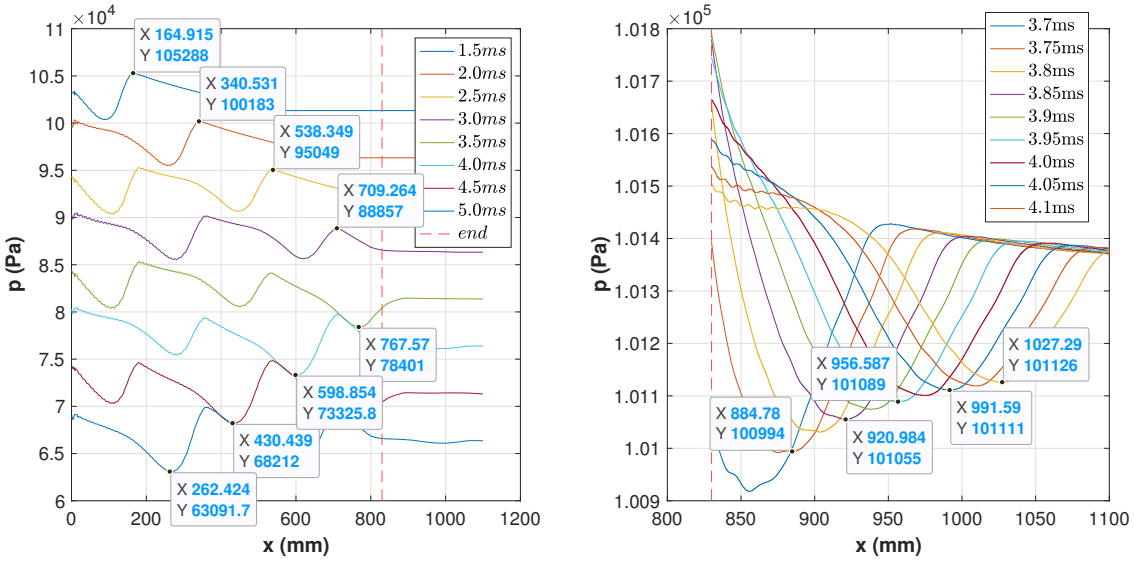

a) **b)**

Figure 5.25: Propagation of the initial pressure wave fronts. a) Inside the instrument: For the sake of clarity, the signals plotted at times 1.5 ms, 2.0 ms, 2.5 ms, 3.0 ms, 3.5 ms, 4.0 ms, 4.5 ms, and 5.0 ms are separated from each other by an offset of 5 kPa. The mean speed of the forward propagation is $\langle v_{res,fw} \rangle = 359.23\,\mathrm{m/s}$, the mean back-propagation is $\langle v_{res,bw} \rangle = 336.03\,\mathrm{m/s}$. The position of the bell's end is marked by the dashed line. b) The signal radiation into free space. The mean propagation velocity is $\langle v_{space} \rangle = 356.27\,\mathrm{m/s}$

Next we consider the propagation speed of the initial pressure wave in the instrument. For this purpose, the maximums and minimums are measured in terms of time and space. We see how the wave front of the initial pressure wave runs up to the end of the resonator and forms a steep flank. According to the boundary condition at the open end, this flank reflects

to negative pressure amplitudes. A small part (approx. 1/10 of the amplitudes) leaves the resonator and get emitted. Examination of the propagation velocities (forward) of the peaks of the pressure waves in the resonator points to a mean propagation speed of $\langle v_{res,fw} \rangle = 371\,\mathrm{m/s}$. For the mean back-propagation we get $\langle v_{res,bw} \rangle = 337.63\,\mathrm{m/s}$. The emitted sound signal of the initial wave propagates with mean speed of $\langle v_{space} \rangle = 356.27\,\mathrm{m/s}$. Figure 5.25a and 5.25b show the propagations inside the instrument as well as the radiation into free space. The numerical results thus confirm the experimentally found fact that trans-sonic pressure waves form in the initial blowing process of the piccolo trumpet.

Now we consider the development of the phases in the instrument. To get access to the phase information we transform the sampled signal of the cross-section $Cs0\_p$ using the Hilbert transform. Unlike in the experiment, the numerical set-up allows any phase at any location to be related. This opens the door to investigations of spatio-temporal phase relationships. The phase relationship between the pressure signal at the mouthpiece and the emitted signal is to be examined more closely here as an example. As we have already seen in the experiment in subsection 5.1.1, the phases at different measurement positions tend to form certain coherencies. This is often referred to as spatial coherency. From the numerical experiment we learn that in the initial transient, particularly in the period of time from $0-4\,\mathrm{ms}$ the phase relation between the cup and the bell of the piccolo trumpet arrange their phase relationship in such a way that phase synchronization occurs, cf. 5.26a. The phase sampled in the cup (blue line) shows a step-wise growing that correspond to the periodical entering of the air stream caused by the lips dynamics (initial condition: saw-tooth velocity with a period of $T = 0.001\,\mathrm{s}, F_0 = 1\,\mathrm{kHz}$). Of cause, this is a nonlinear oscillation. At the bell the phase is also growing in the way just described, but one sees a pronounced plateau here, that leads to a mean phase shift between the cup and the bell of about $\langle \phi_{bell-cup} \rangle \approx 825\,^\circ$. This phase shift results from the propagation length and the generation of the fundamental of $F_0 = 1\,\mathrm{Hz}$ by the lips. The phase difference can be easily estimated. A signal of the fundamental oscillation $F_0 = 1\,\mathrm{kHz}$, which shows the propagation length of 820 mm between the measuring points in the cup and in the bell with the mean speed (back and forth propagation) of approx $\langle c_{res,fw,bw} \rangle \approx 360\,\mathrm{m/s}$ creates a relative phase position of $820\,^\circ$ with respect to the starting point.

The phase differences between the to positions of the bell and the cup (black) become more or less constant from 6 ms to 10 ms (despite of the periodicity caused by the lips dynamics). This behavior is even more evident in the phase relationships between the cup and the radiated signal (magenta) and between the bell and the radiated signal (cyan). In the operation mode shown in Fig: 5.26b one observes a re-adjustment of the phase relations characterized by various phase slips inside the instrument. As a result of these processes the phase of the radiated signal grow essentially linearly (red) and in phase with the signal in the cup, while the phase differences sampled at the different positions (cup, bell, free space) show epochs of constant phase relations interrupted by steps where the phase differences change linearly (and rapidly). The periods of constant phase relations indicate temporal coherence. From nonlinear dynamics such behavior is known as intermittency. In general, coherence is the prior condition for observing stationary interference patterns like standing waves. We will look at such patterns now.

As a last point we want to study the sound generation process inside the instrument by looking at the temporal evolution of the whole pressure distribution sampled at the cross-section $Cs0$. Figure 5.27 shows the this spatio-temporal evolution. Color-coded is the pressure in the range of $\pm 6\,\mathrm{kHz}$. The y-axis shows the cross-section, where $x = 0\,\mathrm{mm}$ is the inlet at the cup and $x = 1100\,\mathrm{mm}$ is the end of the free space in the numerical set-up. At $x = 830\,\mathrm{mm}$ the instrument ends with the bell. One observes the propagation of the initial pressure waves in time as well

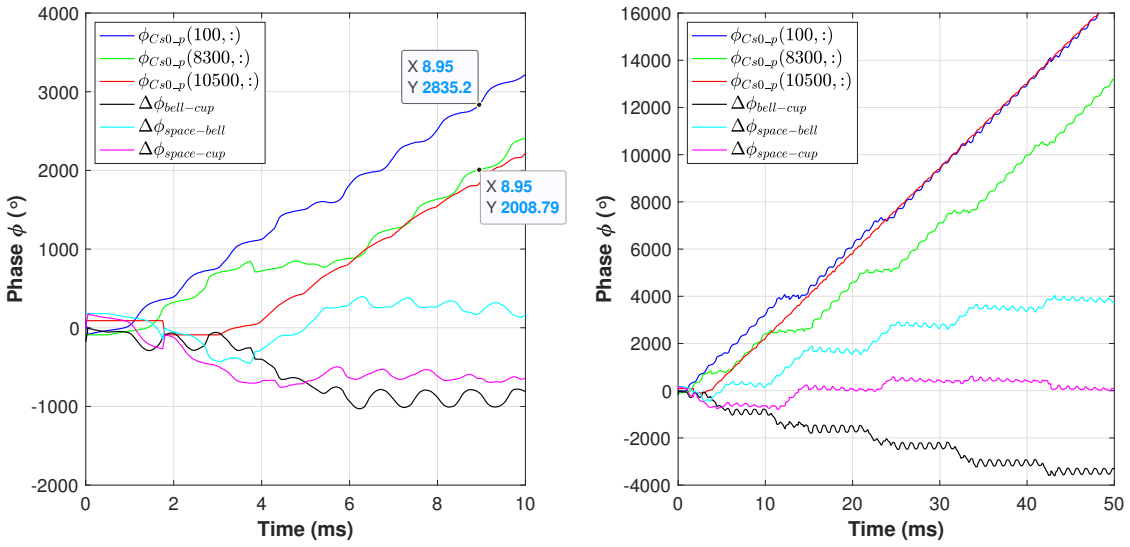

Figure 5.26: Phase evolution in the cup, in the bell and in the free space in the initial transient and in the operation mode of the simulated piccolo trumpet. a) The initial transient. b) Initial transient and operation mode.

as their reflections at the open end which leads to superposition of the traveling and the back-traveling waves in the resonator - the so called standing waves. After 10 ms the system has developed a stable sound generation. The sound waves get radiated into the free space. The amplitudes of the sound emitted are much lesser that the waves within in instrument.

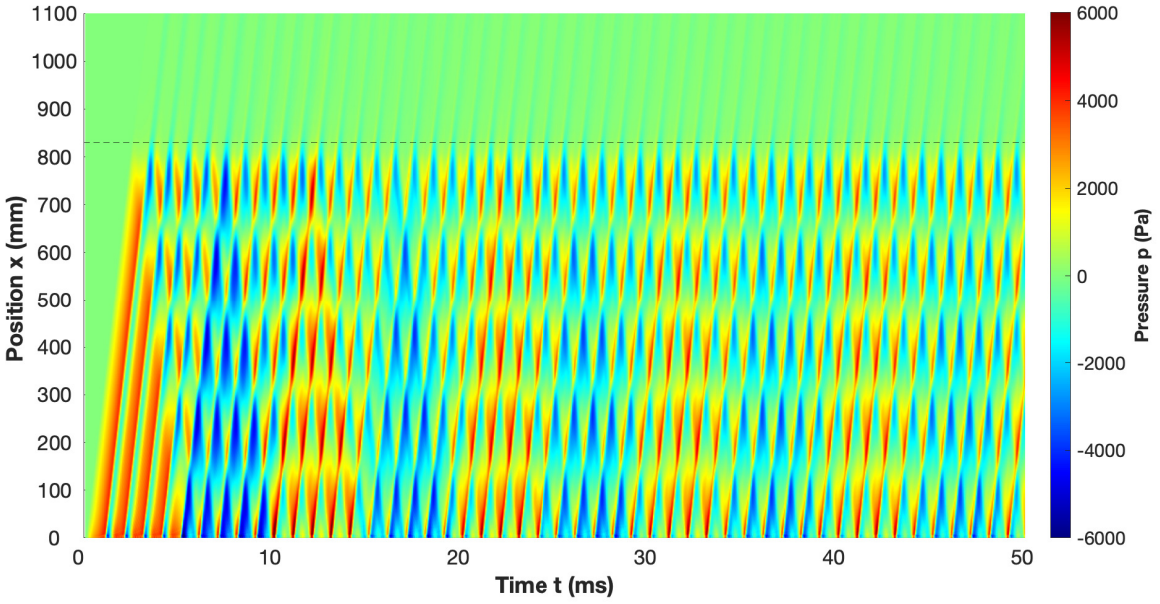

Figure 5.27: Visualization of the initial transient and the operation mode of the simulated piccolo trumpet. Color-coded is the pressure along the cross-section $Cs0$ through the instrument. The dashed line marks the open end of the instrument, the bell.

One can clearly seen how standing waves are created inside the resonator, which are not quite as "standing" as the name and the idealized model suggests - and not only in this numerical simulation, but also in real instruments! Musical instruments are very complex dynamic systems and therefore simple models of linear acoustics sometimes describe the principles of sound production rather roughly. In Fig: 5.27 one recognizes the nodes and the anti-nodes of the standing waves of the pressure of the half-open tube with strongly fluctuating periodic amplitudes at the cup, a total of four nodes inside the resonator and a "half" anti-node at the open end at 830 mm. The nodes represent oscillations with the ninth harmonic of the resonator of $f_9 = 9 \cdot c/4L = 996.56\,\text{Hz}$, which correspond to the fundamental of the blowing process F_0, as already mentioned in the SPL spectrum above, cf. 5.23.

In summary, we can confirm the experimental findings by the numerical simulations. In addition, the numerical simulations give us more detailed insights into the sound generation processes of the piccolo trumpet. In particular, we find

- first indications of the complex coupling of the flow field and the acoustic field in the instrument.
- We see how turbulent coherent structures, such as the jet and various vortex structures form in the mouthpiece.
- We observe trans-sonic wave propagation in the initial transient.
- We see that the initial blowing process generates nonlinear oscillations.
- In the SPL spectrum we see the resonator's modes as well as the fundamental and the higher harmonics that are caused by the blowing process.
- We see a complicated development of the phases at different selected sample points in the instrument and outside the instrument.
- These phase developments reveal an internal process that leads to coherent phase relationships. This leads to phase slips and a re-adjustment of the phases, which leads to a radiation of harmonic sound waves.
- Despite the complicated turbulent dynamics in the mouthpiece, the sound generation process is straight forward and leads to a stable tone production within only 10 ms.

The last point in particular gives reason to assume that there is a very strong coupling of the initial flow field and the acoustic field in the piccolo trumpet.

5.2 The Recorder

Recorders can be characterized by a special design that defines the way of the air entering the instrument's resonator. They are open flutes with a block that includes the windway. Forerunners of recorders were often made by bones as already mentioned in the introduction. Modern recorders are usually made from wood, cf. Fig: 5.28. Recorders are classified by Hornborstel and Sachs with the classification code: 421.221.12. The sound of the recorder is often described as clear with a fast attack time and a stable response. It is often associated with the sound of birds. Recorders are build in many sizes and they are used in many musical styles and

epochs, from baroque music to modern musical contexts. Because of its special construction, the recorder is comparatively easy to play, which explains its widespread use. Despite of the fixed construction, the recorder has many options for articulation. The mentioned aspects of the instrument support the selection of the instrument for the present study.

Figure 5.28: Recorder, made by the German manufacturer Conrad Mollenhauer GmbH, model: Sopran C.

We start with acoustic measurements on the recorder. The first experiment is about measuring the propagation speed of the initial pressure waves in the instrument during the initial blowing process. A two-dimensional microphone array is used for the experiment. According to the common linear theory of acoustics one expects to measure the speed of sound as propagation velocity of the signal.

A second investigation deals with the question how the blowing speed and the blowing angle influence the sound production of a recorder-like instrument. While these aspects seem less relevant to modern Western European recorders because of their special construction (fixed block and fixed position of the air channel with respect to the labium), important clues can be studied for the historical development of this kind of construction. The investigation using methods from Computational Fluid Dynamics and Computational Aeroacoustics (CFD/CAA) was part of a cultural heritage preservation project that showed the possibilities of trans- and interdisciplinary research in systematic musicology by making a bone flute fragment playable.

5.2.1 Speed Measurements on the Recorder

Measurements of acoustic signal propagation have a long tradition. First observations have been done in the 17 $^{\text{th}}$ century by the French philosopher and scientist Pierre Gassendi measuring the time difference between a shot of a gun and listening the event from a long distance. In 1740 the Italien Bianconi showed that the speed of sound in air increases with temperature. A precise experimental value for the speed of sound was obtained at the Academy of Sciences in Paris in 1738. The value measured was 332 m/s, which is close close to the value one measures with modern methods [Cramer (1993)].

Today it is known that the speed of sound is dependent from temperature, humility, pressure and density. For an ideal gas ($p = nRT/V$) one obtains:

$$c_{ideal} = \sqrt{\gamma \cdot \frac{p}{\rho}} = \sqrt{\frac{\gamma \cdot k_B \cdot T}{m}} \tag{5.3}$$

with the adiabatic index for air $\gamma = C_p/C_V \approx 1.4$, the mass of a single molecule m and the Boltzmann constant $k_B \approx 1.380649 \cdot 10^{-23}$ J/K and. Note, that the equation is only valid

when the sound wave is a small perturbation on the ambient condition.

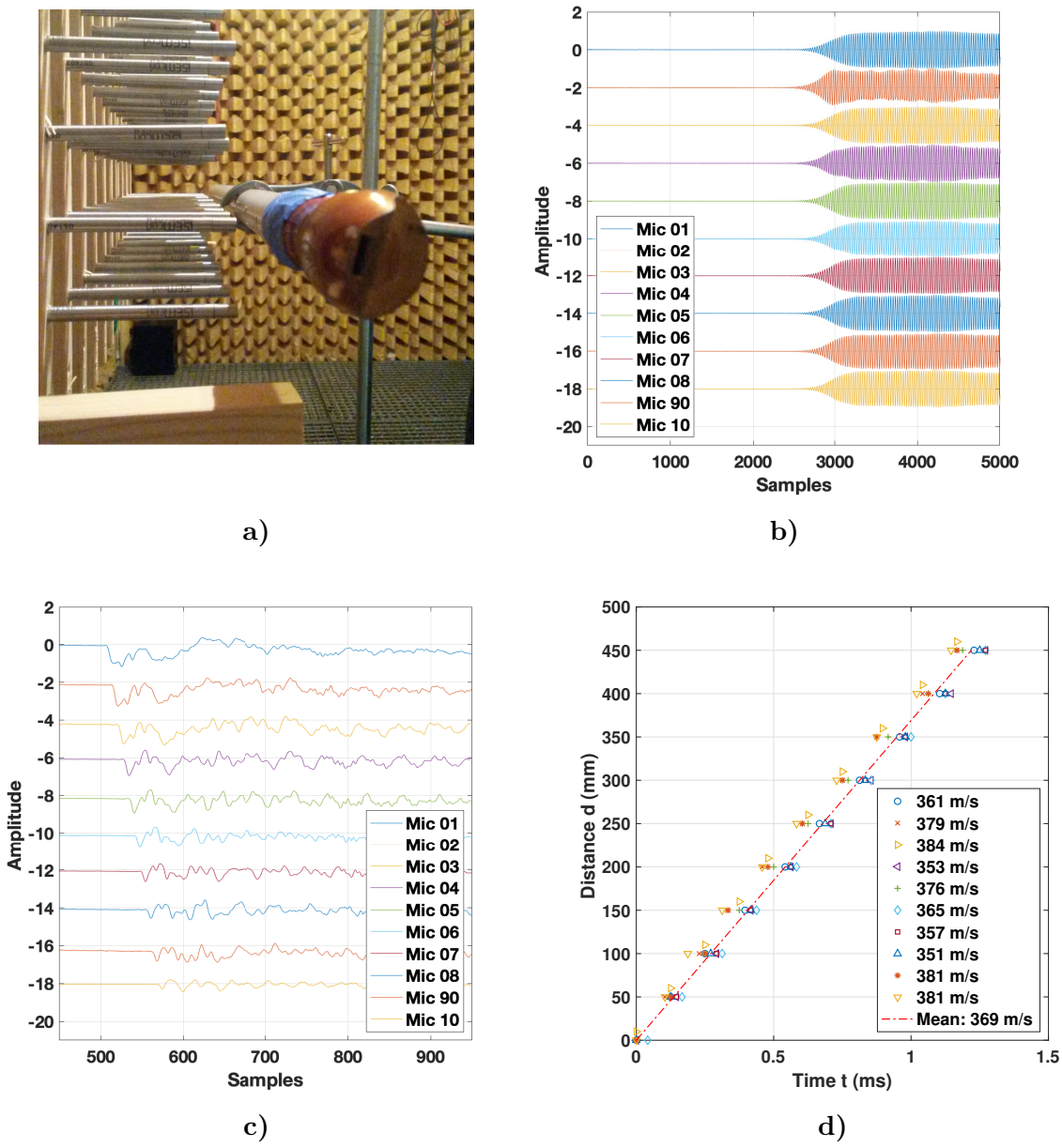

Figure 5.29: Speed measurements on the Recorder. a) Experimental set-up. For the measurement, the instrument was placed in such a way that the microphones lined up exactly with the holes provided in the tube. b) Pressure signals recorded by the equidistant microphone line (Mic 01 - Mic 10) close to the resonator's tube. c) Propagation of the initial pressure waves along the recorder's resonator tube. d) Speed of the initial pressure waves measured on 10 different data sets of blowing on processes of the recorder.

The experiment was carried out in an anechoic chamber at the Institute of Systematic Musicology at University Hamburg. The musical instrument was modified for the object of investigation, the measurement of the speed of the initial pressure waves inside the resonator. The wooden resonator of the recorder was replaced by a plastic tube of the same diameter but of a length of 500 mm to enlarge the spatial precision of the speed measurements. The inner surface of the plastic tube had a twice higher roughness compared to the original. With both changes, we are deliberately worsening the measurement conditions compared to the orig-

inal recorder instrument in order to arrive at lower estimates through the measurements. The measurements have been done using an equidistant distributed microphone array line of 10 microphones (iSEMcon) at distances of 50 ± 0.1 mm apart from each other, cf. Fig: 5.29a. For the actual measurements the modified recorder was placed in such a way that the microphones lined up exactly with corresponding equidistant holes in the tube. The measurements have been done at the following ambient conditions: temperature $T = 18.5\,^{\circ}\mathrm{C}$, humidity $L_h = 40.5\%$ and static pressure $p = 1016\,\mathrm{hPa}$. This leads to a local speed of sound of $c = 342.95\,\mathrm{m/s}$. The sampling rate of the measurements was $f_s = 48\,\mathrm{kHz}$. The recorder was blown manually.

5.2.1.1 Observations

Examples of the recorded signals are shown in Fig: 5.29b, the initial transients are depicted in Fig: 5.29c. The data have been normalized. The normalization do not change anything in the temporal progression of the signals, in particular nothing in the onset times of the signals or the maximums. The x-axis which represents the time is labeled as samples to get a quick overview. To get the time in seconds one just have to divide the samples by the sampling rate $f_s = 1/48,000\,\mathrm{s}^{-1}$. For the sake of clarity the signals are separated by an offset of -2. The propagation velocities are determined from the data of the onsets as well as from the data of the first extreme values (maximums and minimums). The results of the speed measurements of the initial pressure waves are summarized in Fig: 5.29d.

5.2.1.2 Discussion

Contrary to the assumption, the initial pressure fluctuations move at speeds slightly above the speed of sound. The occurence of waves with shock wave characteristics in the initial transient of the recorder is an unexpected and a new result for this class of instruments. In the case of brass instruments, the occurence of shocks is known, both, during the blowing process and in working mode[Campbell (1999)]. However, a detailed physical explanation of this phenomenon has not yet been provided.

5.2.2 The Bone flute - A Resurrection Story

This section presents an interdisciplinary research project investigating a 15th century fragment of a bone flute. The aim of the project is to create a playable replica of the instrument. The fragment is part of the musical instrument collection in Willisau, Switzerland. The flute block is not preserved, therefore the original instrument does not produce sound. In the course of the work a high resolution X-ray computed tomography of the bone flute fragment is performed. By designing a number of various blocks as CAD models and testing them with numerical simulations, the optimal block with respect to sound generation has been evaluated. By using 3d-print technique a playable replication of the original instrument could be made.

5.2.2.1 Digitalization of the Bone flute Fragment

The first step of investigations of the bone flute fragment was to digitize the instrument. This work have been done by the colleagues Dr. Niko Plath and Dipl. rest. Sebastian Kirsch [Plath, Fischer, Kirsch (2020)]. Because the author did not contribute to this process, the procedure is just mentioned by key points here:

1. Scanning of the instrument with industrial X-ray Computed Tomography (CT)

2. 780 single X-ray images were recorded from different angles
3. The spatial resolution was $100\mu m$.
4. The CT data lead to a set of 2D graphics which represent the X-ray attenuation coefficients via grey values.
5. Stacking the 2D cross sections yields a 3D representation of the measurement control volume with the instrument.

The digitalization process is depicted in Figs: 5.30a - 5.30e.

5.2.2.2 Ethnological and Archaeological Indications on Shepherd's Manual Skills

To reconstruct the missing mouthpiece of the bone flute one has to take into account etnological informations as well as knowledge from experimental archeology. The location of the fragment gives reason to assume that the instrument is a shepherd's flute. With the latter one can assume a flexible and simple material that can harden without losing volume and which is present on site. Wax and clay come into consideration here. Furthermore, one has to consider simple technical abilities for the construction of a mouthpiece in rural areas in the 15th century. Ethnological and archeological expertises suggest that the missing mouthpiece easily could have been made by utilizing a thin, flat wooden rod as a scraper. The scraper could have been shaped by a common knife. With these toosl it is possible to wipe a mix of beeswax and clay or charcoal into the upper part of the bone flute to form an air channel [Gill (2012)]. The intonation of the bone flute can be realized by shaping the air channel's angle. Practical experiments show that this can be done with little manual skill effort.

5.2.2.3 Reconstruction of the Block of the Bone flute's Mouthpiece

To investigate the optimal design of the mouthpiece of the bone flute numerically we implemented different geometrical and initial set-ups into a computational grid, the numerical space which is called mesh. For a successful numerical implementation one has to apply the compressible Navier-Stokes equations with appropriate boundary and initial conditions. The process of implementation is explained in principle in chapter 4.
The optimal interaction between the flow field and the sound field, the optimal sound generation and the sound propagation are explored by utilizing six different set-ups with different angles of the air channel of the reconstructed mouthpiece as well as the initial velocity magnitude at the entrance of the air channel, called the inlet. The angles being studied are $0\,^\circ$, $10\,^\circ$ and $20\,^\circ$. The initial velocity magnitudes being studied are $5\,\mathrm{m/s}$ and $10\,\mathrm{m/s}$, implemented as top hat profiles at the inlet. The details of the mesh of the setup of the bone flute is depicted in Fig. 5.31. The different angles of the air channel inside the mouthpiece are labeled. Also shown is the position of the probe point A in the mesh where the time series for analysis are sampled.

5.2.2.4 Fluid Mechanical Characteristic Numbers

An important step is to estimate relevant characteristic fluid mechanical numbers for the given set-ups to fit the numerical implementation of the problem. Most important is to estimate the Reynolds number Re, the dimensionless ratio of inertial forces to viscous forces [Schlichting (2003)]. The forces are represented by the characteristic length L of the dynamics and the absolute value of the characteristic velocity U of the flow field, on the one hand, and the kinematic viscosity on the other, cf. Eq. (5.4). The Reynolds number is used to evaluate the transition from laminar to turbulent flow field characteristics. The flow field in the bone flute is represented by the

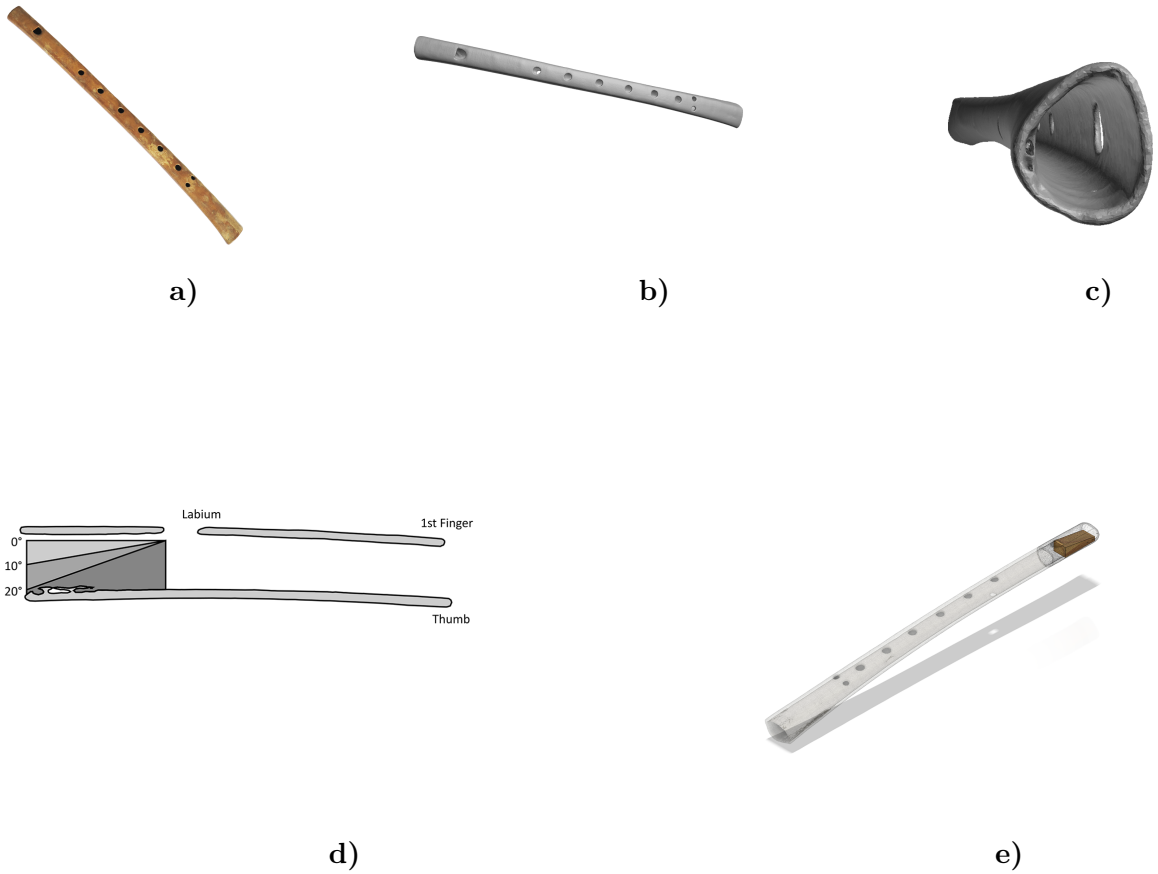

Figure 5.30: a) Fragment of the bone flute. b) 3D model of the bone flute fragment. c) Detail of the 3D model. View from the missing mouthpiece at the top into the bone flute. d) Illustration of various mouthpiece models that could have been made easily by sheperd's know how. The models include different angles of the air channel of $\alpha = 0°$, $10°$, $20°$ inside the mouthpiece. e) Model with a hypothetical block inside the mouthpiece.

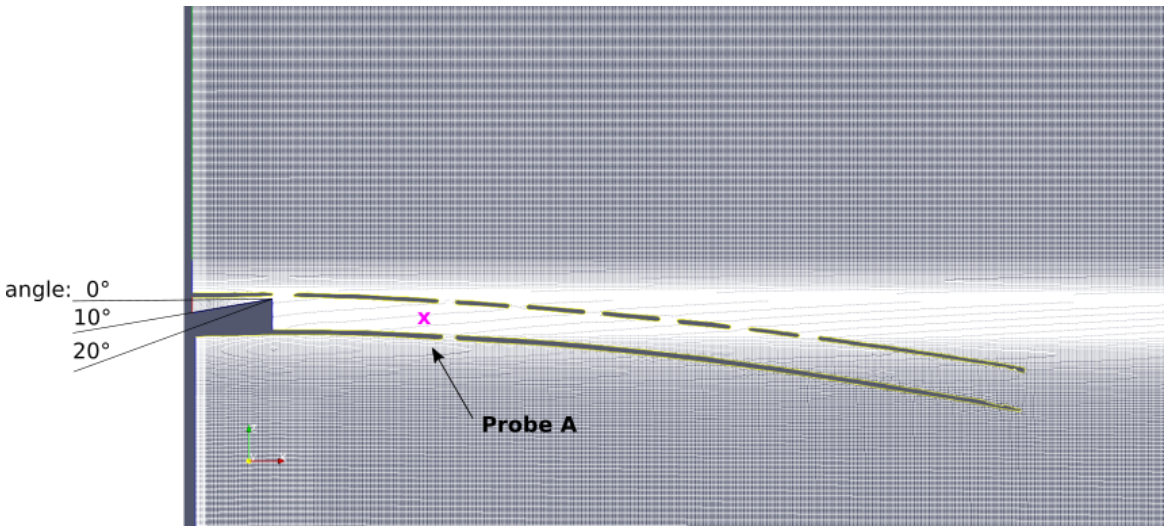

Figure 5.31: Detail of the mesh with the implemented cross-section of the bone flute with the angle inside the mouthpiece of 10 °. The whole mesh has a size of $330 \times 340 \times 0.2$ mm. Marked by the magenta cross is the probe point A where the data for analysis were sampled.

jet, or more precise, the free propagation length of the jet and its velocity. In flow fields with diameter d turbulent flow occurs if $Re_d > 4000$ [Schlichting (2003)].

$$Re = \frac{L \cdot U}{\nu} \tag{5.4}$$

The characteristic length is given by the length of the cut-up of the bone flute, $L = 5.5 \cdot 10^{-3}$ m/s which determines the jet flow area. The characteristic velocity is assumed as the velocity of the jet $U = U_{jet}$. The kinematic viscosity $\nu = \mu/\rho$ of the medium air is about $\nu = 1.53 \cdot 10^{-5}\,\mathrm{m^2/s}$. The absolute value of the initial velocity profile of the jet U_jet at the windway can be estimated by the continuity equation of mass flow

$$U_{inlet} \cdot A_{inlet} = U_{jet} \cdot A_{jet} \tag{5.5}$$

with $A_{inlet} = 24\,\mathrm{mm^2}$ the cross-sectional area of the air channel's inlet and A_{jet} those of the windway's aperture. Thr initial inlet velocity conditions $U_{inlet,1} = 5\,\mathrm{mm/s}$ and $U_{inlet,2} = 10\,\mathrm{mm/s}$ result in the jet velocities $U_{jet,1} = 20\,\mathrm{m/s}$ and $U_{jet,2} = 40\,\mathrm{m/s}$. With these values the Reynolds number can be estimated as $Re_1 = 7190$ and $Re_2 = 14480$. The Reynolds number obtained for the adressed problems indicates that the flow field in the mouth region of the bone flute is turbulent [Schlichting (2003)]. Note, that the Reynolds number estimates the flow characteristics relative to the viscous characteristics of the medium and not the characteristics of the sound field, which acts on a much faster time scale. Therefore the flow velocity has to take into account and not the speed of sound.

As a further important characteristic number the Strouhal number Sr is discussed. The Strouhal-number is the dimensionless ratio between an aeroacoustical quantity, the so-called vortex shedding frequency f, and the fluid mechanical quantities, the characteristic length L and the characteristic velocity U of the flow [Schlichting (2003)].

$$Sr = \frac{L \cdot f}{U} \tag{5.6}$$

The vortex shedding frequency in the mouth region is caused by the oscillations of the jet of the working flute. Here the hypothesis is that the vortex shedding frequency corresponds to

the fundamental frequency of a real operating flute $f \approx 2450\text{Hz}$, which one obtains by measurements on recorder-like instruments with a corresponding resonator length. The Strouhal number is estimated by $Sr_1 = 0.67$ and $Sr_2 = 0.34$ in order to the jet velocities $U_{jet,1}$ and $U_{jet,2}$. The estimated Strouhal number corresponds to values one would expect for the problem considered.

The Prandtl number Pr is defined as the ratio of kinematic viscosity, also known as momentum diffusivity, to the thermal diffusivity, cf. Eq. (5.7).

$$Pr = \frac{\nu}{\alpha} \tag{5.7}$$

The thermal diffusivity of the medium air at normal conditions ($p = 1013.25\,hPa, T = 293\,K$) is given by $\alpha = \kappa/(\rho \cdot C_p)$. Hereby $\kappa = 0.0257\,\text{W}/(m \cdot K)$ is the thermal conductivity, cf. Eq. (4.4) and C_p the specific heat capacity at constant pressure conditions, cf. Eq. (4.6) and Tab. 4.1. The thermal diffusivity is calculated as $\alpha = 1.9 \cdot 10^{-5}\,\text{m}^2/\text{s}$. This leads to the estimation of the Prandtl number of $Pr \approx 0.72$.
Last but not least the Mach number is important to estimate. The Mach number is defined as the ratio of the characteristic velocity U to the speed of sound c. The Mach number in the case being considered is estimated to

$$Ma = \frac{U}{c} \approx 0.058 \quad \text{and} \quad 0.116 \tag{5.8}$$

with $c = 343\,m/s$ the speed of sound at normal conditions. Note, that the occurrence of pressure waves with show shock wave characteristics in the initial transient is not yet expected taking this estimation.

5.2.2.5 Observations and Discussion

The angle of the air channel of the mouthpiece's block is crucial for the sound generation in the bone flute. The air channel's angle determines the angle of attack of the flow field on the bone flute's labium which is less designed as a flat and sharp wedge like in modern recorder-like instruments rather than round shaped and crescent. The other important criterion is the initial velocity the player is blowing on the bone flute.

The sampled time series of the pressure at probe point A of the two cohorts of numerical simulations with initial inlet velocities of $v_0 = 5\text{m/s}$ and $v_0 = 10\text{m/s}$ are depicted in Figs. 5.33a and 5.33b. One recognizes that the numerical runs with air channel's angle of $\alpha = 0°$ do not generate sound. The signals fade away in the transient after time $t = 1\text{ms}$. Therefore we can exclude these cases looking for a playable reconstruction of the bone flute.

At angles of $\alpha = 10°$ and $20°$ the picture becomes more diverse. One has to distinguish between stable and unstable initial sound production processes as well as between different levels of response of the instrument, particularly of the effect of overblowing, another transient process. Exploring this variety of behavior we evaluated the SPL-spectra of the sampled time series. This is shown in Figs. 5.34a and 5.34b.
In Fig. 5.34a it is shown that the SPL-spectrum of the case with angle $\alpha = 20°$ has a prominent peak at 3431Hz with an SPL of 117dB. The theoretical fundamental frequency of the equivalent Helmholtz-resonator is 3440Hz. Also the higher harmonics can be recognized at 6678Hz, 10060Hz, 13450Hz which also matches very good with the theory. This case can be recognized as an optimal balanced mix of air channel's angle and initial condition at the mouthpiece's inlet. In the case of the air channel's angle of $\alpha = 10°$ the peaks of the harmonics can also be

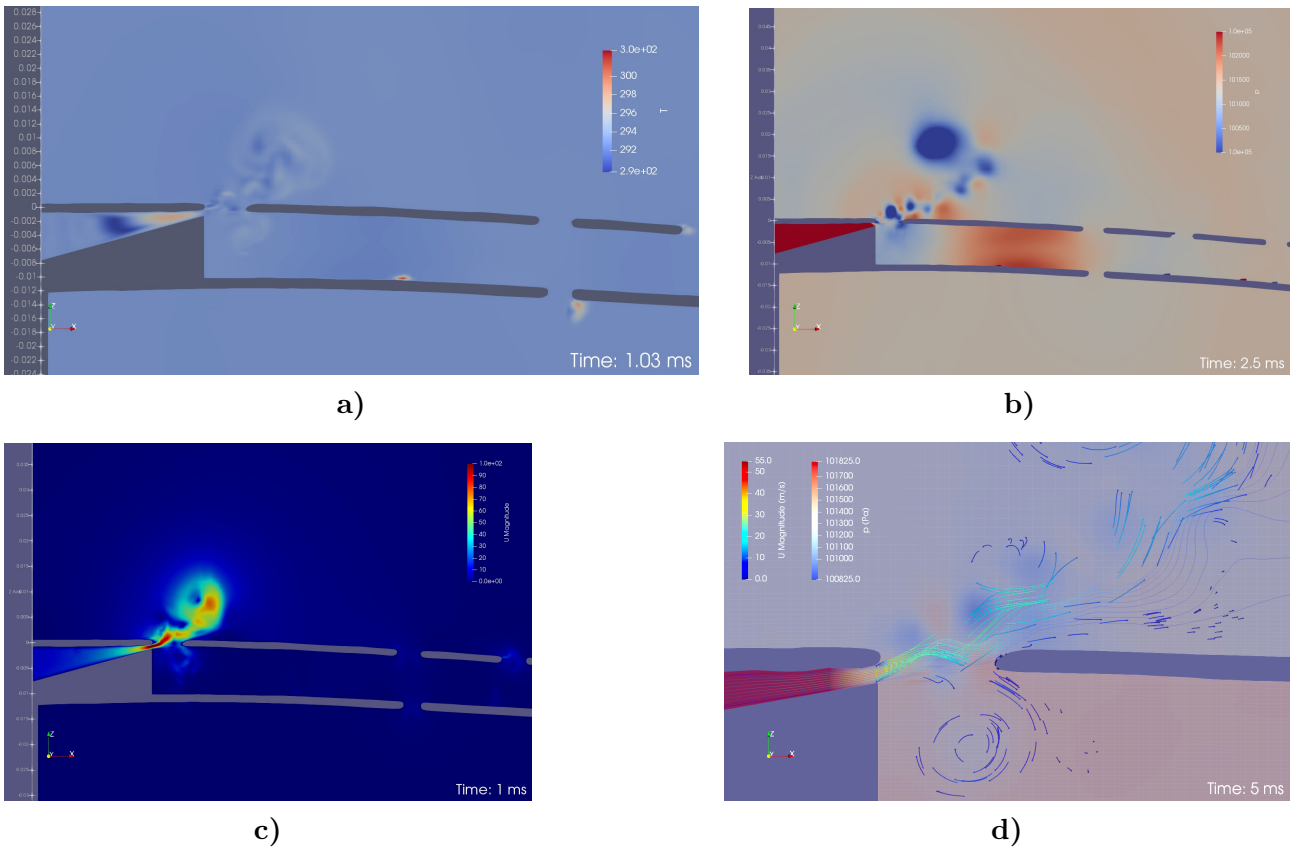

Figure 5.32: Examples of visualizations of the calculated bone flute set-up of the case $v_0 = 10\text{m/s}$, air channel's angle $\alpha = 20°$ of the block, a) Temperature field of the generator region at time $t = 1.03\text{ms}$. b) The pressure field in the initial transient at time $t = 2.5\text{ms}$. c) The velocity magnitude in the initial transient at time $t = 1\text{ms}$. c) Particle tracing in the generator region of the set-up of the bone flute with initial velocity of $v_0 = 5\text{m/s}$ and an air channel's angle of $\alpha = 10°$ of the block. Shown is both, the pressure field as well as the velocity field. The contour lines represent the current velocity field of the flow field of the jet as well as vortices inside and outside the bone flute.

recognized but with lower amplitudes. The fundamental frequency is not as prominent as in the previous case. Moreover some peaks with lower frequencies than the fundamental frequency become prominent. This reflects the unstable initial transient process of sound generation. Although the case shows sound production, it do not represents the optimal fine tuning of the air channel's angle and the initial condition at the mouthpiece's inlet.

In Fig. 5.34b one observes an overblowing process in the initial transient of the case $v_0 = 10\text{m/s}$, $\alpha = 20°$. The prominent peak at 6947Hz has an amplitude of 126dB which is again in very good accordance to the theory. The fundamental at 3553Hz (118dB) can be detected as well as side band peaks of the fundamental at 2564Hz (122dB) and 4620Hz (118dB). This is an interesting observation and a well-known effect of self-sustained and coupled dynamical systems that are able - and in the way - to synchronize. The synchronization of the system simulated in this case with its inherent complex fluid- and aeroacoustic dynamics to a system with a stable periodic behavior with fundamental frequency is disturbed by an entry of too much energy determined by a high amount of initial velocity at the air channels inlet. This leads to an overblowing of the bone flute. The case with an air channel's angle of 10° has no tendency to overblowing. Here we observe the fundamental and its side-bands that lead to an incomplete, or sub-optimal balance of the geometry and the initial conditions at the reconstructed mouthpiece.

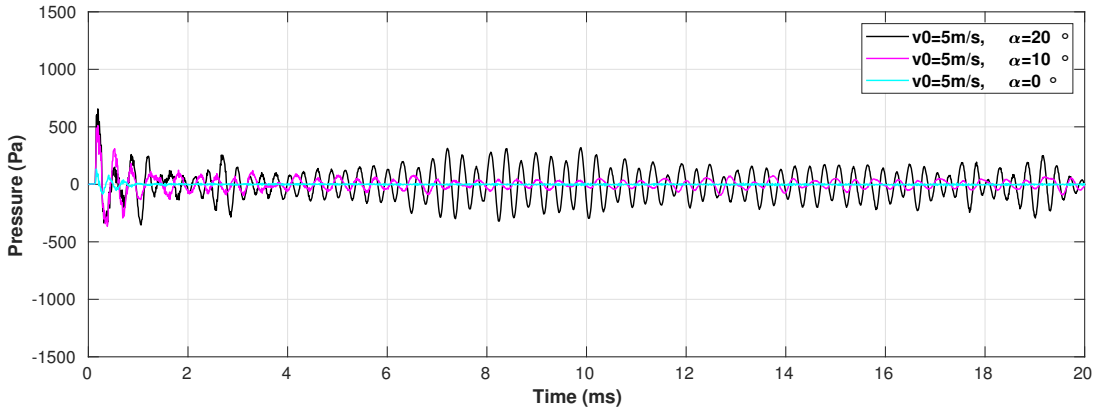

a)

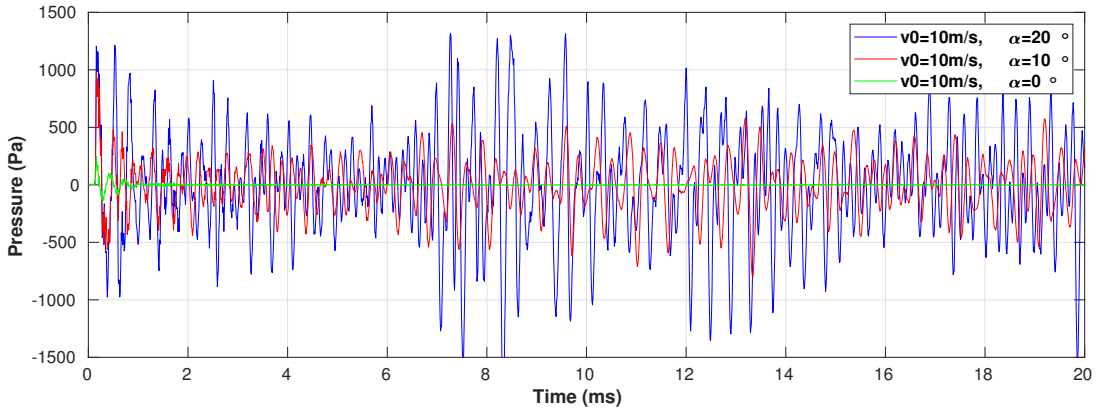

b)

Figure 5.33: Time series of the pressure at probe point A of the numerical simulations of the bone flute with initial velocity magnitude at the inlet of a) $v_0 = 5\text{m/s}$ and b) $v_0 = 10\text{m/s}$ at different angles of the air channel of $\alpha = 0°$, $10°$, $20°$ inside the mouthpiece.

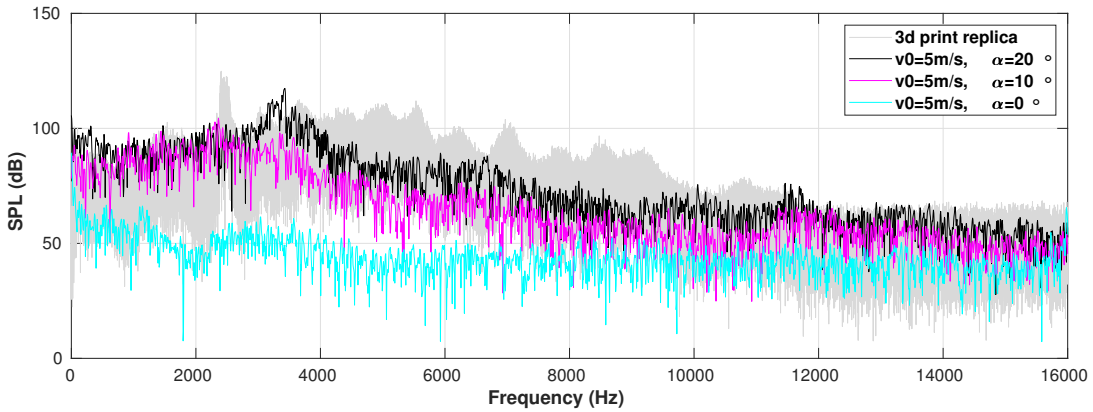

a)

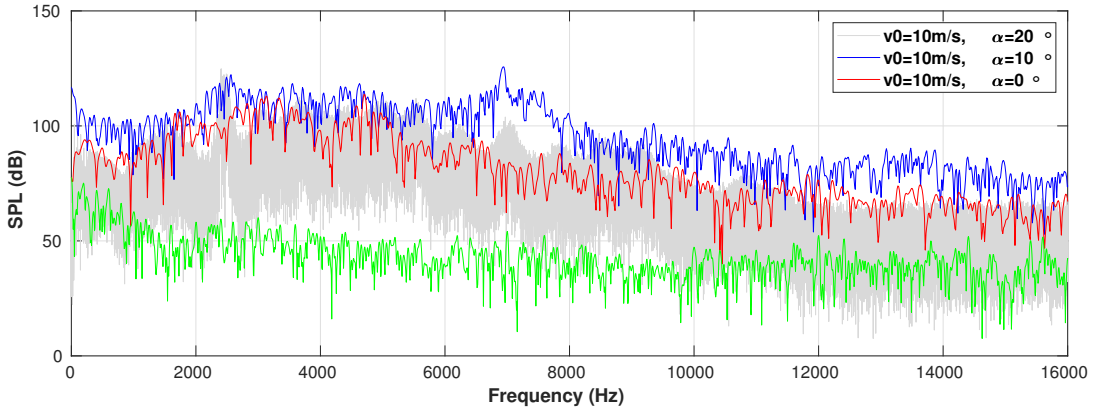

b)

Figure 5.34: SPL-spectra of the time series of the pressure at probe point A of the numerical simulations of the bone flute with initial velocity magnitude at the inlet of a) $v_0 = 5\text{m/s}$ and b) $v_0 = 10\text{m/s}$ at different angles of the air channel of $\alpha = 0°$, $10°$, $20°$ inside the mouthpiece.

The introduced ansatz of investigating a cultural heritage object - the bone flute - reflects the trans- and interdisciplinary access of modern scientific investigation in the field of systematic musicology. It was shown exemplarily how flexible and powerful the combination of tools and techniques from various and very different disciplines, data bases and workflows can be utilized to aim one goal - closing the gaps of knowledge of the subject of interest. Seemingly incompatible requirements of the different disciplines can work together and can stimulate to each other. This opens synergies to their mutual benefit.

5.3 The Organ Pipe

Organ pipes are the sounding parts of organs. These musical instruments are usually made of wood or of metal. Metal pipes are made of lead often alloyed with tin to improve rigidity. Organ pipes are build as open pipes or as closed pipes[5]. The principle design is illustrated in

[5]For closed pipes the terms *stopped* pipe and *gedackt* pipe are also used. The latter term is often used in German-speaking countries.

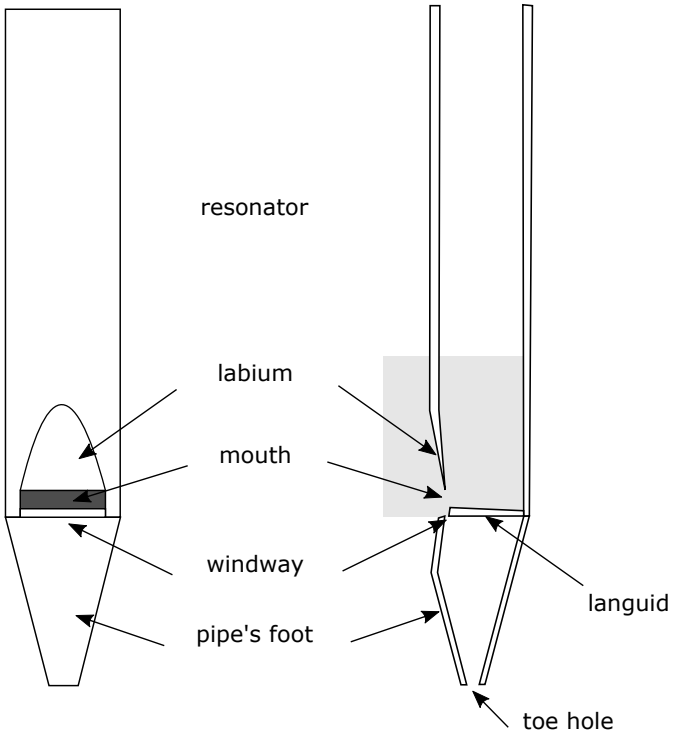

Figure 5.35: Principle design of the of organ pipe.

Fig. 5.35.

One distinguishes three principles of design: reed-pipes, diaphone-pipes and flue-pipes. In this study only the latter sub-class of organ pipes is investigated. For the sake of simplicity we will still use the term organ pipe.

A new approach to investigate the role of pressure waves in the initial transient of an organ pipe is presented in this section. By numerical simulations solving the compressible Navier-Stokes equations with suitable boundary and initial conditions, it becomes possible to trace the full range of acoustic wave phenomena including the sound generation, the propagation, the reflection and diffraction, the damping and the radiation of sound waves. The focus in this section is on the contribution of occurring pressure wave fronts in the initial transient that show shock wave characteristics, in particular their role at the formation process of the initial sound field inside the organ pipe's resonator. Utilizing spectral analysis as well as extended visualization methods, a wide range of aspects of the dynamics of the initial transient of an organ pipe can be discovered. In particular the damping processes in the resonator which are nonlinear are analyzed and discussed in detail. The numerical approach presented in this case study, allows to investigate the initial transient of an organ pipe with an extraordinary level of precision, thereby helping to understand the underlying first principles of the sound field formation, the mutual interaction between the jet's flow field and the sound field inside the organ pipe. Animations of the temporal and spatial development of relevant physical quantities like pressure, turbulent kinetic energy, vorticity and velocity magnitude calculated in the numerical simulations are provided as supplementary material.

5.3.1 The Initial Transient of an Organ Pipe

The investigations were carried out using numerical simulations of a stopped wooden organ pipe which is shown in Fig: 5.36a. The case study discovers the general effects related with sound generation in the resonator of an organ pipe during the initial transient process. The motivation is to learn more about the first principles as well as of the complex dynamics of sound generation in organ pipes. The original instrument which was used in the study as a template for the numerical model was provided by the German organ builder Alexander Schuke Orgelbau Potsdam GmbH [Schuke (2016)].

5.3.1.1 The Mesh and Sample Sets

The set of equations, the initial and boundary conditions, the thermo-physical and the turbulent properties of the problem of concern have to be solved on an suitable computational grid, the numerical space which is called the mesh. The geometry of the organ pipe and its surrounding area was transferred into a structured 2D computational grid. The mesh size of the case (length × width × depth) is (260 mm × 180 mm × 1 mm) with 254342 mesh points, 505170 faces and 126000 hexahedra. The mesh generated for this case study is shown in Fig. 5.36b. The technique how to write an appropriate mesh file and how to generate a mesh can be found in the OpenFOAM User Guide [OpenFoam-v7 U.G. (2019)]. The configuration of the numerical set-up was done as described in chapter 4. The numerical simulations produces an amount of data of ca. 500GB which contains the field information of the calculated physical quantities, pressure, velocity, density, temperature, turbulent kinetic energy, vorticity, etc, at each time step. For the analysis data sets at cross-section *cs_resonator* are sampled. The cross-section *cs_resonator* is displayed in Fig. 5.37 marked by the horizontal pink line. The sample *cs_resonator* has a spatial expansion of 100 mm with 1000 sample points. The resolution is 0.1 mm. Overall 10000 time steps with a resolution of $\delta t = 1 \cdot 10^{-5}$ s corresponding to the simulation time of 100 mm were sampled from the data of the numerical simulations. Note that the time resolution during the calculation of the numerical simulations was much finer with $\delta t = 1 \cdot 10^{-8}$ s. The sampled data were transferred into a time series by spatial integration over the lengths of the particular cross-section.
The snapshot in Fig. 5.37 shows the numerical simulation, visualized at time step $t = 0.15$ ms. Color coded is the pressure field in the interval of 1011 hPa (light blue) to 1018 hPa (dark red). One observes pressure fronts reflecting at the inner walls of the organ pipes resonator, propagating to the closed end of the resonator. The origin of the pressure wave fronts is the jet flow which enters the stagnant air column in the resonator. The initial jet flow produced two vortices at its front caused by shear stress. The vortices which can be seen as blue dots at the orifice opposite to the tip of the labium.

5.3.1.2 Observations

The sound pressure level spectrum of the sampled time series with the length of $t = 100$ ms has been calculated using Eq. 5.9. The reference pressure is the human auditory threshold $p_0 = 2 \cdot 10^{-5}$ Pa. The data have a sampling rate of $f_s = 100$ kHz caused by the temporal resolution of $\delta t = 1 \cdot 10^{-5}$ s written out from the numerical simulation. This corresponds to a resolution in frequency of $\delta f \approx \pm 6$ Hz of the spectrum. In Fig: 5.38 the SPL-spectrum of the spatial integrated time series sampled at the cross-section *cs_resonator* is shown. One sees the fundamental frequency (first harmonic) at $f_1 \approx 757$ Hz followed by the odd higher harmonics $f_3 = 2338$ Hz, $f_5 = 4090$ Hz, $f_7 = 5945$ Hz, $f_9 = 7911$ Hz, $f_{11} = 9663$ Hz, $f_{13} = 11680$ Hz. The deviation of the third harmonic to the theoretical value is 3%, which is an excellent result. The deviations of the fifth and seventh harmonic are 8% and 12% which are good results.

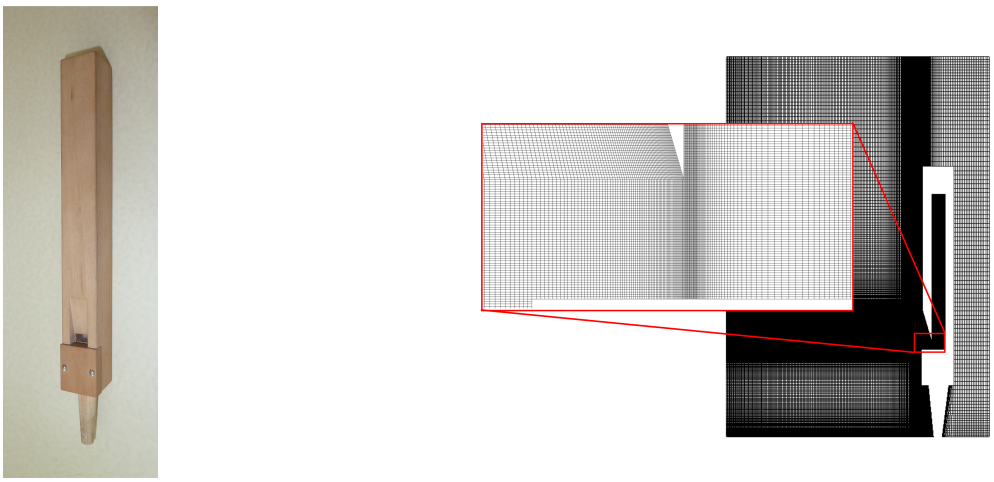

a) **b)**

Figure 5.36: a) Stopped wooden organ pipe with a quadratic profile, built and provided for measurement use by organ builders Schuke Orgelbau Potsdam GmbH. b) Implementation of the organ pipe and the surrounding space into a computational grid. The detail gives an impression of the mesh size in the cut-up region.

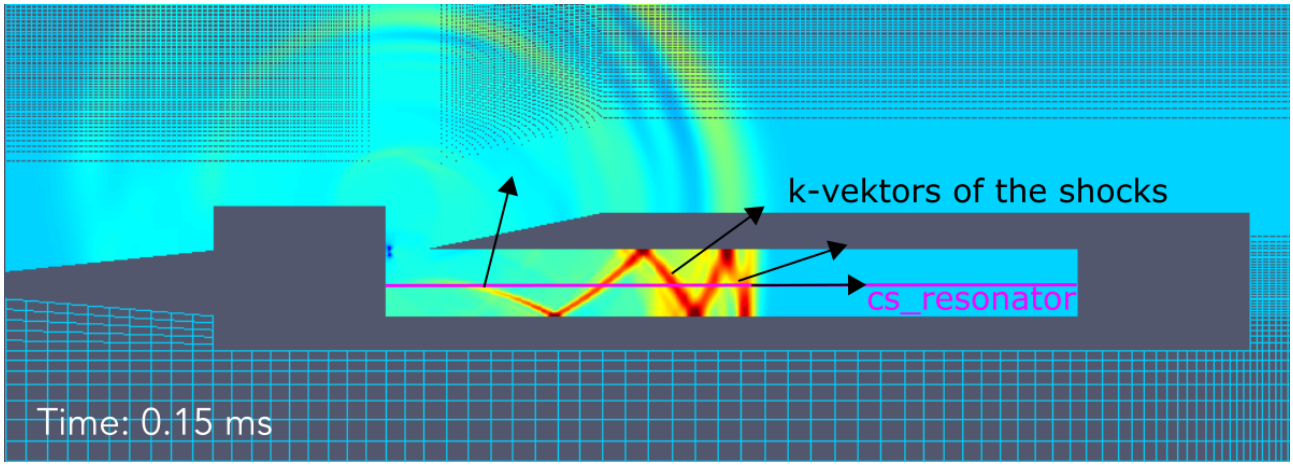

Figure 5.37: Detail of the mesh of the simulated organ pipe. The mean resolution of the calculation grid inside the resonator is $\delta x = 0.1\,\text{mm}$, $\delta y = 0.1\,\text{mm}$. The snapshot at time $t = 0.15\,\text{ms}$ shows the initial pressure wave fronts reflecting at the inner walls of the resonator and propagating to the resonators upper end which is closed. The directions of the k-vectors of different initial wave fronts are indicated by black arrows. Marked by the horizontal pink line along the longitudinal axis of the resonator is the location of the cross-section *cs_resonator*.

$$SPL = 20 \cdot \log_{10}\left(\frac{p}{p_0}\right) \quad \text{dB} \tag{5.9}$$

The visualizations of the numerical simulations give further insights into the dynamics of the initial transient of the organ pipe. The data of the numerical simulations, the spatial and temporal development of the physical quantities pressure, turbulent kinetic energy, vorticity and velocity magnitude are animated and provided as supplementary material. The Figs. 5.39,

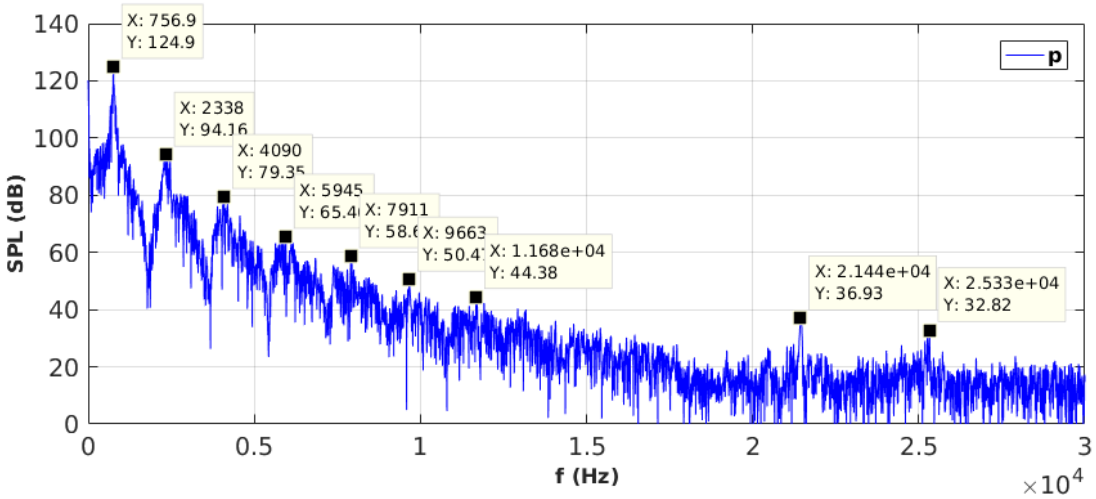

Figure 5.38: SPL-spectrum of the blowing process of the closed wooden organ pipe. Labeled are the fundamental frequency $f_1 = 757\,\text{Hz}$ and the odd higher harmonics $f_3 = 2338\,\text{Hz}$, $f_5 = 4090\,\text{Hz}$, $f_7 = 5945\,\text{Hz}$, $f_9 = 7911\,\text{Hz}$, $f_{11} = 9663\,\text{Hz}$, $f_{13} = 11685\,\text{Hz}$.

5.40, 5.41, 5.42, 5.43 and 5.44 show sequences of the development of the pressure in the time interval $t = 0.01\,\text{ms}$ to $t = 0.96\,\text{ms}$ which includes the first back-and-forth propagation of the initial pressure wave fronts along the longitudinal axis of the resonator. The pressure field is color-coded in the range of 1011 hPa (light blue) to 1018 hPa (dark red).

One can see an emerging initial pressure fluctuation of high amplitude (red) generated by the organ pipe's jet flow, that enters the stagnant air column in the resonator. At the cut-up as well as at the wedge, the lower end of the labium, acoustical diffraction can be observed. This observation shows the excellent quality and the high level of precision of the numerical simulation performed in this study. At the inner walls of the resonator the initial pressure wave front reflects. These reflections generate secondary pressure wave fronts, which propagate with higher velocities than the primary one (but on a longer way). This leads to an accumulation of the wave fronts. The propagation velocities of all observed initial pressure wave fronts are higher than the local speed of sound, they are trans-sonic! This indicates that the observed pressure waves have shock wave characteristics. The detailed analysis of the propagation velocities of pressure wave fronts will confirm this statement later on.

The induced pressure wave front propagates spherically (circular in the 2D set- up) into mouth region of the organ pipe. The accumulation of the reflected pressure wave fronts at one hand and their attenuation on the other hand lead to an dynamical equilibrium that maintain the amplitude and the velocity of the primary pressure wave front. The primary pressure wave front therefore shows properties of an self-reinforcing wave package. Such waves are known as solitons. The dynamics observed leads to a local increase of amplitude density in the upper end of the resonator at time $t = 0.29\,\text{ms}$. While the velocity of the amplitude maximum of the primary pressure wave front is conserved, its basis gets spatially distributed, or disperse into the slipstream. This is shown in detail in Fig. 5.45.
The superposition of the wave fronts which reflect at the upper end of the resonator leads to a doubling of the number of traveling pressure wave fronts in the resonator's air volume, cf. Figs. 5.45, 5.46. The doubling is caused by the width of the upper end, which produces a runtime difference of the reflected wave fronts. The author recommends to study the dynamics

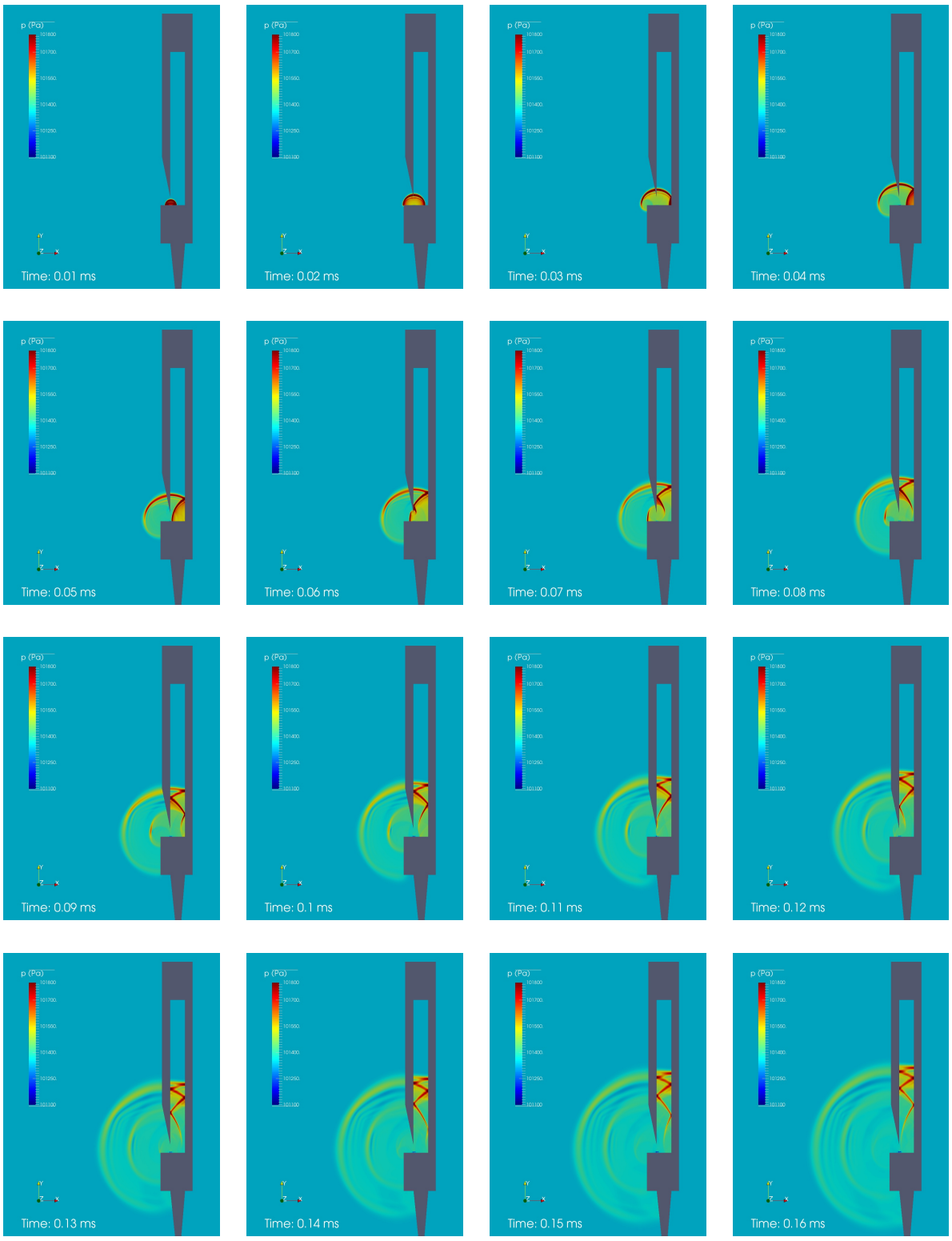

Figure 5.39: Visualization of the numerical simulation of the initial transient of an stopped wooden organ pipe. Color-coded is the pressure field at the period of time of 0.01 ms – 0.16 ms. Shown is the propagation of the initial pressure fluctuation in the resonator and the initial radiation of sound into the free space. One can also see the initial transverse reflections inside resonator that causes fast transverse modes. Also diffraction effects at the organ pipes labium an its outside edges can be detected.

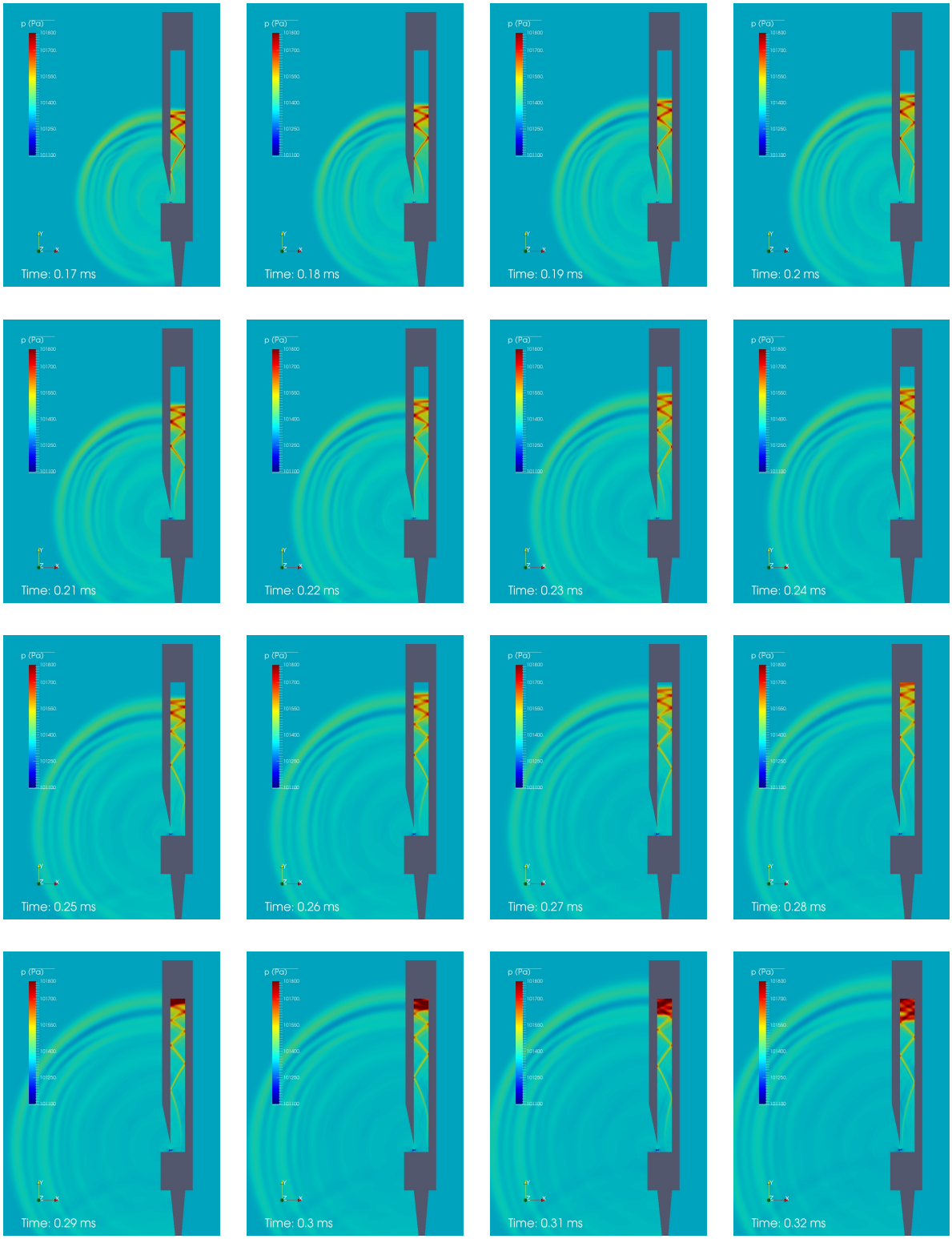

Figure 5.40: Visualization of the numerical simulation of the initial transient of an stopped wooden organ pipe. Color-coded is the pressure field at the period of time of 0.17 ms – 0.32 ms. Shown is the reflection of the initial pressure fluctuation at the upper end of the stopped organ pipe as well as its back-propagation to the lower end of the resonator.

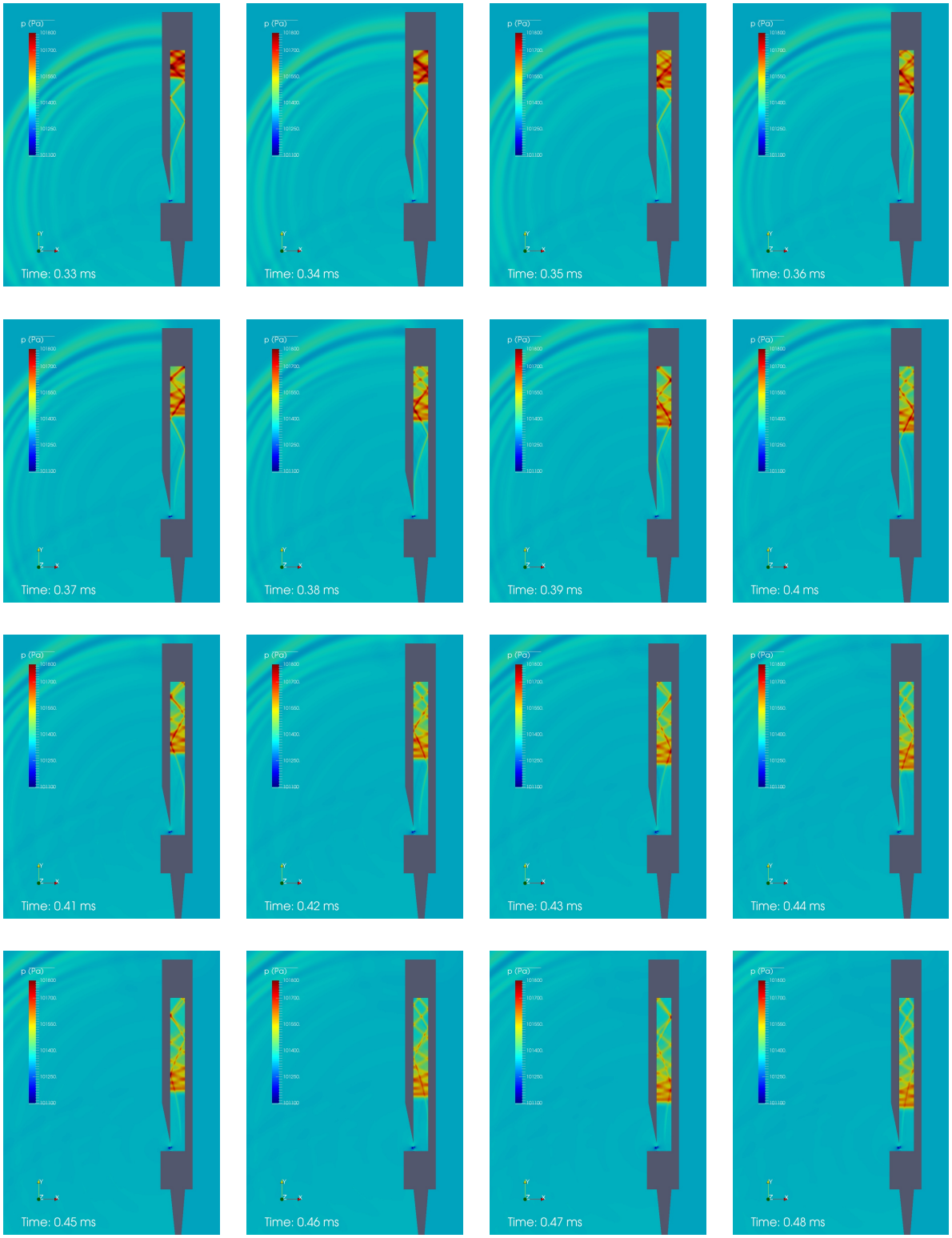

Figure 5.41: Visualization of the numerical simulation of the initial transient of an stopped wooden organ pipe. Color-coded is the pressure field at the period of time of 0.33 ms – 0.48 ms. Shown is the back-propagation of the initial major pressure fluctuation and the reflected (and at the resonators walls reflecting) transverse pressure fluctuations upstream.

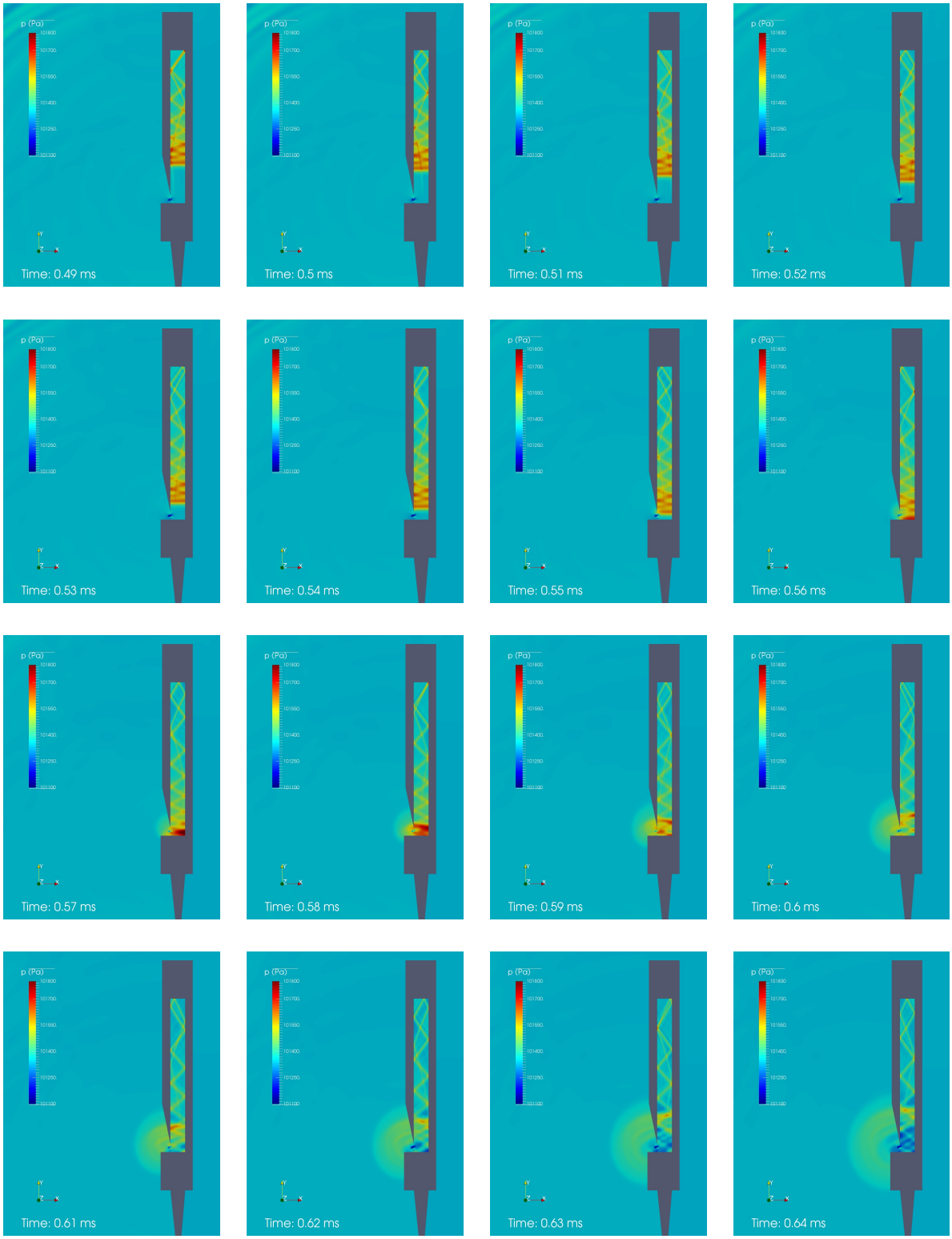

Figure 5.42: Visualization of the numerical simulation of the initial transient of an stopped wooden organ pipe. Color-coded is the pressure field at the period of time of 0.49 ms – 0.64 ms. Shown is the back-propagation of the initial major pressure fluctuation, its reflection at the lower end of the resonator and the radiation of a second wave into the free space.

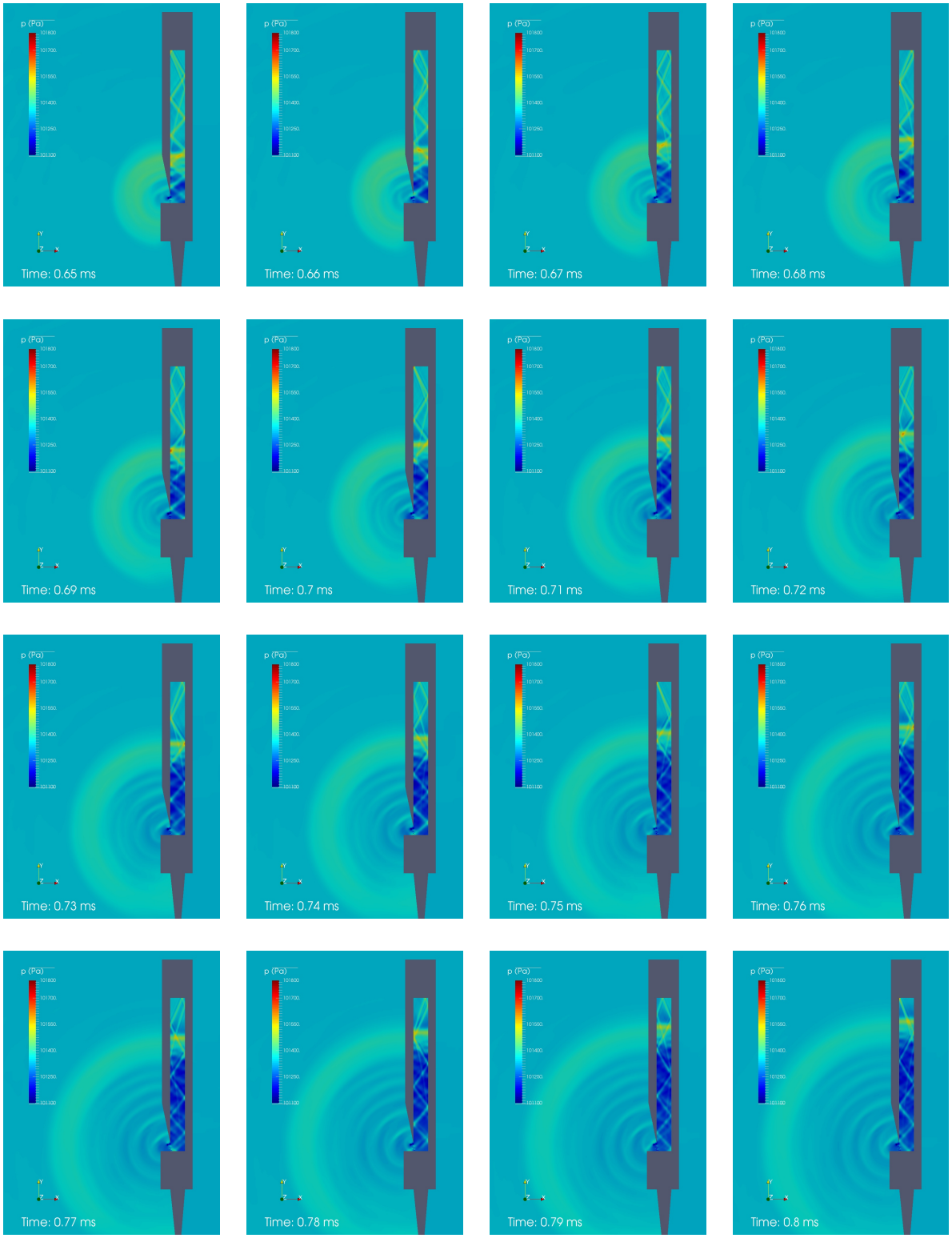

Figure 5.43: Visualization of the numerical simulation of the initial transient of an stopped wooden organ pipe. Color-coded is the pressure field at the period of time of 0.65 ms – 0.80 ms. Shown is the back-propagation of the initial major pressure fluctuation, its reflection at the lower end of the resonator and the radiation of a second wave into the free space.

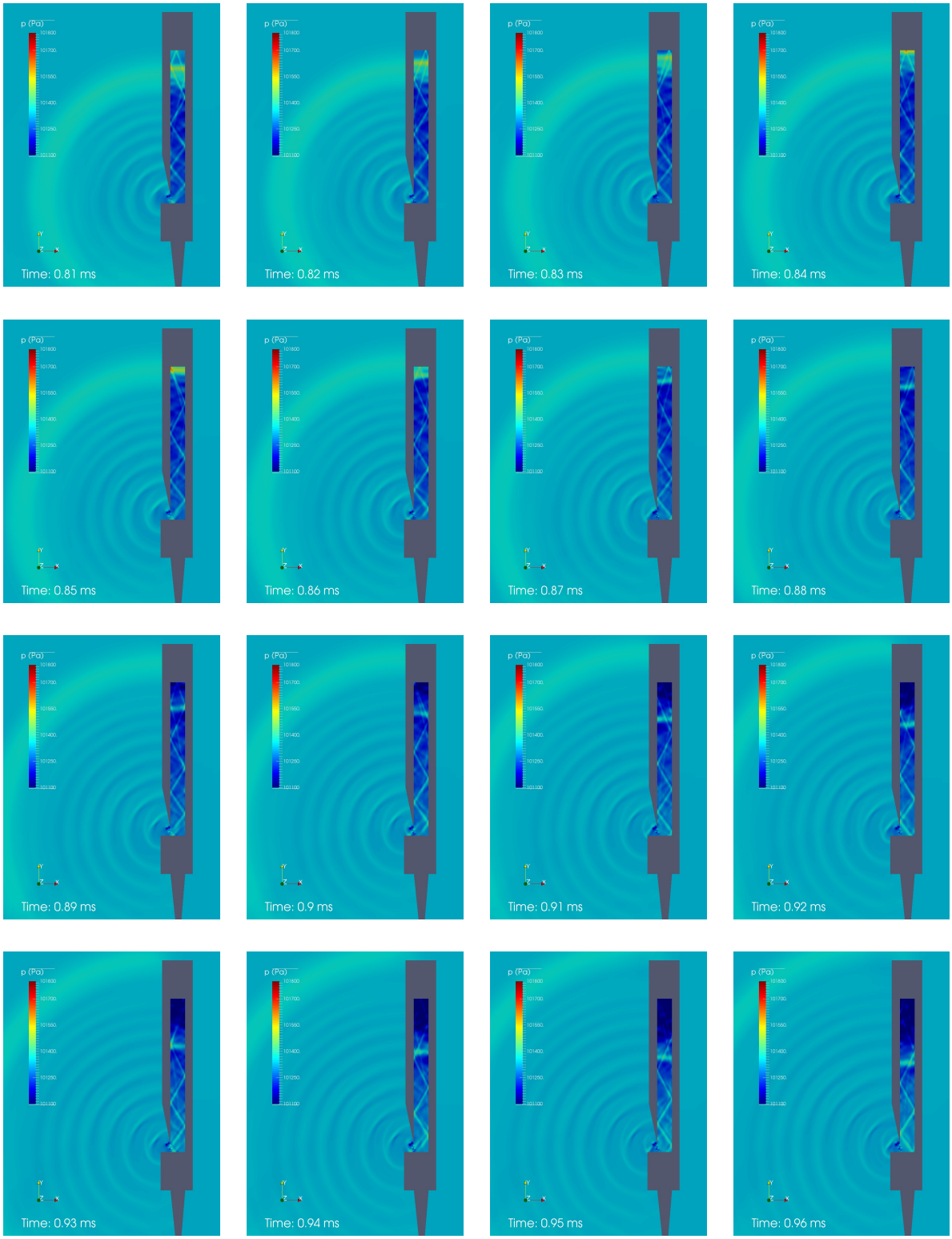

Figure 5.44: Visualization of the numerical simulation of the initial transient of an stopped wooden organ pipe. Color-coded is the pressure field at the period of time of 0.81 ms – 0.96 ms. Shown is the back-propagation of the initial major pressure fluctuation, its reflection at the lower end of the resonator and the radiation of a second wave into the free space.

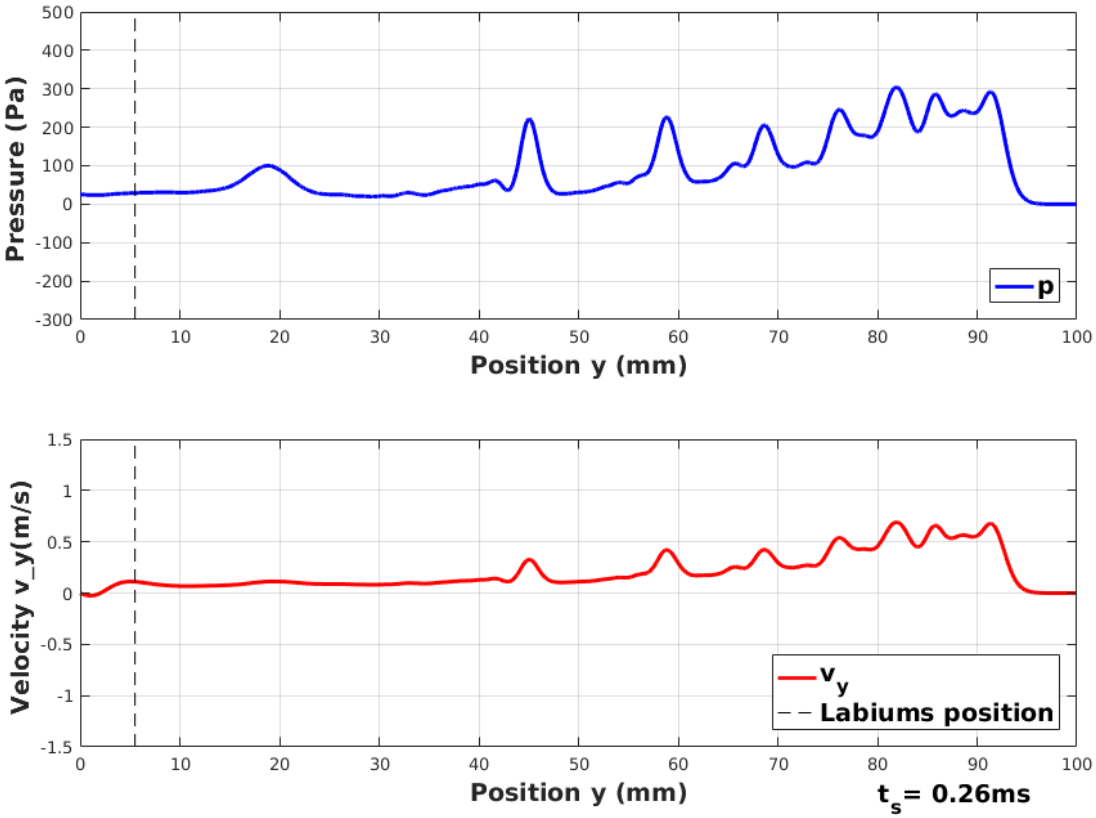

Figure 5.45: Initial wave front propagating in the resonator. Shown is the pressure p and the velocity component v_y at the time $t = 0.26\,\mathrm{ms}$.

watching the animations in the supplement. At the lower end of the resonator the primary pressure wave front reflects again. The high values of amplitude of the accumulated wave front basis induce high values of particle velocity. This can be interpreted as a sound source in the generator region. This is an important fact regarding the formation of the sound field which will be discussed in more detail in a minute. A fraction of the accumulated pressure wave escapes laterally through the instrument's mouth and radiates as a spherical sound wave into the free space. The main fraction of the initial pressure wave however propagates back in the resonator. Again, the reflections cause a doubling of the number of wave fronts caused by the width of the lower resonator.

The generation of the initial pressure waves that show shock wave characteristics is initially driven by the jet flow. The jet flow works on a much slower time scale ($U/c_{shocks} \approx 1 : 20$) than the named pressure wave fronts, which are trans-sonic waves as pointed out. The driving process is interrupted by the pressure field occurring in the slipstream of the primary pressure wave front who disturbs the jet laterally by its produced particle velocity. This leads to an outward deflection of the jet. The jet's lateral sensitivity has its own time scale, determined by particle velocity of the lateral acting sound pressure, the duration of the action and the inherent physical parameters of the jet itself, e.g. its flow velocity, its lateral thickness, its free propagation length, etc. The jet's lateral sensitivity to acoustic disturbances indicates that this property of the jet is crucial for sound generation! When looking at a jet, a distinction must be made between the flow properties and the lateral properties (the stability properties with

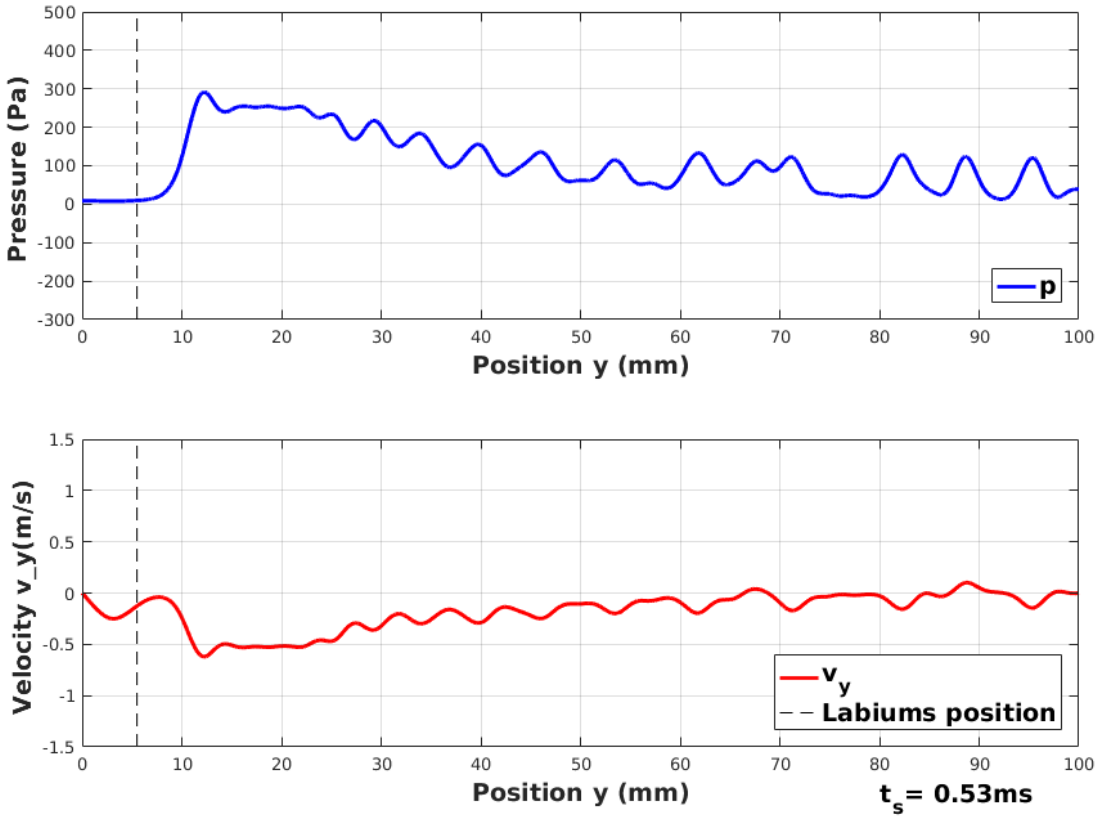

Figure 5.46: Initial wave front propagating in the resonator. Shown is the pressure p and the velocity component v_y at the time $t = 0.53\,\text{ms}$. Doubling of the pressure peak density in the slipstream of the primary pressure wave after reflection at the upper end of the resonator.

regard to lateral disturbances). Both properties possess different time scales.

The jet flow changes its direction to a path outwards the organ pipe, along the upper labium. With its change of direction the jet flow locks up the pressure field of the resonator's air volume from that of the free space. The observations suggest that the lock up is provided by the inherent dynamic pressure of the central jet flow. While the jet is displaced and the primary pressure wave front propagates back to the closed end, dissipation processes generate a sonic pressure field in the slipstream of the primary pressure wave front. The generated sound field in the resonator acts on the jet and vice versa. The pressure gradient between the free space and the air volume in the resonator supports the re-entering of the jet into the resonator, such that the jet continues triggering the air column's oscillation.

The visualizations of the numerical results have delivered first clues to solve the open questions regarding the complex mutual interaction between the flow field of the jet and its self-induced sound field in the resonator which is caused by dissipative initial pressure wave fronts that show shock wave characteristics. Now the dynamics of the pressure wave fronts propagating in the resonator will be examined in more detail.

To study the dynamics in the initial transient in more detail the propagation properties of the initial pressure wave fronts in the resonator are of special interest. The temporal development

of the pressure field at cross-section *cs_resonator* is depicted in Fig. 5.47. Each time step is separated by an offset of 500 Pa for the sake of clarity. The plots show the propagation of the primary pressure wave front followed by secondary pressure wave fronts in the slipstream which are caused by reflections at the inner walls of the resonator. The Figures 5.48 show the marked peaks of the pressure wave maximums which are used for the analysis. It also shows the fit curves of the spatial damping of the initial pressure wave maximums which is nonlinear. The accumulation of the secondary wave fronts lead to a stabilization of the amplitude of the primary wave front.

The velocity of the primary pressure wave front remains constant. The velocities of the secondary pressure wave fronts are higher than the velocity of the primary pressure wave front. Figure 5.49 shows the results of the analysis of the velocities of the pressure wave fronts observed. Matter of interest are the propagation velocities of the amplitude maximums of the pressure waves fronts. Two arguments can be given why for analysis the peaks of the pressure wave fronts are used. The first argument is that the addressed pressure wave fronts are coherent fluid mechanical structures which can be localized, distinguished and therefore be tracked by their main property, the amplitude maximum. The second argument is directly linked to the physical quantity one asks for. Tracking the velocity of the peaks of the pressure wave fronts ensures that one locks for the upper limit of the velocity of the quantity of interest, the propagating pressure fluctuation. Any dissipative property of the considered fluid mechanical coherent object would lead to slower velocities. Any accumulative property leads to a re-build of the primary amplitude maximum at the pressure wave front. This can be retraced by the reader by studying Fig. 5.47 where both the damping as well as the accumulation of the initial pressure wave fronts are shown, in particular the accumulation and the re-build of the primary pressure wave front at times $t = 0.13\,\mathrm{ms}$ to $t = 0.15\,\mathrm{ms}$.

The velocity of the primary pressure wave front is $c_{1.shock} = 363\,\mathrm{m/s}$ and thereby higher than the local speed of sound of $c_0 = 343\,\mathrm{m/s}$. This confirms the statement that the observed pressure wave front has shock wave characteristics. The mean velocities of the secondary pressure wave fronts are even faster with $c_{2,shock} = 408\,\mathrm{m/s}$ and $c_{3,shock} = 457\,\mathrm{m/s}$, but without overtaking the primary pressure wave front, so that one identifies the secondary wave fronts also as pressure wave fronts with shock wave characteristics. The named wave fronts show accumulation properties as well as dispersion and attenuation properties, which are discussed below. The numerical results are comparable with measurements of the velocities of amplitude maximums of the initial pressure wave fronts that propagate in comparable set-ups, cf. section 5.2.

Displayed in Fig. 5.47 is the propagation of the initial pressure wave front in the resonator of the simulated organ pipe. One recognizes a dispersion of the primary pressure wave front. The observed dispersion produces a significant spatial distributed basis, the slipstream of the pressure wave front. The spatially distributed basis indicates that parts of the shocks are damped to a slower velocity regime than the primary pressure wave front acts on. On the other hand the accumulation of the secondary pressure wave fronts re-build the amplitude of the primary pressure wave front. The results of the analysis of the propagation velocities of the peaks of the initial pressure wave fronts is shown in Figs. 5.48 and 5.49. One notices a nonlinear time development of the velocities of the secondary pressure wave fronts relative to the constant velocity of the primary pressure wave front peak at the beginning. Fits of the data give the following proportionalities: $(c_{1,shock} - c_{2,shock}) \sim t^{-0.365}$ and $(c_{1,shock} - c_{3,shock}) \sim t^{-2.518}$ of the damping. Although the damping, which is nonlinear, the velocities of the secondary wave fronts remain higher than the velocity of the primary wave front. This explains the accumulation of the wave fronts which leads to the maintenance of the primary pressure wave

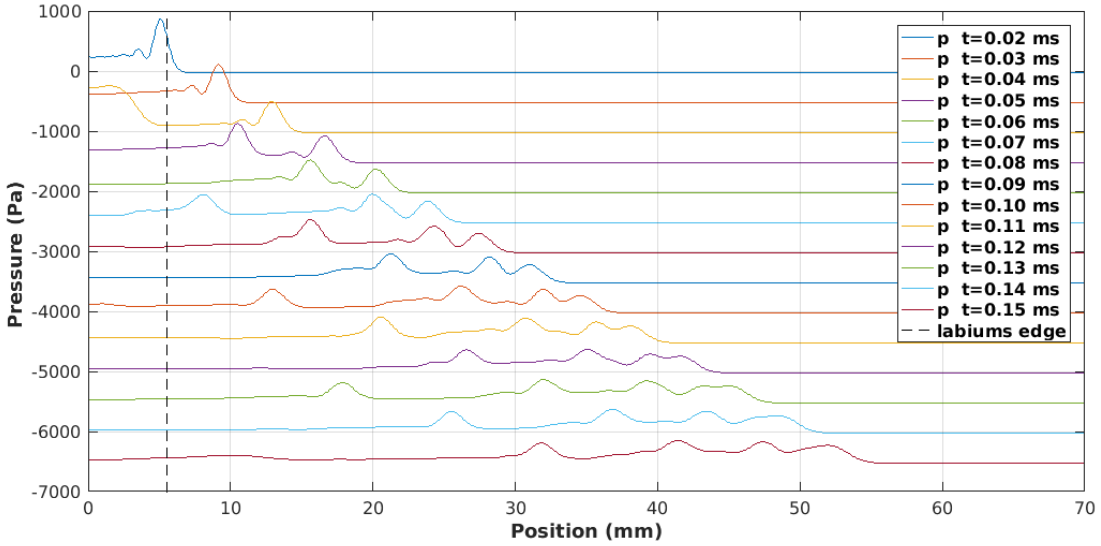

Figure 5.47: Propagation of the initial pressure wave fronts along the longitudinal axis of the resonator. Depicted are the data sampled at cross-section *cs_resonator*. The time steps are separated by an offset of 500 Pa. The dashed line marks the position of the upper labium's edge which determines the height of the cut-up of the organ pipe of 5.5 mm.

maximum. Responsible for the observed dispersion is internal friction. The trans-sonic pressure wave fronts propagate against the inherent viscous properties of the medium, which indicates a deceleration of the particles in the wave front. The deceleration leads to less particle velocities and less particle deflection. This is what energy transfer from trans-sonic into sonic time scales constitutes. In the absence of driving forces this process continues and energy is transferred into even slower times scales up to a complete dissipation [Kolmogorov (1941)] into the heat bath of the system. In the present case the primary pressure wave front is re-build by the accumulating secondary pressure wave fronts which propagate faster but also dissipate in time and space, such that an overtaking does not happen. The property of rebuilding a wave front's amplitude by accumulative processes without an overtaking can be interpreted as soliton characteristics. The details of this property are subject of current research. With this results and statements an important aspect of the dynamics in the initial transient is quantified.

Another aspect is the attenuation of the amplitudes of the initial pressure wave fronts. The amplitudes of the pressure wave fronts observed in the numerical simulation attenuate in the initial transient. This is depicted in Fig. 5.48. Plotted is the time development of the initial pressure wave fronts. The superimposed representation of the data allows to calculate the corresponding attenuation constants for each pressure wave front passing the cross-section *cs_resonator*. The data are fitted by the following power law fit-functions

$$fit_{1,shock}(y) = 2314 \cdot y^{-0.6082} \tag{5.10}$$
$$fit_{2,shock}(y) = 2124 \cdot y^{-0.5154} \tag{5.11}$$
$$fit_{3,shock}(y) = 1778 \cdot y^{-0.4424} \tag{5.12}$$

One recognizes that the attenuation of the amplitudes depends on the velocities of the peaks of the pressure wave fronts. The higher the velocity, the lower the attenuation exponent and

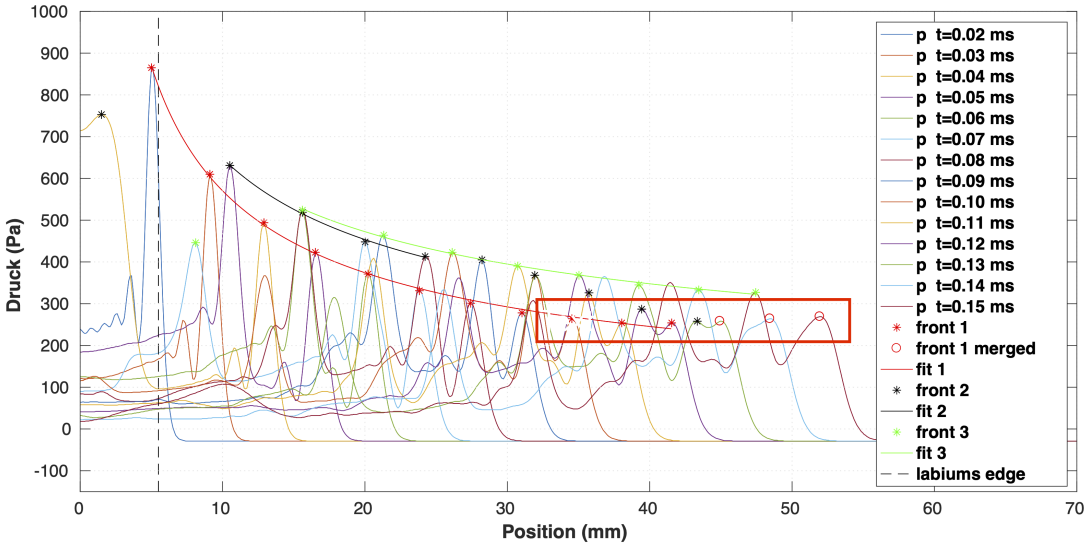

Figure 5.48: Attenuation of the initial pressure wave fronts in the resonator. Note that the amplitude of the primary wave front remains from about $t = 0.10\,\text{ms}$ ($y \approx 35\,\text{mm}$). This is marked by the red frame.

therefore the fewer the attenuation. As a result the waves have to accrue.

This is a further indication that the initial pressure waves have the character of a shock wave. The attenuation of the wave fronts amplitudes is nonlinear which is provided by the properties of the medium as well as of the properties of the resonator's walls, in particular their roughness. The wall properties of the organ pipe in the numerical simulation are modeled by an appropriate wall function, as mentioned in section 4.7. The analysis of the velocity of the peaks of the primary and the secondary initial wave fronts give propagation speeds slightly but significantly higher that the local speed of sound. The velocities are calculated by fitting the peak locations in time and space, cf. Fig. 5.48. Also shown are the differences of the wave front amplitudes which decay in time. While the primary wave front propagates with $c_{1,shock} = 363\,\text{m/s}$, the second wave front speed is $c_{2,shock} = 408\,\text{m/s}$. The third wave front is even faster with a speed of $c_{3,shock} = 457\,\text{m/s}$. It should be emphasized once again that on the one hand one observes an accumulation of the wave fronts and at the same time a damping of the amplitudes in space. Both effects are not mutually exclusive because one is temporal and the other one is spatial. The observations are discussed now.

5.3.1.3 Discussion

With extended visualization techniques more information about the dynamics in the initial transient are accessible. In this section the focus is on the formation of the sound field in the organ pipe's resonator. The time evolution of the pressure at cross-section *cs_resonator* is transferred into a color coded map depicted in Fig. 5.50. The time is on the x-axis, the length of the cross-section *cs_resonator* is on the y-axis, with the lower end of the resonator at $y = 0\,\text{mm}$ and the upper end at $y = 100\,\text{mm}$ which is closed. The introduced representation maps the pressure relative to the standard reference level of $p_{NHN} = 1013.25\,\text{hPa}$, which is color-coded green and labeled as $0\,\text{Pa}$. Depicted is the time interval $0 - 2.5\,\text{ms}$. The propagation of the initial pressure

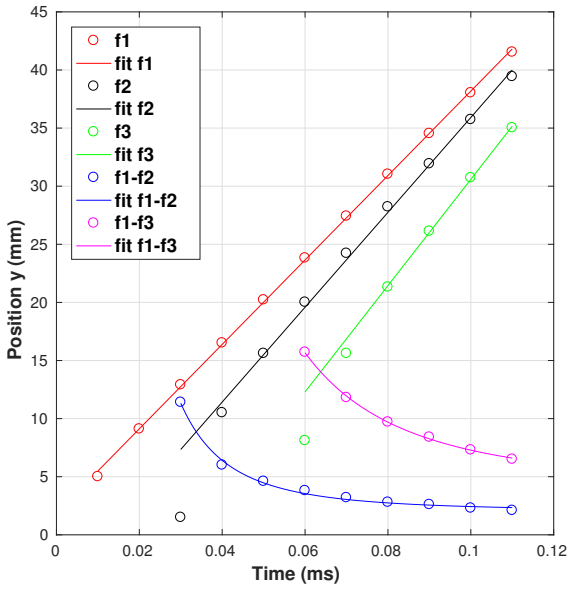

Figure 5.49: Data from the numerical simulation. Depicted are the velocities of the peaks of the initial pressure wave fronts which propagate in the resonator of the simulated organ pipe in the initial transient. Marked by red circles is the propagation of the maximum of the primary pressure wave front along the cross-section *cs_resonator*. The red line fits the data. The slope gives the velocity of the peak of the primary pressure wave front which is $c_{1,shock} = 363\,\mathrm{m/s}$. Labeled by black circles are the data of the second pressure wave front. Its linear fit gives $c_{2,shock} = 408\,\mathrm{m/s}$. Not taken into account are the data points at the very beginning, where the velocity development is nonlinear. The data of the third pressure wave front are labeled green. The fit of the data gives $c_{3,shock} = 457\,\mathrm{m/s}$. The circles and curves marked by the blue and the pink lines are the differences between the velocities of the secondary and the velocity of the primary wave front maximums. In fact the secondary pressure wave front as well as the third one get damped in a nonlinear way relative to the primary wave, but they are still fast enough to accumulate and rebuild the primary pressure wave front.

wave front can be identified as a linear path, colored initially red. The secondary shocks occur as red dots because they just pass the cross-section at their zigzag course in the resonator. The initial pressure wave front, which is called here the primary pressure wave front, reflects at the closed end of the resonator and propagates back with constant velocity. Note that the primary pressure wave front does not change its phase during this reflection. This is what is expected for a trans-sonic pressure wave because of the boundary condition – the closed end of the resonator. Also the secondary shocks reflect at the closed end without a phase change. Because of their higher propagation velocities ($c_{2,3,shock} > c_{1,shock}$) they accrue and reinforce the primary pressure wave front. The accumulation of the secondary wave fronts can also be read from the bow-like distributed dots in the slipstream of the primary wave front in the period of time $0 - 0.5\,\mathrm{ms}$. Note, that the dots have doubled after the reflection at the closed end of the resonator.

The lower end of the resonator is partly open at the mouth and therefore, from an acoustical point of view, one would expect a reflection of sound waves associated with a change of phase of $\delta\varphi = \pi$, which would imply negative amplitudes of sound pressure. The observation in the initial time duration $0.5 - 1.25\,\mathrm{ms}$ is that the primary pressure wave front reflects at the lower

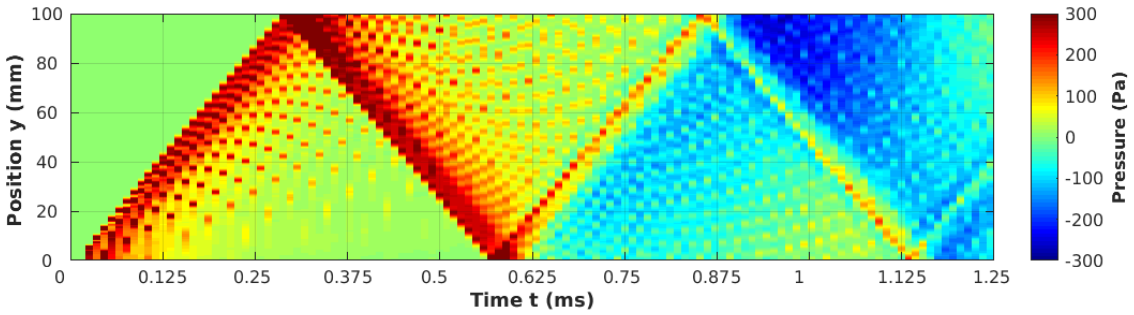

Figure 5.50: Initial pressure fluctuation propagation and reflections in the resonator. Shown is the period of time of 0 ms - 1.25 ms.

end of the resonator not changing its phase nor its absolute value of constant velocity! This indicates that the primary pressure wave front does not see the lower end as an open end, but as a closed end. After the reflection at the lower end the primary pressure wave front maintains its impulse-like characteristics.

Behind of this wave front the situation changes substantially. One recognizes a pressure field with negative values relative to the reference pressure occurring behind the back-propagating primary pressure wave front. This area is called the slipstream. This indicates that the slipstream now reflects with a phase change of $\delta\phi = \pi$ and 'recognize' the open end of the mouth. That implies that the slipstream has become sound pressure characteristics. To explain this, one has to focus on the time scales of the different aeroacoustic objects that constitute the initial pressure field in the resonator. The fractions of the pressure field acting on the fastest time scale are the waves that propagate faster than the speed of sound ($c_{shocks} > c_0$). They are trans-sonic coherent objects. Their propagation velocities have impulse-like characteristics that implies a strong directivity. It is already mentioned that they can accumulate but at the same time they also show dissipation because they work against the compressibility properties of the medium. Dissipation is also characterized by the fact that parts of the initial wave front disperse into the next slower regime generating the slipstream. After the second reflection the slipstream dissipates into the next slower time scale ($c_0 = 343\,\mathrm{m/s}$) and generates the initial sound field. This is the origin of the initial sound field in the instrument's resonator! The speed of sound depends on temperature, density, humidity of the media. The negative pressure (negative with respect to $p_0 = 1013.25\,\mathrm{Pa}$) of the slipstream propagates to the closed end and reflects without a change of phase.

The further development is shown in Fig. 5.51. Looking at the initial sound field generated by the slipstream one recognizes the formation of the fundamental oscillation in the resonator in the period of time from 0.8 ms to 2 ms. Oscillations with the fundamental are characterized by an anti-knot at the resonator's closed end and a knot at the lower end corresponding to $1/4\lambda$. Note that a phase difference occur between the primary pressure wave front and its slipstream caused by the different velocity regimes they act on. The phase difference grows from one reflection to the next. This leads to a superposition of the sound field already generated by the previous slipstream and the following one. The superposition caused by the repeated reflections leads to an increase of the peak density in the resonator, each peak corresponds to a trans-sonic wave front which dissipates into the sound field. The doubling of the peaks at the first six reflection events is shown in Fig. 5.52.

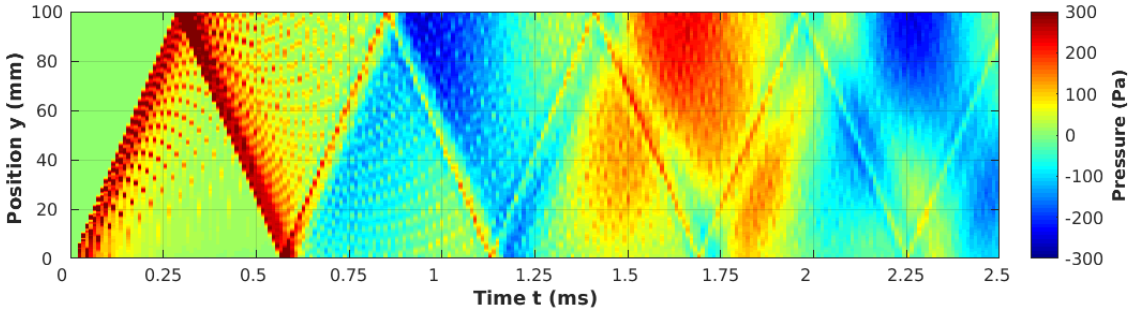

Figure 5.51: Initial pressure wave propagation and reflections in the resonator. The data are sampled at the cross-section *cs_resonator* which is represented as the y-axis. Shown is the spatio-temporal evolution of the pressure in the period of time $0\,ms$ - $2.5\,ms$. The pressure is color-coded in the interval $\pm 300\,\text{Pa}$ relative to the standard reference level $p_{NHN} = 1013.25\,\text{hPa}$ which is colored by green and labeled as $0\,\text{Pa}$.

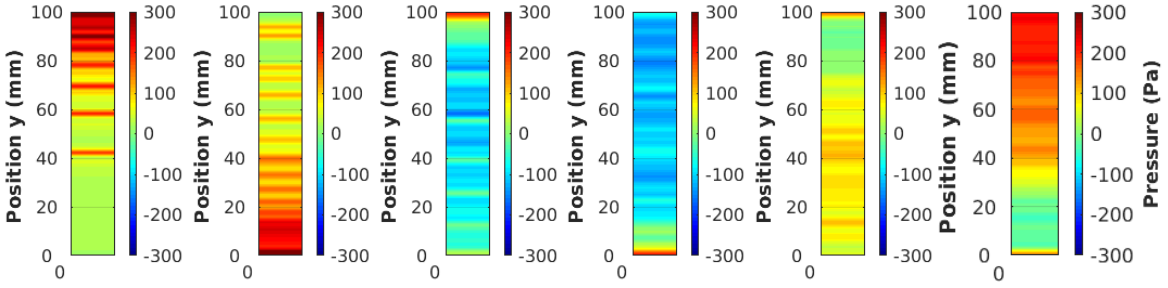

a) $t = 0.29\,\text{ms}$ **b)** $t = 0.57\,\text{ms}$ **c)** $t = 0.85\,\text{ms}$ **d)** $t = 1.13\,\text{ms}$ **e)** $t = 1.41\,\text{ms}$ **f)** $t = 1.69\,\text{ms}$

Figure 5.52: Sample set *cs_resonator* color-coded at the relevant time steps of reflections of the initial pressure fluctuations at resonators ends. The first six times of reflection are at $t_{R1} = 0.29\,\text{ms}, t_{R2} = 0.57\,\text{ms}, t_{R3} = 0.85\,\text{ms}, t_{R4} = 1.13\,\text{ms}, t_{R5} = 1.41\,\text{ms}, t_{R6} = 1.69\,\text{ms}$

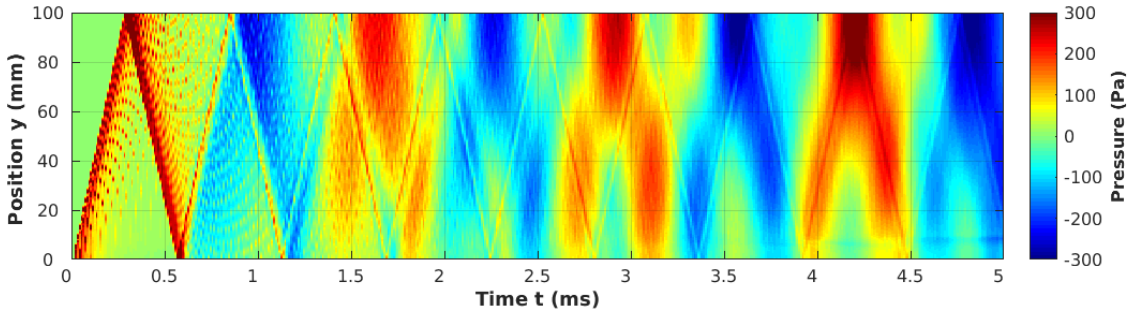

Figure 5.53: Initial pressure fluctuation propagation and reflections in the resonator. Shown is the period of time of $0\,\text{ms}$ - $5\,\text{ms}$.

One may ask when the primary pressure wave and the generated sound field are in an anti-phase relationship to each other, and when the progressive phase shift leads to an in-phase relationship. Related to this is the question what will happen at these times? The answer can be given

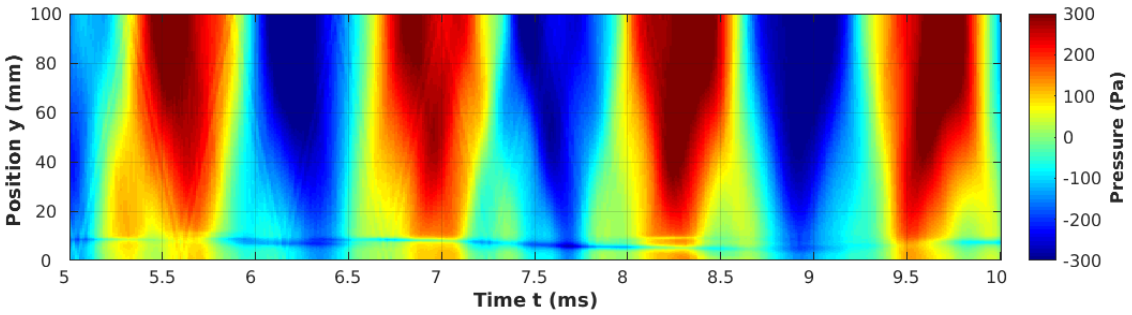

Figure 5.54: Initial Pressure wave propagation in the resonator. Color-coded is the pressure sampled at the cross-section *cs_resonator*. Shown is the period of time of 5 ms - 10 ms.

by looking at the color-coded sequence depicted in Fig. 5.53. At $t = 2.25$ ms the initial shock and the slipstream becomes close to the anti-phase relationship. The shock reflects at the lower end while the sound field has its maximal negative amplitude at the closed end of the resonator. Here the superposition leads to the generation of a kind of second harmonic oscillation. At the next reflection at $t = 2.55$ ms the anti-phase relationship is more or less perfect and the second harmonic-like deflection continues to establish. At time $t = 4.2$ ms both regimes become an in-phase relationship, which leads to an amplification of the sound pressure at the closed end. The in-phase relationship between the shock and the sound field promotes the energy transfer from the shock wave to the sound field significantly, in particular in its fundamental oscillation! Because of the fact that the sound field acts on a slower time scale the amplification holds on while the phase difference grow further again. At about $t = 5.6$ ms the phases again become anti-phase which promotes the second harmonic oscillation. The Interplay continues until in the next in-phase relation at $t = 8.4$ ms where the shock dissipates completely into the sound field amplifying the fundamental, cf. Fig. 5.54. In the following, the acoustic oscillations are maintained. The system oscillates in the operation mode with the fundamental frequency.

In summary, we learn the following from this numerical experiment

- The initial transient can be traced with high accuracy using numerical simulations.
- The SPL spectrum of the resonator sampled data shows the fundamental and the odd higher harmonics in very good agreement with acoustic measurements.
- In the initial transient trans-sonic pressure waves are formed, which can be characterized as shock waves.
- The secondary shock waves accumulate and stabilize the primary shock wave. The shock waves have a directivity that means that the reflections at both ends of the resonator occur without a phase jump. Due to the width of the resonator's ends, the reflections cause phase shifts in the shocks and thus a doubling of the peak density in the resonator after each reflection.
- The shock waves dissipate in space and time and form a wake called slipstream.
- The slipstream has sonic properties (act on a slower time scale, compared with the shocks).
- The slipstream forms the initial sound source – the sound field in the resonator.

- The generated sound field is able to disturb the constituting jet laterally, which leads to a change in direction of the jet.
- Due to the different time scales on which the shocks and their slipstreams act, there are complicated superpositions of shocks and slipstreams as well as increasing phase differences between the primary shock wave and the sound field.
- At times when both coherent objects have an anti-phase relationship, the system temporarily forms oscillations of the second harmonic (and higher harmonics).
- If the primary pressure wave and the sound field are in-phase, the energy transfer is at its maximum, such that after two in-phase relationships, the primary pressure wave is completely dissipated into the sound field. The in-phase relation promotes the fundamental.
- After 10 ms the transient process is complete and the instrument oscillates in operation mode.

5.3.2 The Jet of the Organ Pipe

In this section the focus is on the turbulent coherent structures that constitute in the initial transient of the organ pipe. Firstly the formation and the dynamics of the jet of the organ pipe and its contribution to the sound generation is taken into account.

The jet flow of the organ pipe is a turbulent coherent structure that acts on slow time scales compared with the sound field and the trans-sonic shock waves. ($v_{jet} < c_0 < c_{shock}$). The mean flow velocity of the present numerical set-up is determined by the initial condition at the inlet which was chosen as uniform (hat-profile): $\boldsymbol{u}(x, y, z, t_0) = 18\,\mathrm{m/s} \cdot \mathbf{e_y} = u_y$. This do not mean that the local velocity inside the jet flow is restricted to this value. Without disturbances the time scale of the jet flow is mainly determined by inherent inertial and viscous forces. But, as already pointed out, the jet has also a lateral sensitivity due to acoustical disturbances. In general, one can distinguish internal and external disturbances, due to the origin of the disturbing force (or element). However, it makes sense to define what is to be considered as internal or as external in the individual case. In this study, external disturbances are considered to be forces that are not caused by the instrument itself. This section focuses on internal disturbances of the jet. These are disturbances of the jet, which caused by forces in the resonator, those produced by the jet itself and disturbances caused by geometrical constraints.

The lower resonator region of the organ pipe is bounded at three sides by walls and by the upper labium. It is open at the mouth's side, cf. Fig. 5.37. The height of the cut-up determines the free propagation length of the jet and therefore its fluid dynamical stability. The longer the free propagation length the larger the effects induced by the jet's inherent instabilities [Chandrasekhar (1961)]. Before we dive into the discussion, let's briefly make some comments about jets in aerophones.

The jet is the most fascinating, the most important and the most complicated coherent fluid mechanical structure of the aerophones discussed in this study. The jet arises and constitutes in the initial transient. Physically speaking, the jet is a coherent flow field with a higher momentum in comparison to its ambient medium. If the medium of the jet and the ambient medium are of the same gas and similar density, the radial velocity gradient of the jet flow field and the ambient medium generates shear layers that lead to an entrainment of the ambient medium by the jet. The shear layers induce vortices that rotate clockwise and anti-clockwise with respect to the direction of the addressed velocity gradient inside the shear layers. This is proven

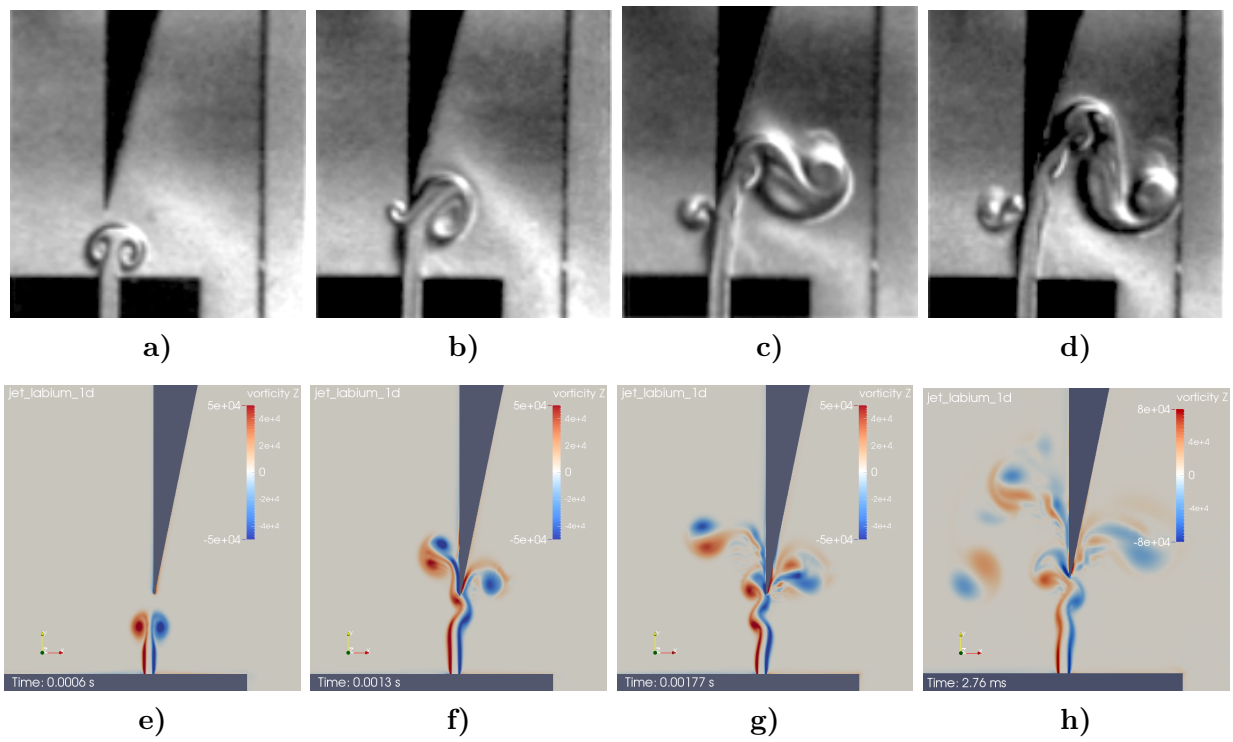

Figure 5.55: Initial transient of a jet of a flue organ pipe. a)-d) Experimental results done by Verge, Fabre, Mahu et al. using the Schlieren technique. e)-f) Numerical simulation of the jet on an organ pipe. Shown are details visualizations of a numerical simulation set-up of the initial transient of a resonator-less organ pipe with an evolving jet at four different time steps: $t = 0.6\,\text{ms}$, $t = 1.3\,\text{ms}$, $t = 1.77\,\text{ms}$ and $t = 2.76\,\text{ms}$. Color-coded is the vorticity component in z-direction. Blue indicates clockwise rotational, red indicates anti-clockwise rotational.

in an excellent way by experiments, such as those carried out by Verge, Fabre, Mahu et al. [Verge, Fabre, Mahu et al. (1994)], who were able to impressively visualize the dynamics of the jet in a flue organ pipe using the Schlieren technique. A sequence of their experimental results are illustrated in Figures 5.55a, 5.55b, 5.55c and 5.55d. Corresponding numerical simulations done by the author trace the experimental results. This is shown for comparison in Figures 5.55e, 5.55f, 5.55g and 5.55h.

The two initial vortices at the jet's front are formed by velocity gradients that occur between the stagnant air volume of the surrounding medium and the central velocity inside the jet. The central velocity of the jet causes a dynamic pressure, cf. Eq.3.191 in the jet which tends to attract the shear layers. On the other side the velocity gradient in the jet's shear layers in combination with the central jet flow produces vortices with a low pressure core. The low pressure vortex cores also tend to attract the central jet flow, but locally, because their are local low pressure spots that move in the shear layer. As a result inbetwenn the two attractive pressure zones – the central jet and vortices of the sear layers – the jet becomes unstable. Fig. 5.55e shows the propagating jet with its frontal vortices and the waist in between caused by the dynamic pressure. This leads to an accelerated isentropic[6] nozzle flow in the center of the jet that promotes the propagation of the coherent structure into the mouth region. The propagation of the jet is characterized by an exponential increase of small disturbances in the shear layers that cause the jet to be disturbed perpendicular to its main flow direction. The shear layers and thus their influence on the jet increase downstream if the damping from the viscosity of the

[6]Isentropic processes are idealized thermodynamic processes that are adiabatic as well as reversible.

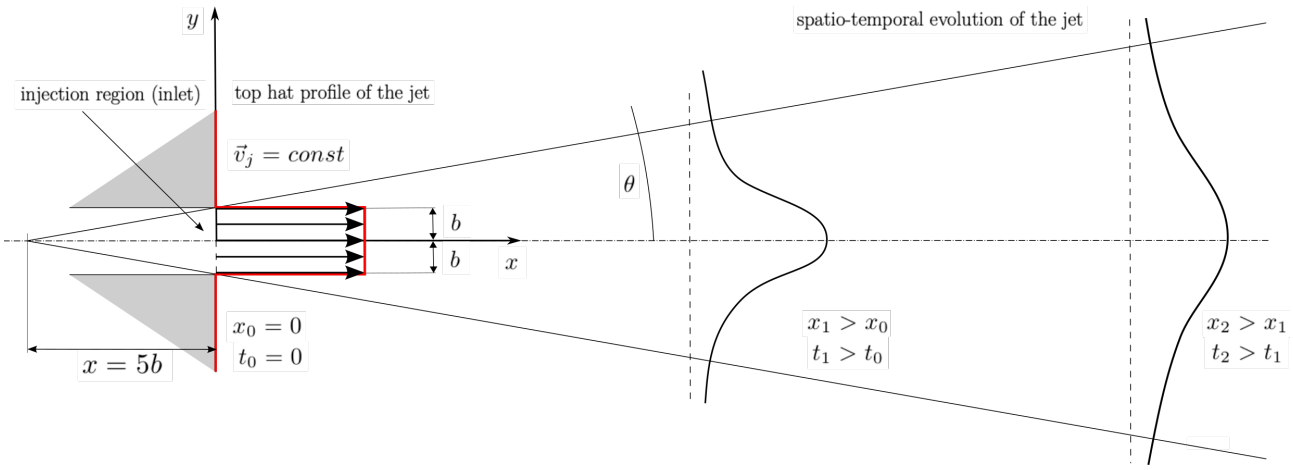

Figure 5.56: Schematic picture of the jet with a hat profile assumed as the initial condition of the velocity at the orifice. In numerical set-ups the orifice is often called the inlet. The initial velocity of the jet is $\vec{v}_{jet} = const$. Half the width of the orifice is denoted by b. Over time, the hat profile becomes a bell-shaped profile. The angle θ is the opening angle of the jet. The illustration is not a true-to-scale representation.

medium is not sufficient to allow the disturbance to subside [Tollmien (1935)]. This leads to the so-called Kelvin-Helmholtz instability (KH-instability) [Chandrasekhar (1961)] in the shear layers of the jet. The progressive entrainment of the propagating jet and the KH-instabilities lead to the formation of turbulent viscose mixing layers that grow both, into the jet and into the ambient medium, with the result that the whole flow becomes turbulent.

As early as 1894 Rayleigh showed that two layers moving against each other with velocities $\pm V/2$ become unstable due to the resulting shear flows. The instabilities arise because the velocity profile has turning points (1st Rayleigh theorem, Tollmien theorem). According to [Rayleigh (1896)], the disturbances grow with a law

$$h_{disturb} = \exp(\pm \mu x) \tag{5.13}$$

with the growth parameter of the disturbance $\pm\mu$. The two signs indicate that the influence of the shear layers can have a destabilizing (+) but also a stabilizing (-) effect.

Rayleigh gave two different types of disturbances, the sinusoidal and the varicose disturbance (Figures 5.57a and 5.57b). The propagation velocities u of the disturbances result from

$$u_{sinuous} = \frac{V}{1 + \cosh kb} \quad \text{and} \quad u_{varicose} = \frac{V}{1 + \tanh kb} \tag{5.14}$$

The growth parameters of the disturbances are written as

$$\mu_{sinuous} = k(\coth kb)^{1/2} \quad \text{and} \quad \mu_{varicose} = k(\tanh kb)^{1/2} \tag{5.15}$$

Here, b is half the width of the orifice, $k = 2\pi/\lambda$ the wavenumber of the perturbation. For large wavelengths (small wave numbers k) the terms tend towards zero. For small wavelengths, the terms become large. If the viscosity of the medium is taken into account, then according to [Bickley (1937)] for the velocity of a laminar jet with an infinitesimal initial width directly at the orifice ($x = 0$)

$$V(x,y) = a \cdot \operatorname{sech}^2\left(\frac{y}{b}\right) \tag{5.16}$$

The profile of the jet can be approximated with this equation. This is the free jet model. We get for the parameters

$$a = 3 \cdot 10^{-5}\left(\frac{K^2}{\nu x}\right)^{1.3} \tag{5.17}$$

and the local half-width of the jet b of

$$b = 700 \cdot \left(\frac{\nu^2}{K}\right)^{1/3} x^{2/3} \tag{5.18}$$

with ν the kinematic viscosity ($\nu_{air} \approx 1.5 \cdot 10^{-5}\,\mathrm{m^2 s^{-1}}$) and K is the flow integral, which corresponds to the quotient of the total momentum flow in the jet M and the density ρ. M is constant over all vertical cross-sections along the jet.

$$M = \rho K = \rho \int_{-\infty}^{+\infty} V^2 dy \tag{5.19}$$

From Eq. 5.16 one can see that the profile of the model jet assumes a bell-shaped profile, which decays in the x-direction and widens in the y-direction. The local latitude b of the jet increases $\sim x^{2/3}$. The central velocity of the profile decays $\sim x^{-1.3}$.

Figure 5.56 illustrates the model of the free jet with a hat profile as initial condition of its velocity field. Of cause, in real situations the initial profile is much more complex, it decreases towards the walls in the injection region (windway) caused by wall friction forces.

The jet is sensible with respect to external forces. In compressible media like air the jet is in particular sensible to sound waves[7]. Also geometrical obstacles, edges and wedges like the labium of a lingual organ pipe can influence the dynamics of jet. In such cases the concept of the free jet is no longer valid. Figures 5.55f, 5.55g and 5.55h show a jet which gets disturbed by a labium. The KH-instabilities and the disturbance caused by the labium produce a system of spatio-temporal alternating shear layer vortices. We will discuss the causes of the alternating dynamics further below. Such an alternating coherent turbulent structure is called the *oscillating jet*. Lord Rayleigh postulated two different types of jet disturbances, the sinusoidal and the varicose disturbance, cf. Fig. 5.57 We will see that the alternations of the jet, which is identical with the sinusoidal mode of the jet is crucial for the stable sound generation.

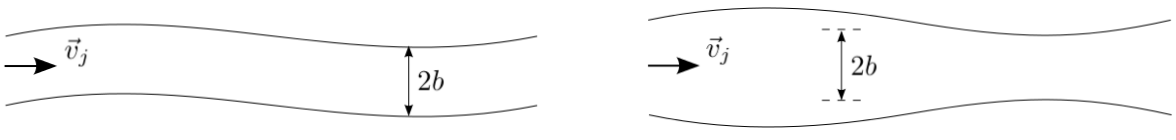

a) **b)**

Figure 5.57: Schematic representation of the two perturbations of a jet according to Rayleigh: a) sinusoidal disturbance, b) the varicose disturbance.

[7]The jet is also sensitive with respect to disturbances caused by trans-sonic and supersonic waves, depend on the angle of attack to the mean flow of the jet as well as of the time of impact.

The initial velocity profile $v(y, t = 0)$ of the jet at the orifice is assumed to be a top hat profile. The medium into which this profile flows is assumed to be at rest. This initial configuration can be written by

$$v(y,0) = \begin{cases} const. & -b \leq y \leq b \\ \\ 0 & else. \end{cases} \tag{5.20}$$

where b is half the width of the orifice. The profile of the initial velocity at the orifice $v(y, 0)$ changes over time with increasing propagation length x approximately into a bell shaped flow profile, cf. Fig.: 5.56.

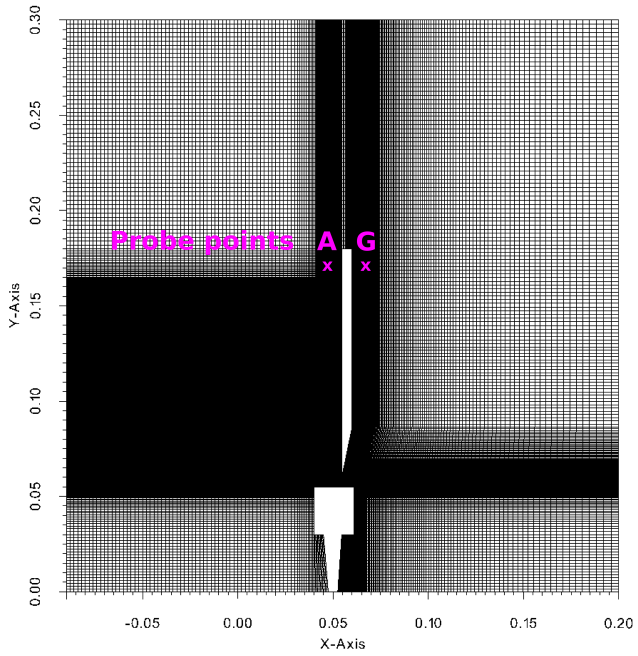

Figure 5.58: Positions ($X \times Y \times Z$) of the probe points A (49.8 151 0) and G (64.8 151 0) in millimeter in the mesh.

The observation in the previous section was that the fast primary pressure wave do not disturb the jet significantly. One reason is that the jet is not yet constituted when the initial shock propagate and reflect for the first time ($t = 0 - 0.6\,\text{ms}$). The second reason is the shock wave characteristics, namely its directivity, represented by the k-vector of the primary pressure wave front which is directed along the longitudinal axis of resonator and not lateral to the jet flow, cf. 5.37. The third reason is that the shocks are very thin structures, which causes a small time of impact ($t_{impact} < 5-10\,\mu\text{s}$). The slipstream of the primary pressure wave front is not trans-sonic but sonic. Consequently the slipstream has no directivity[8] and can pass the open mouth. The slipstream is able to deflect the jet while propagating through the cut-up into the free space. In addition, the emitted sound wave generated by the slipstream is a spatially extensive object compared with the cross-section of the jet and therefore it affects the jet over a longer period of time compared with impluse-like shocks. The time of impact is about $t_{impact} \approx 70 - 80\,\mu\text{s}$. Due to its extension the sound wave simultaneously acts on the whole propagation lengths of the jet in the cut-up region. This can be studied in detail in the animations of the initial transient

[8]In isotropic media, a sound wave, starting from a point source, propagates equally in all directions, if no obstacles lead to diffraction or reflection.

of the organ pipe in the supplement.

We now want to study what influence the labium has on the dynamics of the jet. For this we modify our numerical experiment by removing the resonator tube of the organ pipe and only keeping the labium as a geometric perturbation of the jet flow. The modified set-up is shown in Fig. 5.58. On either side of the remaining geometry sample points are set and time series are extracted. Figure 5.59a shows the initial process and the temporal evolution of the signals sampled at the probe points A and G in the period of time of $0-16$ ms. In the first millisecond the initial shock passes the probe points. The signals in this period of time are in-phase at both sides. This changes dramatically for $t > 1$ ms. The system switches to periodic oscillations which lead to an anti-phase relationship at the sample points A and G. The oscillations are stable but the frequency switches from time to time from about 3 kHz to about 1.5 kHz, which indicates some kind of harmonic behavior related with the position of the labium. Accordingly the SPL-spectra of the time series at the probe points A and G show peaks at about 3 kHz, cf. Fig. 5.59b.

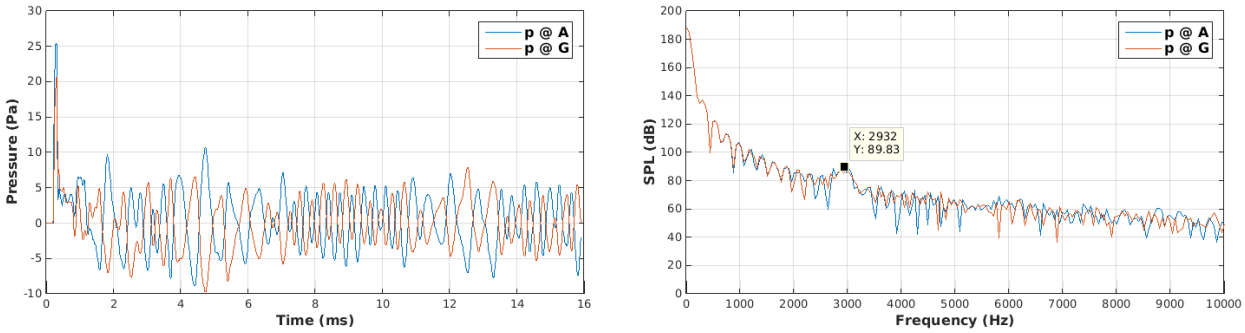

a) b)

Figure 5.59: (a) Signals of pressure at probe points A (blue) and G (red). After the run time 1 ms the signals start to oscillate in anti-phase. b) SPL spectra of the sampled signals of pressure at probe points A and G. In the noisy spectra one peak of ca. 90 dB at a frequency of ca. 3 kHz can be observed.

5.3.2.1 Turbulent Kinetic Energy

The advantage of numerical simulations is that all relevant physical quantities are accessible at any point in the numerical space. An important quantity to recognize and describe turbulent structures is the turbulent kinetic energy. Physically speaking, the turbulent kinetic energy is characterized by the root-mean-squared velocity fluctuations. The turbulent kinetic energy is defined by

$$k = \frac{1}{2}\overline{u_i' u_i'} \quad i = 1, 2, 3 \tag{5.21}$$

where u_i' is the fluctuation part of the decomposition of the velocity vector components $u_i = \overline{u_i} + u_i'$. The quantity $\overline{u_i}$ is the mean part of the velocity vector components. In Eq: (5.21) the Einstein notation is used. Local fluctuations in the velocity field are exactly what vortices and jets are currently determine.

To take a closer look to the dynamic of the jet and the turbulent kinetic energy we sampled 10 equidistant cross-sections 0.5 mm apart, lateral to the jet flow in the cut-up region with

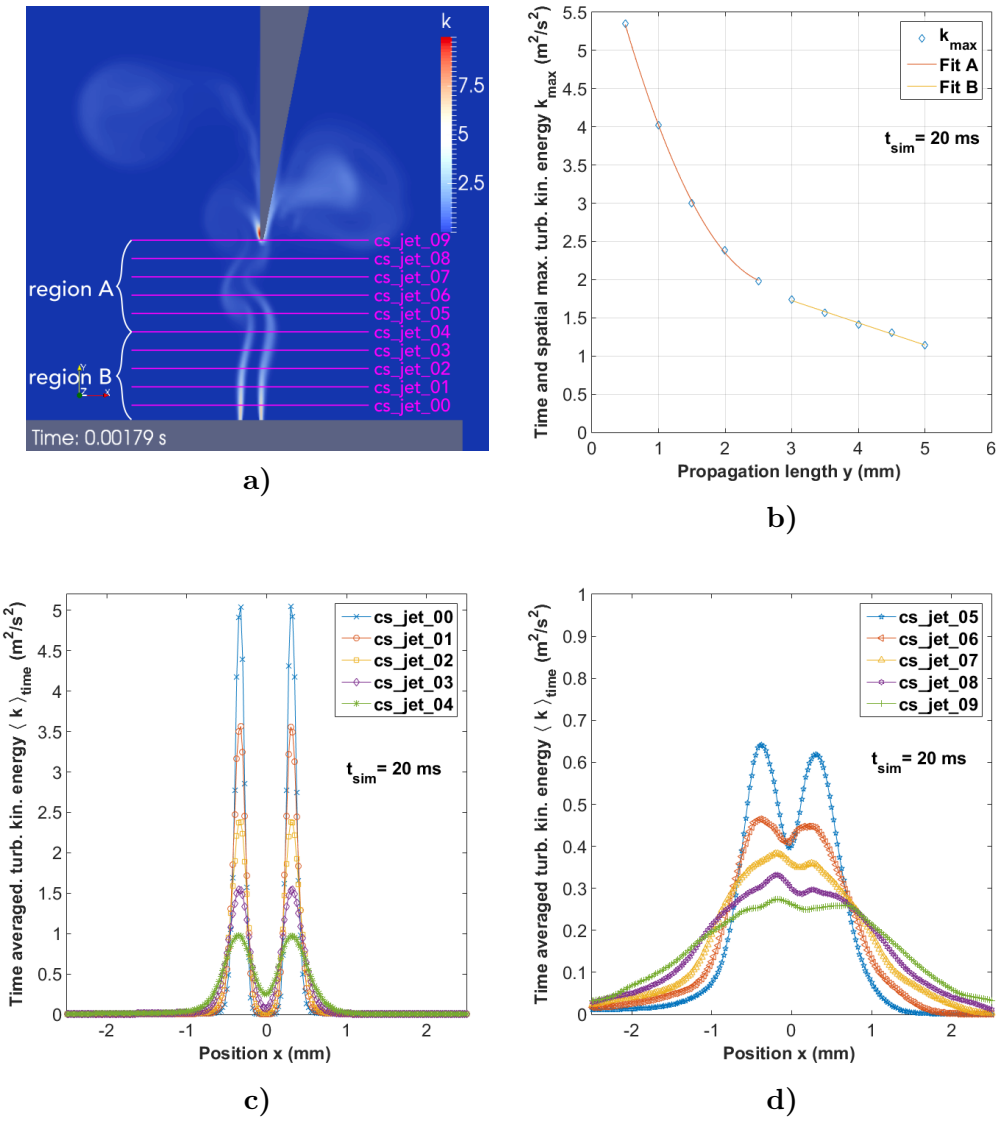

Figure 5.60: a) Cross-sections *cs_jet_00* - *cs_jet_09* in the cut-up region of the organ pipe without a resonator tube. The length of each cross-section is $x_{cs} = 18.6\,\text{mm}$ with 186 sample points which corresponds to a spatial resolution of $\delta x = 0.1\,\text{mm}$. b) The propagation of the jet can be split into two regions, the region A where the decay of the turbulent kinetic energy maximums is inverse proportional to the square of the propagation length and the region B where decay is negative linear with the propagation length. c) The spatio-temporal averaged maximal turbulent kinetic energy $\langle k_{max} \rangle_{t,sp}$ of the jet profile at the cross-sections *cs_jet_00* - *cs_jet_04* (region A). d) The corresponding jet profiles at the cross-sections *cs_jet_05* - *cs_jet_09* (region B). The average time is $t_{sim} = 20\,\text{ms}$, the spatial average is taken over the length of the particular cross-section.

a spatial resolution of 0.1 mm, cf. Fig. 5.60a. The visualization shows the turbulent kinetic energy in the cut-up region at time $t = 1.79\,\text{ms}$. The two shear layers of the jet and other vortex structures to the left and right of the labium are clearly visible. At the tip of the labium one can see high values of turbulent kinetic energy, indicating high fluctuations in the velocity field. One also finds that the amplitudes of the turbulent kinetic energy in the shear layers decrease with propagation length. The analysis shows that the decrease is not continuous. Up to about half of the cut-up length (region A), the maximum values of the turbulent kinetic energy decay quadratically. In the second half, from about 3 mm to the tip of the labium

(region B), the values decrease approximately linear. The decay can be approximated by the fit functions $FitA(y) = 0.6394y^2 - 0.3593y + 6.977$ and $FitB(y) = -0.2917y + 2.901$. This is shown in Fig. 5.60b. The spatio-temporal averaged profiles of the turbulent kinetic energy of the jet at the cross-sections are shown in Figs: 5.60c and 5.60d. One observes the decay of the turbulent kinetic energy with respect to the propagation length as well as the growth of the KH-instabilities that lead to a generation of a bell-shaped mean profile of the jet.

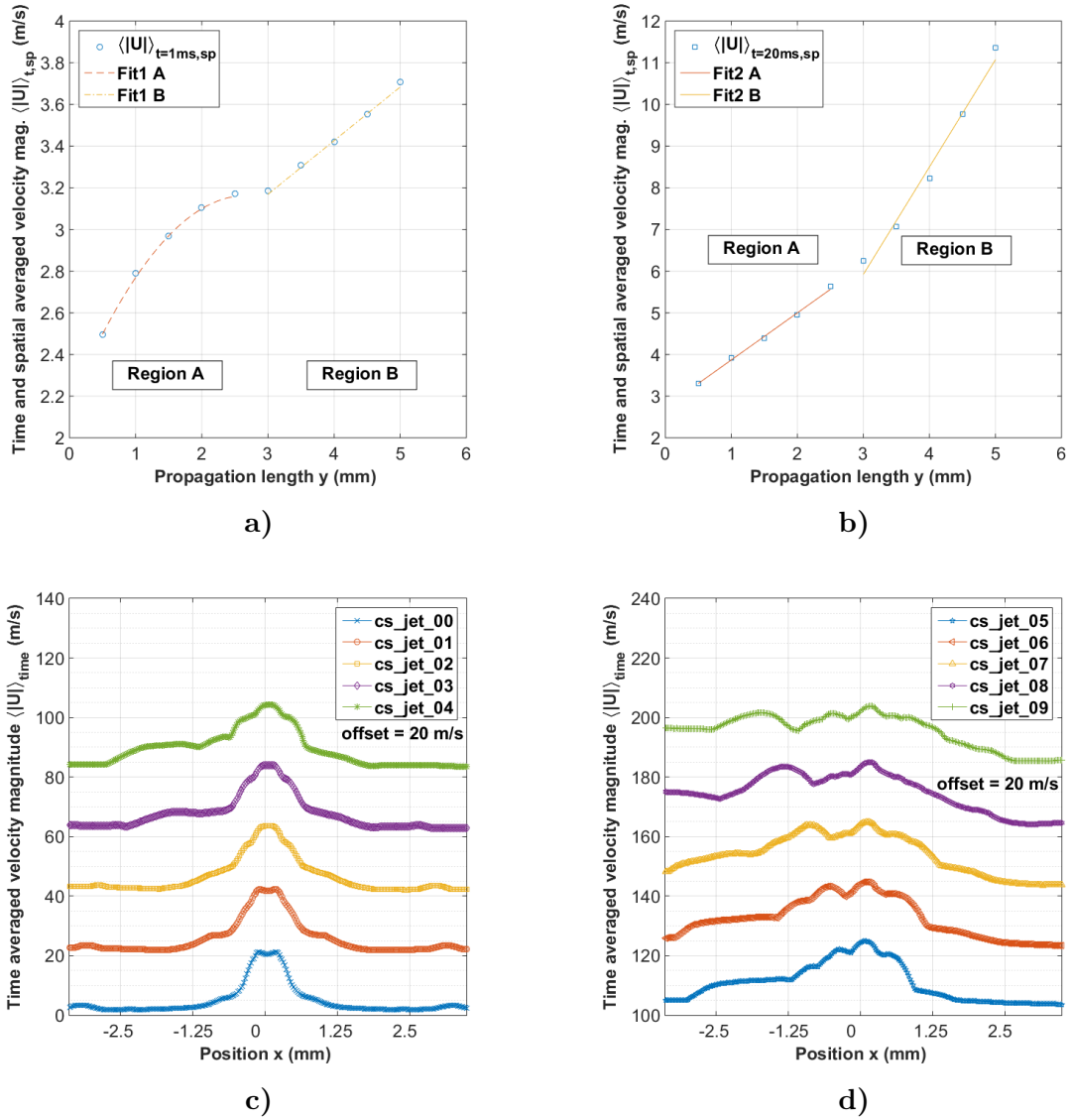

Figure 5.61: Evolution of time and spatial averaged velocity magnitude $\langle |U| \rangle_{t,sp}$ with propagation length y of the jet. The average times are a) $t = 1\,\text{ms}$, the first hitting time to the labium, and b) $t = 20\,\text{ms}$, the whole simulation time. Spatial average length is the length of the cross-sections $x_{cs} = 18.3\,\text{mm}$ with 186 data points, accordingly a spatial resolution of $dx = 0.1\,\text{mm}$. The data indicate that the jet behaves qualitatively different for propagation lengths $0\,\text{mm} < y < 2.5\,\text{mm}$ (*cs_jet_00-cs_jet_04*) called region A in comparison to propagation lengths $3.0\,\text{mm} < y < 5.0\,\text{mm}$ (*cs_jet_05-cs_jet_09*) labeled as region B. The data are fitted by the following Fit curves $Fit1\,A(y) = -0.142y^2 + 0.7562y + 2.155$, $Fit1\,B(y) = 0.2576y + 2.396$, $Fit2\,A(y) = 1.129y + 2.741$, $Fit2\,B(y) = 2.575y - 1.8$.. c) The time averaged velocity magnitude $\langle |u| \rangle_{time}$ at a) cross-sections *cs_jet_00* - *cs_jet_04*, and d) at cross-sections *cs_jet_05* - *cs_jet_09*.

5.3.2.2 Deflection of the Jet

Next, let's discuss the jet's velocity field. Analogue to the investigations of the turbulent kinetic energy one can analyze the time and spatial averaged velocity magnitude $\langle |U| \rangle_{t,sp}$. In Fig. 5.61a the results of average time over the first 1 ms is depicted. In contrast to the turbulent kinetic energy the mean velocity magnitude increases with the propagation length. This is caused by the nozzle effect of the vortices in the jet's shear layers.

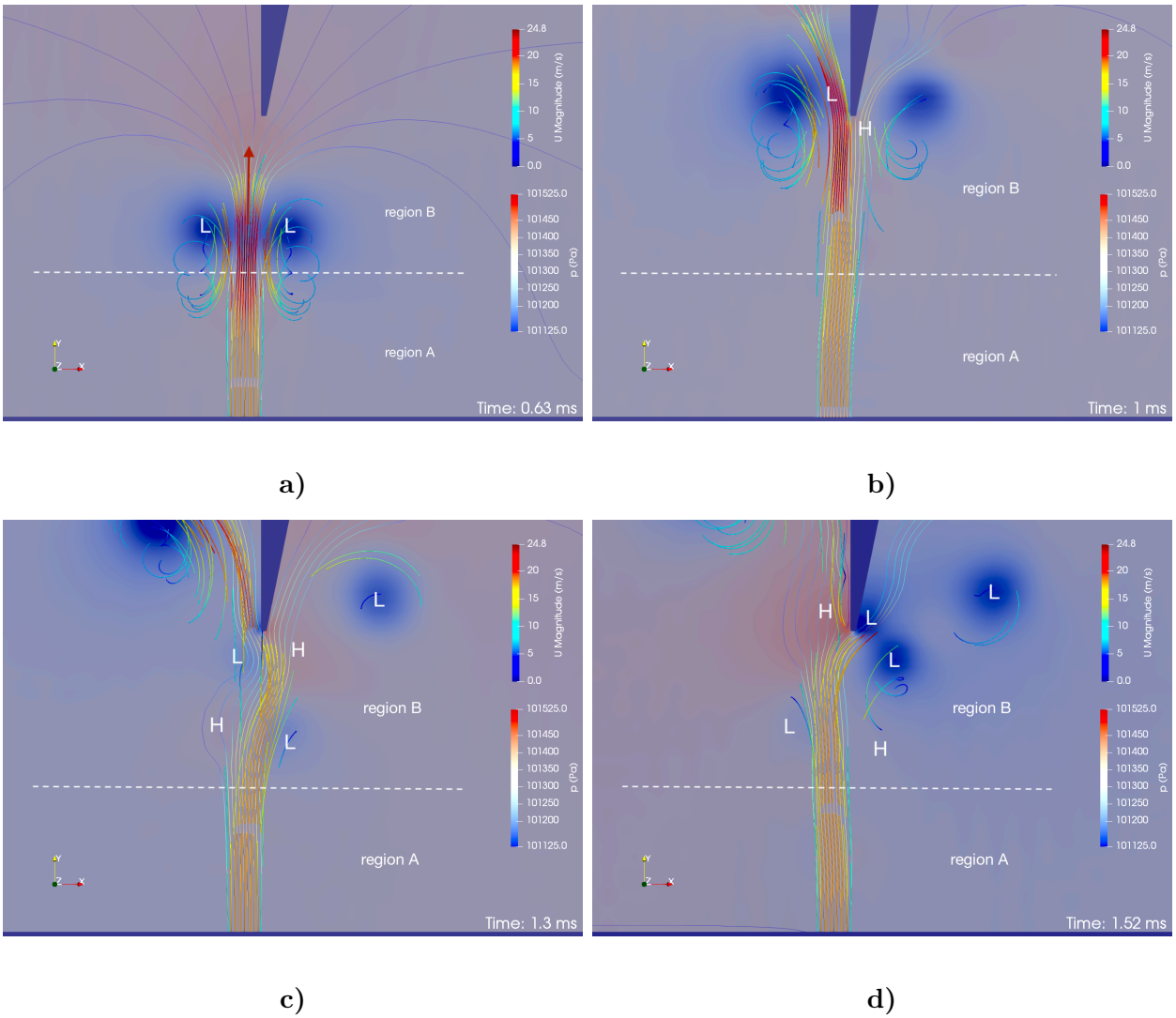

Figure 5.62: a) The jet enters the cut-up region. The snapshot shows the pressure field with the two low pressure cores (L) produced by the vortices in front of the jet. The rotating vortices generate a nozzle that accelerates the central flow of the jet. The streamlines represent the velocity field of the jet. b) The jet gets unstable in the region B caused by hitting the labium which induces an asymmetrical distribution of the vortices and a pressure difference at the labium's tip (L, H). c) While the vortices in the shear layers of the jet propagate to the tip of the labium the induced alternating pressure regime (L, H ; H, L) leads to deflections of the jet. d) The deflections of the jet generate an acoustic dipole at the tip of the labium, which leads to sound generation.

Again one identifies two regions A and B with different rates of growth. In the region A, which is closer to the windway the mean velocity magnitude increases nonlinearly, but with a nonlinear damping. This can be approximated by the fit curve $Fit1\ A(y) = -0.142y^2 + 0.7562y + 2.155$.

In region B, which is closer to the labiums's tip the growth is linear and therefore the rate of growth a constant. This can be approximated by the fit curve $Fit1\,B(y) = 0.2576y + 2.396$. In Fig. 5.61b the results are plotted for the average time of 20 ms. The mean velocities are now significant higher than those the in the initial period of time. One also identifies the regions A and B. In contrast to the initial period of time the mean velocity magnitude $\langle |U| \rangle_{t,sp}$ averaged over $t = 20$ ms shows linear growths but with different rates of growth. The data can be fitted by the linear fit curves $Fit2\,A(y) = 1.129y + 2.741$, $Fit2\,B(y) = 2.575y - 1.8$.
We learn that changing the average time leads to different pictures, which indicates a change of the dynamics of the jet for $t > 1$ ms. We already have seen that from this time on the system shows oscillations. This influences the inherent properties of the jet significantly! The corresponding averaged velocity magnitude jet profiles sampled at the cross-sections *cs_jet_*00 - *cs_jet_*09 are plotted in Figs: 5.61c and 5.61d. One recognizes an increasing asymmetry in the jet profiles in region B compared with those in region A, which means the influence of the labium already starts at the half cut-up length. In the profiles in region B two local maximums emerge, which characterize the mean deflection movements of the jet. The growth of the distances of the local maximums with the propagation length is nonlinear.

The dynamics of the jet in the two different regions A and B in the cut-up can be studied in detail looking at the vorticity field. The physical quantity vorticity is a pseudo-vector[9] field that quantifies the rotational movements in a fluid field. The vorticity is defined by the cross product

$$\vec{\omega} = \nabla \times \vec{u} \tag{5.22}$$

the curl of the del-operator ∇ and the flow velocity field $\vec{u}$.

In Figures 5.55e, 5.55f, 5.55g and 5.55h a sequence of the vorticity field in the cut-up region is already shown. The entire animation of the vorticity ω_z component can be found in the supplement. The vorticity gives a deep insight into the dynamics of the turbulent coherent structures in the cut-up region because it resolves the shear flows that occur in the initial transient. Clockwise rotations are color-coded by blue, anti-clockwise rotations are color-coded by red. While the jet propagates as a free jet in the period of time of $t = 0 - 1$ ms, hitting the labium for $t > 1$ ms induces significant disturbances of the shear flow of the jet. This leads to increasing vortices in the region B that promote the deflections of the jet. The KH-instabilities of the free jet get controlled caused by the presence of the labium. As time progresses, the jet begins to oscillate. We want to understand want this control mechanism is about. To do this, we need to understand what a vortex implies in the shear layer of the jet. The vortex itself is a rotating coherent structure that produces a low pressure core. The two counter-rotating vortices in the front of the constituting jet ($0 - 1$ ms) which propagates into the cut-up act as a local nozzle that accelerates the central flow of the jet up to 25 m/s, cf. Fig: 5.62a. The visualization shows the pressure field with the low pressure cores (L) of the two rotating vortices in front of the jet. The streamlines represent the velocity field of the jet coming from the windway. Its color-coding is the velocity magnitude. The generated nozzle accelerates the initial velocity of the central jet flow from 18 m/s up to about 25 m/s. In the slipstream of

[9] A pseudo-vector is a vector that behaves differently than a vector under certain transformations. A pseudo-vector retains its direction in a point reflection of the physical system under consideration. The angular momentum

$$\vec{L} = \vec{r} \times \vec{p}$$

for example, do not change its direction while the position vector $\vec{r}$ and the momentum $\vec{p} = m\vec{v}$ reverse their direction in a point reflection. The vectors $\vec{r}$ and $\vec{p}$ are called polar vectors, while the pseudo-vector $\vec{L}$ is referred to as an axial vector. The angular velocity $\vec{\omega}$ is an axial vector that is, mathematically, a pseudo-vector.

the vortices in the jet's shear layers the velocity field becomes turbulent. The nozzle effect increases with the propagation length because of the growth of the vortices in the jet's shear layers. There exist several mathematical vortex models, like the Rankine vortex model, that assumes a solid body rotation of the vortex core (linear increase of the centerline velocity of the core) or more sophisticated models like the Lamb-Oseen vortex model which includes a transfer of kinetic energy into viscosity with time. For our considerations, it is more important to examine the effects of the vortices on the jet flow. Beside the acceleration of the central jet flow, the low pressure spots of the vortex cores cause local changes of direction of the jet such that the low pressure cores tend to attract the local flow due to Bernoulli's principle. One the other hand local high pressure spots tend to repel the local flow. Depending on the position of the windway to the labium, the jet flow hits the labium to the left or to the right. Hitting the labium leads to an asymmertry of the pressure spots in the shear flow of the jet. The resulting different flow velocities at both sides of the labium create a pressure difference at the tip of the labium, cf. Fig: 5.62b which has a sonic characteristics due to the high turbulent kinetic energy (high velocity fluctuations).

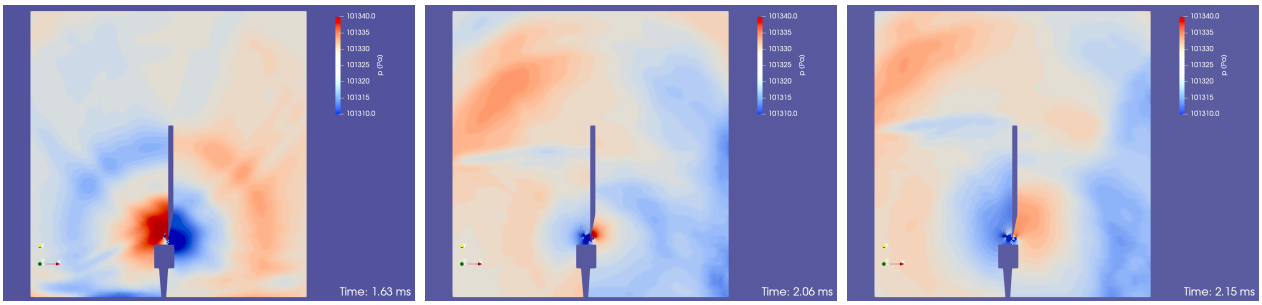

a) **b)** **c)**

Figure 5.63: Generation of acoustic waves at the tip of the labium. a) $t = 1.63\,\text{ms}$, b) $t = 2.06\,\text{ms}$, c) $t = 2.15\,\text{ms}$. The amplitudes of the sound waves are quite low ($\pm 15\,\text{Pa}$).

The pressure difference at the tip of the labium leads to a deflection of the jet, cf. Fig: 5.62c. While the propagation of the jets holds on, the sonic pressure difference at the tip of the labium switches, which in turn leads to a deflection of the jet in opposite direction, cf. Fig: 5.62d. The pressure spots generated in the shear layers of the jet can be understand as local potentials (L=attractive, H=repulsive) that promote the jet's deflections. The deflections generate an oscillating acoustic dipole at the tip of the labium with the result that acoustic waves with low amplitudes ($\pm 15\,\text{Pa}$) are generated. This is shown in Figs: 5.63a, 5.63b and 5.63c. Note, that the acoustic dipole is a sonic object and therefore acts on a faster time scale the flow of the jet does. We find that the deflections of the jet have two origins: the vortices that develop in the shear layers of the jet and the labium, which disrupts the free propagation of the jet and leads to the formation of periodic oscillations of the jet caused by the acoustic dipole at the tip of the labium.

5.3.2.3 Self-similarity and Stability of the Jet

We want now examine a property of some jets called self-similarity. A jet is said to be self-similar if the normalized velocity profile is the same for different successive cross-sectional profiles. The normalization is based on the velocity profile of the jet and half the radial distance (half the width) of the jet $x_{1/2}$. The method was introduced by [Wygnanski, Fiedler (1969)]. At that time, this property was also called the self-preserving jet. For our modified numerical set-up,

the organ pipe's jet without the resonator, we analyzed both, the mean axial velocity $\langle U \rangle / U_0$ and the mean lateral velocity of the jet $\langle V \rangle / V_0$ with respect to the normalized radial distance $x/x_{1/2}$ measured from the jet's center line, for all cross-sections *cs_jet_*00 - *cs_jet_*09. While the jet propagates in the cut-up and spreads with the propagation length, its mean velocity changes as shown in Fig: 5.61c and 5.61d. Its shape doesn't change significantly. This is shown in Figs: 5.64a - 5.64d. The self-similarity of the jet which is disturbed by the labium, a wedge-like geometry with a fix location and a sufficient distance to the orifice of the windway, is initially counterintuitive and in a certain sense unexpected.

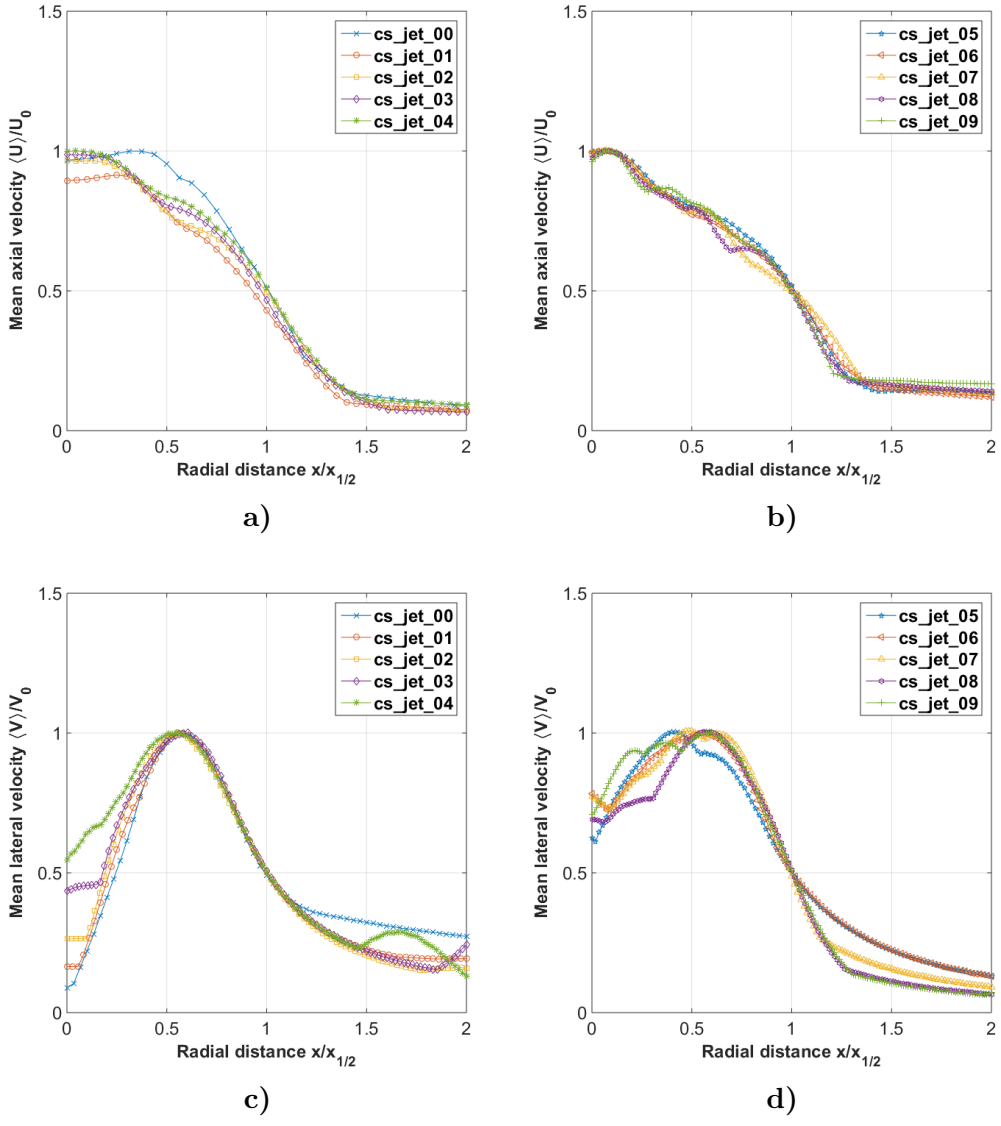

Figure 5.64: a) Mean axial velocity $\langle U \rangle / U_0$ at cross-sections *cs_jet_00-cs_jet_04* b) at cross-sections *cs_jet_05-cs_jet_09*. c) Mean lateral velocity $\langle V \rangle / V_0$ at cross-sections *cs_jet_00-cs_jet_04*, d) at cross-sections *cs_jet_05-cs_jet_09*

However, it shows that intrinsic order parameters of the jet are at least not disturbed by the labium. On the contrary, it can be assumed that the periodic oscillations induced by the labium tends to stabilize the dynamics of the jet by generating an acoustic dipole. The justification for this is provided by the sensitivity of the jet to the local pressure regime through which the jet propagates. We have seen that the central jet flow reacts very sensitively to the vortex structures arising in the jet's shear layers and thus to the corresponding pressure spots, with

acceleration and with change of direction (which in turn promotes the formation of vortices). This is no different with an "externally" generated pressure regime. The jet generates the pressure difference at the tip of the labium through its inflow. The impinging jet flow induces high turbulent kinetic energy and large values of wall shear stress at the tip of the labium which promotes the generation of a sound source at this location. However, the resulting acoustic pressure field at the tip of the labium affects the motion of the jet, which in turn changes the pressure field.

The relationship between motion and pressure gradient in fluid mechanics is comparable to the considerations in general relativity, in which it is precisely the curvature of spacetime (described by the metric tensor) that determines the motion of a body in the gravitational field. If the moving body is sufficiently massive, it noticeably disturbs (changes) the potential in which it propagates, and gravitational waves arise. In our case, the jet inflow into the cut-up changes the local initial pressure distribution and thus the metric described by the Cauchy-stress tensor (Eq: 3.184) or the deviatoric stress tensor (Eq: 3.190) respective, (cf. subsubsection 3.2.2.3 in chapter 3). The spatio-temporal pressure distribution determines the local movement of the fluid volume. The moving fluid element, which is subject to mass, determines the change in pressure distribution (Bernoulli) and leads to the generation of an acoustic dipole at the tip of the labium. The acoustic dipole which acts on a faster time scale than the pressure regime in the shear layers of the jet establishes a new condition the jet has to follow. So, if one asks about cause and effect in this complex interplay, one always have to keep in mind that in the mathematical sense one is dealing with a field theory in which cause and effect are in a certain respect in the eye of the beholder, or to put it another way, from the point of view of the observation depends. Fact is that the motion of the jet is strongly influenced by the local pressure field, whatever its origin is. This is especially true for the oscillating acoustic dipole at the tip of the labium. It is initially induced by the jet flow impinging the labium. But the acoustic field forces the jet to oscillate periodically and, seen in this way, is the cause of its oscillations. We can go even further and say that the jet gets enslaved in its motion by the local acoustic field through which it moves.

A similar picture emerges in oscillating pipe flows. In the case of oscillating flows, the nonlinearity of the Navier-Stokes equations results in a change in the mean movement compared to the case without oscillation. For the same reason, in addition to the fundamental frequency, multiples of the fundamental frequency also occur in the oscillations in the flow field. At high frequencies, the kinetic energy of the oscillating movement is particularly high near the walls, and there is a phase shift of $-45\,^\circ$ between the fluctuations in the wall shear stress and the velocity out of the boundary layer. The wall shear stress (the pressure respective) precedes the velocity, as shown by [Uchida (1956)]. In the following we want to come back to the sound generation in the organ pipe's resonator. We will now discuss the interplay of the resonator and the jet which leads to stable sound generation.

5.3.2.4 Interplay of the Resonator's Sound field and the Jet

We now want to discuss the interaction of the sound field generated initially in the resonator and the jet. As we already have seen in subsection 5.3.1 an initial sound field is generated in the resonator by the slipstream of the propagating initial pressure waves, called shocks. We also have learned that the jet is sensitive to lateral disturbances, in particular to acoustic disturbances. We have worked out that the jet get enslaved by such lateral acoustic disturbances and is therefore able to adjust its ability to oscillate. It is also intuitively clear that the jet

must be responsible for the amplification or maintenance of the sound field inside the resonator, because the jet is the only energy source in the system. It remains to be clarified how the jet contributes to the amplification of the sound field in the resonator.

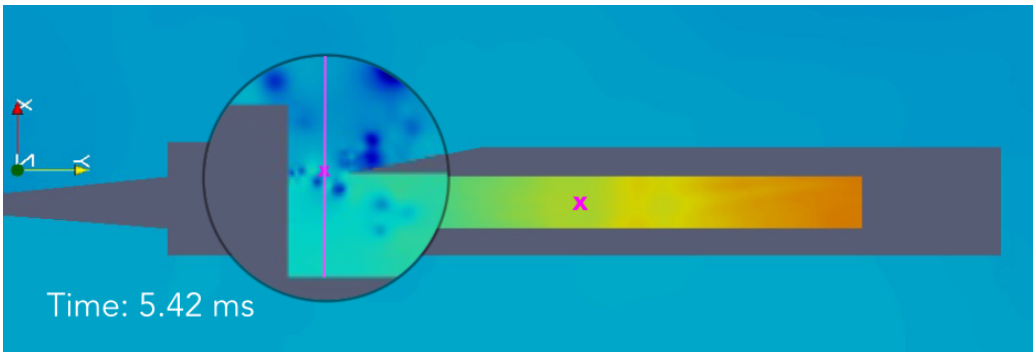

Figure 5.65: Coarse-grained locations of the resonator ($x = 4.5\,\text{mm}$, $y = 50\,\text{mm}$), and the jet located in region B in the central jet flow ($x = 9.5\,\text{mm}$, $y = 2.75\,\text{mm}$), which is $y = 2.25\,\text{mm}$ away from the labium. The magnified area shows the jet variable ϕ_{jet} as well the cross-section cs_jet used for analysis.

We have seen that the triggering process of the initial sound field is a complex process in which the dissipation of trans-sonic structures plays an important role. At certain phase conditions between the primary shock and the generated sound field (particularly the fundamental oscillations), the triggering is either strengthened (in-phase at times $t = 4.2\,\text{ms}$ and $t = 8.4\,\text{ms}$) or weakened (anti-phase). The latter phase relation lead to the development of higher harmonic oscillations in the resonator. After the transient time (in the present case approx. 10 ms) the shock waves are completely dissipated in the sound field. Nevertheless, the sound field is still triggered or maintained to such an extent that the instrument emits sound in the so-called operation mode.

With the research done so far, the answer is now becoming clearer. It is the sound field in the resonator that forces the jet to in-phase oscillations. The sound field in the resonator is established after 1 ms which corresponds to just two back and fourth propagation events of the initial shock wave. During this time, the reflections of the shocks produce a distribution of dissipating shock wave fronts that double per reflection. $(8, 16, 32, 64)$. From this time on the sound field in the resonator is an object with strong coherent internal phase relations – a coherent object. The coherency allows to describe the dynamics of the sound field by just one phase variable, taken at any point in the resonator[10]. For the phase analysis a point in the center of the resonator is chosen, cf. Fig: 5.65. The time evolution of the coarse-grained phase variable ϕ_{res_p} of the sound field in the resonator is plotted in Fig: 5.66 shown as the blue curve.

After the transient of ($t = 1\,\text{ms}$) the phase grow linear with time which indicates harmonic oscillations in the resonator. The coarse-graining of the jet can be realized in the same way in principle. The jet is established as as a coherent structure when it initially impinges the tip of the labium after about $t = 0.7\,\text{ms}$. In contrast to the sound field in the resonator, the jet in the cut-up is a turbulent coherent structure which makes it a bit more advanced to assign a single phase variable. The variable relevant for the deflection is the lateral velocity component v_x of the jet. As already mentioned the propagation properties of the jet can be split into the regions A close to the windway (more of less free jet characteristics) and the region B, which is

[10]This is exactly what the coarse-graining method is all about. Reasonable reduction in the complexity of the system.

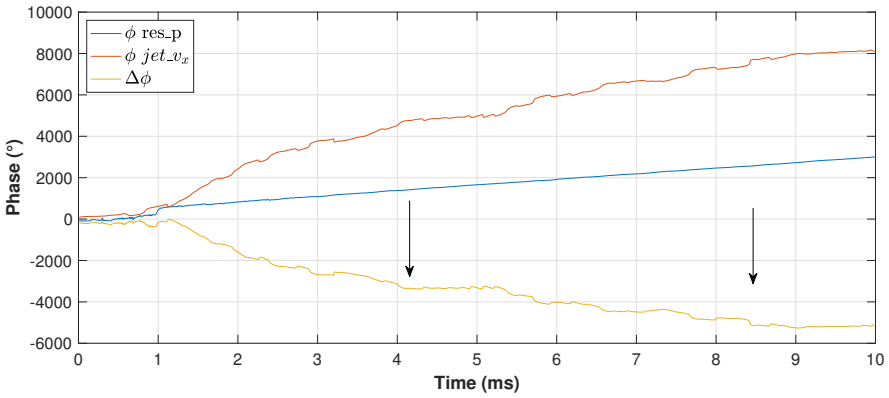

Figure 5.66: Phase evolution of the resonator and the jet. The probe point inside the resonator is located in the center of the resonator tube. The probe point of the jet is located $y = 2.75\,\text{mm}$ away from the windway (2.25 mm away from the labium) in region B as well as in the (undeflected) central jet flow ($x = 9.5\,\text{mm}$ away from the inner wall of the resonator).

affected by acoustic disturbances (acoustic dipole and/or other acoustic impacts). That's why it makes sense to choose the region B to find a proper phase variable to describe the deflective dynamics of the jet caused by acoustics. It is also clear that – when looking at the deflections caused by acoustics – the turbulent aspects of the jet which are essentially flow properties are not as relevant as the lateral properties of the jet. The central flow of the jet is the area were the turbulence of the jet is minimal compared to the jet's shear layers. Taken both arguments into account one has to concentrate to an area of the central jet flow which is sufficiently close to the labium to get affected by the initial acoustic disturbances and at the same time not too close to the tip of the labium to avoid artifacts caused by turbulence (irregular deflections caused by Kelvin-Helmholtz instabilities). Therefore a point in the central flow of the jet in the lower part of region B is chosen, e.g. the point ($x = 9.5\,\text{mm}; y = 2.25\,\text{mm}$), cf Fig: 5.65.

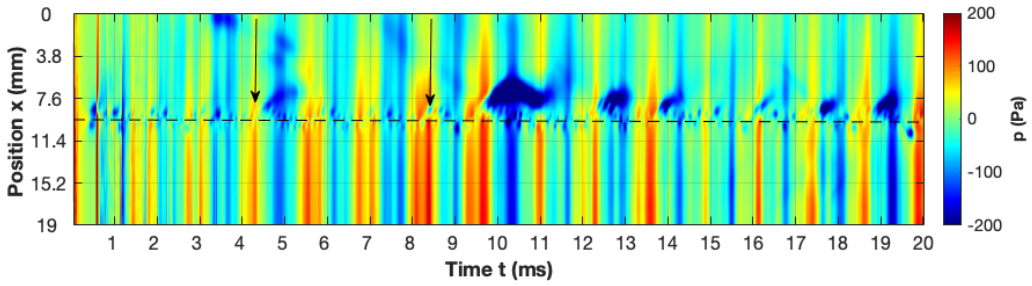

Figure 5.67: Time evolution of the pressure in the cut-up region and in the mouth region of the organ pipe. The data were sampled at the cross-section cs_jet which has a length of 19 mm,190 sample points and a spatial resolution of 0.1 mm. The cross-section is located 2.75 mm away from the windway of the instrument. The dashed line marks the position of the coarse-grained jet variable $\phi_{jet\_v_x}$.

The evolution of the phase $\phi_{jet\_v_x}$ of the central jet flow's velocity component v_x at this location is shown in Fig: 5.66. Compared with the phase evolution of the resonator variable the phase of the jet variable behaves differently. After the transient of $t = 1\,\text{ms}$ the phase starts to grow with a growth rate of approx. $3,000\,°/\text{ms}$ which correspond to the frequency of the acoustic dipole at the tip of the labium of $f_{ac-dipole} \approx 3\,\text{kHz}$. In the course of time one observes several phase plateaus of short duration as well as phase slips, which lead to a flattening of the curve, until at time $t = 4.2\,\text{ms}$ the slope becomes (abruptly) equal to that of the phase evolution

of the resonator. The dynamics repeats itself starting at $t = 5\,\text{ms}$ and results in a renewed synchronicity at $t = 8.4\,\text{ms}$. Both events of adjustment can be seen in the phase difference $\Delta\phi$ (yellow curve) as pronounced synchronization plateaus, which in addition are marked by arrows. The observed dynamics is in excellent agreement with the theory of synchronization [Pikovsky et al.(2001)]. The lateral sensitivity of the jet, modeled by the jet variable $\phi_{jet\_v_x}$ can be understand as the neutral stable phase quantity of the oscillating jet with respect to acoustic disturbances. This allows (internal and external) acoustic forces to shift the phase of the jet and therefore to adjust the jet oscillations.

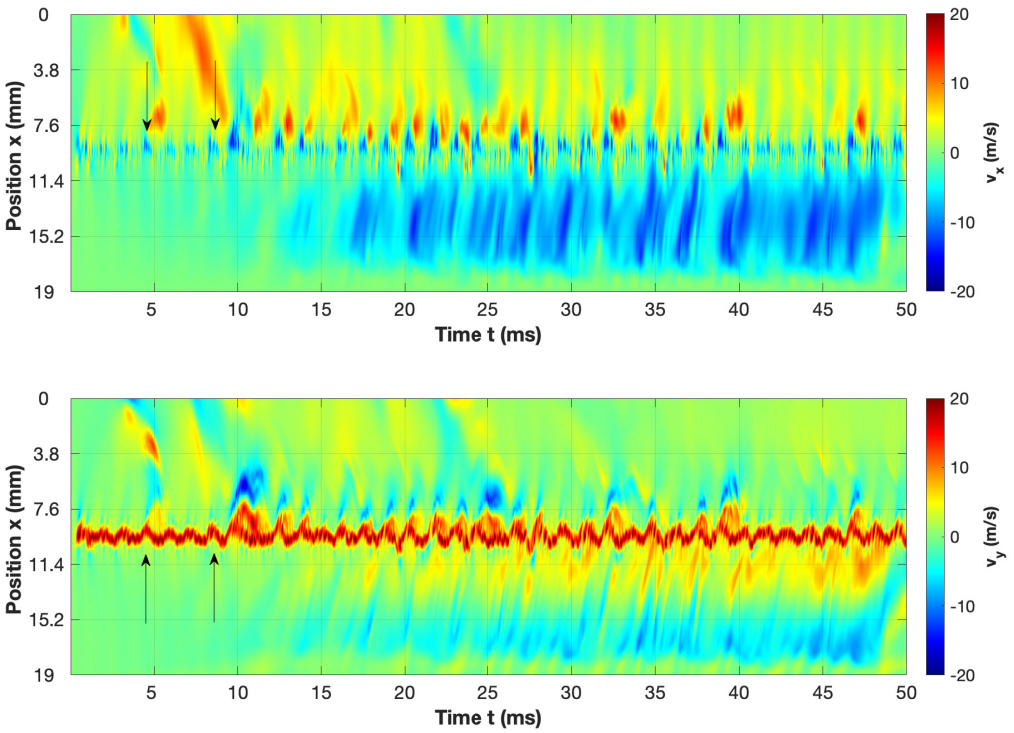

Figure 5.68: Time evolution of the lateral and the axial velocity components jet v_x and v_y.

The lateral dynamics of the jet ($\phi_{jet\_v_x}$) is shifted and get enslaved by the sound field of the resonator such that both coherent structures oscillate in-phase. The maintenance of the sound field is now organized by the in-phase oscillations of the jet which enters the resonator's air column with the periodicity the resonator enforces. This re-amplifies (or maintains) the sound field although energy dissipates by emission of sound. For this reason, such oscillations are also called self-excited oscillations. To analyze this mechanism one can switch back from the coarse-grained phase description to the fluid-mechanical and aeroacoustic point of view. To do this, one considers the temporal development of the cross-section cs_jet, which contains the point in the central flow of the jet at which the jet variable $\phi_{jet\_v_x}$ was modeled and which runs over the entire section of the instrument , cf. Fig: 5.65.

Looking at the time evolution of the pressure along the cross-section cs_jet shown in Fig: 5.67 one identifies the events of adjustment at $t = 4.2\,\text{ms}$ and $t = 8.4\,\text{ms}$ (arrows). The location of the coarse-grained jet $\phi_{jet\_v_x}$ is marked by the dashed line. Below the dashed line the temporal development of the cross-section inside the resonator volume is color-coded. Above the dashed line is the part of the cross-section that runs through the mouth outward the instrument. The in-phase relationship between the primary shock and the initial sound field lead to a significant

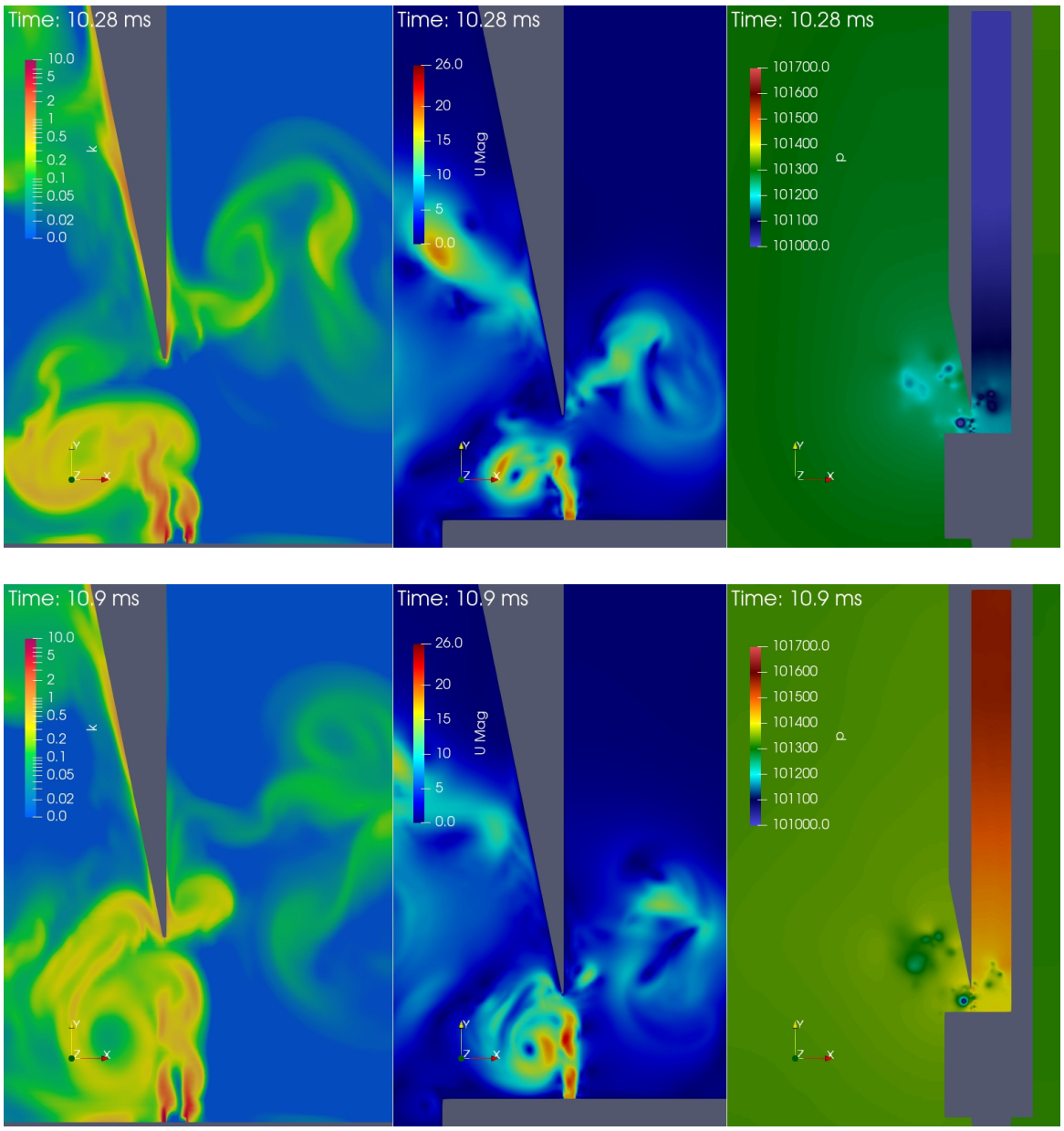

Figure 5.69: Vortex shedding induced by acoustic disturbance of the jet. Shown are sequences of the numerical simulation of the organ pipe at times $t = 10.28\,\text{ms}$ and $t = 10.9\,\text{ms}$. The left visualizations show the turbulent kinetic energy which is color-coded with a logarithmic scale to resolve the details of the turbulent flow in the cut-up region of the organ pipe. In the middle visualizations depict velocity magnitude of the same time step. Clearly seen by the color-coding is the shed vortex in the mouth region of the organ pipe and its rotation with is anticlockwise. The right pictures show the corresponding pressure filed in the generator region of the organ pipe as well as in the resonator. In the lower sequence it is shown that that both turbulent coherent structures, jet jet and the shed vortex are drawn back into the cut-up region by the sound field in the resonator.

amplification of the sound field and to an emission of sound into the free space. From $t = 10\,\text{ms}$ the coupled system (jet-resonator) starts to maintain the oscillations with the fundamental frequency, despite of some disturbances in the period of time of $12 - 14\,\text{ms}$ where the coupled system tries to switch into the next harmonics. The reason for that is a large vortex in the mouth region that temporarily generates a strong low pressure spot, which disturbs the internal synchronization. In Figs: 5.68 the time evolution of the velocity components v_x and v_y along

the cross-section *cs_jet* are color-coded in the period of time of $0 - 50\,\text{ms}$.

Again the initial events of adjustment are labeled by arrows. In the initial transient the jet oscillations are dominated by the acoustic dipole, ans from $t = 4.2\,\text{ms}$ significantly by the sound field of the resonator. After the internal synchronization of the jet and the resonator's sound field the system generates stable oscillations. The stability of the synchronized coupled system is remarkable, it compensates the perturbation by the vortex within a few periods as the visualization of axial velocity component v_y shows. Note, the axial velocity component of the v_y is an asymptotic stable quantity that tends to relax. This is intuitive, because the axial velocity component of the jet is essentially determined by the flow and – in absence of (geometric or acoustic) disturbances – tends to maintain its main flow direction as long as the free propagation length does not become too large, such that Kelvin-Helmholtz instabilities dominate the jet. But even then the jet is only spread[11] but its mean central flow direction remains.

During the perturbation of the jet by the vortex one observes the occurrence of two relaxation maximums in axial flow which different relaxation rates. The explanation for this is that the massive deflection of the jet leads to vortex shedding. The shed vortex – like the jet itself – is drawn into the cut-up by the sound field in the resonator. The second maximum is not the jet but the shed vortex structure, cf. Fig: 5.69. This can be studied in detail in the corresponding animation in the supplement.

Vortices are another turbulent coherent structures occurring in the initial transient of aerophones. As mentioned before their rotation generate local low pressure spots. The periodically re-entering of the jet into the stagnant air column of the resonator produces a mass flow into the resonator. The stagnant air column of the resonator has a much bigger volume compared with periodical in-flow of the jet. The inertia of the stagnant air column and the conservation of mass lead to a generation of a vortex in the lower resonator area. The vortex rotation transports the jet in-flow back into the cut-up region where it periodically can escape the resonator[12]. The vortex in the lower resonator region caused by the jet's dynamics produces a locally stable low pressure spot. This promotes the re-entering of the jet after deflection outwards and therefore stabilizes the operation mode of the instrument. In Fig: 5.68 is shown that the vortex in the lower resonator region fully establishes much later after the initial transient at about $t = 15\,\text{ms}$. This is reasonable because the vortex can only form when the jet is synchronized and generates the mass flow by its periodic in-flow. The rotation of the vortex is driven by the jet's periodical in-flow. The jet's periodical in-flow is promotes bey the low pressure spot of the vortex in the lower resonator region. This again shows very clearly the mutual dependency in the complex interplay of turbulent coherent structures in aerophones. At the end of this section the results can be summarized by the following statements:

- The jet is a turbulent coherent structure which constitutes in the initial transient of the organ pipe within the first millisecond.
- The cut-up region where the jet propagates can be split into two regions, the region A close to the windway, where the jet propagates more or less as a free jet, and region B where the jet moves under the influence of the labium.
- The free jet can be characterized by its central flow and by its shear layers in which

[11] Turbulent free jets have a typical angle of spread of $19.5 - 24.6\,^\circ$ depending on the viscosity of the medium.

[12] If the escape of the mass flow is not permanently complete secondary vortices can occur in the lower resonator. Such vortices rotate opposite to the pre-generated vortex

vortices are generated by Kelvin-Helmholtz instabilities that influences the dynamics, particularly its lateral stability.

- The rotation of the vortices produces local low pressure spots that forces the central jet flow to change its direction. The jet is sensitive with respect to the pressure regime through which it propagates.

- The lateral sensitivity of the jet due to disturbances caused by the local pressure field includes acoustical disturbances.

- By impinging the labium the jet generates an acoustic dipole at the labium's tip.

- Although the acoustic dipole is induced by the jet, the generated acoustic dipole field forces the jet to oscillate regularly and thus to change its characteristics, particularly its lateral dynamics.

- The jet shows self-similarity characteristics both as a free jet and as an oscillating jet.

- The interplay of the jet and the resonator (or more precisely the sound field in the resonator) can be described by coarse-grained phase variables.

- The lateral velocity component v_x of the jet is a neutral stable quantity. This property determines the jet's lateral sensibility to the local pressure regime and the ability to get adjust (shift of phase).

- The axial velocity component v_y is an asymptotic stable quantity caused by the flow properties of a free jet.

- In the initial transient the generated sound field inside the resonator adjusts the lateral dynamics of the jet. with the result that both coherent structures oscillate in-phase. The sound field synchronizes the jet's lateral dynamics – in other words: the sound field enslaves the jet.

- The internal synchronization of the sound field and the jet is the prior condition for the jet to be able to trigger the sound field and thus maintain it.

- The synchronized coupled system is stable against subsonic disturbances, e.g. shed vortices.

- The periodically entering of the jet flow into the stagnant air column of the resonator generates a large vortex in the lower resonator region, a further turbulent coherent structure, that promotes the jet deflections back into the resonator. This in addition stabilizes the operation mode of the instrument.

Only the interplay of all coherent objects (shocks and sound field) and the turbulent coherent structures (jet and vortices) lead to a successful sound generation. Creating the structural conditions for this is the task of all the talented instrument builders and voicers that create the instrument and form the sound we love.

5.4 The Turkish Ney

Rim-blown flutes are musical instruments played worldwide in which an open or semi-closed reed is blown by shaping a stream of air with the lips and directing it onto the rim of a reed opening. The tube may have finger holes. The Andean panpipes, the Japanese shakuhachi and the Turkish ney are prominent examples of this class of instruments. What these instruments have in common is that the air flow generated is not directed to the edge by a fipple or other constructions, as this is the case with the recorder[13]. This makes playing such instruments a complex task because the player has to form and to control the sensible airflow by varying the blow angle, the position and the lip opening, the oral cavity volume, and the mass flow simultaneously. On the other hand, this number of degrees of freedom opens many possibilities of articulation. Let's examine this more closely by analyzing results from acoustic measurements of sound generation and overblowing.

The Turkish ney belongs to the family of the rim-blown[14] flutes which are prominently played in Middle Eastern music. The instruments have been continually used since 4,000-5,000 years. The Turkish ney is considered the most typical instrument of Classical Turkish music.

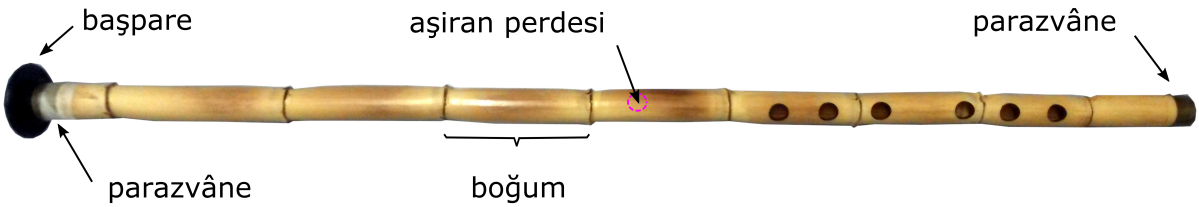

Figure 5.70: The Turkish ney.

The Turkish ney is made of the giant reed (Arundo donax). The instrument has a conical mouthpiece at the upper end (*başpare*) which is traditionally made of horn, ebony or ivory. Commercial instruments of lower quality have mouthpieces of durable materials like plastic. The Turkish ney has six finger holes on the front side and one thumb hole (*aşiran perdesi*) on the back side. Depending on the size, the instrument has three to nine segments or knots (*boğum*) caused by the naturally growth of the stalk of the plant. The ends of the stalk are fixed by metal rings (*parazvăne*), cf. Fig: 5.70.
The Turkish ney is played by forming a small aperture with the lips, pressing them onto the mouthpiece under a proper angle and generating a narrow air stream - the jet. Subsequently the jet is blowing against the interior edge of the mouthpiece. By varying the air stream – the blow pressure, the blow angle and the jet's diameter – the player can overblow the instrument up to fourth or fifth harmonics. The interplay of angling, lip forming and jet generation is an advanced task. Sound generation and playing the instrument is considered particularly difficult.

5.4.1 Blowing and Overblowing the Turkish Ney

In particular the overblowing technique is the essential techniques when playing the Turkish ney. The entire musical repertoire of classical Turkish music can only be represented by applying the overblowing technique. The same applies to the Persian nay, which sometimes only has

[13] In the case of the recorder, this is the block that directs the air flow to the edge of the labium.
[14] Rim-blown flutes are often referred to as end-blown or edge-blown flutes.

five finger holes instead of six at the Turkish ney.

Blowing on the fundamental of the Turkish ney is particularly challenging because the player has to create a comparatively slow airflow. The giant reed, from which the instrument is usually made, is segmented by so-called growth knots as shown in Fig. 5.70 and has a high internal roughness due to plant fibers in the hollow interior of the resonator tube. The slow air flow and the roughness in the resonator mean that the sound field is subject to strong dissipation and can only be triggered with difficulty by the weak jet. High-quality instruments are therefore smoothed on the inside of the resonator by various grinding and pushing techniques. However, this in turn must be done very carefully in order not to "grind away" the characteristic and beautiful noisy sound of the instrument. The rougher and more uneven the inner surface of the resonator, the more difficult is it to excite the fundamental. In such cases, the initial transient process can be extremely long (up to 2 seconds). With less high-quality instruments it is often not possible to stimulate the fundamental at all.

The overblowing is created by the player increasing the air flow in a controlled manner. Often the player regulates not only the airflow, but the angle of attack and the lip opening simultaneously. Correct overblowing of the Turkish ney requires a lot of practice and special motor skills in the mouth area. The measurements have been done on a standard instrument of length 700mm, a so called Kız ney, which means girl's ney. The microphone position was 300 mm apart of the player's mouth, orthogonal to the instrument. The signals were recorded by an AKG microphone with a sampling rate of $f_s = 44.1\,\text{kHz}$.

5.4.1.1 Observations

Figure 5.71 shows the recorded signal of a blowing process where the instrument gets blown on as well as overblown several times. The corresponding mean SPL-spectrum and the Short Time Fourier transform (STFT) of the processes are depicted in Figure 5.72. Note, the measurements were done using a standard (low-quality) Turkish ney instrument. Reading both representations of the signal one observes an initial transient in the period of time from $t = 0 - 0.2\,\text{s}$ followed by a process where the fundamental frequency of $f_1 = 226.15\,\text{Hz}$ is going to create $t = 0.2 - 0.6\,\text{s}$. Subsequently the dynamic of the system gets re-arranged by overblowing into the second harmonic at the period of time $t = 0.6 - 0.8\,\text{s}$. This process lead to stable oscillations with a leading frequency of $f_2 = 452.31\,\text{Hz}$ in the time duration $t = 1 - 3.5\,\text{s}$. Such stable oscillations are referred to as the working mode of the instrument.

While the player increases the air flow, after about 3.5 s, the instrument gets overblown again to the 3^{rd} harmonic of $f_3 = 678.46\,\text{Hz}$ as the leading frequency. The instrument again stabilizes its oscillations in a working mode. The player keeps increasing the air flow if, at the time period of $t = 6.2 - 6.3\,\text{s}$, the system gets overblown into the 4^{th} harmonic as the leading frequency. Again the system stabilizes its oscillations in a working mode, which now has the leading frequency $f_4 = 915.38\,\text{Hz}$. At about 8.8 s the player stops the blowing process and the oscillations decay.

At the left side of the mean SPL spectrum (taken over the whole process) one can see four distinct peaks with frequencies $f_1 = 231.51\,\text{Hz}$, $f_2 = 457.63\,\text{Hz}$, $f_3 = 683.76\,\text{Hz}$ and $f_4 = 920.65\,\text{Hz}$, the leading frequencies, which arise after the respective overblowing processes. The amplitudes of the peaks mentioned show that the fundamental frequency is very weak and the leading higher harmonics are very strong after overblowing. This shows that the fundamental is overblown very quickly before it is formed. The measured frequencies and the corresponding SPL's of all processes are summarized in Tab: 5.1. The processes are ordered vertically, the corresponding

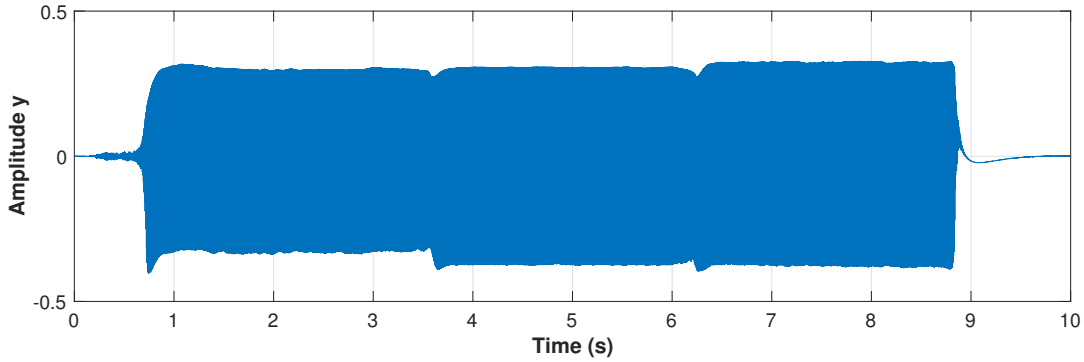

Figure 5.71: Example of a signal recorded by an acoustic measurement. One can see and initial transient as well as different parts separated by different amplitudes. A decay process can be seen at the end of the signal.

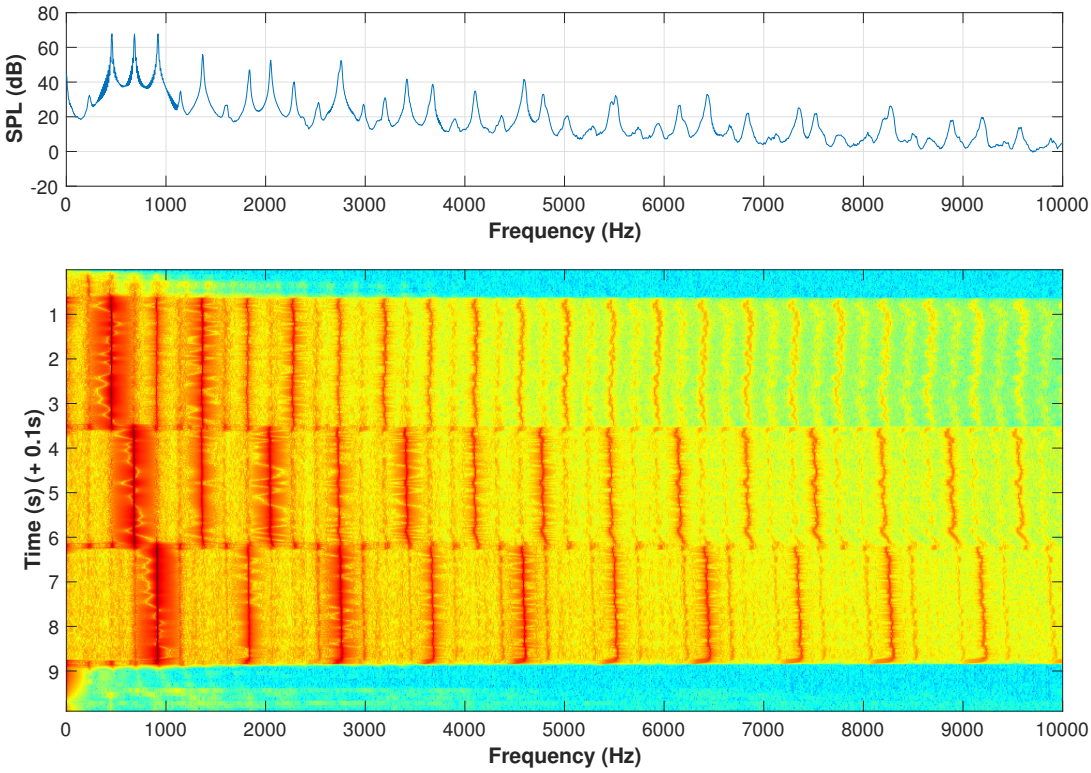

Figure 5.72: Overblowing process of the Turkish ney. The upper chart shows the SPL-spectrum taken over the whole blow process ($t = 10\,\mathrm{s}$). The lower chart shows the Short Time Fourier-transform (STFT) of the whole process.

harmonics are ordered horizontally starting with the leading frequency and their sound pressure

levels. In the STFT-spectrum[15] which often referred to as spectrogram one observes the brief emergence of all possible natural frequencies of the system. For the overblowing process from the second to the third harmonic this is shown as an example in Fig: 5.73. One can see that the process of rearranging the overblow, in which the leading frequency changes from 452.31 Hz to 678.46 Hz, is staggered in time. First, the possible states of lower energy are occupied. The higher harmonics are occupied afterwards. The whole rearrangement process takes about 10 ms. This is of the same length of time as the initial transient process.

harmonics	leading					
blowing on the	226.15 Hz	441.54 Hz	689.23 Hz	926.15 Hz	1216.92 Hz	1421.54 Hz
fundamental	41.99 dB	30.40 dB	26.39 dB	17.86 dB	6.59 dB	5.53 dB
1. overblowing	452.31 Hz	915.38 Hz	1367.69 Hz	1830.77 Hz	3650.77 Hz	4113.85 Hz
	77.82 dB	53.22 dB	63.83 dB	45.44 dB	52.40 dB	38.99 dB
2. overblowing	678.46 Hz	1367.69 Hz	2056.92 Hz	2735.38 Hz	3424.62 Hz	4103.08 Hz
	78.38 dB	60.51 dB	64.27 dB	53.76 dB	54.52 dB	47.23 dB
3. overblowing	915.38 Hz	1841.54 Hz	2756.92 Hz	3683.08 Hz	4598.46 Hz	5513.85 Hz
	78.65 dB	58.89 dB	65.42 dB	51.78 dB	55.60 dB	45.27 dB

Table 5.1: The fundamental frequency and the overtones of the blowing process of the Turkish ney. The leading frequencies and the SPL's of the overblowing processes are labeled separately in the first column.

5.4.1.2 Discussion

For a better illustration let's consider the initial blowing on process, the formation of the fundamental and the overblowing processes in detail, namely by the signal and by the corresponding the phase portrait. Figures 5.74a and 5.74b show the signal and the related phase portrait of the initial transient. The initial transient process is characterized by a more or less irregular signal curve until the first deflections occur at around 0.13 s. In the phase portrait, these amplitude curves are recognizable as loops that are vaguely reminiscent on irregular perihelion rotations. In fact, the initial oscillations can be interpreted as some kind of precession movement[16] around the trivial state of equilibrium of the system $(0;0)$, the static one where no movement takes place. This is not the only state of equilibrium that the system develops during the blowing process. In the present context equilibrium state can mean both a static or a dynamic equilibrium. The latter one describes the balance that occurs between an excitation force, e.g. caused by the air flow and restoring forces that control the dynamics of the jet such that regular oscillations close to blown edge at the mouthpiece get established. The Figures 5.74c and 5.74d show the evolution of the initial transient from 0.2 s to 0.4 s.

[15] In this analysis we used the discrete Short Time Fourier Transform:

$$STFT\{x[n]\}(m,\omega) \equiv X(m,\omega) = \sum_{n=-\infty}^{\infty} x[n]w[n-m]e^{-j\omega n}$$

with discrete window w and discrete ω. The step-size was 1 ms and the chunk length was 0.1 s.

[16] Precession movements are always caused by external disturbances that affect an oscillating system.

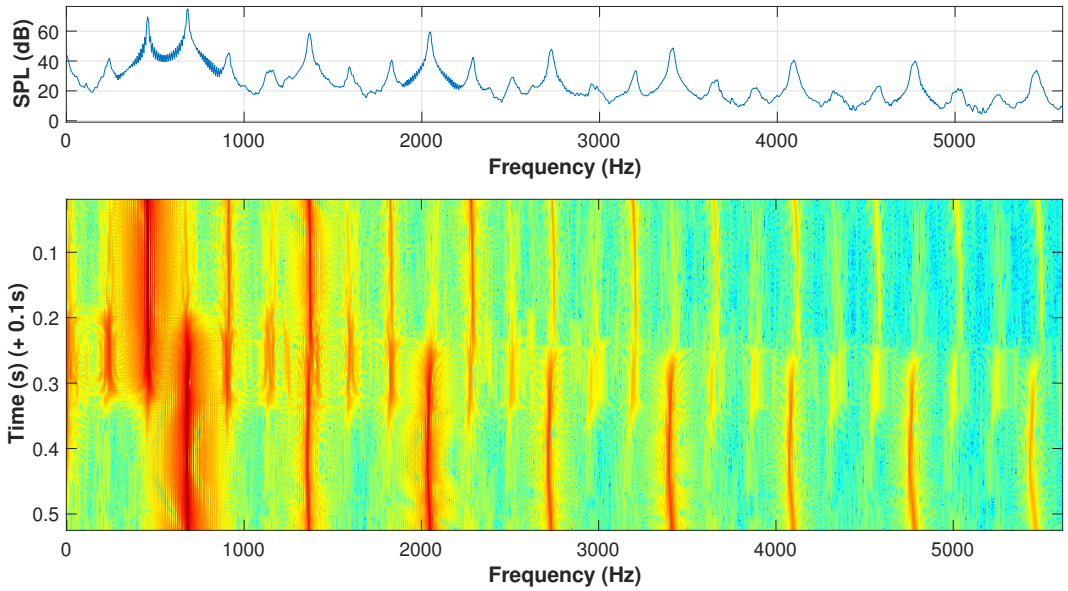

Figure 5.73: Overblowing process of the Turkish Ney from the second to the third harmonic. The upper chart shows the SPL-spectrum of the process from about $t = 3.3\,\mathrm{s}$ to $4.1\,\mathrm{s}$. The lower chart shows the spectrogram of the overblowing process.

The oscillations become more regular and harmonious, which is clearly shown in the phase portrait, where the trajectory becomes more circular and more compact as a whole which indicates less disturbances with respect to the oscillating process. There are no longer strong precession movements, but there are loops[17], which is an expression of the formation of higher harmonics with non-synchronized phase relations. Roughly speaking, the system "searches" for a stable state of oscillation. This is still the case during the period from $0.4\,\mathrm{s}$ to $0.6\,\mathrm{s}$, cf. Figs: 5.75a and 5.75b. In the signal representation one observes oscillations with the fundamental frequency of $f_1 = 226\,\mathrm{Hz}$ which are disturbed. This results in large fluctuations in amplitude. It is already mentioned that can be quite difficult blowing the fundamental frequency of the instrument and bring it to a stable operation mode.

From $0.6\,\mathrm{s}$ to $0.75\,\mathrm{s}$ the signal rapidly increases its amplitudes while the oscillations become harmonic. The system starts to oscillate with the second harmonic frequency of about $f_2 = 452\,\mathrm{Hz}$, which is sufficiently close to the theoretical value of fundamental mode of an ideal resonator tube of the same length[18].

Note, the Turkish ney, especially the instrument under consideration has various (quite desirable) shortcomings, starting from the knots of the reed to the rough surface inside the resonator tube. In the phase portrait one also recognizes that from $t = 0.75\,\mathrm{s}$ the oscillations becomes weakly nonlinear. The orbits are characterized by a small but significant deviation from the elliptical shape in the form of some kind of angularity which indicates weak anharmonic oscil-

[17] The loops which represent higher harmonics can also be interpreted as a special kind of precession movement around the static equilibrium point $(0, 0)$.

[18] For an ideal open tube of length $700\,\mathrm{mm}$ one calculates:

$$f_2 = 2 \cdot \frac{c}{2L} = \frac{343\,\mathrm{m/s}}{2 \cdot 0.7\,\mathrm{m}} = 490\,\mathrm{Hz}$$

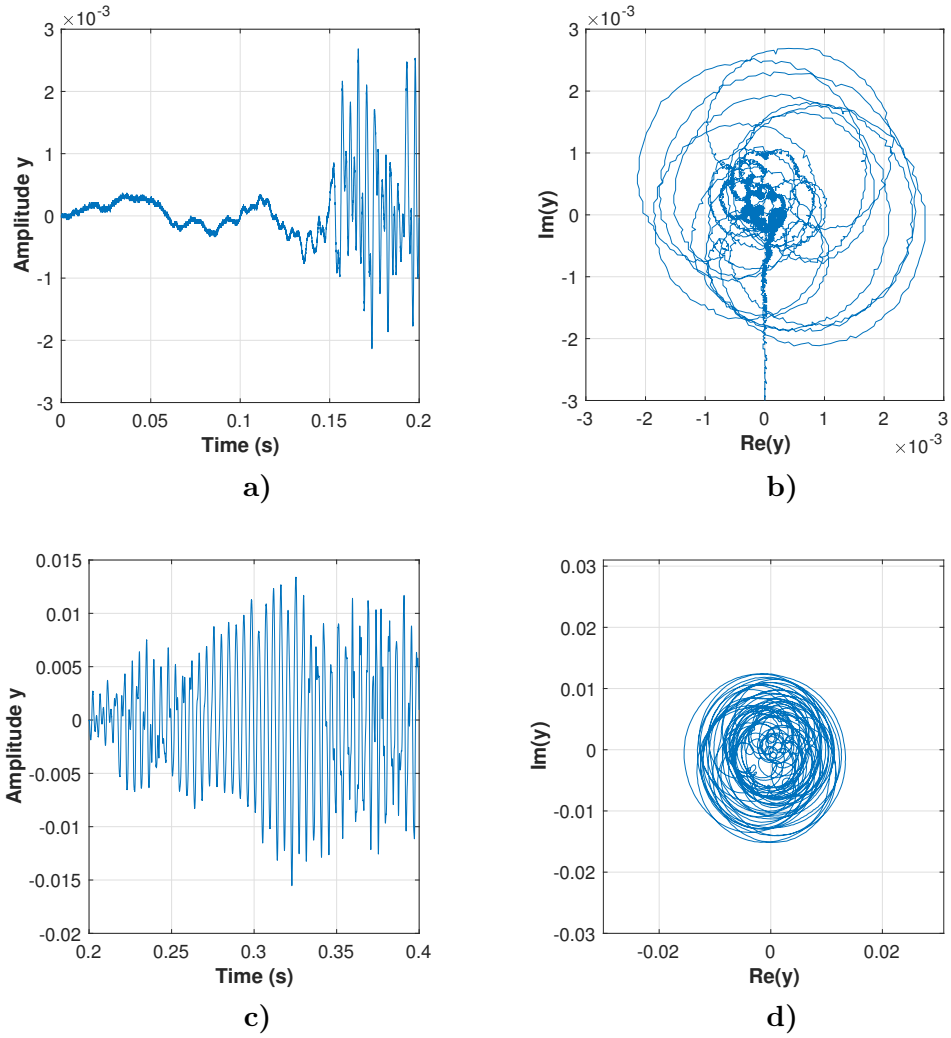

Figure 5.74: Initial blow on process of the Turkish ney - Signal and phase portraits for the period of time from $t = 0 - 0.4\,\mathrm{s}$.

lations. This seems to be caused by a limitation of possible amplitudes inside the resonator. The system forms a so-called limit cycle. This becomes even more evident looking to the subsequent dynamics of the system. The initial transient results in stable weakly nonlinear oscillations - the operation mode of the system, with the second harmonic as the leading frequency. The weak nonlinearity of the operation mode can be studied in Figures 5.76a and 5.76b. Such oscillations are known as (weak) relaxation oscillations. A prominent model of a system that can generate relaxation oscillations is the van der Pol oscillator model, cf. subsection 3.1.5.

The Figures 5.76c and 5.76d show the situation of the second overblowing process. This happens within the period of time from 3.55 s to 3.65 s. As mentioned the oscillations are nonlinear. The system switches to the next higher harmonics by changing the phase velocity on every second period. The patterns in periodicity on the one hand are an expression of the fact that the system (the sound field in the resonator tube) is forced more and more into relaxation oscillations. On the other hand the ”gaps” in periodicity lead to shorter zero crossings in the subsequent half period. Both are connected with a change in amplitude. A gap leads to an immediately following decrease of amplitude. The subsequently following shorter period leads to an increase of the amplitude. This is because the gapping generates steeper flanks on the immediately following half period. A steeper flank means a higher (particle) velocity which leads to larger

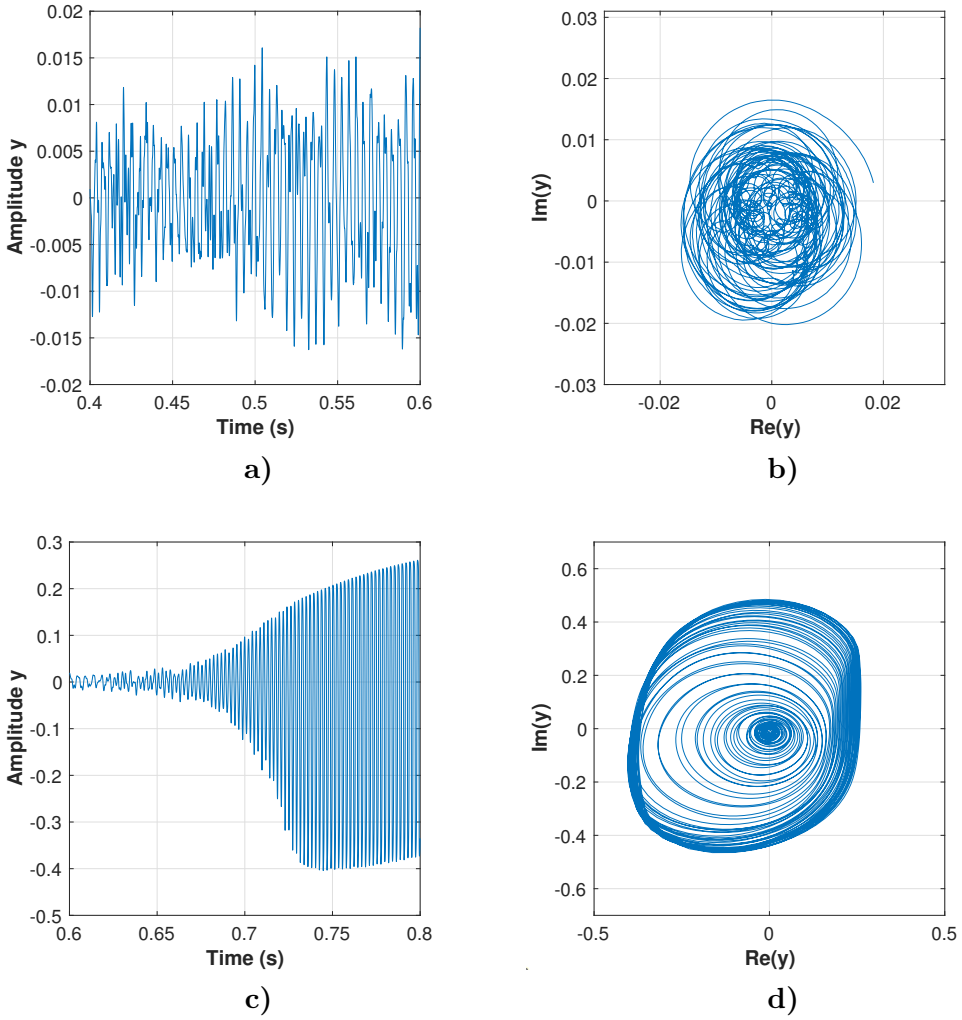

Figure 5.75: Initial blow on process of the Turkish ney - Signal and phase portraits for the period of time from $t = 0.4 - 0.8\,\mathrm{s}$. a) The system oscillates with the fundamental as the leading frequency but these oscillations are massively disturbed which leads to fluctuating amplitudes. b) In the phase space representation this results in a precession movement of the trajectory. c) The system get overblown and starts generating regular oscillations of the second harmonic. d) The increase of air flow leads to increasing amplitudes up to values of deflection inside the resonator that are limited.

amplitudes. In nonlinear oscillating systems the period (phase dynamics) and the amplitude are not longer independent to each other. One also can give an acoustical interpretation. A longer period (a gap) corresponds to a lower frequency and vice versa. Of cause, these are fictive frequencies, because they have just half a period! Nevertheless, this picture can help to understand this complicated process. Let's dwell on this image for a moment.

The forcing process which leads to an increase of gaps in periodicity generates fictive frequencies. Measuring the gaps which increase with time results in a decrease in frequency, starting from at the frequency of the previous operation mode of $f_2 = 458.7\,\mathrm{Hz}$ down to values of less than 260 Hz. The relation between the change of the periods measured by zero-crossing and the change of the corresponding decrease of the next following amplitude is approximately inversely proportional. One may ask when will this gapping (or shrinking) process comes to an end? Or to put it another way, how wide does the gaps in periodicity have to be enforced such that a new natural frequency determined by the resonators length can fit in? The answer can given at

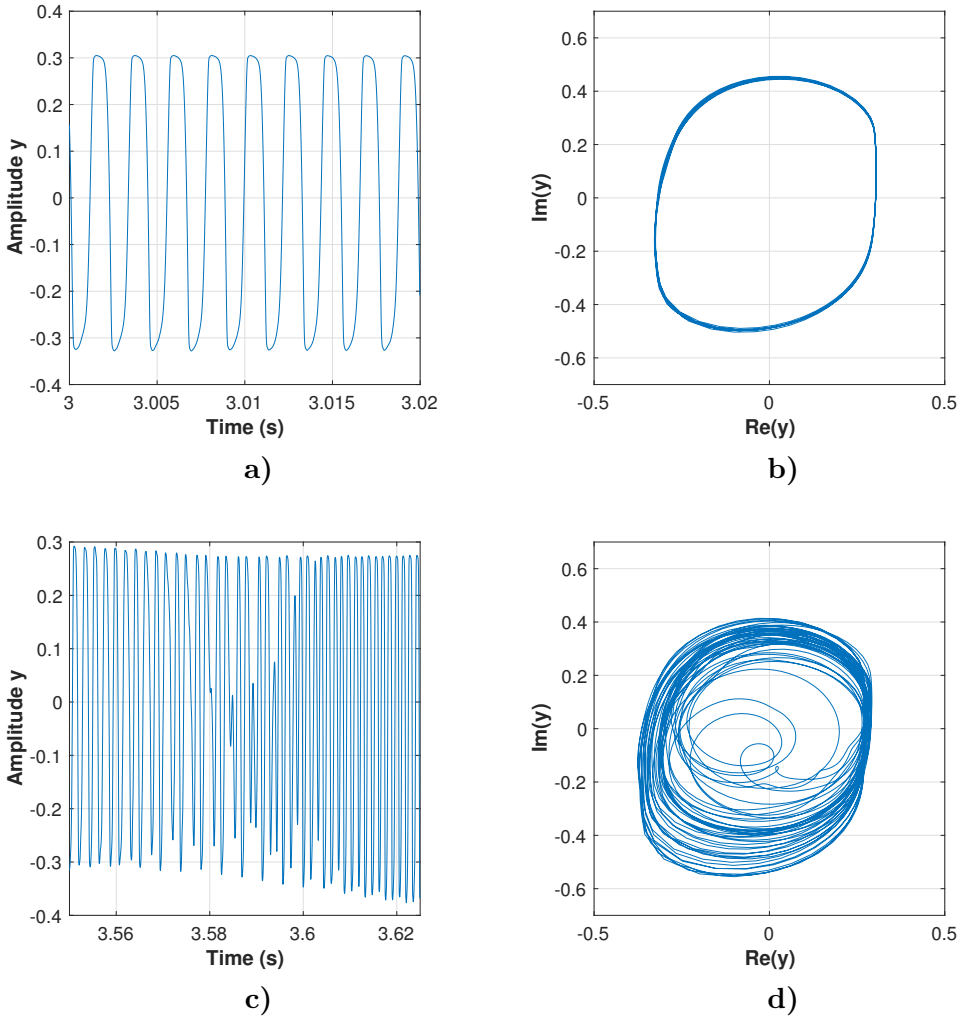

Figure 5.76: Initial blow on process of the Turkish ney - Signal and phase portraits for the period of time from $t = 3.0 - 3.62\,\mathrm{s}$. a) The operation mode with the leading frequency of $f_2 = 452.31\,\mathrm{Hz}$ and relaxation oscillations. b) The corresponding phase portrait shows a limit cycle. The deviations from a elliptical trajectory (harmonic oscillations) indicates that the oscillations are nonlinear. c) The overblowing process from the second to the third harmonic ($f_2 = 452\,\mathrm{Hz} \rightarrow f_3 = 678.5\,\mathrm{Hz}$). The process is characterized by a temporal phase shift on every second period. This nonlinear re-arrangement of the phase velocity is want we call gapping process. When the gaps become a critical time duration a filling with the next higher eigenmode starts. d) The corresponding phase portrait of the gapping process. On every loop starting from 3.58 Hz the phase velocity increases because of the new mode of higher frequency which fills the gap.

this point. If the process exceeds the formation of (half) periods, which escape the frequency of the leading frequency of the previous operation mode, here $f_2 = 452\,\mathrm{Hz}$, then filling the gaps with the next multiple of the natural frequency becomes possible. The next resonator mode is $f_3 = 683.76\,\mathrm{Hz}$. The described gapping process (shrinking process respective) continues until the third harmonic is fully established in period and in amplitude. For the sake of clarity the dynamics is shown in Fig: 5.77. The gapping process is marked by red arrows. The reader also should study the dynamics by watching the animation of the process in the supplement. From the theory of nonlinear oscillations we know that the amplitude on a limit cycle is an asymptotic stable quantity while the phase is neutral stable, which means the phase can be

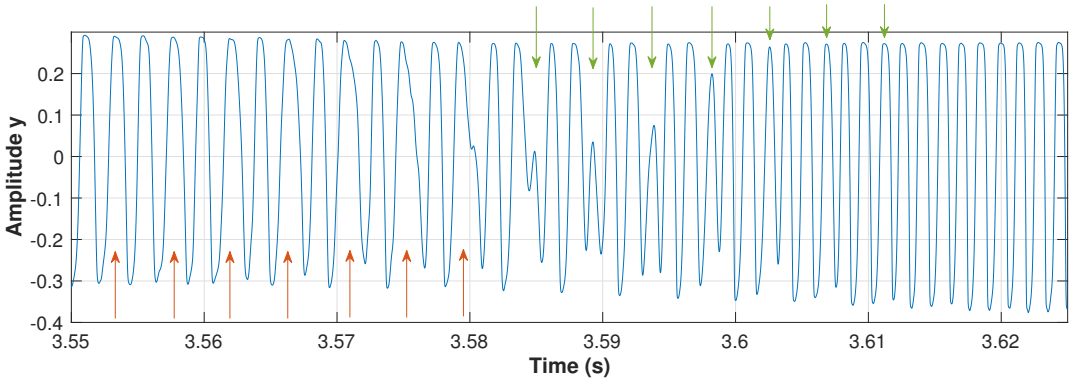

Figure 5.77: Transition process of overblowing the Turkish ney from the second harmonic ($f_2 = 452\,\mathrm{Hz}$) to the third harmonic ($f_3 = 678.5\,\mathrm{Hz}$). The gapping process on every second period is marked by arrows. The red arrows indicate the gapping, the green arrows indicate the filling process while the gapping continues.

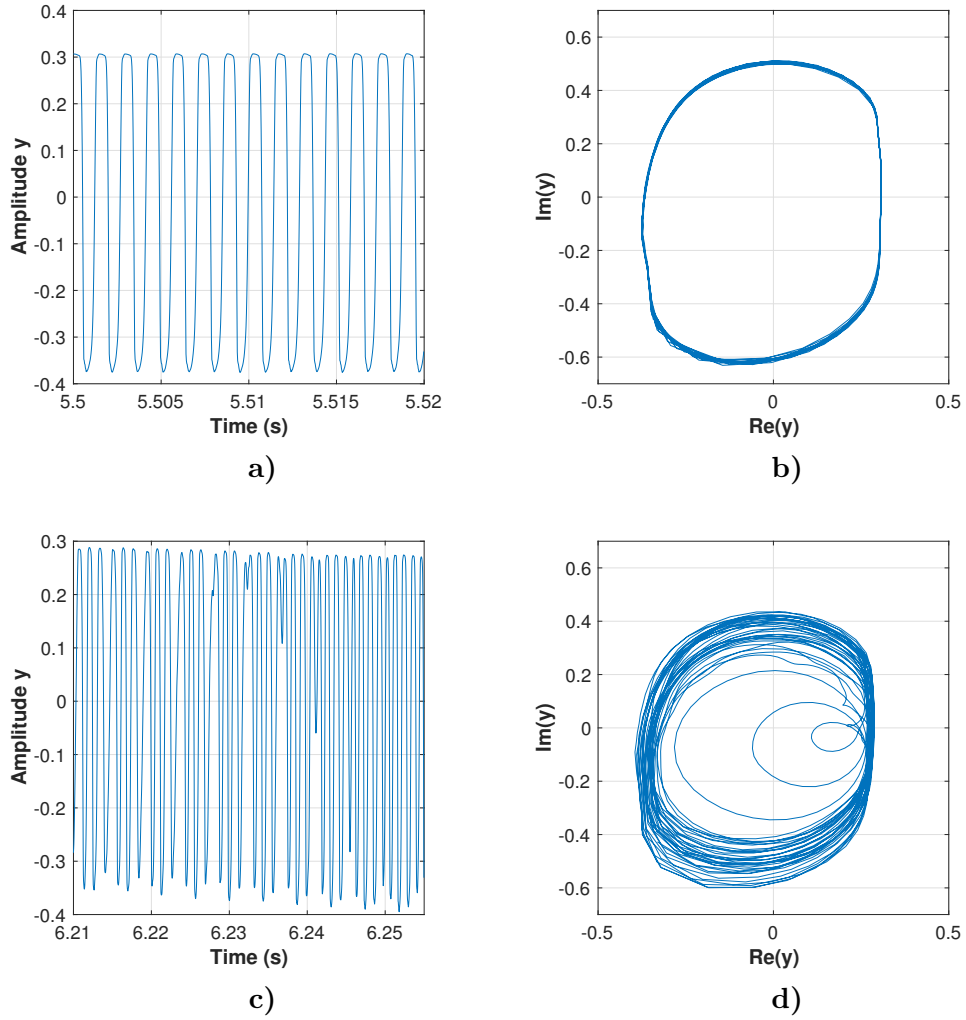

Figure 5.78: Initial blow on process of the Turkish ney - Signal and phase portraits for the period of time from $t = 0.4 - 0.8\,\mathrm{s}$.

shifted by forces[19] (and kicks too) [Pikovsky et al.(2001)]. This is the key to understand the

[19]These forces can be infinitesimal small.

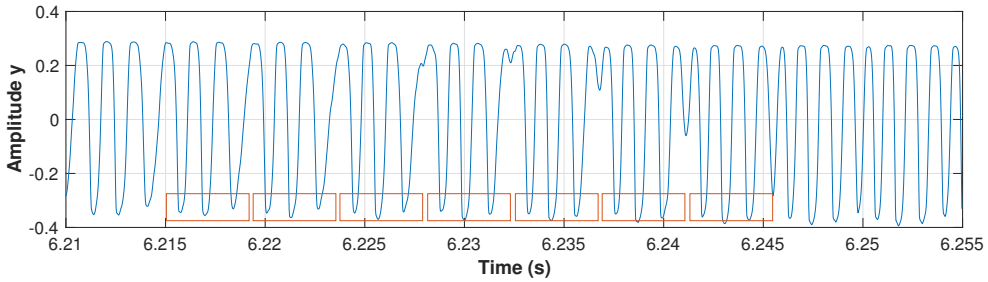

Figure 5.79: Transition process of overblowing the Turkish ney from the third harmonic ($f_3 = 678.5\,\mathrm{Hz}$) to the fourth harmonic ($f_4 = 915.36\,\mathrm{Hz}$). The patterns associated with the gapping process are marked by arrows.

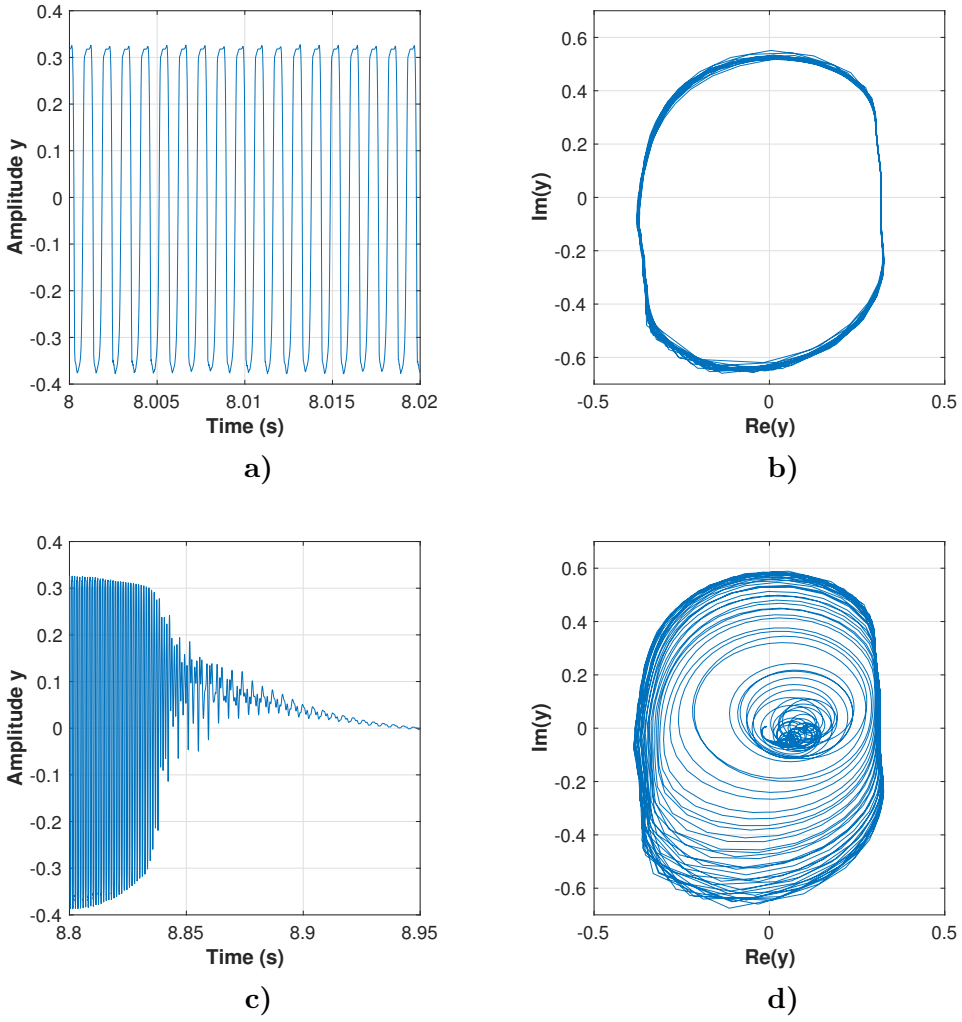

Figure 5.80: Initial blow on process of the Turkish ney - Signal and phase portraits for the period of time from $t = 8 - 8.95\,\mathrm{s}$. a) The signal of the operation mode with the leading frequency of about 915 Hz. b) The corresponding phase portrait show the limit cycle generated in the operation mode. c) The decay process where signal fades out. d) The phase portrait of the decay process.

overblowing process.

After the transition process the systems finds a new stable state of oscillations, the operation mode with the leading frequency of about $f_3 = 678.5\,\text{Hz}$. Here the system again forms a limit cycle. This is shown in Fig: 5.78a and 5.78b. The deformed trajectory again indicates nonlinear oscillations in the new operation mode. The next transition takes place in the period of time from 6.21 s to 6.25 s. This is the overblowing process from the third to the fourth harmonic. Again a temporal decrease of phase velocity, associated with a decrease of amplitudes emerge, but now in more complex alternating patterns within third periods, cf. Figs: 5.78c and 5.78d. The details of the dynamics of this transition process illustrates Fig: 5.79. Here the patterns are labeled by rectangles. The author recommends studying the dynamics of this process by the help of the animation in the supplement. What we see in all overblowing processes is a phase shift by changing the phase velocities within the periods of oscillation. This leads to "gaps" in period that are "filled" by higher oscillation modes if the gap reaches a critical duration. Note, that the amplitudes appear to be bounded upwards and downwards. Therefore increasing the amount of energy by increase the air flow cannot result in arbitrarily large amplitudes. The reason for this limitation is not yet entirely clear, but the fact for the moment is that the system responds the increasing energy input delivered by the jet's air flow with a change of its internal phase relationships by using its nonlinear capabilities. A possible explanation for the limited amplitudes or the limited sound pressure in the resonator tube is the coupling of amplitude and phase. The assumption is that the different stability properties of the amplitude and of the phase (asymptotic stable and neutral stable) are responsible for the limitation. It costs less energy to shift the phase as to increase the amplitude.

After the overblowing process the system again develops a stable state of oscillations, the operation mode with the leading frequency of about 915 Hz. The mode shows relaxation oscillations with steeper flanks compared with the previous operation mode.

For the sake of completeness, we also consider the dynamics at the end of the entire process, the so-called decay process where the instrumentalist stops blowing. In Figs: 5.80c and 5.80d it is easy to see that the system oscillates for a certain time, with all the oscillation states generated gradually fading away, in sequence, starting with the highest generated harmonics up to the fundamental. The oscillations then die out more or less irregularly, which can be attributed to the jet oscillating accordingly.

We want briefly summarize the results of the investigations of the acoustic measurements of the blowing process and the overblowing processes on the Turkish ney:

- The initial transient is characterized by irregular oscillations caused by the constitution process of the jet.
- Blowing on the fundamental frequency of the instrument and leading it to a stable operation mode is a difficult task because of internal losses caused by friction inside the resonator. The normal case on standard instruments is that the fundamental get overblown immediately.
- In the first stable operation mode the system (sound field inside the resonator tube) oscillates with the second harmonic of about $f_2 = 452\,\text{Hz}$. The system generates so called relaxation oscillations, that lead to an anharmonic oscillations and to a limit cycle in the phase space representation. The Amplitudes are limited in the system an enforce the nonlinear characteristic of the operation mode.
- In the overblowing process the system switches its leading frequency caused by an increase of air flow by changing the phase velocity periodically. This process generates gaps in the

periodicity of the signal such that the next eigenmode can filled in.

- After the overblowing process the system oscillates in a new operation mode with the next higher eigenmode as the leading frequency.

- By continuing the increase of air flow the system switches into the next overblowing process. The gapping process of higher overblowing processes takes place in an increasingly complex way by generating gaps in the periodicity on different periods depending on the eigenmode. This is associated with more complex patterns of amplitude change depending on increase and decrease of phase velocity periodically. The dependency of change of phase velocity and change of amplitude is inversely proportional.

Summary and Outlook

> There's nothing happier than being busy.
>
> Wolfgang Fischer, German botanist.

In this study which is worked out as the authors habilitation thesis different aspects of sound generation and sound formation have been discussed based on different acoustic measurements and complex numerical experiments. The selected aerophones are characterized by a comparable complexity in relation to the topic. In order to make it easier for the reader, especially musicology students, to get started with the subject, the pedagogical focus was on imparting the necessary mathematical, physical and numerical knowledge that helps to trace the details of the investigations. The focus of investigation was on researching the initial blowing process, but also on other transient processes such as overblowing the instrument. Various turbulent coherent structures could be identified and characterized, such as the turbulent jet and its shear layers, certain vortex structures that either enable, disrupt or promote the formation of sound. It could be shown how the initial sound field is created in the resonator and which coherent structures are responsible for that. Is has been shown that shock waves, or at least transsonic waves, occur in the initial transient process of aerophones, not only in brass instruments. The fluid mechanical and aeroacoustic relationships of the mutual interaction of the coherent structures generated in the initial transient provides new insights into the complex processes of sound generation in aerophones. It has been shown that geometrical constraints and obstacles, such as the position of the recorder's windway, the position of the labium of the organ pipe, the cup and the waist in the mouthpiece of brass instruments, play an important role in the formation of sound. With methods of nonlinear dynamics and coarse-graining, internal synchronization phenomena could have been proven, which are the prior condition for the successful generation of sound. Various mechanisms of internal damping and internal excitation processes have been traced. Complex nonlinear relationships and interactions have been found in all the instruments examined and discussed within the framework of the respective complex question of sound generation and sound formation in aerophones. The results are briefly recapitulated according to the selected instruments.

With acoustic high precision speed measurements using a linear microphone array it has been demonstrated that waves with shock wave characteristics occur in the initial transient of all selected brass instruments, the piccolo trumpet, the trumpet, the trombone (already known to be), the French horn and the tuba. The significance of the shock wave characteristics increases with the size of the instrument. The generation of harmonic frequencies takes place step by step in time, starting with the fundamental, in analogy to the occupancy of energy states in quantum mechanical oscillatory systems. The nonlinear sound generation process and forming process exceeds the dimensions of the instrument. The nonlinear characteristics of the oscillations (sound) increases with the size of the instrument. The larger the instrument, the more significant are the relaxation oscillations. The player produces by its lips several turbulent

coherent structures in the mouthpiece, particularly in the cup. Vortices in the cup as well as in the wait of the mouthpiece accelerate the central jet flow and lead to impulse-like initial waves in the resonator tube. The sound field inside the resonator enforces the jet's deflections by phase synchronization. The jet mass flow determines which resonator mode is amplified. The coupling of the jet and the resonator is very strong and straight forwards which leads to a short initial transient.

The acoustic high precision speed measurements on the recorder show in agreement with the results of the investigations by brass instruments impulse-like pressure waves in the initial transient. The block of the instrument is essential for a successful sound generation. The inherent windway, in particular its angle with respect to the labium determines the upstream of the jet which is generated in the cut-up region of the recorder. By re-defining the angle of attack the sound generation of the recorder can be optimized. With this procedure, which, with the help of ethnological and archaeological expertise, can be assumed to have been in use for centuries or even millennia, and which was traced within the framework of this study with numerical simulation, a fragment of a bone flute could be made playable.

The investigations on the organ pipe show trans-sonic waves in the initial transient in accordance with the findings on recorders and on brass instruments. The numerical approach delivers deep insights into the complex process of sound generation in the initial transient of the instrument. The jet plays an essential role, both in the initial generation of the sound field as wells as in maintaining the working mode of the instrument. The jet is a turbulent coherent structure that self-induces its sensitivity to lateral pressure disturbances by producing turbulent shear layers. The jet is able to self-excite its central flow velocity by generating vortices in the jet's shear layers. The free jet has self-sustained properties because it maintains periodic vortex shedding. In presence of obstacles – geometric objects like the labium – this can lead to self-sustained oscillations by generating an acoustic field related with the obstacle (the case of a labium this is a acoustic dipole). Finally, the jet is capable of self-sustaining its periodic oscillations in the presence of a resonator volume. When the jet enters the stagnant air column of the resonator, its mass flow produces impulse-like pressure fluctuations which are initially trans-sonic. Trans-sonic waves are referred to as shock waves or shocks. The trans-sonic characteristics, e.g. accumulation as well as their damping properties lead to dispersion which generates a slipstream in the wake of the trans-sonic waves. The nature of the slipstream is sonic because the trans-sonic properties decay into the next slower velocity regime. This is the origin of the initial sound field within the resonator. The energy transfer into the sonic regime depends on the phase relation of the shocks and the initial sound field in the initial transient. This is known as superposition. In-phase relations promote the energy transfer and amplify the sound field, anti-phase relations lead to a perturbuation of the amplification process and therefore lead to the generation of higher harmonics. The resonator, due to its linear properties provides a quantized set of achievable modes that can be amplified depending on the amount of energy of the driving force. Which mode preferentially gets amplified depends on the jet's mass flow, which determines the energy input. The sound field which is characterized by a strong coherency enforces the jets deflections by phase-adjustment. The mode synchronizes the jet. This is called entrainment, or roughly speaking, the resonator enslaves the jet. The phase synchronization of the jet by the resonator (its sound field) is only possible because the jet represents a nonlinear system. The ability to synchronize is essentially due to the lateral sensitivity of the jet to acoustic disturbances. This is expressed by the neutral phase stability of the jet's lateral velocity component. The synchronized coupled system jet-resonator is asymptotic stable due to flow disturbances. In this sense the jet is a self-preserving dynamic system. The neutrally stable property of the jet with respect to lateral acoustic disturbances opens the

door for external synchronization, e.g. with loudspeakers as shown by [Abel et al.(2009)] or with other jet-driven instruments shown by [Fischer (2012)] and [Fischer (2014)] as well as for interaction with external geometrical constraints shown by [Fischer (2017)].

With the investigation of the overblowing at the Turkish Ney, another important transient process has been focused on. Overblowing is the most important articulation technique in connection with rim-blown flutes, but also with brass instruments. Using precise Short Time Fourier transform the initial sound generation, the formation of the fundamental and a cascade of overblowing processes have been analyzed. The difficulties in blowing the fundamental of a standard Turkish ney instrument could be traced back to strong internal damping caused by the construction in combination with the weakness of the jet flow which would provide the fundamental mode. The internal damping disturbs the excitation process such that it becomes difficult to succeed. Increase in jet mass flow or energy input, leads to an nonlinear oscillations with the second harmonics forming a limit cycle in the phase space representation of the dynamics. Further increase in jet mass flow leads to an increase of the nonlinear character of the oscillations which is expressed in the fact that the phase velocity is periodically slowed down or accelerated and the oscillations degenerate more and more into relaxation oscillations. This process leads to gaps in the periodicity of the oscillation. If the gaps reach the duration of the initial oscillation, periods of the next higher harmonic will be inserted according to the energy supplied by the jet mass flow. The energy transfer into the next higher harmonic is realized in this way and the system forms a new working mode, now with the leading frequency of the higher harmonics. Even higher overblowing processes lead to more complex pattern in phase and amplitude dependence in the transient. When the player stops blowing the instrument, the cascade of higher harmonics development reverses and the oscillations start to decay, beginning at the instrument's highest excited natural frequency.

The work presented builds on the many preliminary works of exceptional and passionate researchers of musical instruments over the past decades. This study is a small, incomplete contribution towards a deep scientific understanding of aerophones. But it is also a start and a call to all students of musicology to continue to deal intensively with the topic of sound generation in aerophones. Some open questions should be announced at this point. How do pre-chambers like those located in organ pipes foots influence the sound generation? Intuitively is that they promote the compression of the inflow and thereby the initial velocity of the jet, which in turn leads to more sharpened, impulse-like initial shocks. Interesting would be the question of phase relation between the pre-chamber and the jet as well as of the pre-chamber and the resonator. Can couplings or even synchronization also be determined between these volumes? This also could be very important for understanding articulation processes where the oral cavity plays a dominant role, such as in playing brass instruments and rim-blown flutes. Another big question is the production of noise in aerophones which can be interpreted as disturbance of the transient processes by chance. Producing noise is not necessarily undesirable when blowing aerophones. It is often generated and actively controlled, for example when playing the jazz trumpet or when playing Sufi music. Beside the initial transient and the overblowing much more transient processes have to be taken into account. For instance, no word has been said about the huge class of transient process with respect to the use of finger holes, valves or sliding features to change the resonator length of the instrument. Brassiness is another interesting topic related to sound production and articulation in brass instruments. The player seems to have a significant influence on the shape of the shock wave. Another important field of research deals with the question how mouthpieces have to be designed to avoid common musicians health problems like focal dystonia or repetitive strain injury (RSI). Last but not least, the transient process of many other instruments such as the western concert flute, the didgeridoo, and the huge class

of reed instruments are waiting to be discovered. Much research remains to be done, and many veils on aerophones can be lifted.

References

[Abel et al.(2009)] M. Abel, K. Ahnert, B. Bergweiler (2009). *Synchronization of sound sources. Phys. Rev. Lett., 103(114301).*

[Adelung (1991)] W. Adelung (1991). *Einführung in den Orgelbau. Leipzig: Breitkopf & Hartel.*

[Andronov, Chaikin (1949)] A. A. Andronov, C. E. Chaikin (1949). *Theory of Oscillations. Princeton University Press, (1949) - pp 358.*

[Bader (2008)] R. Bader (2008). *Individual reed characteristics due to changed damping using coupled flow-structure and time-dependent geometry changing Finite- Element calculation. Proceedings Forum Acusticum Joined with American Acoustical Society Paris 2008, pp. 3405–3410 (2008)*

[Bader (2013)] R. Bader (2013). *Nonlinearities and Synchronization in Musical Acoustics and Music Psychology Springer Series Current Research in Systematic Musicology, Vol. 2, Springer Heidelberg, (2013).*

[Benade (1968)] A. H. Benade, D. J. Gans (1968). *Sound Production in Windinstruments. Annals of the New York Academy of Sciences, 155: 247-263. doi:10.1111/j.1749-6632.1968.tb56770.x*

[Bickley (1937)] W. G. Bickley (1937). *The plane jet. Phil. Mag. 23 (1937), Vol. 23, Nr. 156, pp. 727-731*

[Birkhoff (1912)] G. D. Birkhoff (1912). *Quelques théorèmes sur le mouvement des systèmes dynamiques. Bulletin de la Société mathématique de France 40: 305-323. In Birkhoff (1950), t. 1, 654-672.*

[Callen (1985)] H.B. Callen (1985). *Thermondynamics and an Introduction to Thermostatistics 2nd Edition. Wiley, pp. 1-512*

[Campbell (1999)] D. M. Campbell (1999). *Nonlinear dynamics of musical reed and brass wind instruments Contemporary Physics, Volume 40, Number 6, 1 November 1999, pp. 415-431(17).*

[Campbell, Gilbert, Myers (2021)] D. M. Campbell (2021). *The Science of Brass Instruments Springer Cham (2021).*

[Chandrasekhar (1961)] S. Chandrasekhar (1961). *Hydrodynamic and hydromagnetic stability, Oxford-Clarendon Press and New York-Oxford Univ. Press, 1961.*

[Cramer (1993)] O. Cramer (1993). *The variation of the specific heat ratio and the speed of sound in air with temperature, pressure, humidity, and CO_2 concentration The Journal of the Acoustical Society of America, Volume 93, Issue 5, May 1993, pp.2510-2516 (1993)*

[Cremer, Ising (1967)] L. Cremer, H. Ising (1967). *The Self-Exited Vibrations of Organ Pipes Acustica - Acta Acustica, Volume 19, No. 3, pp. 143–153(11), (1967).*

[Coltman (1976)] J. W. Coltman (1976). *Jet drive mechanisms in edge tones and organ pipes. The Journal of the Acoustical Society of America 60, 725 (1976); https://doi.org/10.1121/1.381120*

[Davis (1992)] R. S. Davis (1992). *Revised formula for the density of moist air. Metrologica, 29, p. 67-70, 1992*

[Darwin (1858/1859)] Darwin, C. (1858/1959). *The Origin of Species. New York, NY: Mentor Book.*

[Densmore (2007)] D. Densmore, S. Heath, T. Little (2007). *Euclid's Elements. Green Lion Press, 2007*

[Drazin (2004)] P. G. Drazin, W. H. Reid (2004). *Hydrodynamic Stability. (2nd ed., Cambridge Mathematical Library). Cambridge: Cambridge University Press (2004). doi:10.1017/CBO9780511616938*

[Elder (1992)] S. A. Elder (1992). *The thirteen. The Journal of the Acoustical Society of America 54, 1554 (1973); https://doi.org/10.1121/1.1914453*

[Fabre et al.(1996)] B. Fabre, A. Hirschberg, A. P. J. Wijnands (1996). *Vortex shedding in steady oscillation of a flue organ pipe. Acustica - Acta Acustica, 82: pp. 863–877.*

[Fabre, Hirschberg 2000] B. Fabre, A. Hirschberg (2000). *Physical modeling of flue instruments: A review of lumped models. Acustica - Acta Acustica, 86: pp. 599–610, (2000).*

[Fabre, Hirschberg (1997)] M. P. Verge, B. Fabre, A. Hirschberg, A. P. J. Wijnands (1997). *Sound production in recorderlike instruments. I. Dimensionless amplitude of the internal acoustic field. The Journal of the Acoustical Society of America, 101(5), pp. 2914-2924, (1997).*

[Fischer (2012)] Fischer, J. L. (2012). *Über Synchronisationsphänomene nichtlinearer akustischer Oszillatoren*, Diploma-Thesis, available at University of Potsdam.

[Fischer (2014)] Fischer, J. L. (2014). *Nichtlineare Kopplungsmechanismen akustischer Oszillatoren am Beispiel der Synchronisation von Orgelpfeifen*, Ph.D. thesis, available at University of Potsdam.

[Fischer (2017)] J. L. Fischer (2017). *Feedback of Different Room Geometries on the Sound Generation and Sound Radiation of an Organ Pipe. Current Research in Systematic Musicology, Volume 4, Chapter 4, pp. 109-142, Studies in Musical Acoustics and Psychoacoustics, Editor: Schneider, A., Springer (2017).*

[Fischer, Bader (2017)] J. L. Fischer, R. Bader (2017). *Numerical simulations of the turbulent flow and the sound field of the Turkish Ney end-blown flute. The Journal of the Acoustical Society of America 141, 3960 (2017)*

[Fischer (2019)] J. L. Fischer (2019). *Shock Wave Characteristics in the Initial Transient of an Organ Pipe Springer, Volume: Computational Phonogram Archiving pp. 269-304, (2019)*

[Fischer, Bader, Abel (2019)] J. L. Fischer, R. Bader, M. Abel (2019). *On the Dynamics of the Flow and the Sound Field of an Organ Pipes's Mouth Region.*

[Ffowcs-Williams, Hawkings] J. E. Ffowcs Williams, D. L. Hawkings (1969). *Sound Generation by Turbulence and Surfaces in Arbitrary Motion. Philosophical Transactions of the Royal Society, Vol. A264, Nr. 1151, pp. 321–342, (1969).*

[Fletcher (1974)] N. H. Fletcher (1974). *Nonlinear Interactions in organ flue pipes. The Journal of the Acoustical Society of America 60, 725 (1974); https://doi.org/10.1121/1.381120*

[Fletcher (1976)] N. H. Fletcher (1976). *Transients in the Speech of Organ Flue Pipes - A Theoretical Study, Acustica - Acta Acustica, Vol. 34, No. 4: pp. 224–222(10).*

[Gill (2012)] F. Gill (2012). *Flute lines - Experiencing Reconstructions Concerning Music, Bachelor thesis, Linnéuniversitetet Kalmar Växjö.*

[Heuser, H. (1994)] H. Heuser(1994). *Lehrbuch der Analysis, Teil 1. B.G.Teubner Stuttgart, (1994)*

[Hirschberg et al. 1996] A. Hirschberg, J. Gilbert, R. Msallam, A. P. J. Wijnands (1996). *Shock waves in trombones The Journal of the Acoustical Society of America 99, 1754–1758 (1996)*

[Hornborstel, Sachs (1914)] E. M. Hornbostel, C.Sachs (1914). *"Systematik Der Musikinstrumente. Ein Versuch." Zeitschrift Für Ethnologie, Vol. 46, No. 4/5, (1914), pp. 553–590. JSTOR, www.jstor.org/stable/23031207.*

[Howe, M. (2002)] M. Howe (2002). *Theory of Vortex Sound (Cambridge Texts in Applied Mathematics). Cambridge: Cambridge University Press (2014). doi:10.1017/CBO9780511755491*

[Hirschberg (1996)] A. Hirschberg (1998). *Shock waves in trombones, The Journal of the Acoustical Society of America, 99, 1754 (1996); doi: 10.1121/1.414698.* South

[Kolmogorov (1941)] A. N. Kolmogorov (1941). *The local structure of turbulence in incompressible viscous fluid for very large Reynolds numbers. Dokl. Akad. Wiss. USSR, Bd. 30, pp. 301–305, (1941).*

[Lighthill (1952)] M. J. Lighthill (1952). *On sound generated aerodynamically. Part I: General theory. Proceedings of the Royal Society of London A211: 564–587. (1952)*

L.I.Mandelstam

[Miyamoto et al. (2010)] M. Miyamoto, Y. Ito, K. Takahashi, T. Takami, T. Kobayashi, A. Nishida, M. Aoyagi (2010). *Applicability of compressible LES to reproduction of sound vibration of an air-reed instrument. (2010) Proceedings of the International Symposium on Musical Acoustics, Sydney and Katoomba, Australia, pp. 37–43, (2010).*

[Montagu (2017)] J. Montagu (2017). *How Music and Instruments Began: A Brief Overview of the Origin and Entire Development of Music, from Its Earliest Stages (A. Nikolsky, Ed.). Frontiers in Sociology. (2020)*

[Morse (1968)] P. M. Morse, K. U. Ingard (1968). *Theoretical Acoustics. Princeton, NJ: Princeton University Press.*

[Newton (1687)] I. Newton (1687). *Philosophiae Naturalis Principia Mathematica. London: Streater J.*

[OpenFoam-3.0.0 U.G. (2016)] OpenFOAM® - The Open Source Computational Fluid Dynamics (CFD) Toolbox Organization - OpenCFD Limited - User Guide (2016).
URL http://www.openfoam.com

[OpenFoam-3.0.0 P.G. (2016)] OpenFOAM-3.0.0® - The Open Source Computational Fluid Dynamics (CFD) Toolbox Organization - OpenCFD Limited - Programmer's Guide (2016).
URL http://www.openfoam.com

[OpenFoam-v7 U.G. (2019)] OpenFOAM® - The Open Source Computational Fluid Dynamics (CFD) Toolbox Organization - OpenCFD Limited - User Guide (2019).
URL http://www.openfoam.com

[OpenFoam-v7 P.G. (2019)] OpenFOAM-v7® - The Open Source Computational Fluid Dynamics (CFD) Toolbox Organization - OpenCFD Limited - Programmer's Guide (2019).
URL http://www.openfoam.com

[Cramer (1993)] O. Cramer (1993). *The variation of the specific heat ratio and the speed of sound in air with temperature, pressure, humidity, and CO2 concentration*, The Journal of the Acoustical Society of America 93, 2510-2516 (1993) https://doi.org/10.1121/1.405827

[Paál, Angster, Garen, Miklós (2006)] G. Paál, J. Angster, W. Garen, A. Miklós, (2006). *A combined LDA and flow-visualization study on flue organ pipes. Experiments in fluids 40 (2006), Nr. 6, S. 825–835*

[Pikovsky et al.(2001)] A. Pikovsky, M. Rosenblum, J. Kurths (2001). *Synchronization—A Universal Concept in Nonlinear Science. Berlin: Springer.(2001)*

[Plath, Fischer, Kirsch (2020)] N. Plath, J. L. Fischer, S. Kirsch (2020). *From Bone Fragment to Sound - Virtual Reconstruction of a 15th Century Bone Flute, Playing and operating: functionality in museum objects and instruments Cité de la musique-Philharmonie de Paris, Paris (2020).*

[Poincaré (1892-1899)] H. Poincaré. (1892–1899). *Méthodes nouvelles de la mécanique céleste. Paris: Gauthier-Villars.*

[Powell (1964)] A. Powell (1964). *Theory of Vortex Sound.* The Journal of the Acoustical Society of America 36(1) (1964).

[Rayleigh (1896)] J. W. S. B. Rayleigh (1896). *The Theory of Sound*, Republished 1945 by Dover Publications, New York.

[Schlichting (2003)] H. Schlichting, K. Gersten (2003). *Boundary-layer theory.* Berlin: Springer.

[Schuke (2016)] Alexander Schuke Orgelbau Potsdam GmbH, (2018).
URL http://www.schuke.com/

[Spalding (1961)] D. B. Spalding (1962). *A single formula for the law of the wall. Applied Mechanics, 28(3):455, 1961.*

[Strutt (1894)] J. W. Strutt Baron Rayleigh (1894). *The Theory of Sound New York, NY : Dover, 1945. - 2 v.,Dover reprint, publ. originally by Macmillan, 2nd. ed., (1894).*

[Tollmien (1935)] W. Tollmien (1935). *Ein allgemeines Kriterium der Instabilität laminarer Geschwindigkeitsverteilungen. Vandenhoeck & Ruprecht, (1935)*

[Truk, Otte (2020)] M. Turk, M. Otte (2020) *The Neanderthal Musical Instrument from Divje Babe I Cave (Slovenia): A Critical Review of the Discussion Appl. Sci. 2020, 10, 1226*

[Uchida (1956)] S. Uchida (1956). *The pulsating viscous flow superposed on the steady laminar motion of incompressible fluid in a circular pipe. Journal of Applied Mathematics and Physics (ZAMP) 7, 403-422 (1956)* https://doi.org/10.1007/BF01606327

[van der Pol (1926).] B. van der Pol (1926). *"On "relaxation-oscillations". The London, Edinburgh, and Dublin Philosophical Magazine and Journal of Science. Informa UK Limited. 2 (11): 978-992.*

[Verge, Fabre, Mahu et al. (1994)] M. P. Verge, B. Fabre, W. E. A. Mahu, A. Hirschberg, R. R. van Hassel, A. P. J. Wijnands, J. J. de Vries, & C. J. Hogendoorn (1994). *Jet formation and jet fluctuations in a flue organ pipe, The Journal of the Acoustical Society of America, 95, 1119 (1994); doi: 10.1121/1.408460.*

[Wygnanski, Fiedler (1969)] I. Wygnanski, H.E. Fiedler (1969). *Some measurements in the self-preserving jet. J. Fluid Mech., 38 (1969), pp. 577-612*

[Yoshikawa (2000)] S. Yoshikawa (2000). *A Pictorial Analysis of Jet and Vortex Behaviours during Attack Transients in Organ Pipe Models, Acustica - Acta Acustica, Volume 86, Number 4, July/August 2000, pp. 623-633(11).*

Supplementary Material

In the thesis some numerical simulations are presented in order to investigate fluid mechanical and aeroacoustic processes in transient processes of aerophones. Where appropriate, animations are referred to which the reader can study in order to better understand the respective processes. The supplementary material for the individual investigations is listed below, sorted by musical instrument.

1. **Piccolo trumpet**
   - 1.1. Animations
     - 1.1.1. Initial transient of the piccolo trumpet - pressure.avi
     - 1.1.2. Mouthpiece of the piccolo trumpet - temperature.avi
     - 1.1.3. Mouthpiece of the piccolo trumpet - velocity magnitude.avi
   - 1.2. Numerical case
2. **Bone flute**
   - 2.1. Animations
     - 2.1.1. Bone flute v05 alpha 0 - pressure.avi
     - 2.1.2. Bone flute v05 alpha 0 - velocity magnitude.avi
     - 2.1.3. Bone flute v05 alpha 10 - pressure.avi
     - 2.1.4. Bone flute v05 alpha 10 - particle tracking velocity magnitude - pressure.avi
     - 2.1.5. Bone flute v05 alpha 10 - particle tracking velocity magnitude - vorticity.avi
     - 2.1.6. Bone flute v05 alpha 20 - velocity magnitude.avi
     - 2.1.7. Bone flute v05 alpha 20 - pressure.avi
   - 2.2. Numerical case
3. **Organ pipe**
   - 3.1. Animations
     - 3.1.1. Organ pipe - Initial transient and working mode - pressure and particle velocity.avi
     - 3.1.2. Organ pipe - Initial transient and working mode - pressure.avi
     - 3.1.3. Organ pipe - Cross-section resonator - pressure.avi
   - 3.2. Numerical case
4. **Jet - Labium**
   - 4.1. Animations
     - 4.1.1. Jet - Labium - Cross-section Labium tip - pressure.avi